Provisional PhD Thesis

Submitted for the degree of Doctor of Philosophy from

UNIVERSITÉ POLYTECHNIQUE HAUTS-DE-FRANCE

And INSA HAUTS-DE-FRANCE

And POZNAN UNIVERSITY OF TECHNOLOGY

Subjects: Mechanics of solids, materials, structures, and surfaces (UPHF), Mechanical Engineering (Poznan) and History and Civilizations: history and archaeology of ancient and medieval worlds, art (UPHF)

Presented and defended by François BERKMANS.

On 02/12/2025, Valenciennes

Doctoral school:

Doctoral School Polytechnique Hauts-de-France (ED PHF n°635)

Doctoral School Poznan University of Technology

Research unit:

Laboratory of Industrial and Human Automation control Mechanical engineering and Computer science (LAMIH – UMR CNRS 8201)

Research Laboratory Societies & Humanities (LARSH)

Division of Metrology and Measurement Systems (Poznan University of Technology)

Surface Topography and Multi-scale Complexity: A Study from Materials to Works of Art

Provisional JURY

Reviewers

- Rosén, Bendt-Göran. Professor. Halmstad University, Halmstad, Sweden
- Borel, Anthony. Assistant Professor (HDR). National Museum of Natural History UMR 7194 CNRS, Paris, France
- Pawlus, Pawel, Professor, Rzeszów University of Technology, Rzeszów, Poland

Examiners

- Królczyk, Jolanta. Professor. Opole University of Technology, Opole, Poland
- Marteau, Julie. Assistant Professor (HDR). Université Technologique de Compiègne, Compiègne, France
- Huftier, Arnaud. Vice-President of University and Professor. Université Polytechnique Hauts-de-France, Valenciennes, France

Thesis co-supervisor: Bigerelle, Maxence. Professor. LAMIH UMR CNRS 8201, Université Polytechnique Hauts-de-France, Valenciennes, France
Thesis co-supervisor: Wieczorowski, Michał. Professor. Poznan University of Technology, Poznan, Poland

Invited members

- Nys, Ludovic. Professor. LARSH, Université Polytechnique Hauts-de-France, Valenciennes, France
- Bartkowiak, Tomasz. Assistant Professor (HDR). Poznan University of Technology, Poznan, Poland

Thèse de doctorat provisoire

Pour obtenir le grade de Docteur de

l'UNIVERSITÉ POLYTECHNIQUE HAUTS-DE-FRANCE

et de l'INSA HAUTS-DE-FRANCE

et l'UNIVERSITÉ POLYTECHNIQUE DE POZNAN

Disciplines : Mécanique des solides, des matériaux, des structures et des surfaces (UPHF), Ingénierie Mécanique (Poznan) et Histoire et civilisations : histoire et archéologie des mondes anciens et médiévaux, de l'art (UPHF)

Présentée et soutenue par François BERKMANS.

Le 02/12/2025, à Valenciennes

École doctorale :

École Doctorale Polytechnique Hauts-de-France (ED PHF n°635)
École Doctorale de l'Université Polytechnique de Poznan

Unité de recherche :

Laboratoire de Recherche Sociétés & Humanités (LARSH)
Laboratoire d'Automatique, de Mécanique et d'Informatique Industrielles et Humaines (LAMIH – UMR CNRS 8201)
Division de Métrologie et Systèmes de Mesures (Université Polytechnique de Poznan)

Topographie de Surface et Complexité Multiéchelle : Une Étude des Matériaux Industriels aux Œuvres d'Art

JURY provisoire

Rapporteurs

- Rosén, Bendt-Göran. Professeur, Halmstad University, Halmstad, Suède
- Borel, Anthony. Maitre de conférences (HDR), Muséum National d'Histoire Naturelle UMR 7194 CNRS, Paris, France
- Pawlus, Pawel, Professor, Rzeszów University of Technology, Rzeszów, Pologne

Examinateurs

- Królczyk, Jolanta. Professeur. Université Technologie d'Opole, Opole, Pologne
- Marteau, Julie. Maître de conférences (HDR). Université Technologique de Compiègne, Compiègne, France
- Huftier, Arnaud, Vice-Président d'Université et Professeur d'Université. Université Polytechnique Hauts-de-France et LAMIH UMR CNRS 8201, Valenciennes, France

Co-directeur de thèse : Bigerelle, Maxence. Professeur. LAMIH UMR CNRS 8201, Université Polytechnique Hauts-de-France, Valenciennes, France
Co-directeur de thèse : Wieczorowski, Michał. Professeur. Université Technologique de Poznan, Poznan, Pologne

Membres invités

- Nys, Ludovic. Professeur. LARSH, Université Polytechnique Hauts-de-France, Valenciennes, France
- Bartkowiak, Tomasz. Maître de conférences (HDR). Université Technologique de Poznan, Poznan, Pologne

Acknowledgements

First and foremost, I would like to express my deepest gratitude to the Université Polytechnique Hauts-de-France and to Poznań University of Technology for providing me with a stimulating academic environment as well as invaluable support throughout this doctoral research. Their institutional and scientific assistance has been fundamental to the completion of this work. I am also sincerely grateful to my two supervisors, Maxence and Michał, for their constant guidance.

I wish to extend my heartfelt thanks to the Région Hauts-de-France for its financial support and for placing its trust in this project, which greatly facilitated its development. My thanks also go to the Fondation Polytechnique Hauts-de-France for their mobility grant.

To my parents, I am infinitely grateful for their unwavering support, their patience, and their encouragement: none of this would have been possible without them. I also wish to thank my brother Nicolas and his partner Anaïs for their constant kindness, their presence, and their valuable advice during the key moments of this journey.

To my colleagues in the laboratory, Julie Lemesle, Robin Guibert, Clément Moreau, and Patryk Mietlinski, with whom I had the honour and pride to collaborate for four years: may their talent guide them towards the scientific careers they so rightly deserve.

To Ludovic Nys, who believed in me from the very beginning and told me at the end of my master's degree: "You must pursue research."

To Sylwia, without whom I would not be where I am today, who has undoubtedly been the wisest and most insightful person I have ever met, and who shares my life.

To my friends, who patiently waited for me without ever showing frustration.

To all the people who contributed, directly or indirectly, to this journey, I wish to express my sincerest gratitude.

Remerciements

Je tiens tout d'abord à exprimer ma plus profonde gratitude à l'Université Polytechnique Hauts-de-France et à l'Université Technologique de Poznan pour m'avoir offert un environnement académique stimulant ainsi qu'un soutien inestimable tout au long de cette recherche doctorale. Leur appui institutionnel et scientifique a été fondamental pour la réussite de ce travail. Je remercie également mes deux directeurs de thèse Maxence et Michał pour leur accompagnement constant.

J'adresse aussi mes sincères remerciements à la Région Hauts-de-France pour son soutien financier et sa confiance dans ce projet, qui ont grandement facilité son développement. Même remerciement pour la Fondation Polytechnique Hauts-De-France pour leur bourse de mobilité.

À mes parents, je suis infiniment reconnaissant pour leur soutien indéfectible, leur patience et leurs encouragements : rien de tout cela n'aurait été possible sans eux. Je remercie également mon frère Nicolas et sa compagne Anaïs pour leur bienveillance constante, leur présence et leurs conseils avisés lors des moments clés de ce parcours.

À mes collègues de laboratoire Julie Lemesle, Robin Guibert, Clément Moreau et Patryk Mietlinski, avec qui j'ai la fierté et l'honneur d'avoir collaboré pendant 4 ans. Que leur talent les guides vers les carrières scientifiques qu'ils méritent.

À Ludovic Nys, qui a cru en moi dès le début et m'a dit au terme de mon master : « Tu dois faire de la recherche. »

À Sylwia, sans qui je ne serais pas là où je suis à aujourd'hui, qui a sans doute été la personne la plus sage et avisée que j'ai rencontré et qui partage ma vie.

À mes amis qui m'ont patiemment attendus sans jamais montrer d'agacement.

À toutes les personnes qui ont contribué, de près ou de loin, à cette aventure, je tiens à exprimer ma gratitude la plus sincère.

Contents

List of Figures

List of Tables

General Introduction

In surface metrology, it is very common to use a classical methodology that constitutes most studies found in the literature. This methodology is composed of two major axes: on one hand, the study of the influence of a modification process on the surface (e.g., the influence of rolling on surface roughness), and on the other hand, the optimization of a surface functionality (e.g., increasing surface hydrophobicity). These two axes are not limiting; in reality, they correspond to relevant industrial issues that help improve the quality of objects produced by industry. The problem is that these two very linear axes do not allow for a different methodological approach to the discipline of surface metrology.

This thesis aims to present a new methodological approach through which several issues directly affecting the field of surface metrology remains under-studied (some never). This new methodology is presented in the form of a spectrum called the 'Surface Information Acquisition Spectrum' (SIAS). The objective is to study the informational complexity aspects at all scales of this spectrum. To achieve this, various tools have been created, including linguistic tools, analogies, roughness parameters, and applications in various fields, demonstrating that the spectrum can be applied well beyond the industrial environment. The spectrum is defined in Figure 0.1, with its two ends representing, on one side, human perception and the qualitative aspect of things, and on the other, the quantification of elements.

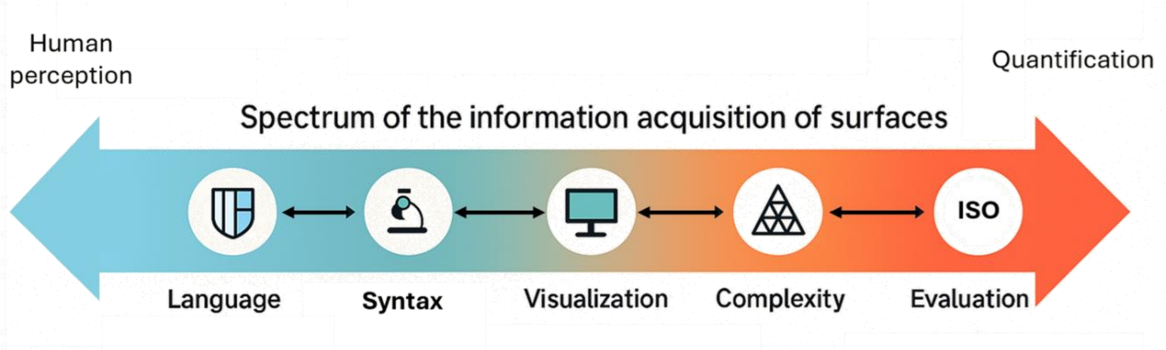

Figure 0.1 *Surface Information Acquisition Spectrum*

To understand the elements of the spectrum, it is necessary to define the concepts that constitute it (Figure 0.2). First, the notion of Language defines the function of expression of thoughts and communication between humans expressed as signs systems enabling communication. The different elements of a surface are named in various ways, as we will see in Chapter 1, and the current method of terminology for surface components presents certain issues. This notion requires a system to be standardized, which brings us to the concept of Syntax. Syntax aims to determine the system in which the terminological aspect of surface objects is placed, because without a system, a sequence of words remains incoherent (a similar observation can be made in computing). Syntax, in a way, determines contextualization. As we will see in Chapters 2 and 5 the syntax of an image can be closely related to its style, in other words, how the arrangement of elements constitutes a work with a particular style. Halfway between human perception and quantification lies the aspect of visualization. Indeed, the visualization of surfaces is merely a visual representation made by a computer system of an object that we cannot observe with the naked eye. This concept is present in almost every chapter but takes on major importance in Chapter 3, which deals with visualization artifacts in the discretization of the Von Koch snowflake. The notion of complexity is closely related to fractals, placing it between visualization and evaluation. Fractals are non-Euclidean geometries that are not only visual but also used in the evaluation of surfaces as a model of complexity. Finally, evaluation is represented here by the computation of a system to obtain quantitative information, such as roughness parameters or the graphical complexity of heraldry. To address the thesis title 'Surface Topography and Multiscale Complexity,' one can indeed use all the concepts of the spectrum to determine the dissemination into chapters: language complexity, which tends to be minimized here; syntactic complexity (i.e., stylistic), which tends to be determined; and structural complexity (heraldic, fractal, and surface), which tends to be quantified.

This methodological approach allows for the incorporation of a relevant interdisciplinary approach into the field of surface methodology, which, through results, enables the creation of new sub-disciplines.

In Chapter 1 of this thesis, we present the outline of a terminological system that allows for better description and indexing of surface topographies. The chapter provides a state-of-the-art review of the terminological aspects concerning surfaces currently and proposes a standardized system that addresses both language and syntax points. This system is a first attempt at interdisciplinary practice with surface topographies as the main subject.

Staying on the topic of language the author undertakes a study on the multi-scale heraldic complexity, starting from the premise that heraldry is a system whose graphical and textual complexity can be quantified. This study, presented in Chapter 2, introduces a calculation method and gives element of answer. Using an approach that compares coats of arms to 2.5-D surfaces, we shed light on the true nature of heraldry and determine whether it functions more like a language-type system or a fractal one, hence its positioning between language and visualization.

Following a logic of multi-scale graphical complexity, Chapter 3 deals with a well-known fractal geometry, the Von Koch snowflake, and the problems encountered in its discretization when created digitally. Indeed, since the fractal dimension of the Von Koch snowflake is known in advance, various algorithms adopting the philosophy of mathematician Richardson are used to determine which one minimizes computation problems.

Chapter 4 presents a new method for fractal characterization of surfaces. Using the roughness parameter Sdr and a Gaussian filter, it is possible to characterize the complexity of sandblasted surfaces. This method is also applied in Chapters 5.

Chapters 5 presents an original way of studying the surfaces of art objects using methods like those developed for industry in Chapter 4.

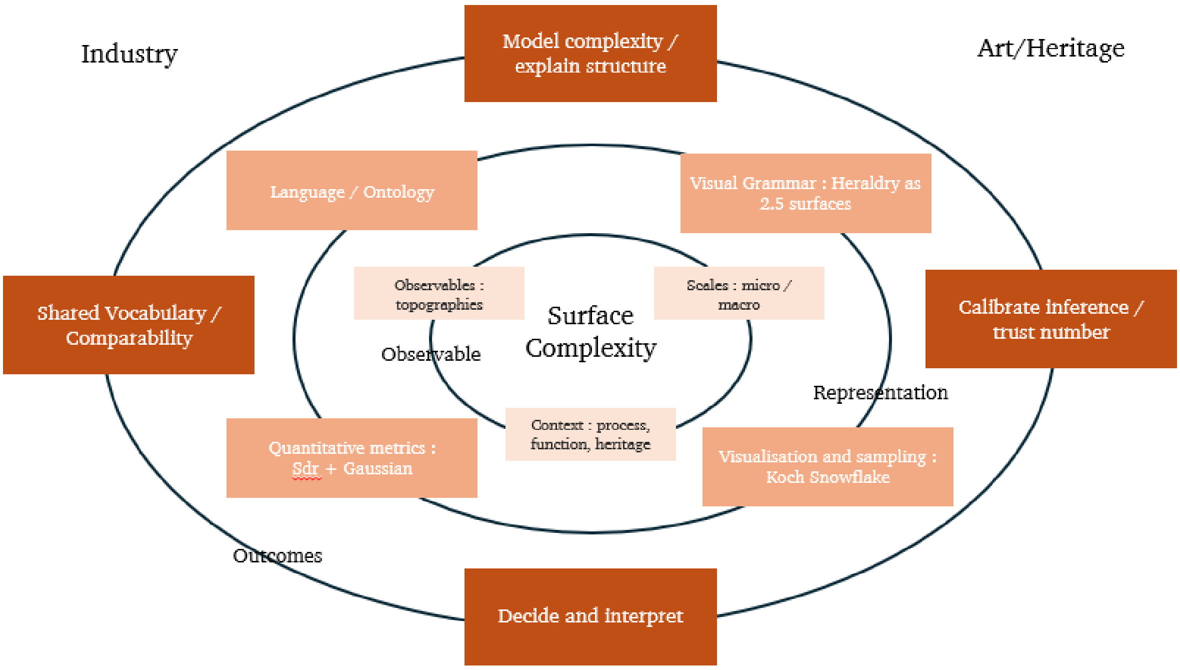

Figure 0.2 *Schematic overview and conceptual framework centred on Surface Complexity*

Thesis contributions. (1) SIAS conceptual framework linking language, visual syntax, visualization/discretization, and evaluation. (2) Unified, phenomenon-centred OWL ontology (Chap. 1). (3) Formalization of the heraldic surface as a 2.5D information system and quantification of its complexity (Chap. 2). (4) Discretization-error model and resolution criteria via the Koch snowflake (Chap. 3, Art. I). (5) Multi-scale Sdr + Gaussian-filter method, more stable than the “Richardson patchwork” (Chap. 4, Art. II). (6) Uncertainty quantification via Bootstrap and process–topography analysis in an industrial context (Chap. 4, Art. III). (7) Transfer to the artistic domain: topographic signatures and the cross-domain reach of the SIAS (Chap. 5, Art. IV).

Chapter 1

Description of Surface Topography

A Terminological Ontology for Surface Metrology

Prolegomena of the Chapter 1

In the framework established by the general introduction, this first chapter occupies the "language" tier of the Surface Information Acquisition Spectrum (SIAS), the stage at which surface knowledge remains qualitative and entirely dependent on the words we choose. Despite the spectacular rise in instrumental resolution (from white-light interferometry to atomic-force microscopy), the terminology of surface metrology is still fragmented: the same kind of phenomenon may be labelled striations, scratches, or grooves, depending on the norm, the language or the industrial sector. This dispersion impedes data comparability, obstructs knowledge sharing and seeds ambiguity in every downstream operation of the SIAS. Consequently, the chapter seeks to establish a phenomenon-centred, machine-readable vocabulary capable of describing surface features unambiguously across engineering and other contexts. After mapping the overlaps and gaps in existing glossaries (ISO 25178-2, ASTM B.46-1, VIM and others), we build a ontologic meta-model, phenomenon, attribute, context, and implement it in OWL, complete with possibility of SPARQL queries and examples of data architecture. By transforming scattered terminology into a coherent ontology, the chapter lays the cornerstone of the SIAS: it anchors all subsequent levels, visual syntax, numerical evaluation and fractal analysis, in a shared linguistic substrate, ensuring that every measurement henceforth refers to precisely the same concepts.

1.1 Chapter Introduction

In the field of surface metrology, the case study addressed here concerns the terminology used to describe surface-related phenomena, what could be referred to as topographical phenomena, insofar as they emerge from the actual shape of the surface. The term topographical phenomena, by contrast, would imply that these phenomena derive exclusively from surfaces quantified through 3D topographic measurements using the appropriate instruments. The terminological issue addressed here does not concern the methods or instruments related to surface metrology, which are already adequately defined by standards such as ISO 25178 [1]. The elements we are referring to provisionally and by way of example, called "scratch," "groove," "dimples," and so on, are phenomena that require a certain degree of magnification to be properly observed and identified as such. Indeed, visual-tactile inspections or visual observations without the possibility of magnification do not allow for an accurate assessment of the components of surface phenomena, making it difficult to differentiate them precisely (e.g., depth, edge type, shape). While perception plays a fundamental role in the initial identification of surface phenomena, our concern here is not with the subjective variability of perception itself [2]. Rather, we focus on the semantic relationship between the signifier (i.e., the term) and the signified (i.e., the mental representation of a thing) (Figure 1.1). According to Ferdinand de Saussure, the signified is distinct from its referent, the real world object (in our case the surface phenomena) designated by the sign (i.e., concept and terms) [3]. Ogden and Richards argued that any linguistic sign involves three interconnected components: the symbol (the term or signifier, e.g., *dog*), the referent (the real-world object or action to which the word refers), and the thought or reference (the concept evoked by the symbol, which may vary across individuals). This model emphasizes that meaning arises not directly from the word object link, but through the mediation of conceptual interpretation [4].

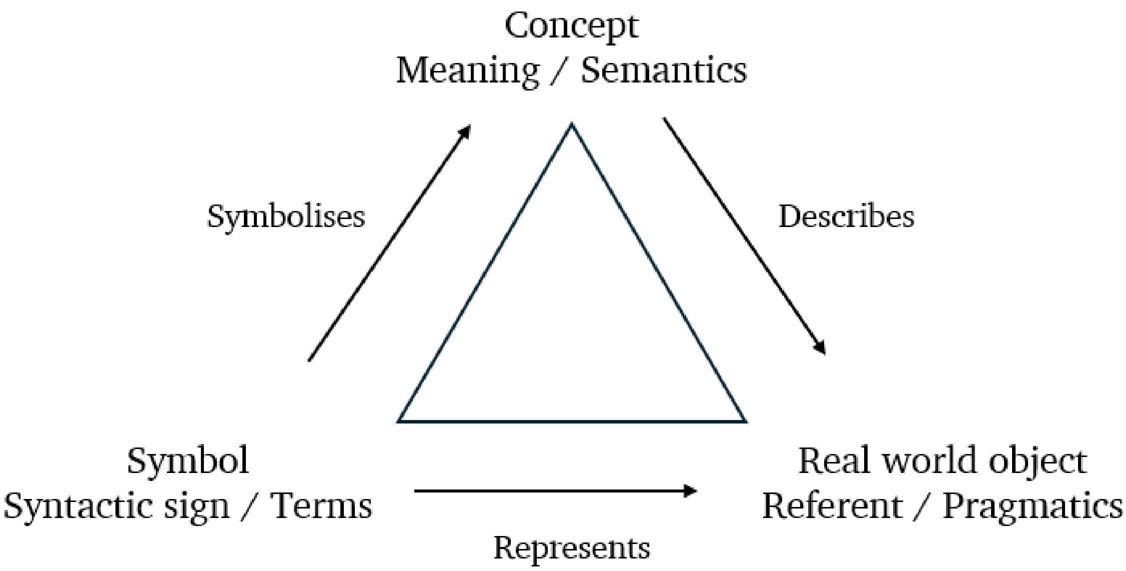

Figure 1.1 *The Semiotic Triangle (Ogden & Richards)*

Surface metrology is usually approached from a technical or normative perspective, focusing on measurement principles, instrumentation, and the application of standards. However, the way we describe surfaces, the vocabulary we use to designate what is seen or measured, has a profound impact on how these phenomena are understood, communicated, and compared. Terminology is not treated here as a neutral or passive lexicon, but as an active system of meaning that reflects and shapes technical practices. The terms used in metrology are not merely labels; they encode assumptions about what is measurable, visible, and relevant. In this context, the challenge lies less in how a feature is perceived individually, and more in how a shared and standardized terminology can accurately and consistently map onto objectively measured surface phenomena.

This chapter examines how topographical phenomena are named, classified, and describe. This observation is accompanied by a proposed solution: the development of a standardized resource description framework aimed at creating a new type of systematic phenomena-centred surface classification.

1.1.1 Definition of Terminology

Terminology refers to the systematic study and use of terms within a specific field of knowledge. It encompasses not only the vocabulary used to describe concepts, phenomena, and procedures, but also the relationships between those terms and the underlying conceptual structures they represent. In scientific disciplines, accurate and consistent terminology is essential for clear communication, reproducibility of results, and the development of shared standards. Terminology serves as both a linguistic and cognitive tool: it enables specialists to categorize and convey complex ideas while also shaping the way knowledge is structured and transmitted. In fields such as surface metrology, where concepts are often interdisciplinary drawing from physics, engineering, and materials science, terminological clarity becomes even more crucial to ensure that measurements, methods, and interpretations are understood and applied consistently across domains. This definition is derived from a combination of two sources: the ISO 704:2022 standard [5] and the book on terminology by Castellvi [6].

Terminology is related to what is known as specialized languages, which refers to the use of a natural language to convey domain-specific knowledge. It is not an autonomous system with its own linguistic rules but rather a subset or fragment of the general language [7]. Therefore, it does not involve distinct syntactic or lexical structures, and no linguistic theory has successfully separated its functioning from that of the natural language as a whole. While specialized languages can be identified through the presence of specific terminology, this approach has limitations. Nearly every human activity, technical or not, generates its own vocabulary, which could suggest the existence of countless specialized languages, thereby diluting the concept. Moreover, technical terms lack specific morphological or lexicological markers distinguishing them from ordinary words [8,9], unlike scholarly terms that may have unique etymological roots [10]. Semantically, even within specific disciplines, many terms (e.g., *sustainable growth* or *open government*) do not denote precisely defined concepts, and some may even appear contradictory or metaphorical, further challenging the technical rigor expected in specialized language.

1.1.2 Surface Metrology

The analysis of surface topographies using metrology involves the study of the microgeometry of these surfaces once quantified using appropriate measurement devices [11]. Surfaces are complex elements that can also be defined as solid-gas or solid-liquid interfaces, and their properties depend on the nature of the solid, the surface preparation methods, and the interaction of the surface with its environment [12]. Leach describes surface as the "overall surface structure of a part, surface form as the underlying shape of a part and surface texture as the feature that remain once the form have been removed" [13]. Surfaces contain irregularities of varying orders, ranging from simple deviations from the nominal shape to the scale of interatomic distances. Surface texture is a series of repetitive or random deviations from the nominal form, which constitutes the three-dimensional topography of the surface. It includes: 1) roughness, 2) waviness, 3) lay, 4) forms and 5) flaws. Roughness is characterized by the presence of hills (local maxima) and valleys (local minima) with varying amplitudes and spacings.

Historically, surface metrology has key dates marking the transition between paradigms, much like other sciences. These paradigms are characterized by the emergence of new instrumentation technologies that enable surface analysis at different scales. The history of instrumentation development is well summarized in Chapter 4 of Whitehouse's book [14] . To be concise, we will directly discuss the period of the last 'paradigm shift in surface metrology' [15,16]. The current shift in surface metrology is highlighted by three key transitions: from profile (2D) to areal characterization (3D), from stochastic to structured surfaces, and from simple geometries to complex freeform geometries, covering scales from millimeters to sub-nanometers. The gradual transition in the 1980s from 2D profiles obtained via tactile profilometers since the 1930s to optical devices enabled the acquisition of 3D maps (Note: Although a more accurate definition would be to refer to it as 2.5D if we consider that the normal measurement of the surface hides elements such as re-entrants [17]).

Pioneering work on areal surface texture characterization was conducted by a European consortium led by Ken Stout and Thomas Matthia, resulting in the 'Blue Book' [18] and the 'Birmingham-14' parameters. Subsequent ISO standardization efforts revealed the need for further research, leading to the 'SURFSTAND' project (1998-2001) led by Liam Blunt from the University of Huddersfield. This project produced the 'Green Book' [19], which laid the foundation for future specification standards. The standards used in these works defining areal surface texture parameters are ISO 25178-2 [1] and ASME B46.1 [20].

The issue of terminology in surface metrology is undeniably linked to the plurality of disciplines that engage with it. Since surfaces cover the entirety of solid objects, it is unsurprising that a wide range of scientific fields study surface properties for various applications, as illustrated in Table 1.1. As we will see later, these disciplines often use different terms to describe similar surface phenomena, due to the lack of a standardized terminology. In the Science Direct search engine for scientific communications, corresponding to the key words *surface roughness*, the number of scientific articles corresponding to this entry are 5168 in 2000, 10291 in 2010 and 27124 in 2020. The development of measuring equipment and the new possibilities for modifying surfaces are considerably expanding the research possibilities (e.g., Table 1.2 is only showing a few manufacturing processes to modify the surface). The results of research i.e., scientific publications and expert-to-expert communications, show new surface state.

Surface Topography application	
Wettability	Photolithography
Conductivity	Archaeology
Optics	Photo-voltaic panels
Biomedical	Cosmetics
Tribology	Sealing

Table 1.1 *Domains of research analysing surface topographies*

Manufacturing process			
Drilled	Filed	Broached	Bored
Ground	Reamed	Polished with stamping	Stoned
Polished	Buff polished	Sand cast	Shell moulded
Precision cast	Forged	Die cast	Hot rolled
Mandrel-formed	Punched	Cold rolled	Drawn
Sheared	Flame cut	Emery cloth polished	Sandblasted
Shot blasted	Abrasive ground	Milled	Turned

Table 1.2 *Various surface modification processes extracted from among many others in Scheffer's book [21]*

1.1.3 The Objects of Observation

Somewhat, the real-world object defined in the semantic triangle presented in the introductory section of this chapter is not the actual surface as such. Indeed, surface phenomena only become fully observable beyond a certain level of magnification. What we are referring to is not the physical object itself, which is imperceptible to the naked eye, but rather its digital representation, which allows us to name and analyse it. These digital representations are generated by various apparatuses associated with the discipline of surface metrology, typically in the form of 2D profiles or height maps (Figure 1.2). A height map represents the height of points along the z-axis within a regular sampling grid of the x and y image axes, forming a matrix. These height maps can be visually modified to help researchers better understand surface phenomena. Conventionally, a colour scale is applied to the map, allowing pixels to be color-coded according to their height. The choice of colour scale is of little importance in the context of our analysis, although the issue of selecting the most appropriate visualization is discussed in the article by Crameri et al [22].

To better visualize surface phenomena, a 3D mesh can be generated from the height map. A polygon mesh is a three-dimensional object used in computer graphics, composed of vertices, edges, and faces arranged into polygons. These faces are typically made up of triangles, quadrilaterals, or other simple convex shapes, as this simplifies rendering. However, they can also be combined to form more complex concave polygons or polygons with holes.

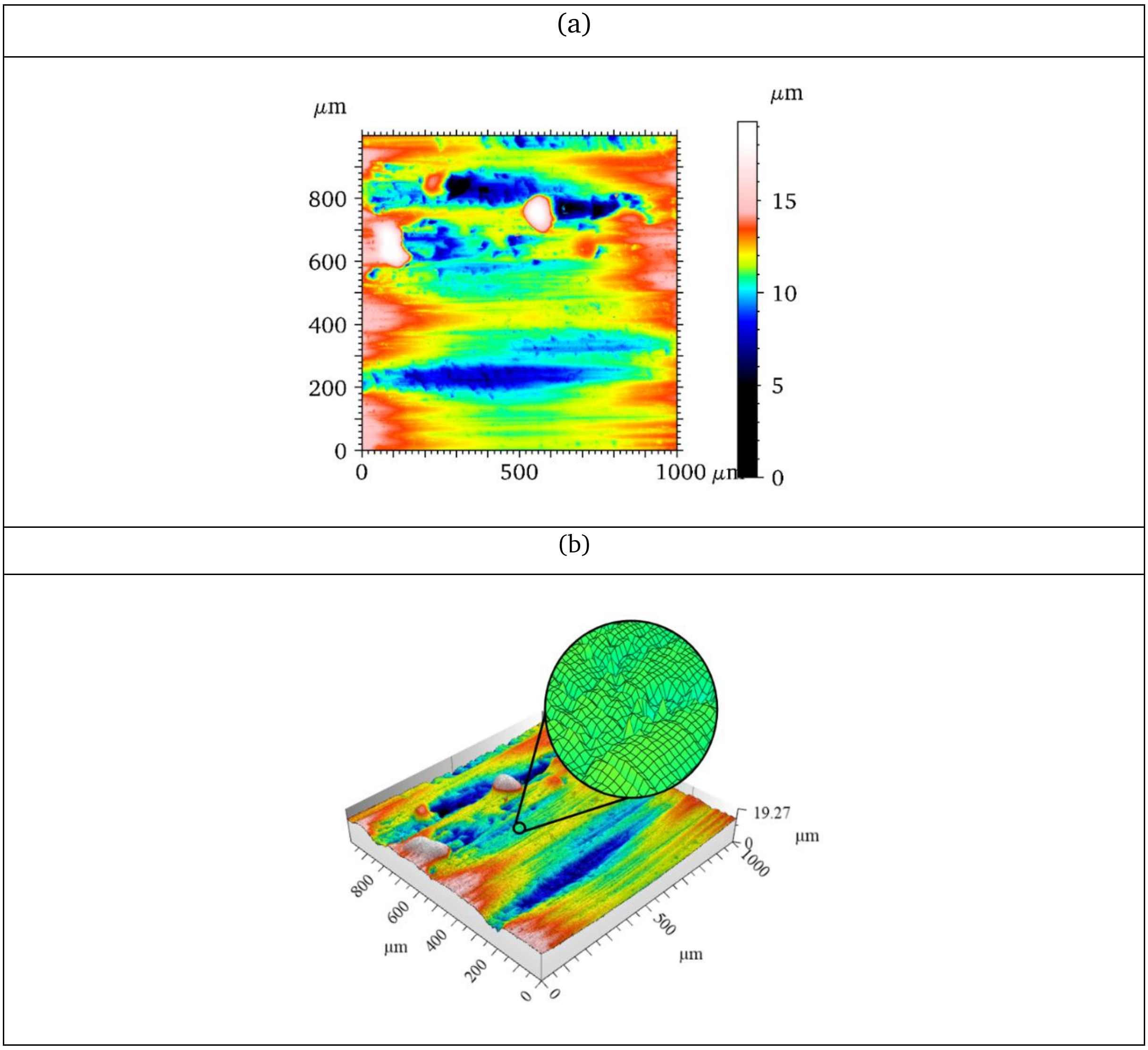

Figure 1.2 *Surface topography visualization: (a) heightmap in normal view, (b) in 3D mesh view*

1.1.4 Surface Roughness, Waviness and Form

Surface phenomena are typically categorized according to their scale and origin. Roughness refers to fine-scale deviations that arise directly from manufacturing processes, such as tool marks generated by turning or surface impressions produced by grinding or polishing operations. These phenomena persist even at the nanoscale, where machining still leaves discernible process signatures. At higher structural level, waviness encompasses longer-wavelength surface variations, often resulting from dynamic instabilities during fabrication, such as relative vibrations between the workpiece and the grinding tool. It is important to recognize that the most significant effect of waviness is observed in the radial geometry of the component, specifically in roundness deviations, rather than in axial measurements, which capture only a projection of the full waviness profile. At the largest scale, form errors describe systematic deviations from the intended geometry, typically induced by machine tool imperfections (e.g., misalignments in slideways or imbalances in rotating components) or by thermally induced deformations during processing [23].

Surface irregularities roughness, waviness, and form errors are often grouped under the general term *surface texture*, although each has distinct origins, characteristics, and functional impacts [24]. The figures 1.3 and 1.4 show a reference shim surface from a set of surface roughness comparison specimens (No.130 Rupert & Co. Ltd., Cheadle, Cheshire, England), measured using a Bruker Contour GT$^{\text{TM}}$ white light interferometry system (San Jose, CA, USA) with a X50 magnification. Part (a) of the figure shows what is referred to as the real surface, with the red curve representing the form to be removed, known as the F-operator. In this case, the operator is a first-order polynomial [25], but different form removal operators exist depending on the underlying form such as fitted shapes [26], digital filters [27], and morphological techniques [28]. After applying a form removal using an F-operator, the surface is referred to as the S-F surface. The roughness can then be separated from the waviness by using an L-filter, which removes large-scale phenomena from the profile, typically through a Gaussian or robust low-pass filter. A Gaussian low-pass filter with a 50 μm cutoff is applied here (i.e., The cutoff value is arbitrary and depends on the scale and the type of the profile) to the S-F surface, resulting in the S-L surface [29].

Regarding surface phenomena, they may appear as form, waviness, or roughness depending entirely on the scale of observation. Take, for instance, the term *peak*, defined in ISO 25178-2 as “a point on the surface which is higher than all other points within a neighbourhood of that point.” While this definition is clear from a geometrical standpoint, its interpretation varies with scale. A peak observed at a macroscopic level, when magnified, may reveal additional peaks nested within it, illustrating a fractal logic of self-similar structures across scales. The original peak can then be viewed as the nominal form for a set of smaller peaks, which themselves constitute waviness and roughness when observed at a finer resolution.

This observation reveals a key challenge in the classification of surface phenomena: although it is necessary to distinguish surface components by their characteristic spatial frequencies (form, waviness, roughness), the definition of a feature such as a peak should ideally remain scale-invariant. Otherwise, the same geometrical entity may be classified differently depending on the resolution of observation leading to inconsistencies in terminology, interpretation, and standardization. A robust descriptive system must therefore decouple the semantic definition of phenomena from the scale at which they are measured, enabling coherent classification across contexts and applications.

(a) Real Profile and F-operator

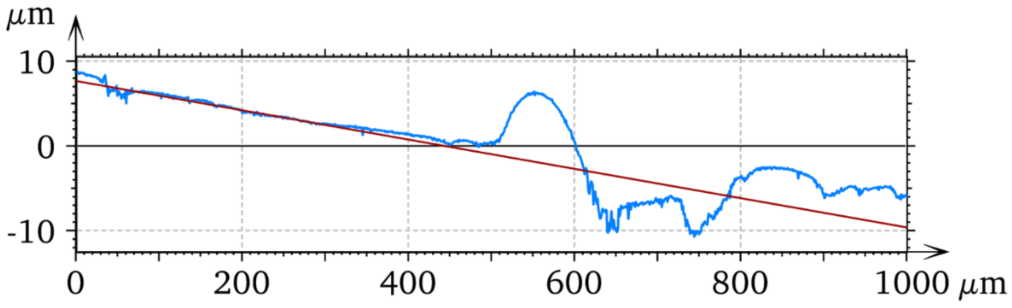

(b) S-F Profile and L-filter

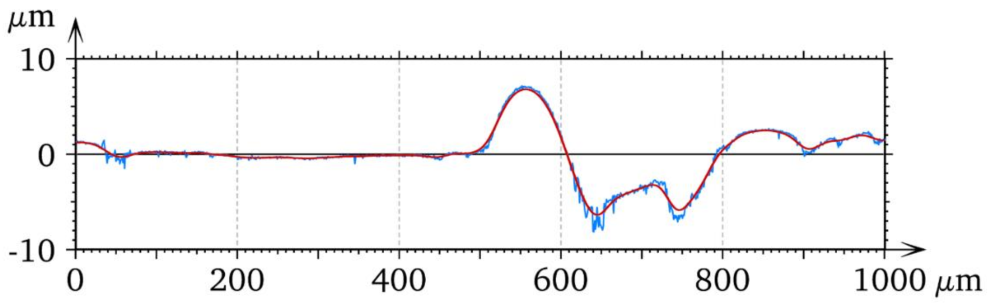

(c) S-L Profile

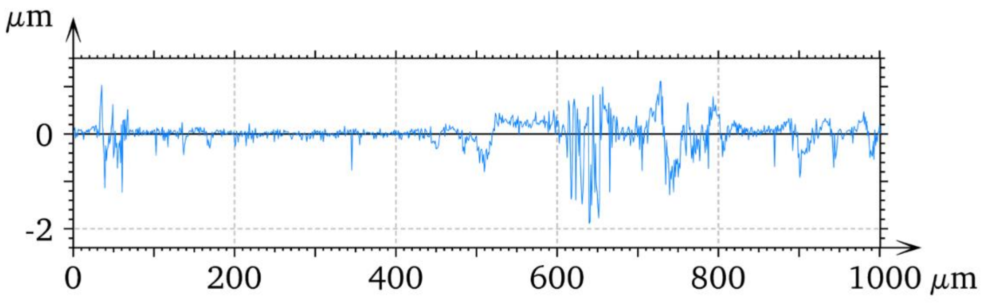

Figure 1.3 *1 mm^2 profile of specimen N9 from No.130 Rupert & Co. Ltd (Horizontal Milling specimen), 100% Nickel. (a) real surface in blue, polynomial of order 1 as F-operator in red, (b) S-F surface in blue, in red L-filter as High Pass gaussian filter with a 50 µm cut off, (c) S-L surface roughness profile*

(a) Measured Surface

(b) F-operator

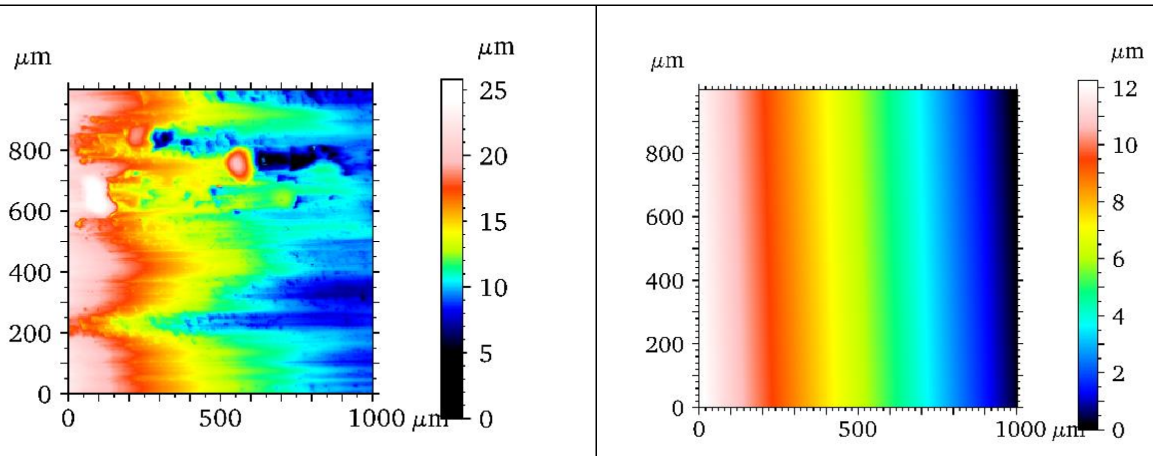

(c) S-F Surface

(d) Waviness profile after L-filter

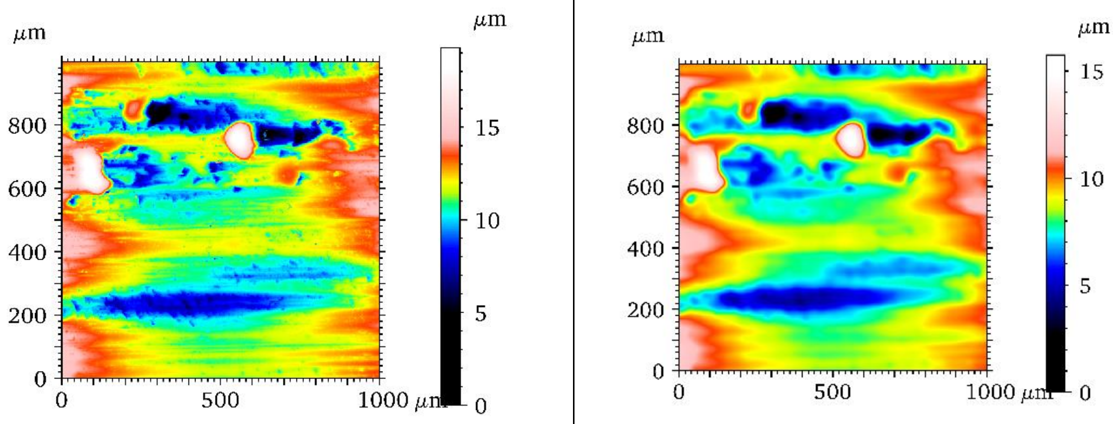

(d) S-L Surface

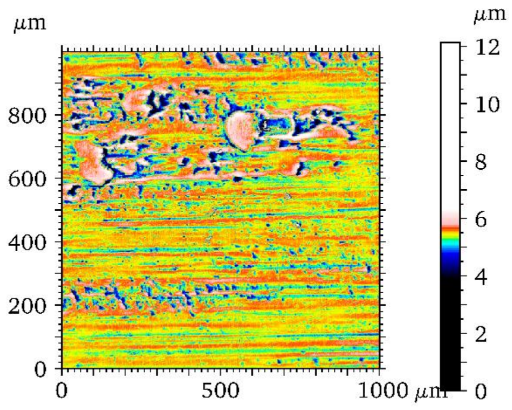

Figure 1.4 *1 mm^2 profile of specimen N9 from No.130 Rupert & Co. Ltd (Horizontal Milling specimen), 100% Nickel (a) Measured surface (b) form removed (c) surface after form removed (d) waviness wavelength removed (d) S-L surface roughness profile*

Areal Surface Texture Parameters

The roughness parameters of the ISO 25178-2:2021 and EUR 15178N standards are divided into different groups, each with a unique approach to surface geometry (Table 1.3). The combination of values from different parameters across surfaces provides researchers with information on how the surface evolves (e.g., during wear tests) or changes from one surface to another. It is important to note that surfaces that are topographically very different can have similar parameter values, which necessitates a visual examination of the surface topographies in addition to the analysis of parametric values. The formulas and classifications of areal surface parameters can be found in the chapter by François Blateyron [30].

Symbol and unit	**Name of parameter**	**Standard**
	Amplitude parameters	
Sq (μm)	Root mean square height	ISO 25178
Ssk (no unit)	Skewness	ISO 25178
Sku (no unit)	Kurtosis	ISO 25178
Sp(μm)	Maximum peak height	ISO 25178
Sv (μm)	Maximum valley height	ISO 25178
Sz(μm)	Maximum height	ISO 25178
Sa(μm)	Arithmetic mean height	ISO 25178
St (μm)	Total height	EUR 15178N
	Spatial parameters (ISO 25178)	
Sal (mm)	Auto-correlation length	ISO 25178
Str (no unit)	Texture-aspect ratio	ISO 25178
Std (°)	Texture direction	ISO 25178
	Hybrid parameters (ISO 25178)	
Sdq (no unit)	Root mean square gradient	ISO 25178
Sdr (%)	Developed interfacial area ratio	ISO 25178

Sds (1/mm^2)	Density of summits	EUR 15178N
Ssc(1/mm)	Arithmetic mean summit curvature	EUR 15178N
Sfd (no unit)	Fractal dimension of the surface	EUR 15178N
Functional parameters		
Sk (μm)	Core roughness depth	EUR 15178N
Spk (μm)	Reduced summit height	EUR 15178N
Svk (μm)	Reduced valley depth	EUR 15178N
$Sr1$ (%)	Upper bearing area	EUR 15178N
$Sr2$ (%)	Lower bearing area	EUR 15178N
Spq (no unit)	Plateau root mean square roughness	EUR 15178N
Svq (no unit)	Valley root mean square roughness	EUR 15178N
Smq (no unit)	Material ratio at plateau-to-valley transition	EUR 15178N
Smr (%)	Areal material ratio	EUR 15178N
Smc (μm)	Inverse areal material ratio	ISO 25178
Sxp(μm)	Extreme peak height	ISO 25178
Sdc (μm)	Areal height difference	ISO 25178
Volume functional parameters		
Vm (mm^3/mm^2)	Material volume	ISO 25178
Vvv (mm^3/mm^2)	Void volume	ISO 25178
Vmp (mm^3/mm^2)	Peak material volume	ISO 25178
Vmc (mm^3/mm^2)	Core material volume	ISO 25178
Vvc (mm^3/mm^2)	Core void volume	ISO 25178
Vvv (mm^3/mm^2)	Dale void volume	ISO 25178
Functional indices		
Sbi	Surface bearing index	EUR 15178N

Sci	Core fluid retention index	EUR 15178N
Svi	Valley fluid retention index	EUR 15178N
Feature parameters		
Spd(1/mm²)	Density of peaks	ISO 25178
Spc (1/mm)	Arithmetic mean peak curvature	ISO 25178
$S10z$ (μm)	Ten point height	ISO 25178
$S5z$ (μm)	Five point peak height	ISO 25178
$S5v$ (μm)	Five point valley height	ISO 25178
Sda (mm²)	Mean dale area	ISO 25178
Sha (mm²)	Mean hill area	ISO 25178
Sdv (mm³)	Mean dale volume	ISO 25178
Shv (mm³)	Mean hill volume	ISO 25178
Other 3D parameters (from MountainsMap software)		
$Smean$ (μm)	Mean height in absolute	No standard
$Sdar$ (mm²)	Developed area	No standard
$Spar$ (mm²)	Projected area	No standard
(µ$\boldsymbol{m^3}$)	Number of islands	No standard
(μm)	Mean height of islands	No standard
(μm²)	Mean surface of islands	No standard

Table 1.3 *Areal Surface parameters from ISO 25178-2 EUR 15178N and implemented in MountainsMap software (Digital Surf*^{TM}*, Besançon, France)*

1.2 Morphomeca Philosophy

Morphomeca is a research platform focused on the characterization of surface topographies within the Mechanical Department of the LAMIH UMR CNRS 8201 laboratory (Université Polytechnique Hauts-de-France). This platform has developed a unique approach in the field of surface research, which, instead of focusing on a particular process or functionality, aims to design a methodological ontology that can be summarized by the term 'Morphomechanics,' which gives the platform its name. This philosophy enables Morphomeca to be highly agile in identifying research opportunities and has a recognized capability to manage interdisciplinary research projects. As shown in Figure 1.5, the philosophy of Morphomeca can be represented by the desire to study surface topography beyond the classical dichotomy between manufacturing and functionality. The first axis aims to consider the genesis of the surface and its parameters to model functionality subsequently. The second axis is directly related to the relationship between the genesis of the surface and its physico-chemical properties. The third axis addresses the relationship between the physical aspect and the chemical properties. This allows for additional inferences beyond the classical quality control analysis of functionality. The fourth axis allows for the determination of birth parameters of forms on the surface, which dissociates mechanical and morphological signatures from functionality. This methodology has enabled Morphomeca to address numerous research topics and develop many tools. Among others, these include the adhesion of osteoblast cells [31], the characterization of fluctuation of measurements [32,33], stitching algorithm [34], art [35], tribology [36], material characterization [36], multiscale characterization [37] and so on.

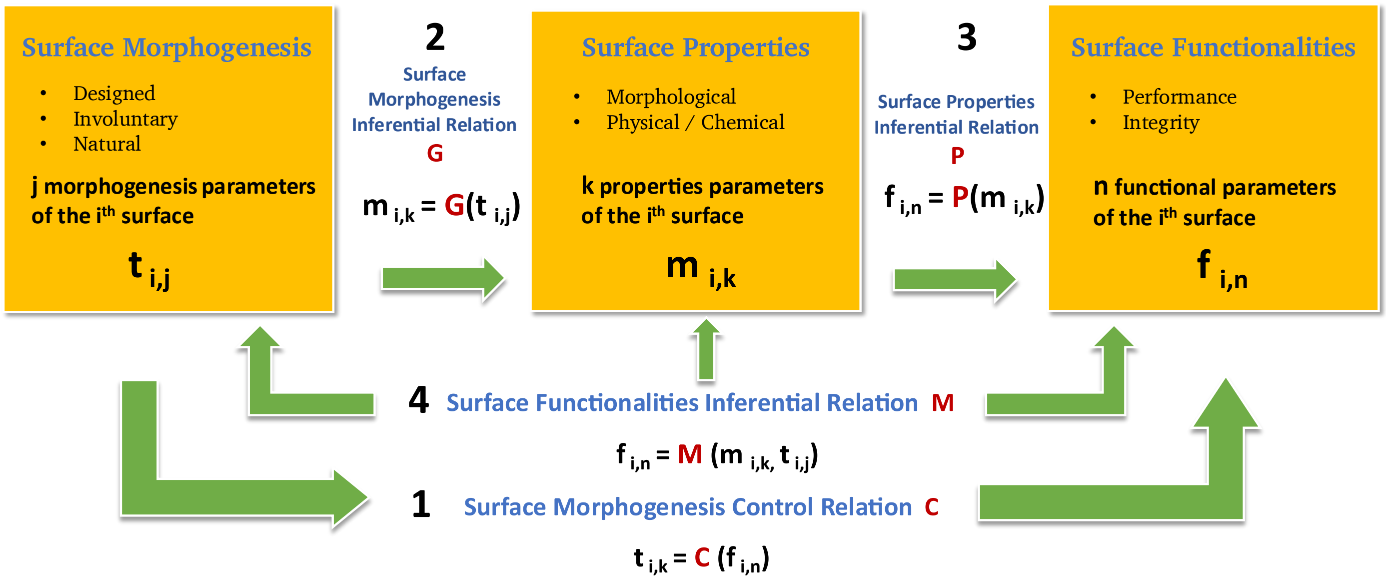

Four cases for analysis
1: Allows to find $t_{i,j}$ parameters, which model the **functionality**
2: Allows to dissociate morpho-mecanic features depending on parameters of **morphogenesis** of surface $t_{i,j}$
3: Allows to dissociate morpho-mecanic features depending on parameter of **functionality** $f_{i,n}$
4: Allows to determine parameters $t_{i,j}$ of **morphogenesis** of surface which dissociate morpho-mecanic signatures of **functionality** $f_{i,n}$

Figure 1.5 *Diagram of the Morphoméca philosophy*

1.2.1 Measurement Devices

The measurement systems presented in this section are those that were used in the context of this thesis. There are many other measurement systems, starting with tactile or laser profilometers, and other 3D profilometry technologies such as confocal microscopes. The details of these other technologies are specified in reference handbooks as well as in standards, notably ISO 21920 [38], and ISO 25178 [39]. Each measurement system has a resolution window, which requires determining in advance what one intends to analyse on a surface before selecting the appropriate system (Figure 1.6).

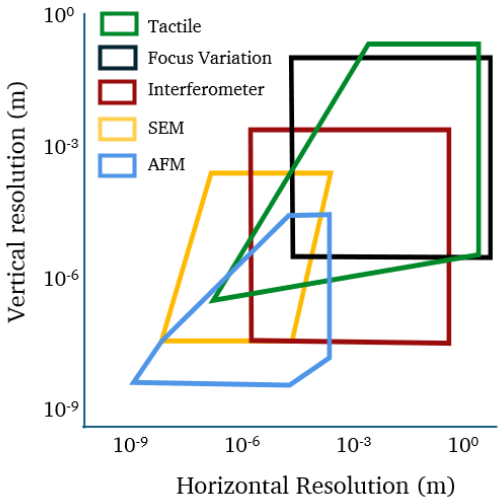

Figure 1.6 *The Stedman Diagram, Scale Ranges for Profilometers*

Optical measurement systems employ a combination of light sources, lenses, a photosensor (typically a CCD sensor), and mirrors to capture surface topography. As non-contact instruments, they preserve the integrity of the sample, allowing measurements without altering the surface. However, rather than directly recording height values, optical measurement systems infer them from data such as light intensity or phase maps. As a result, measurements may be affected by errors due to improper light reflections or signal noise, requiring correction or filtering. Points identified as low quality are replaced by non-measured points, which do not contain height information. There are three main optical techniques used in profilometry: interferometry, focus variation microscopy, and confocal microscopy.

1.2.1.1 Focus variation microscope

In the last decades, the development of light microscopy-based measurement techniques has accelerated significantly. Similar to confocal microscopy, FVM relies on image acquisition through depth-of-field analysis a principle established by H. von Helmholtz in the mid-1920s [40]. However, the modern development of this technique, including the design and construction of focus variation instruments, began in the early 1990s. Some of the pioneering research in this field was documented in studies by F. Helmli [41] and F. Helmli, R. Danzl, M. Prantl, M. Grabner, and S. Scherer [42,43].

Focus variation microscopy determines surface topography by detecting the point of optimal focus using a contrast-based algorithm that analyses intensity differences between neighbouring pixels (Figure 1.7, Figure 1.8). The highest contrast indicates the best focus. Similar to focus stacking in macro photography, this method provides both topographic data and an optical image of the surface, often including colour information, unlike interferometry. The standardized procedure for focus variation microscope is defined in ISO 25178-606 [44].

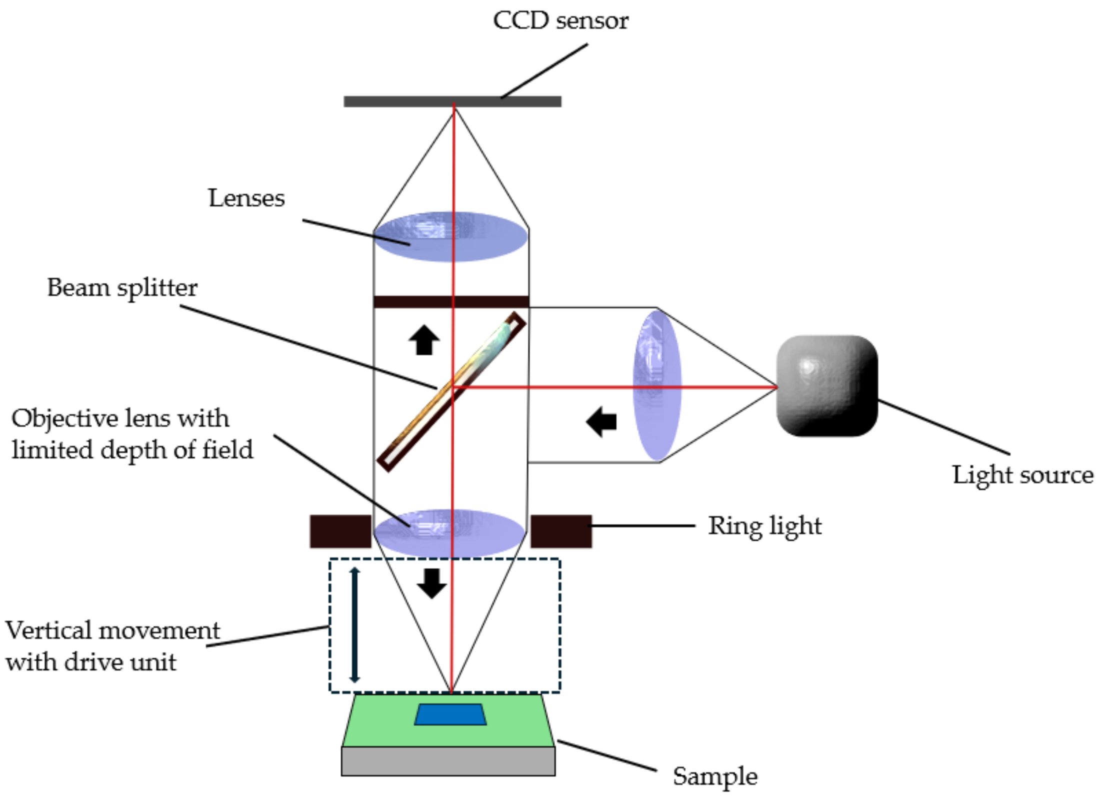

Figure 1.7 *Schematization of the focus variation microscope*

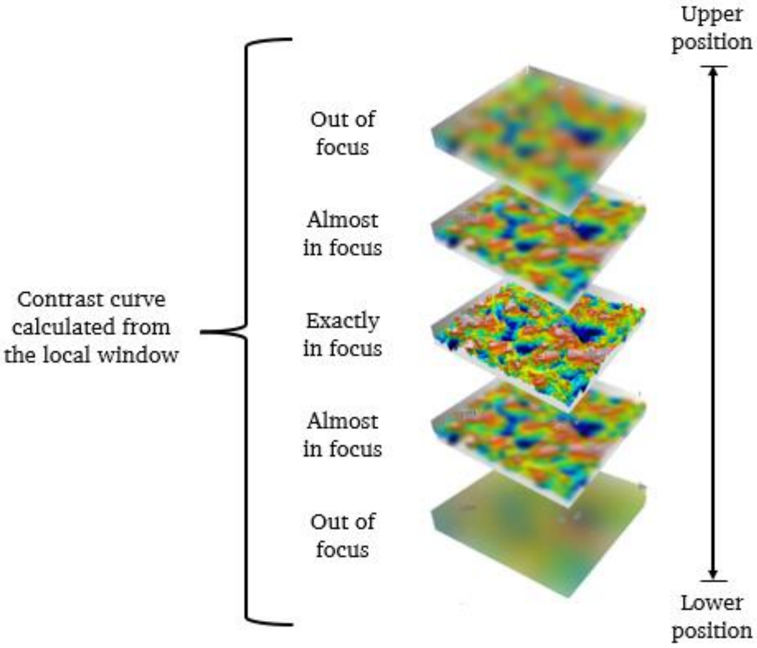

Figure 1.8 *Schematization of the contrast curve calculated from the local window*

1.2.1.2 Coherence Scanning Interferometry

Coherence Scanning Interferometry (CSI) is a non-contact technique used to measure surface topography by detecting interference fringes created by differences in optical path lengths during scanning. A mechanical scanner moves the interference objective (or the sample) along the vertical axis, while a computer captures light-intensity data for each pixel at different heights. Using a broadband incoherent light source (e.g., tungsten halogen or white-light LEDs), CSI systems produce high-resolution 3D surface maps [11].

The setup typically includes a two-beam interference objective (e.g., Michelson, Mirau, or Linnik types) and Köhler illumination optics to maximize lateral resolution. Interference occurs between light reflected from the sample and a reference mirror, with the resulting fringe patterns analysed to reconstruct surface height. Unlike other methods, CSI requires modelling both spatial and spectral coherence due to its use of low-coherence light and broadband illumination [45] (Figure 1.9).

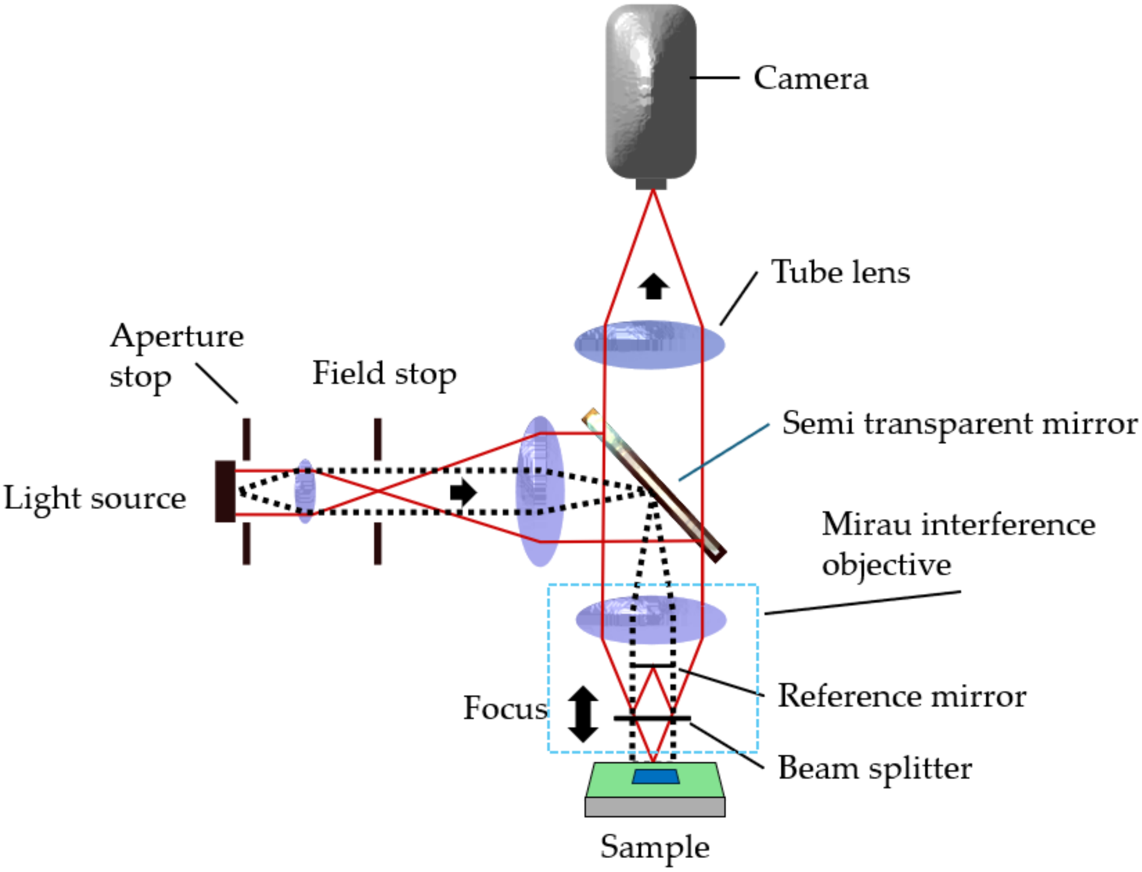

Figure 1.9 *Schematization of the Coherence Scanning Interferometer with Mirau configuration*

1.3 State of the art on terminology in surface metrology

As an introduction to the state of the art on surface phenomena terminology, and after defining our object of study, we will begin by examining standardized vocabulary, followed by non-standardized terminology.

1.3.1 DIN 4761:1978-12

The DIN 4761 standard [46], published in 1978 and derived from the Swiss VSM 58070:1976 [47], provides a descriptive and standardized classification of surface textures based on qualitative geometric phenomena. It does not address quantitative measurements (such as roughness parameters) but instead aims to establish a structured vocabulary for identifying and describing typical surface forms visible to the naked eye or under low magnification.

The standard distinguishes two main categories of surfaces:

- Grooved surfaces (rillige Oberflächen), produced by machining processes (turning, milling, grinding), characterized by grooves defined by their shape, spacing, orientation, and regularity.
- Non-grooved surfaces (nichtrillige Oberflächen), resulting from non-cutting processes (casting, coating, corrosion, etc.), classified according to basic geometric forms: pits (muldig), bumps (kuppig), waviness (gewellt), or flake-like structures (schuppig).

It also includes a typology of surface defects (scratches, cracks, pores, dents, burrs, etc.), enabling a clear distinction between functional textures and unintentional damage. The images in the standard are arranged as follows: a diagram of an isometric view, normal view and horizontal view, accompanied by a definition in German. Finally, a system of abbreviated codes and symbols is associated with each category for use in technical documentation and engineering drawings. An appendix provides equivalencies with DIN ISO 1302 [48] notation now withdrawn and replaced by ISO 21920-1:2021 [49]. For example, one can refer to the representation of point-like depressions (Figure 1.10) found in the standard: "Point-like depressions are sharply defined indentations whose depth is relatively large compared to their width. They result from either intentional or unintentional material removal (e.g., etching, corrosion, etc.). In some cases, these depressions can serve as lubricant pockets."

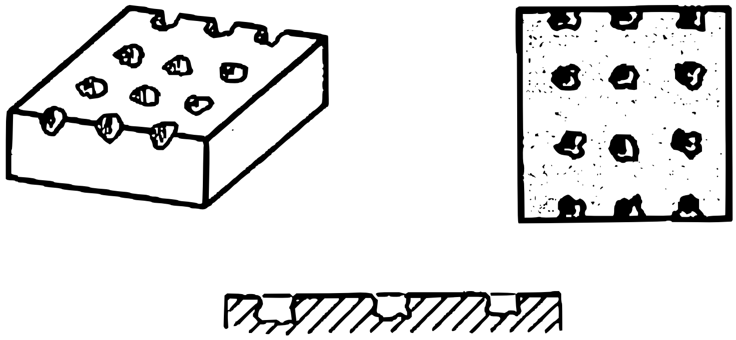

Figure 1.10 *Illustration for point-like depression reproduction with modification from DIN 4761*

1.3.2 ISO 8785

The most well-known reference in this context is the ISO 8785:1998 [50] standard (a new version of the 8785 is currently in process). This International Standard defines terms related to surface imperfections. It replaces the DIN 4761:1978-12 standard, which has now been withdrawn [46]. Its purpose is to establish a common vocabulary to be used in technical documents, technical drawings, scientific publications, for specifying permissible imperfections and measurement methods. However, this standard is more focused on quality control than on providing objective definitions of surface phenomena. The terms used in this standard are regarded here as surface defects, even though the phenomena described may be desirable in certain manufacturing processes. The standard is structured as follows: a schematic representation of the phenomena is provided alongside the term and a brief definition and its translation in French (Figure 1.11).

Groove Surface imperfection which is a longitudinal recession with a rounded or flat bottom	**Sillon**,m Creux longitudinal à fond plat ou arrondi

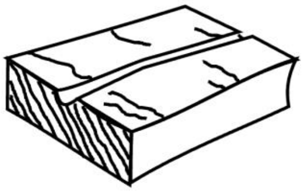

Figure 1.11 *Illustration for groove reproduction with modification from ISO 8785*

The 31 terms defined and illustrated in the standard undeniably provide a terminological foundation for generalized standardization. However, several criticisms can be made regarding the design of this standard. From both a scientific and terminological perspective, it is essential to acknowledge the decoupling between surface phenomena and the functional value attributed to them. A given topographic phenomenon, such as a pore, a groove, or a crack, cannot be intrinsically classified as either a defect or a functional element. Its interpretation depends entirely on the context of use, the performance criteria of the application, and the disciplinary viewpoint. What is considered a defect in one domain (e.g., pores in aerospace components) may be regarded as a functional asset in another (e.g., pores in biomedical implants or filtration systems). This observation challenges any binary classification of surface phenomena into defects versus functional structures and reinforces the need for a descriptive framework that remains neutral with respect to function. In such a framework, morphology precedes interpretation, allowing for greater interoperability across disciplines.

1.3.3 ISO 25178-2

The terms describing surface phenomena as defined in ISO 25178-2 [1], section 3.3 *Geometrical feature terms*, are general concepts that encompass different types of phenomena. For example, the term peak is defined as: "point on the surface which is higher than all other points within a neighbourhood of that point." The terms defined in ISO 25178-2, such as *peak* or *dale*, are not descriptions of specific instances but rather abstract topographical concepts or generic surface feature terms used to classify local geometrical phenomena. These concepts are primarily intended for the calculation of roughness parameters and for the mathematical description of the surface, rather than for a literal or concrete description of the surface itself. These terms are classified under section *6.2 Type of texture feature* (Table 1.4). The designations are used to indicate the location of phenomena in diagrams (Figure 1.12).

Class of limited feature	Type of scale-limited feature	Designation
Areal	Hill	H
	Dale	D
Line	Course line	C
	Ridge line	R
Point	Peak	P
	Pit	V
	Saddle point	S

Table 1.4 *Type of scale-limited phenomena from ISO 25178-2 [1]*

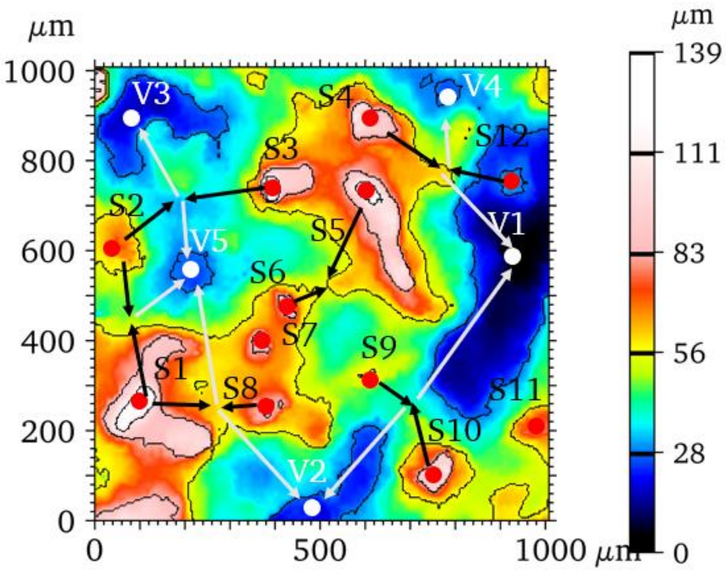

Figure 1.12 *Contour map showing critical lines and points*

Philosophically, the ISO 25178 standard is grounded in the principles formulated by Scott in 1997 [51], which assert that a surface should not be understood as a continuous entity, but rather as a composition of elementary topographical entities. Drawing on Maxwell's method [52], this *feature-based* approach decomposes the surface into critical points (peaks, pits, saddle points) and characteristic lines (ridges, grooves), enabling the extraction of the most functionally relevant phenomena. This structural and hierarchical perspective departs from purely statistical models and forms the conceptual foundation of modern surface characterization as defined by the standard.

1.3.4 ASME B.46-1

The ASME B46.1-2019 [20] document is an American standard dedicated to the characterization of surface texture. It serves as a major reference in surface metrology, complementing or running in parallel with ISO standards such as ISO 25178 or ISO 4287. We take the term *area valley* as an example, but the term *area peak* also exists (Figure 1.13). This term, used in ASME B46.1 and inherited from DIN 4761:1978-12, refers to a geometrically defined region that lies below its surroundings, often identified through segmentation or thresholding methods. In contrast, the term *dale* in ISO 25178-2 is defined as a topographic feature characterized by a local minimum within a defined neighbourhood, independent of global thresholds. While *area valley* is rooted in a practical, visually intuitive classification of surface phenomena, *dale* belongs to an abstract topological framework based on mathematical criteria. This distinction reflects the broader difference between descriptive and conceptual approaches in surface metrology, with ASME favouring operational clarity and ISO emphasizing formal ontological structure. This conceptual distinction explains why the terms are accompanied by a diagram in ISO 25178-2, whereas in ASME B46.1 they are presented with an illustration.

Other terms that describe the nature of surface phenomena include the indication of surface lay. Lay is defined in the standard as: "the predominant direction of the surface pattern, ordinarily determined by the production method used”. This is the only definition found in the standards that describes the arrangement of surface phenomena as a system. The term *lay* may be accompanied by adjectives such as *circular* or *radial*, providing information about the deterministic organization of phenomena.

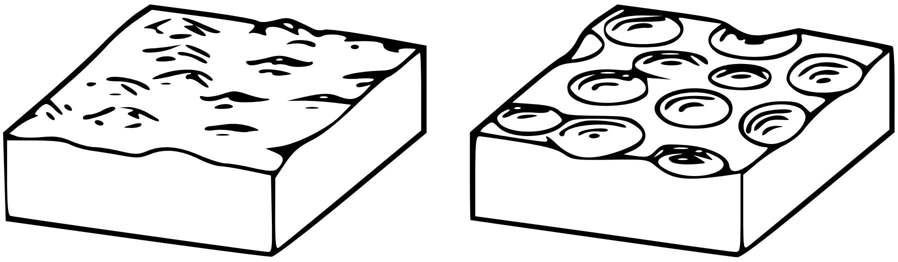

(a) (b)

Figure 1.13 *Reproduction with modification of the illustration used in ASME B46.1 for the description of (a) area peak and (b) area valley*

With these standards and their descriptive terminology as a starting point, we can already identify the terminological limits for a more analytical description of the phenomena present on the surface. The first issue concerns conceptual homogeneity: the three standards employ terminologies based on different logics (mathematical, empirical, descriptive) without any clear terminological interoperability. The second issue relates to their restriction to industrial contexts: these terminologies are primarily designed for machining or quality control. They are not suited to natural or biological surfaces, for example, where shapes do not conform to a standardized model.

1.3.5 Non-standard Terminology: Scientific Practices and Empirical Classifications

Rather than presenting an exhaustive inventory of reused or redefined terms, it is more insightful to examine a representative example: “roughness”. In metrology, *roughness* is a standardized term, defined by precise mathematical parameters (such as Sa, Sq, or Sdr), constrained by scale, measurement procedure, and filtering methods, as outlined in ISO 25178 or ASME B46.1. These standards ensure interoperability and reproducibility.

In a wide range of scientific publications particularly outside industrial or strictly metrological contexts *roughness* is often used as a conventional term, detached from its standardized meaning. Researchers may use it to describe visual irregularity, tactile sensation, or general surface heterogeneity, sometimes without any quantitative basis. This kind of usage reflects a community-specific consensus rather than a shared, formal definition. In the introduction to his book on surface metrology, the author Thomas says: "I can't define roughness, but I know it when I see it"[53]. This remark on the definition of the concept of roughness is taken up again this time to define the deterministic side of the surface in an article of which Thomas is contributor. In fact, the article on structured surfaces, synonymous with deterministic surfaces, uses the same vague formulation word for word to talk about an almost opposite concept [54].

The gap between standardized terminology and conventional usage reveals a broader issue: the semantic drift of technical terms as they migrate into diverse scientific domains. In these cases, terminology becomes flexible and adaptive, but also ambiguous. A word like *roughness* can thus refer to a precisely measured amplitude at the nanometer scale in one article, and to a loosely described topographic impression at the millimeters scale in another, without clarification or disambiguation.

This terminological ambiguity illustrates how scientific language often evolves outside normative frameworks, producing what could be seen as “local terminologies”, functional within a research group or discipline, but opaque or misleading when viewed from another field. According to Lefèvre [55], scientific and technical discourse is elliptical: dialogues are reduced to the essentials, while descriptions are based on diagrams, symbols and, in our case, parameters. However, as soon as a new activity requires scientists to re-evaluate and compare research content, the lack of available terminology leads them to form islands of discourse [56].

1.3.5.1 Description and classification

In the context of surface analysis, it is important to clearly distinguish between the description of topographic phenomena and the classification of surfaces. Description aims to name and characterize locally observable entities, such as striations, cavities, edges, or specific patterns, whereas classification groups surfaces according to global or statistical criteria, often derived from instrumental measurements. Some commonly used notions, such as *isotropic* or *anisotropic*, belong to the latter category. These terms do not refer to discrete, localized phenomena on the surface, but rather describe emergent properties resulting from the analysis of the spatial organization of surface irregularities. A surface is considered *anisotropic* when a preferential orientation can be identified in the arrangement of its phenomena (e.g., parallel striations), and *isotropic* when no dominant direction is observed. These are therefore global qualifiers that complement morphological descriptions without replacing them. The classification of areal surface textures has progressively evolved to better align with the needs of design, manufacturing, and metrology. In the 1980s and 1990s, Suh and Saka [57] , followed by Stout [58], proposed a basic distinction between engineered and structured surfaces. Evans and Bryan [54] refined this by linking each category to specific functional purposes: structured surfaces are defined by deterministic patterns designed to fulfil a particular function, while engineered surfaces involve modifications of both the surface and subsurface to enhance performance.

Later, Stout and Blunt [59] expanded the model to include non-engineered surfaces, defined as those resulting directly from manufacturing processes without intentional control over surface characteristics. These categories were further divided into subtypes (random, systematic, structured, unstructured), depending on manufacturing routes, and organized into a hierarchical framework.

While this approach aimed to clarify surface classifications and support the design of functional textures, it remains ambiguous, particularly in dealing with newer manufacturing methods. To address this, the author of this manuscript proposes a revised system based on identifying key surface attributes and linking them to their functions.

In a phenomena-centred terminological approach, it is essential to maintain this distinction, to avoid conflating observable entities, suitable for descriptive inventories, with statistical or functional properties that pertain to a different analytical logic.

1.4 Corpus based analysis

Given the lack of available terminological resources in the field of surface metrology, a corpus-based approach was adopted to identify and analyse the vocabulary currently in use. In the absence of a standardized or comprehensive lexicon, it became necessary to construct an arbitrary, yet representative corpus drawn from recent scientific publications. A little over 100 articles were used to construct the corpus, and the first observation was that the presence of topographic images or micrographs was a *sine qua non* condition for the occurrence of descriptive terms. This already suggests a strong connection between terminology and visual representation, which will be further developed later. The list of articles is provided in the appendix. This allowed for the collection of terms that are used in practice, including those that do not appear in official standards or that deviate from precise scientific definitions. The objective was to observe how surface phenomena are described by researchers in diverse disciplinary contexts, and to highlight the semantic ambiguity or informal usage of certain descriptors. This empirical strategy provides an essential starting point for developing a more structured and interoperable terminological framework.

Since the study focuses on non-standardized terms as they appear *in situ* within scientific publications, automatic extraction using concordance software, commonly employed in terminological research, is not feasible. As a result, term identification and extraction must be carried out manually. As for the corpus under study, the articles were selected through a keyword-based search on scientific search engines such as Scopus and Google Scholar using the terms "surface roughness," "surface topography," and "surface texture." As a result, the selected publications span a variety of topics, including tribology, laser texturing, functional surface studies, and others.

A manually compiled corpus of approximately 250 descriptive terms was extracted from the corpus of scientific publications concerned with surface topography. The aim of this collection was to identify the diversity of expressions used to describe surface phenomena, regardless of their degree of technical precision or formal definition. Several recurrent descriptors dominate the corpus, most notably *dimples*, *grooves*, *pits*, *pores*, *cracks*, and *holes*. These terms appear in numerous variants (e.g., *micro-dimples*, *circular dimples*, *grooved surface*, *pore distribution*) and are often used in combination or interchangeably, despite significant morphological or functional differences. This recurrence highlights a tendency to rely on a limited set of intuitive phenomena, which are then modified contextually through qualifiers of scale, arrangement, or shape.

The analysis of the corpus reveals a broad heterogeneity in the nature of the descriptors. A first group refers to geometric or morphological aspects of the surface, with shapes such as *triangular*, *circular*, *elliptical*, *hexagonal*, or *spherical* used either in isolation or as modifiers. A second group concerns topographical discontinuities or structures, including terms like *groove* [60], *dimple* [54,61–68], *crack* [69], *ridge* [70], *valley* [69], *asperity* [71], or *scallop* [72]. A third category includes references to spatial organization, with expressions such as *array*, *pattern*, *grid*, *cluster*, *network*, or *distribution*, often used to qualify recurring or ordered structures (i.e., structured surfaces). These terms indicate the perceived regularity or randomness of the feature distribution but rarely follow a shared definition. A fourth category concerns phenomena derived from or associated with manufacturing processes: terms like *laser-induced*, *brushed*, *ground*, *polished*, *coined*, or *etched* serve as shorthand for both origin and appearance, further blurring the boundary between physical feature and process-based attribution. This terminological variety is further compounded by the coexistence of several descriptive levels. Some terms relate to local phenomena (e.g., *pit*, *groove*, *dimple*), others to meso- or macro-scale patterning (e.g., *grid*, *cluster*, *crosshatch*), and others still to functional interpretations (e.g., *oil pocket*, *reservoir*, *lubrication groove*). Moreover, expressions frequently include scale qualifiers, such as *micro-*, *nano-*, *fine*, or *hierarchical*, without always defining their thresholds or implications. The result is a terminological system in which the same feature may be described differently depending on context, discipline, or measurement resolution.

The linguistic register also varies considerably. Alongside technical terms grounded in metrological or mechanical vocabulary, one encounters metaphorical or visually inspired expressions such as *flower-like*, *coral network*, *petal-like flakes*, and even interpretive formulations like "*the arrow indicates the motion direction of textured surfaces*", or "*there is no contact between the dimples*". These expressions illustrate the empirical and often subjective nature of surface description, where the boundaries between measurement, perception, and interpretation remain porous.

The coexistence of geometric, functional, processual, and visual descriptors, often applied to the same object, underscores the lack of a unified framework for naming and categorizing surface phenomena. While this richness reflects the multiplicity of perspectives brought by different scientific communities, it also poses challenges for clarity, reproducibility, and data comparability. A structured terminological effort appears necessary to clarify these usages, reduce ambiguity, and establish coherent correspondences between observed phenomena and the language used to describe them.

1.4.1 An illustration: the term "dimple"

In the collected corpus, the term *dimple* is the most frequently used among descriptors of surface phenomena (Figure 1.14). Yet this term does not originate from any ISO standard; rather, it reflects the informal use of a common word referring to "*any slight depression in a surface*".

Figure 1.14 *Cloud of the terms extracted from the corpus of scientific articles based on surface roughness, surface texture and surface topography*

The predominance of images in articles describing surface phenomena, combined with the informal and visually grounded nature of many terms (e.g., *dimple*, *groove*, *pit*), suggests that definitions in this field often rely on ostensive strategies. This corresponds to what ISO 704 [5] refers to as "demonstrative definitions," and aligns with Sager's pragmatic view of terminological practice [73], where illustration becomes a functional complement, or even substitute, for formal conceptual description. In this sense, the terminological landscape of surface metrology currently operates within an image-based, onomasiological logic [74], in which concepts are shown before they are named. However, without standardization, these concepts correspond to what were previously referred to as islands of discourse [56]. Figure 1.15 shows three occurrences of the term *dimple* used in three different publications: all related to laser texturing. One can observe the visual differences between the publications, even though all three surfaces could be referred to using the term *dimple* without additional information. In metrology, the link between image and text has a defining function in that the topographical image gives meaning to the terms used to describe the surface morphology [75].

(a)

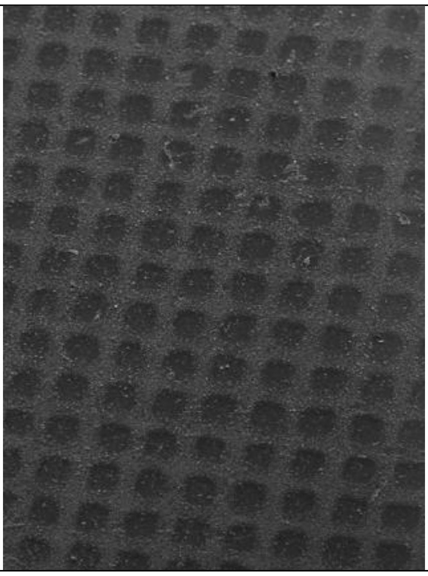

(b)

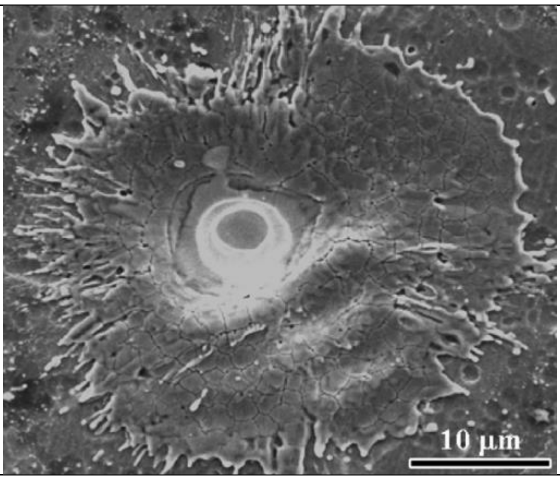

(c)

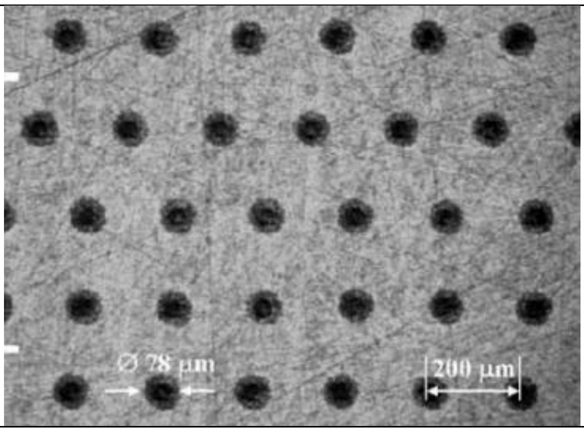

Figure 1.15 *Three examples of dimple occurrences in scientific publications (a) the dimples are here presented in array and having a square shape [61], (b) the dimple here is presenting a flat bottom shape and rounded edge [62], the dimples are presented in array with round shape, straight edge and flat walls [64]*

1.4.2 About Lack of Terminological in Industrial Environment

The foundation of research in the field of surface metrology was developed within the domain of mechanical engineering. In industrial contexts, surface measurements are often used as threshold values or technical indicators without the need to explicitly name or conceptualize the underlying phenomena.

Therefore, in the industrial environment, the need for terminology to describe surfaces is lessened by the principle of duality [76]. Insofar as the specification and verification phases can be satisfied with sketch and parameters to be respected for production (Figure 1.16). As surfaces are closely linked to the industrial environment, there are several levels of communication, from the formal to the informal, resulting in a proliferation of ad hoc and trivial names creating a duality of discourse [77].

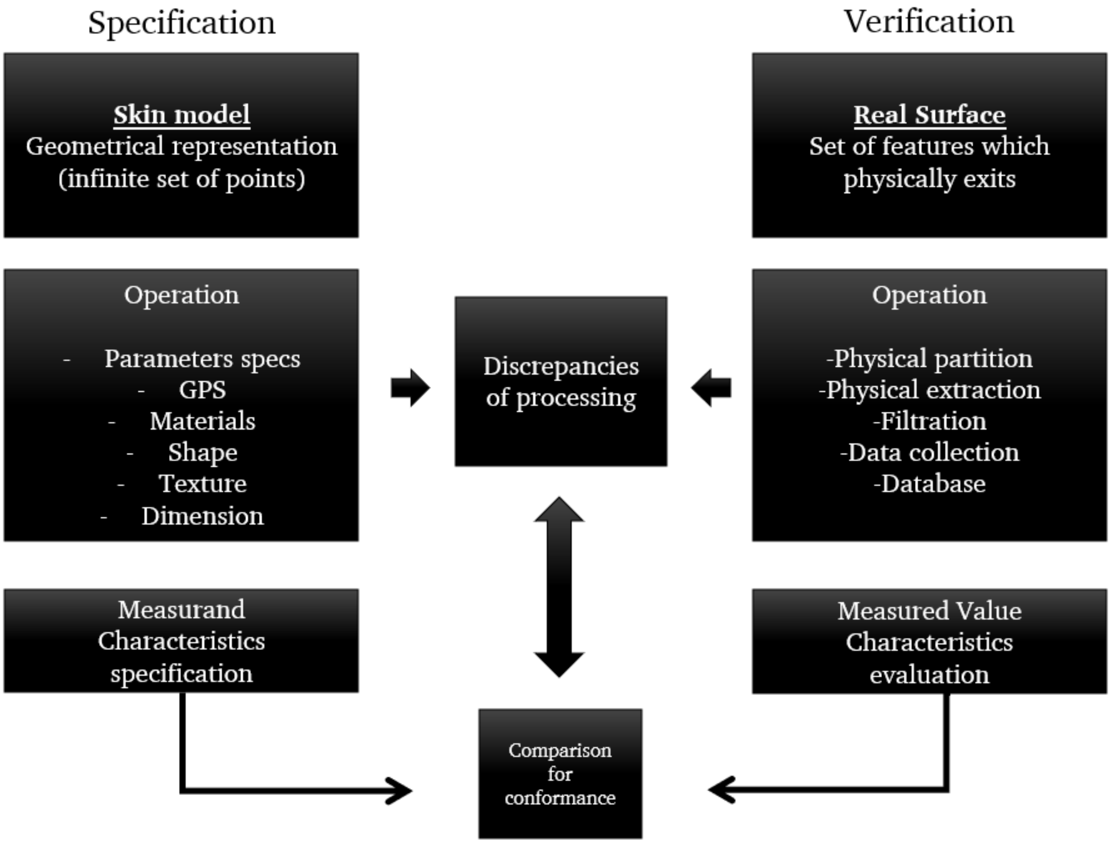

Figure 1.16 *Schematic representation of the duality principle, illustrating the industrial specification and verification process, which could explain the lack of standardized terminological resources for surface phenomena in industrial environment [76]*

1.5 Ontology introduction

To address the limitations caused by terminological imprecision and the lack of conceptual formalism in the description of surface phenomena, the author has developed an ontology based on OWL 2 [78] (Web Ontology Language). *OWL* is a formal knowledge representation language grounded in Description Logics (DL), allowing for the definition of *classes* (concepts), *individuals* (concrete instances), and *properties* (relationships between classes or individuals), while supporting automated reasoning through a well-defined semantics. The ontology encodes a hierarchical taxonomy of topographic phenomena as classes, using subclass axioms (*rdfs:subClassOf*) to structure generic-specific relationships, and object properties (*owl:ObjectProperty*) to model relations such as composition, morphological dependence, or co-occurrence. OWL also enables the specification of class restrictions, for example, stating that a certain type of surface must possess at least one *feature* of type *depression*. The ontology of surface phenomena becomes a tool available to researchers, centralizing the information on available definitions, whether they come from ISO standards (such as ISO 8785), or from widely used terms not found in standards but present in general dictionaries (such as the Oxford Dictionary), by adding annotation properties such as : *owl:isDefinedBy*, which make it possible to indicate and compare the definitions from different resources. Moreover, thanks to the ontology, it is possible to go beyond simple definitions by adding object properties that allow for greater precision, especially by including additional information about surface phenomena. While some characteristics are already embedded in the definition (for instance, the term "crater" implies a circular depression shaped like a bowl), other, more vague terms may require further specification, such as the shape of a dent (e.g., pyramidal, conical, vertical walls, etc.).

The resulting ontology is declarative, interoperable, and formally verifiable: it can be queried using *SPARQL* [79], leveraged by software agents through OWL APIs, or validated using reasoners (e.g., HermiT, Pellet) to infer implicit logical consequences. By structuring surface phenomena in an ontological framework, the author aims to produce more consistent descriptions, reduce dependency on disciplinary variation, and ensure compatibility with automated systems for analysis, documentation, or classification.

Unlike traditional relational databases, which rely on rigid schemas and a tabular organization of data, an ontology allows for the explicit representation of the semantics of the concepts involved and their interrelationships, based on a formal logic. While a database stores values in rows and columns without inherent conceptual meaning, an ontology defines classes, properties, and logical constraints, thereby enabling automated reasoning (inference, classification, consistency checking). This makes it easier to integrate heterogeneous data, to evolve the data model flexibly without breaking compatibility, and to ensure interoperability with other systems through Semantic Web standards (RDF, OWL, SPARQL). Moreover, an ontology is not merely a data container, it plays an active role in structuring, validating, and interpreting knowledge. This makes it particularly well-suited to domains where concepts evolve, overlap, or vary in meaning depending on context, such as surface phenomena in heritage science or surface metrology. This ontology project based on surface phenomena echoes the concept of Information Rich Metrology as proposed by Senin and Leach [80,81]. Indeed, feature extraction and characterization methods can be used to add quantitative information while maintaining a semantic foundation for knowledge structuring. The second reference that served to structure the concepts is an ontology created to reference heraldic coats of arms based on sources available [82,83]. The ontology presented here, prior to its online publication, was developed using Protégé version 5.6.5 and is exported in .ttl, RDF/XML, and OWL/XML formats.

1.5.1 Classes

In knowledge representation, a class refers to a group of individual entities or objects. A class can be defined either extensionally, by listing its members, or intentionally, by specifying the conditions that its members must satisfy, an approach commonly used in ontology languages such as OWL. Following the type–token distinction, an ontology typically distinguishes between individuals, which represent concrete objects or events in the real world, and classes, which represent abstract types or categories grouping such individuals. For the surface ontology, the classes were structured as shown in the Figure 1.17 and defined as follows.

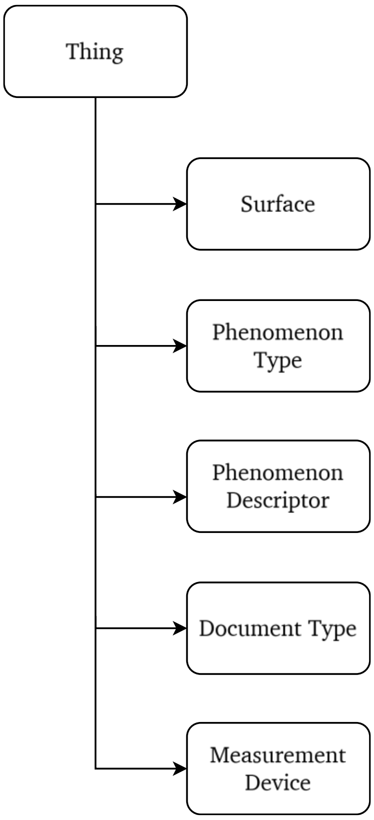

Figure 1.17 *Main classes of the ontology*

"Thing" is the root element, the most general class from which all other classes inherit. It provides a common foundation for all concepts and makes it possible to retrieve all elements of the ontology through a query if needed. The class "Surface" represents the concept of a surface as an entity that can contain information such as the types of surface phenomena present, the method by which the surface was measured, and the type of document in which the surface appears. This may include a PDF of a scientific article, a surface file processed by software such as MountainsMap (.sur), or a raw file coming directly from a measurement device (.opd, .al3d, etc.). The higher-level classes are linked using the standard RDF triple assertion model: "subject, predicate, object". A surface contains surface phenomena, which are defined in the subclasses of *PhenomenonType*. This relation can thus be described as: *Surface* → *hasPhenomenon* → *PhenomenonType*. Similarly, surface phenomena have properties that can support classification: *PhenomenonType* → *hasDescriptor* → *PhenomenonDescriptor* (Figure 1.18). Here, we will focus on the subclasses of *PhenomenonType* and *PhenomenonDescriptor*, as they are the main subject of this chapter. A broader discussion may lead to the definition of other classes and subclasses based on user needs. For example, should a class be created for each existing measurement instrument, or should users simply enter this information as a data property with a string? A similar question arises for document types: if the surface comes from a scientific article, the article's metadata could potentially be automatically associated with the surface.

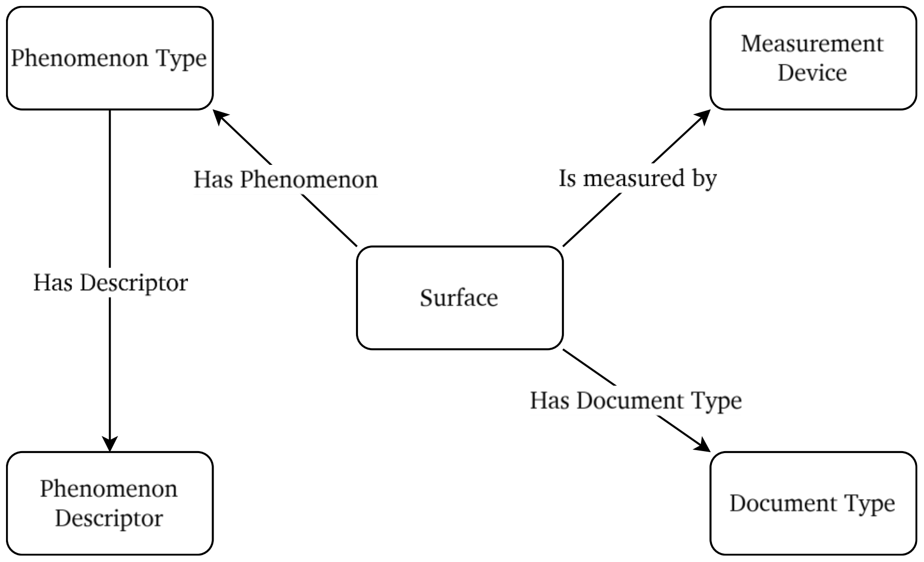

Figure 1.18 *Schematic representation of surface ontology logic (simplified)*

1.5.1.1 Bioinspired

The class of surface phenomena includes four subclasses: *Bioinspired*, *Depression*, *Elevation*, and *Discontinuity*. Bioinspired surfaces are those that take inspiration from natural phenomena, the most well-known example being the Lotus effect, inspired by the lotus leaf, whose hydrophobic properties have been extensively studied. The surface phenomena of the lotus leaf consists of pillars uniformly distributed across the surface to use the liquid's surface tension to keep it as drops. The semantic link between the designation "lotus leaf" [84,85] and the actual representation of the surface is sufficiently strong to consider that additional information about the nature and arrangement of the surface elements is unnecessary. The terminology used for bioinspired surfaces is generally not subject to ambiguity due to its specificity. Other concepts included in the *Bioinspired* subclass are the shark skin effect, snakeskin, gecko feet, and rice leaf. Even if a user is unsure whether the surface to be referenced qualifies as a bioinspired surface, each type of bioinspired surface in the ontology includes annotations linking to scientific articles, which are available for users to read.

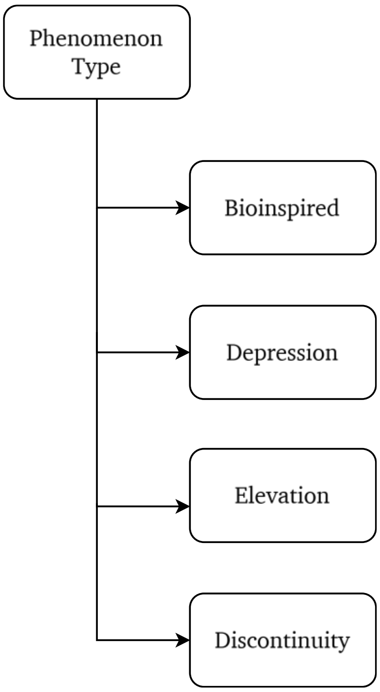

Figure 1.19 *Subclasses of phenomenon type*

1.5.1.2 Depressions and Elevations

The classes of depressions and elevations each have two subclasses that distinguish between linear and non-linear phenomena (Figure 1.20). For example, a groove is a linear phenomenon, whereas a dimple is more localized. Depressions and elevations are defined relative to the mean plane: if a feature has a height value greater than the mean plane, it is considered an elevation; if it is lower, it is considered a depression. The concepts in the class of non-linear depressions include cavity, crater, dimple, dent, pit, pore, and hole. For linear depressions, the terms are crack, groove, and scratch. For each class of these terms, translations in English, French, German, and Polish are included to facilitate user consultation by adding labels. Definitions are also provided, referring both to standards and to dictionary definitions.

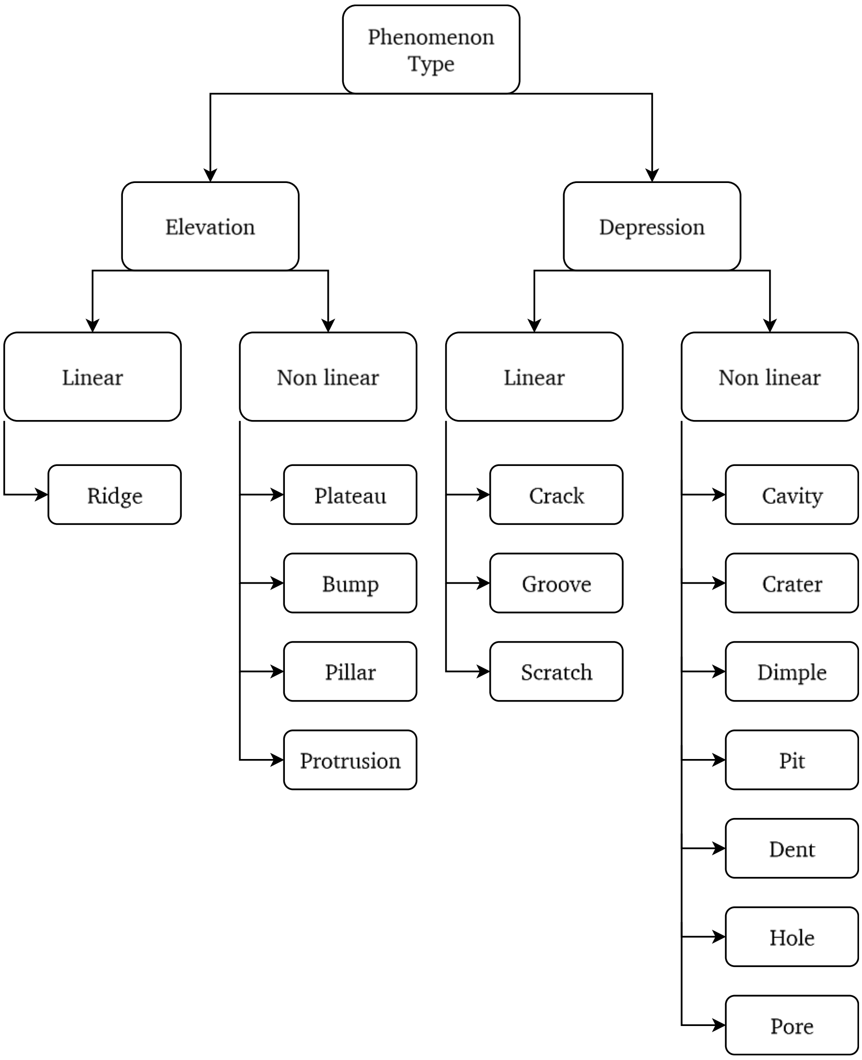

Figure 1.20 *Subclasses of phenomenon type only showing elevation and depression*

1.5.1.3 Discontinuity

In addition to elevations and depressions, a third category of surface phenomena is defined as discontinuities. Discontinuities are characterized by local breaks in the material continuity of the surface that cannot be described solely by height deviations relative to the mean plane. They include phenomena such as flaking, chipping, and spallation, which involve material detachment, as well as inclusions, incrustations, and foreign deposits, where external material is introduced or embedded into the surface. These phenomena differ from geometric protrusions or indentations in that they reflect structural or compositional anomalies, rather than simple topographic variation. Discontinuities thus form a distinct semantic and ontological class in surface characterization, enabling a more comprehensive description of complex surface states.

1.5.1.4 RDF/OWL classes structuration

The OWL/XML format offers several advantages for ontology modelling. It combines the formal expressiveness of the OWL language with the structured clarity of XML, making it well-suited for data exchange, validation, and integration in complex information systems. OWL/XML enables the explicit and formal representation of concepts, their relationships, and constraints, while remaining both machine-readable and relatively human-readable (Figure 1.21, Figure 1.22). The advantage of using an IRI over a URI is that it is not limited to ASCII characters and can include characters from any language. The class declaration also indicates the hierarchical structure of concepts. Here, the concept *Crater* is a subclass of *Non-Linear Depression*, which is itself a subclass of *Depression*, and so on.

```xml
<!-- http://www.semanticweb.org/fberkma_/ontologies/2025/surface_ontology#crater -->

<owl:Class rdf:about="http://www.semanticweb.org/fberkma_/ontologies/2025/surface_ontology#crater">
    <rdfs:subClassOf rdf:resource="http://www.semanticweb.org/fberkma_/ontologies/2025/surface_ontology#nonlineardepression"/>
</owl:Class>
```

Figure 1.21 *Declaration of a class for the concept Crater. The term about precedes the IRI (International Resource Identifier), which enables the encoding of other resources by linking them to the ontology once published on the web.*

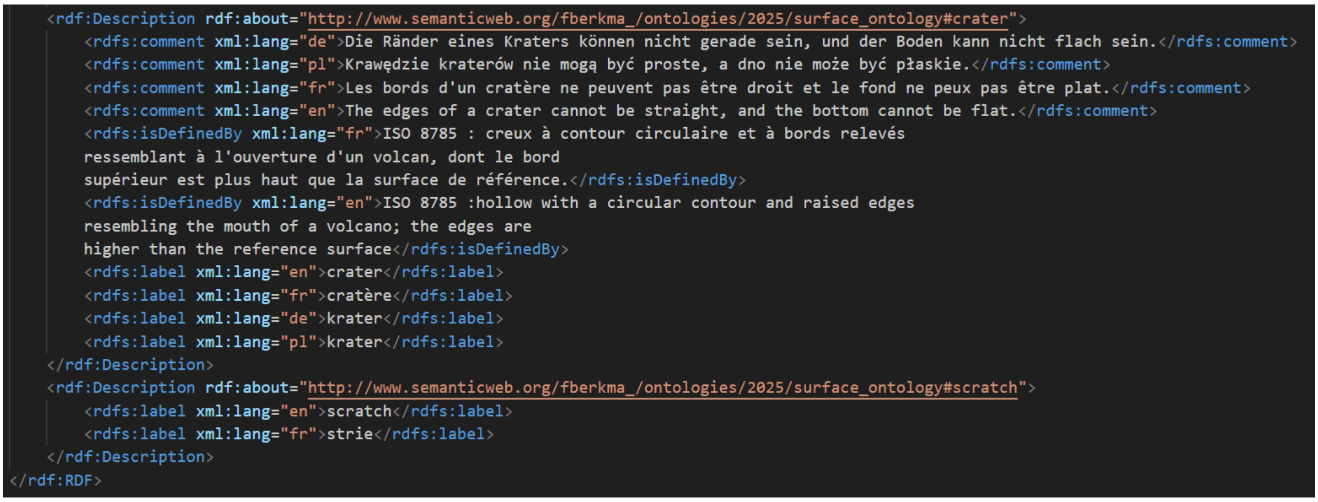

```xml
    <rdf:Description rdf:about="http://www.semanticweb.org/fberkma_/ontologies/2025/surface_ontology#crater">
        <rdfs:comment xml:lang="de">Die Ränder eines Kraters können nicht gerade sein, und der Boden kann nicht flach sein.</rdfs:comment>
        <rdfs:comment xml:lang="pl">Krawędzie kraterów nie mogą być proste, a dno nie może być płaskie.</rdfs:comment>
        <rdfs:comment xml:lang="fr">Les bords d'un cratère ne peuvent pas être droit et le fond ne peux pas être plat.</rdfs:comment>
        <rdfs:comment xml:lang="en">The edges of a crater cannot be straight, and the bottom cannot be flat.</rdfs:comment>
        <rdfs:isDefinedBy xml:lang="fr">ISO 8785 : creux à contour circulaire et à bords relevés
        ressemblant à l'ouverture d'un volcan, dont le bord
        supérieur est plus haut que la surface de référence.</rdfs:isDefinedBy>
        <rdfs:isDefinedBy xml:lang="en">ISO 8785 :hollow with a circular contour and raised edges
        resembling the mouth of a volcano; the edges are
        higher than the reference surface</rdfs:isDefinedBy>
        <rdfs:label xml:lang="en">crater</rdfs:label>
        <rdfs:label xml:lang="fr">cratère</rdfs:label>
        <rdfs:label xml:lang="de">krater</rdfs:label>
        <rdfs:label xml:lang="pl">krater</rdfs:label>
    </rdf:Description>
    <rdf:Description rdf:about="http://www.semanticweb.org/fberkma_/ontologies/2025/surface_ontology#scratch">
        <rdfs:label xml:lang="en">scratch</rdfs:label>
        <rdfs:label xml:lang="fr">strie</rdfs:label>
    </rdf:Description>
</rdf:RDF>
```

Figure 1.22 *Description of the resource, including the definition of standards (here ISO 8785); multilingual labels for ontology visualization (in French, English, German, and Polish); and comments in various languages that provide guidance to users, specifically in this case, indicating that a crater cannot have straight edges or a flat bottom. Such comments are useful when adding object properties or data properties to ensure semantic consistency and prevent confusion between concepts.*

The choice for IRI naming was to ensure that class IRIs is human-readable to facilitate navigation through the ontology structure. In contrast, instances (or individuals) have automatically and randomly generated IRIs to avoid redundancy between instances and with class concepts.

1.5.2 Supplementary information for the definition of surface phenomena

Given the sometimes-vague nature of definitions, it is possible to associate additional information with surface phenomena concerning their spatial arrangement or intrinsic characteristics, to provide a more precise description of surfaces and enable more effective indexing. Phenomena descriptors are based on orientation, position, shape, count, and spatial distribution (Figure 1.23). The orientation category mainly concerns linear surface features. It is useful to understand how these linear features are arranged relative to one another. If the grooves are concentric, they can be described as circular. If the surface results from a manufacturing process such as honing, the grooves can be described as arranged in a crosshatch pattern.

As for position, if the features cover the entire surface, it is not necessary to specify it. However, if specific features are observed in a particular area, positional information helps to determine the exact location of those elements. The shape of the features is complementary to their definition. For each descriptor, such as bottom shape, several options are possible. For example, a feature may have a flat, hemispherical, conical, or stepped bottom. As for the edges, they can be rounded, as in the case of a crater, or sharp for other types of features. The top shape can be flat, pyramidal, or rounded (Figure 1.24).

Structures may be organized in various configurations or spatial pattern, each carrying a different semantic nuance. An array refers to a general ordered collection of elements, typically arranged linearly or in multi-dimensional patterns, where position is determined by index, not necessarily by spatial proximity. An array can take various forms: honeycomb, cross-shaped, square, or even random. A cluster designates a group of elements that are closely packed together based on density or similarity, but not necessarily in a regular pattern, it conveys localize aggregation, not overall order. A network refers to a system of nodes and connections (edges), highlighting relationships or interactions rather than geometric position; a network can be irregular, hierarchical, or even non-spatial. Finally, something is tessellated when a space is entirely filled with non-overlapping shapes, usually repeating polygons such as triangles or hexagons, indicating a complete and seamless coverage of a surface, often used in geometry and texture mapping.

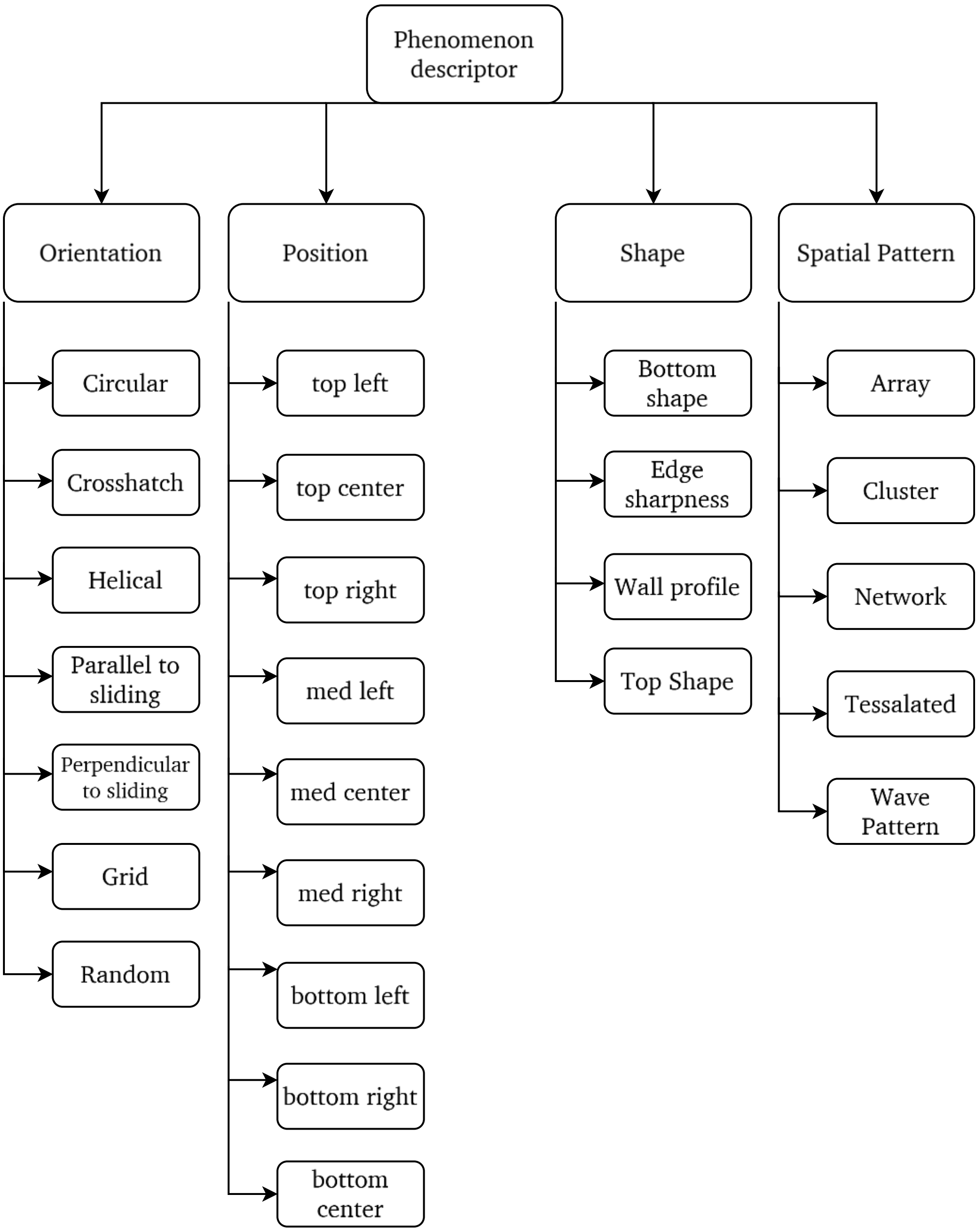

Figure 1.23 *Subclasses of phenomenon descriptor*

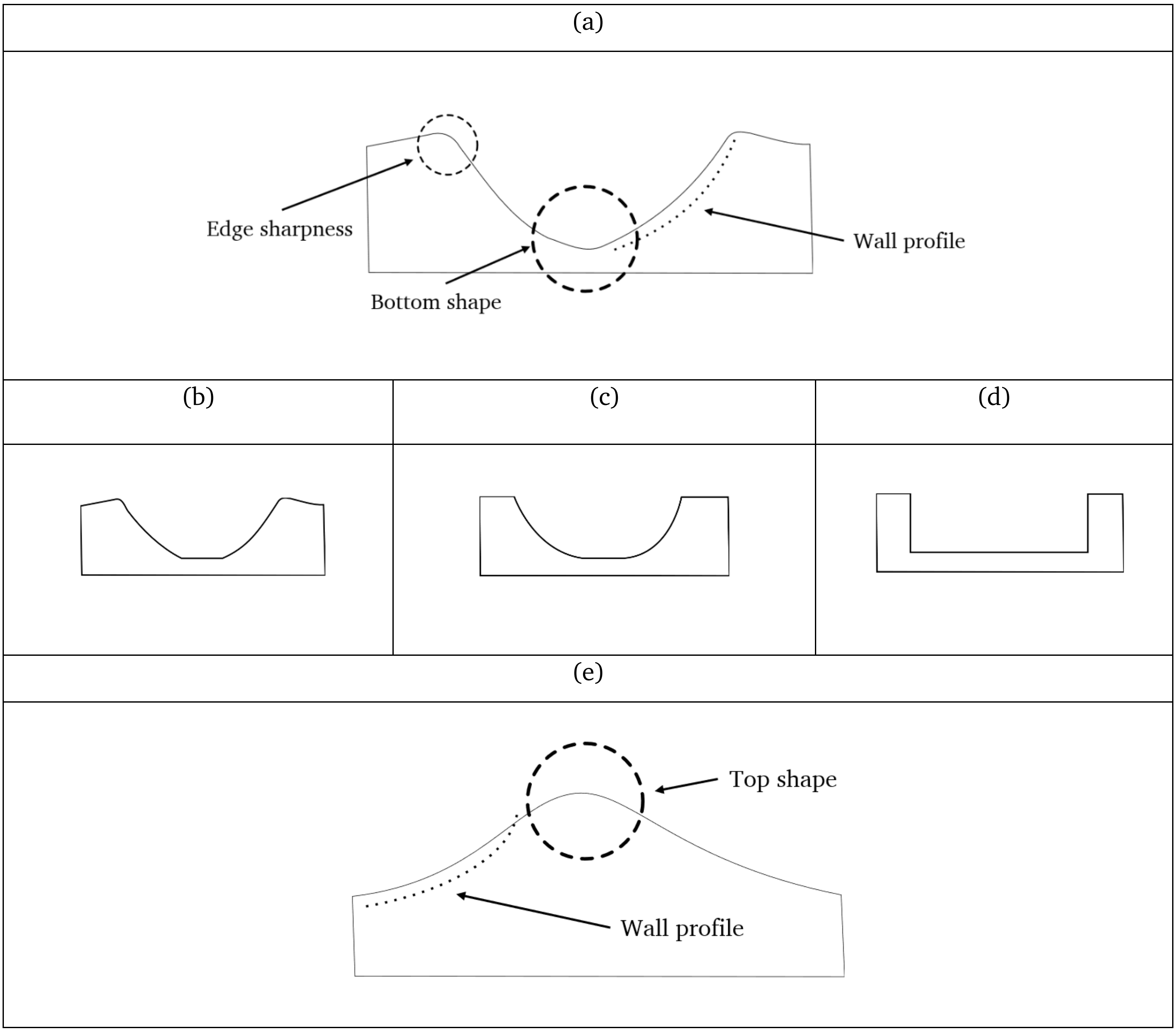

Figure 1.24 *Examples of different phenomena shape (a) elements of depressions (b) depression with flat bottom shape (c) depression with flat bottom shape and sharp edge (d) depression with flat bottom, straight edge and straight walls (e) elements of elevations*

1.5.2.1 Object Properties and Data Properties

In an ontology, the class hierarchy can be enriched by introducing more flexible relationships known as object properties and data properties. Object properties link two individuals, one acting as the subject, the other as the object, through a defined predicate. In contrast, data properties associate an individual with a literal value or attribute, such as a number, string, or date [86]. Individuals, also known as instances, represent the most fundamental or 'ground-level' elements within an ontology. While an ontology doesn't necessarily have to include individuals, one of its core functions is to provide a framework for classifying them. Individuals, or instances, are the concrete elements of the surface metrology domain, derived from existing concepts. In themselves, the classes *groove* or *dimple* refer to all grooves and dimples in the world, but individuals refer to those that exist and are observed.

It is possible for a surface to be measured multiple times using different apparatuses. The notion of scale implies that surface features may appear differently depending on the observation method, e.g. a cavity observed with a focus variation microscope may reveal pores when examined with an interferometer or an AFM. This is why an intermediate entity is introduced to provide information about the measurement protocol: who performed the measurement, with which device, the date, and other potentially useful metadata (Figure 1.25). Thanks to this approach, it becomes possible to create several individuals linked to a single surface.

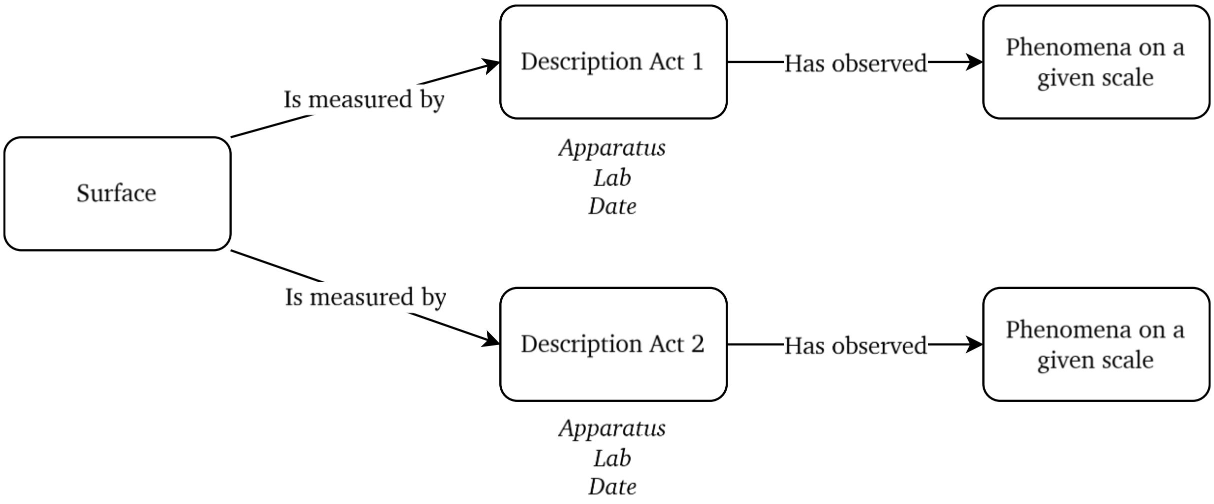

Figure 1.25 *Schematic representation of the description act that ensure traceability of measurements*

The author presents here some object properties that allow individuals to be linked to one another and to contextualize the information:

- **Has main feature**
  Links a surface to its most dominant or defining topographic phenomena.
- **Has secondary feature**
  Associates a surface with a subordinate or supporting phenomena that complements the main one.
- **Has morphological attribute**
  Connects a phenomenon to a morphological characteristic such as top shape, wall profile, or bottom shape.
- **Has orientation**
  Defines the directional or angular disposition of a phenomenon in space.
- **Has spatial pattern**
  Relates a surface to the spatial distribution or arrangement of its phenomenon (e.g. array, tessellated, cluster).
- **Has superposed feature**
  Links a phenomenon to another that is overlaid on top of it, usually formed later in time.
- **Has embedded feature**
  Connects a phenomenon to another that is embedded within it or partially enclosed by it.

To precisely characterize surface phenomena, a set of numerical data properties has been defined using the *xsd:double* datatype. These properties capture key geometric and morphological attributes observed in surface topography. The property *hasDepth* allows the recording of the depth of a feature (in μm), while *hasHeight* describes its elevation above the surrounding surface. *hasWidth* refers to the lateral extension of the phenomenon, and *hasDiameter* is used for circular structures such as craters. The occupied surface area is quantified using *hasArea* (e.g., in μm^2), whereas *hasVolume* measures the total volume enclosed by the feature, whether it be a cavity or a relief. The *hasAspectRatio* property expresses the ratio between width and height, offering insight into the general shape profile. Additionally, *hasSlopeAngle* specifies the steepness of the walls (in degrees), and *hasCurvature* captures the local mean curvature, which is essential to distinguish between flat, convex, or concave features. Together, these properties offer a robust numerical framework to support both semantic description and quantitative analysis of surface phenomena. The *hasNumber* data property is used to specify the total count of individual surface phenomenon when they are not part of a structured pattern or array. For regularly arranged features, two additional data properties, *hasRowNumber* and *hasColumnNumber*, are introduced to describe the number of row and column, respectively, allowing for a precise representation of array-like distributions on the surface.

1.5.3 Instance encoding

In an RDF ontology, instances, also called individuals, are specific entities that belong to a general class. While classes define categories or types of things (such as Photograph, Surface, or Material), instances represent concrete examples of those categories. For example, an individual surface named :Surface 1 would be an instance of the class :Surface. Following the same logic, each observed phenomenon is represented as an instance, with individuals connected to one another through object properties (Figure 1.26, 1.27).

1.5.3.1 Example 1

Encoding of surface phenomena using the ontology; the document type elements and the act description have been deliberately omitted for clarity. The way one could describe the elements presented here would be: “surface with 3 linear ridges 9 dimples in an array of 3 columns and 3 rows imbedded in ridges”.

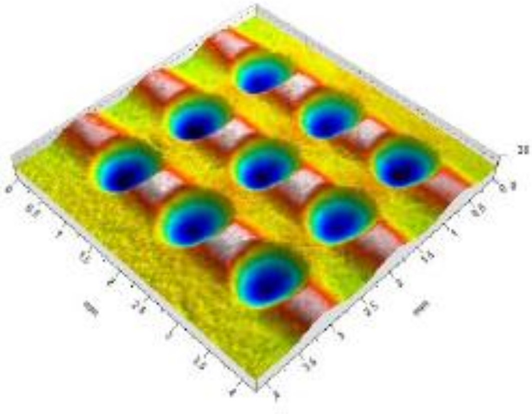

Figure 1.26 *Surface topography of shot peening on EN AW 7075 aluminium. Reproduction of the illustration from the paper of Matuszak et al [87]*

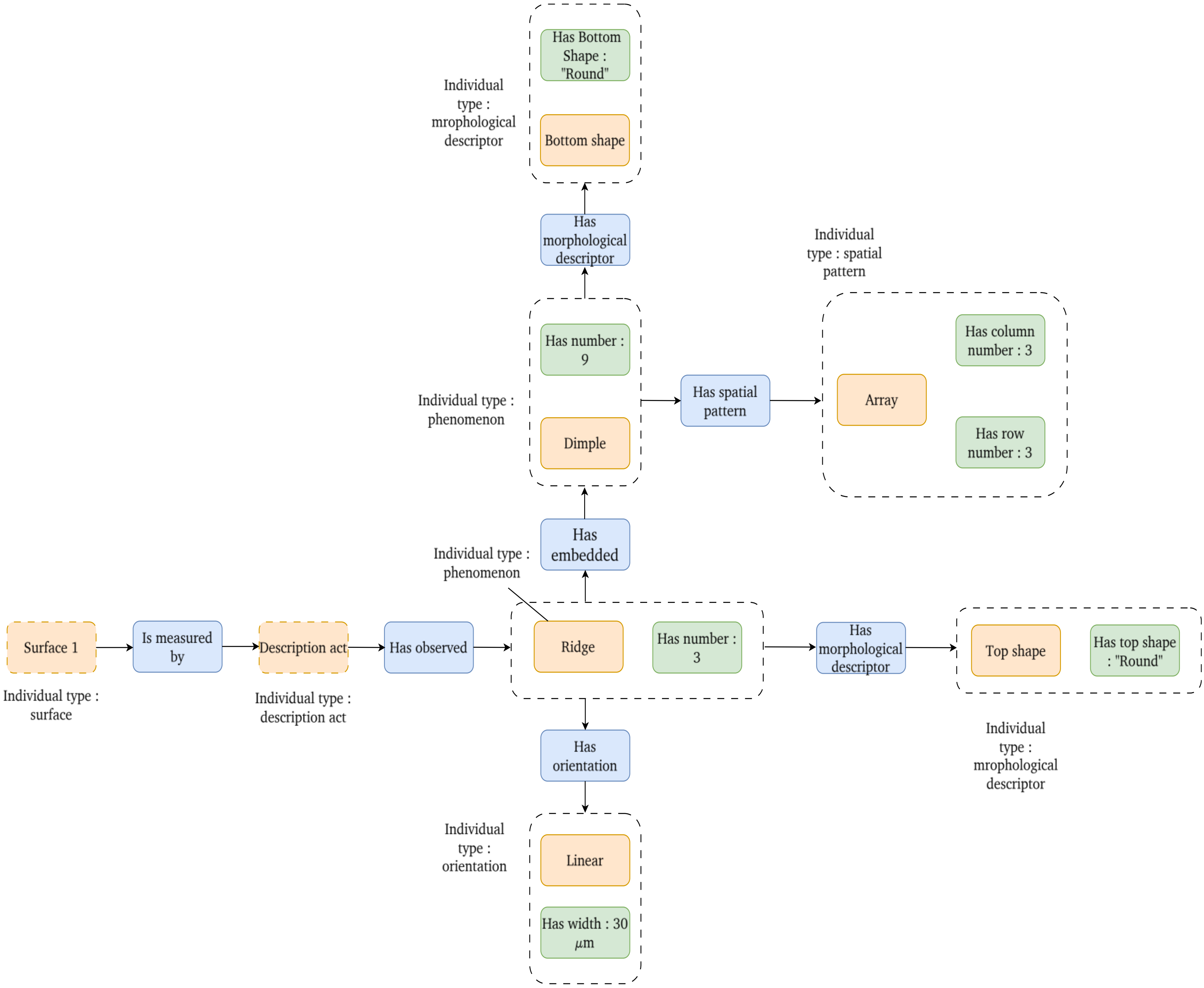

Figure 1.27 *Schematic representation of surface encoding using the RDF ontology. Individuals are represented in red; object properties connecting individuals are shown in blue; and data properties specific to individuals are represented in green. Each individual is assigned an IRI to ensure traceability and facilitate indexing.*

1.5.3.2 Example 2

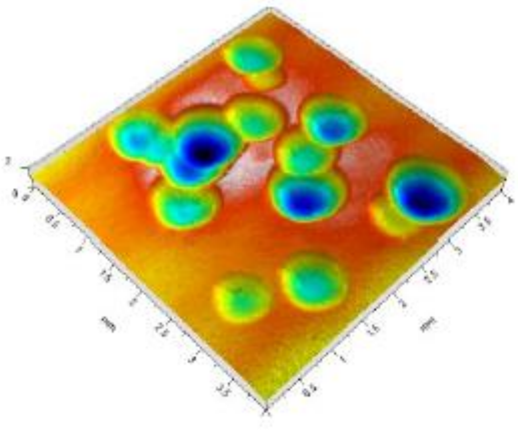

Figure 1.28 *Surface topography of shot peening on EN AW 7075 aluminium. Reproduction of the illustration from the paper of Matuszak et al [87]*

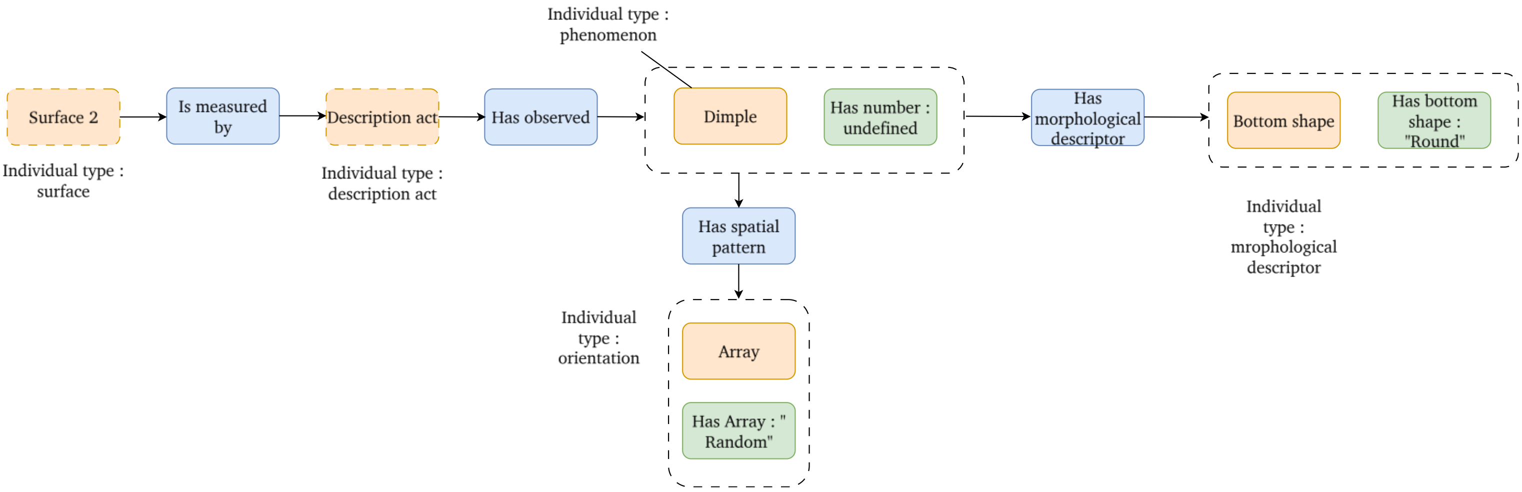

Figure 1.29 *Schematic representation of surface encoding using the RDF ontology. Individuals are represented in red; object properties connecting individuals are shown in blue; and data properties specific to individuals are represented in green. Each individual is assigned an IRI to ensure traceability and facilitate indexing.*

1.5.3.3 Example 3

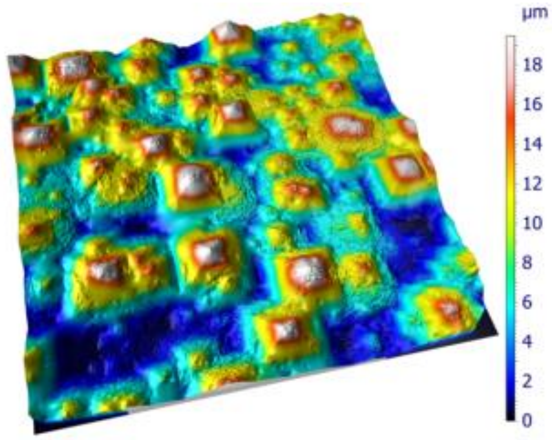

Figure 1.30 *Surface topography of solar cell pyramids array from the documentation of MountainsMap software (Digital Surf^{TM}, Besançon, France)*

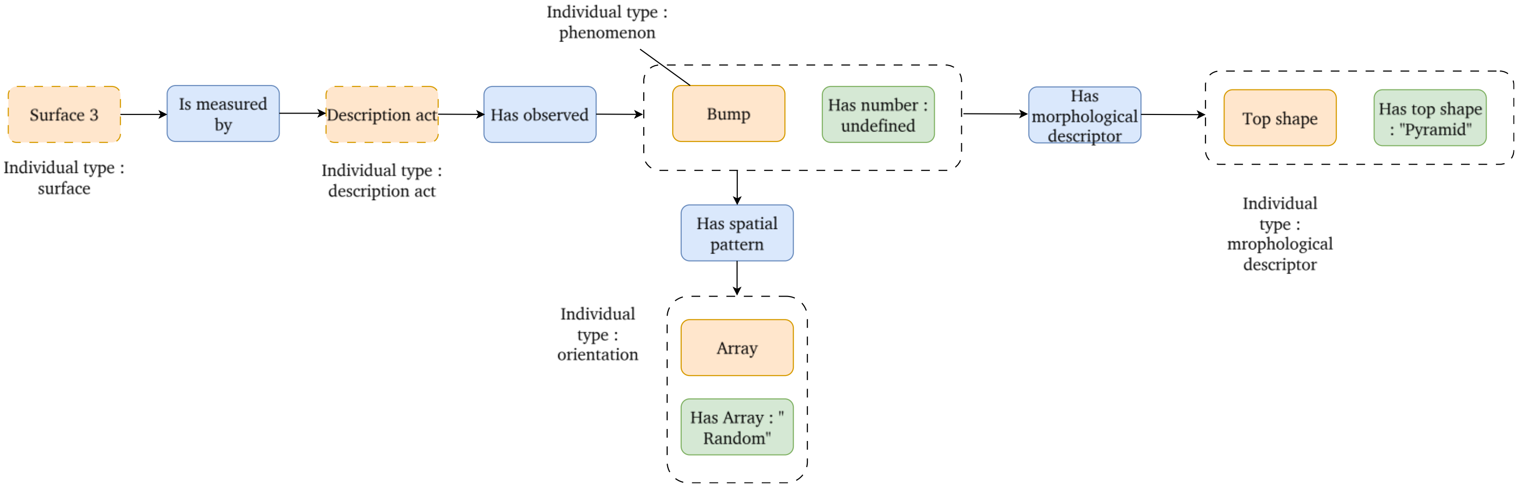

Figure 1.31 *Schematic representation of surface encoding using the RDF ontology. Individuals are represented in red; object properties connecting individuals are shown in blue; and data properties specific to individuals are represented in green.*

1.5.4 SPARQL Queries

SPARQL (SPARQL Protocol and RDF Query Language) queries enable the interrogation of structured data within an OWL ontology expressed in RDF [88]. Unlike traditional relational databases, where queries target fixed tables, SPARQL allows for flexible querying based on the semantic structure of the knowledge graph. Thanks to the surface phenomenon ontology developed here, it becomes possible to formulate complex queries that combine semantic relationships, class hierarchies, and numerical property constraints. For example, one can query all topographical features classified as *depressions* with a depth greater than 50 μm and an average curvature above a certain threshold or retrieve all *arrays* of *pits* with more than 10 rows and 10 columns. Other queries may target *embedded* phenomena using object properties like “has Embedded”, or specific configurations such as *pits* with a height-to-width ratio below 0.5. In this way, the ontology goes beyond a mere collection of definitions: it becomes a powerful tool for annotation, semantic exploration, and data mining in the fields of metrology and surface science.

1.6 Discussion of the Chapter

One of the fundamental choices in the modelling process was to structure the ontology around the surface phenomena themselves, defining them as central classes within the ontology. This approach makes it possible to directly capture the observable features on surfaces, independently of the functional or technological contexts in which they appear. Rather than classifying the phenomena according to preexisting normative criteria or by their origin (such as defects, machining marks, or wear), the decision was made to categorize them based on their intrinsic morphological properties, such as depressions, elevations, or discontinuities. This allows for greater extensibility, particularly by integrating phenomena that are not yet standardized but are commonly encountered in characterization practices.

The distinction between classes (types of phenomena) and instances (concrete observations on measured surfaces) was also carefully maintained. For example, the class *crater* refers to a morphological type, while an instance of *crater* may be associated with specific quantitative properties such as its diameter, depth, or slope angle. This separation between types and their occurrences enables comparative analysis of analogous phenomena across different surfaces and paves the way for a more refined formalization of morphological description, while adhering to the principles of the OWL formal ontology.

The ontology makes it possible to centralize information from various standardized and non-standardized terminological sources, thereby formalizing the elements that can be used to describe surfaces. Definitions are included in the ontology through dedicated resources, and the properties associated with individuals are sufficiently flexible to allow for a wide range of descriptive possibilities. However, some limitations still need to be addressed. Despite the advantages offered by the ontological modelling of surface phenomena, the present proposal has several limitations. First, the structuring of concepts relies largely on heterogeneous sources (ISO standards, technical dictionaries, scientific literature), whose definitions are sometimes contradictory or imprecise. The choices made to create unified classes may therefore introduce interpretations that are not universally accepted across the various relevant disciplines (tribology, materials science, heritage conservation, etc.). Moreover, some fine morphological distinctions, such as those between a peak, a tooth, or a protrusion, are highly dependent on the context of observation or the measurement methods used, making their formalization challenging. In addition, the ontology currently includes only a limited number of instances and does not yet cover the full range of topographic phenomena observed in complex surfaces. Finally, although promising, the section dedicated to quantitative properties still requires a more rigorous metrological grounding to ensure interoperability with real-world measurement systems. These limitations do not undermine the overall approach but highlight the need for gradual enrichment and ongoing interdisciplinary validation.

The main limitation of the ontology lies in its ability to distinguish isotropic surfaces in general. Indeed, some surfaces do not exhibit clearly distinguishable features other than a uniform roughness, making them particularly difficult to describe. However, it is possible to define a class that groups these homogeneous surfaces to assign them data properties related to ISO roughness parameters. For users conducting a search, a quantitative approach may be more suitable than a descriptive one for this type of surface.

The developed ontology, although initially designed to structure the terminology of topographic phenomena, paves the way for applications in many other domains. For instance, in materials science or heritage conservation, it could support better standardization of descriptive vocabulary and facilitate interoperability between databases, normative documents, and experimental results. Similarly, by integrating additional modules (such as an ontology of surface treatments or of functional properties like adhesion or hydrophobicity), it could support

Knowledge Graph-based approaches to identify correlations between surface morphology and functional properties. Finally, thanks to its modular design, the ontology could be adapted to other scales (microscopic, macroscopic) or to different types of materials (organic, mineral, biological), providing a flexible foundation for multidisciplinary approaches.

Finally, the question of data indexing and encoding arises, as it remains a key aspect in the development of any ontology, database, or search system. The issue of morphological phenomena carries a strong semantic dimension, which, for now, can only be addressed through human description of the phenomena in connection with their definitions. Two avenues can help facilitate this process: first, providing support for manual encoding, and second, developing long-term automation of the encoding process. This perspective opens opportunities in artificial intelligence, particularly in the development of annotation systems or tools to assist with the automated analysis of topographic images, where the ontology can serve as a semantic mediator. For the manual encoding assistance phase, a simple graphical interface could be envisioned, as illustrated in Figure 1.32, allowing the user to directly select surface elements and their object properties through dropdown panels. Saving the file would automatically generate the necessary instances and add them to the triple store.

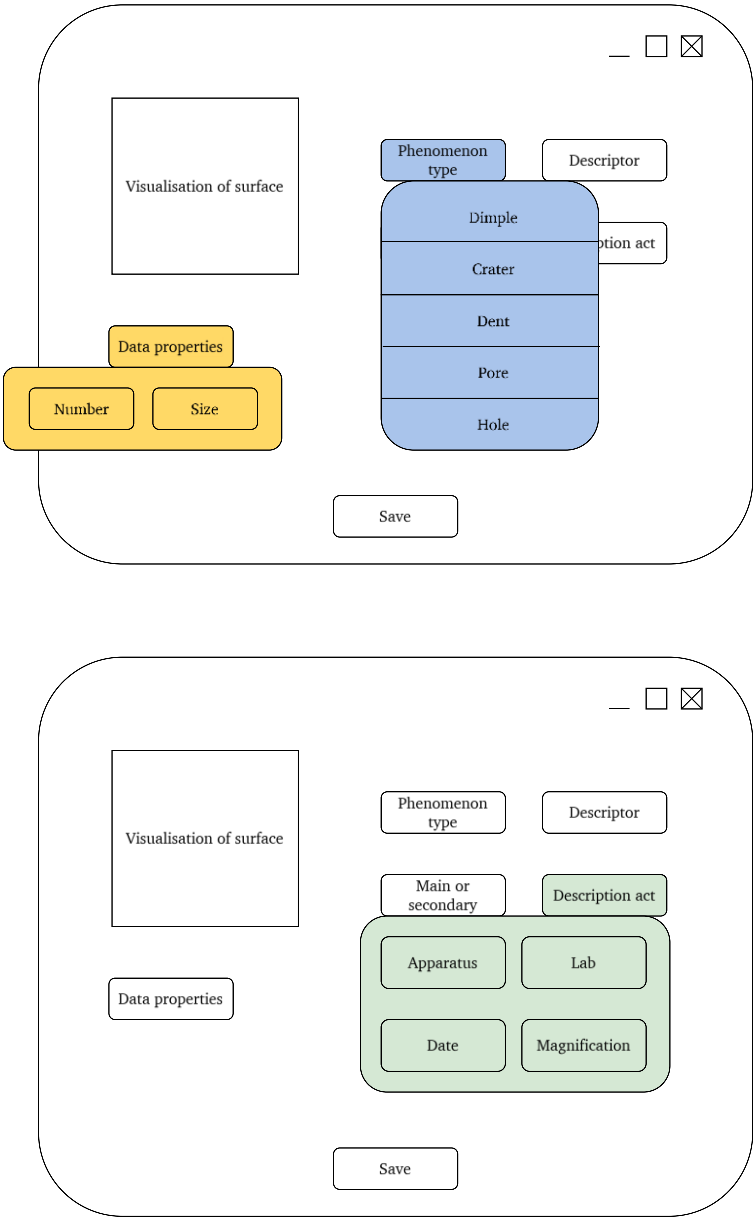

Figure 1.32 *Wireframe for an interface to create instance for Surface Ontology*

1.7 Conclusion of the Chapter

The terminological challenges in surface metrology, far from being a merely semantic or marginal issue, directly affect how surface phenomena are perceived, analysed, and communicated across scientific and industrial domains. This chapter has highlighted the fragmentation of existing terminologies, the mismatch between formal standards and actual usage, and the crucial role played by visual representations in the naming and understanding of surface features.

In response to these challenges, we have proposed a conceptual shift: moving from ad hoc or process-specific descriptors to a unified, phenomenon-centred ontology. Designed in OWL and grounded in formal logic, this ontology allows for the explicit representation of surface phenomena, their morphological descriptors, and the relationships that link them. It integrates both standardized and non-standardized terms, enabling richer and more interoperable surface descriptions.

By consolidating scattered vocabularies into a single OWL-based ontology, Chapter 1 resolves the linguistic ambiguities that have long clouded surface-metrology research and practice. Every scratch, groove or crest now maps to an explicit *phenomenon–attribute–context* triple, ensuring that subsequent analyses refer to the same objects of discourse. With this common language secured, the thesis can progress to the next tier of the Surface Information Acquisition Spectrum: visual syntax.

Chapter 2

Complexity of Heraldic System

Taking Coats of Arms as a 2.5D Surface

Prolegomena of the Chapter 2

Having established in Chapter 1 a phenomenon-centred vocabulary for every kind of topography, we now turn to surface systems, entities whose morphology is not merely a physical state but a carrier of information. Medieval coats of arms occupy a unique position among such systems: simultaneously a painted surface (*2.5 D* when the relief of the enamel is considered) and an encoded message, they blend geometry, colour, and compositional rules.

The founding question of this chapter is therefore: Does the heraldic surface operate primarily as a language, governed by an explicit syntax, or as a fractal-like object whose complexity emerges from repetition and self-similarity? To address it, we situate the study at the "visual-syntax" tier of the Surface Information Acquisition Spectrum (SIAS), the hinge between the *language* level (already clarified) and the forthcoming *fractality* level. In other words, heraldry serves here as a laboratory where a single surface articulates both the rigour of a formal grammar and the escalation of complexity typical of fractal structures.

This prolegomenon thus sets the dual, semiotic and geometric, framework within which partitions, tinctures, and charges will be analysed: each coat of arms will be treated simultaneously as a graphic sentence and as a nested scale series, so that we can determine whether the heraldic surface leans more toward linguistic or fractal behaviour.

2.1 Heraldry: Definition and History

It is necessary from the outset to introduce the reader to the realm of heraldry, which invites a multitude of interpretative angles. This can be explained using coats of arms across various fields. The social, historical, and emblematic themes present in heraldry can be explored separately as historical or stylistic study topics. Recent research aimed at understanding and analysing this discipline remains scarce in comparison to the scholarly approach that prevailed among specialists in the 19th century. This is largely due to the lasting cliché dating back to the French Revolution, which attributed to heraldry obscure esoteric notions and falsely princely values, relegating this noble science to a marginal and hermetic branch of art history [89].

Considering such preconceived ideas, it is necessary to return to the foundations of this science to clarify the stakes of a study whose purpose is to facilitate research and analysis. Let us first consider heraldry from both a historical and socio-cultural perspective. Heraldry appeared in 11th-century Europe during the feudal era. At that time, social elites, attached to their fiefs and territorial possessions, sought to identify themselves visually. According to some theories now considered fanciful [90] heraldry may have originated in the East between the First and Second Crusades. However, for Michel Pastoureau, this is not the case: heraldry is a purely Western invention [91]. The compositional rules, which form the basis of heraldry's specific language, emerged between the First and Second Crusades. It seems that systems we might call pre-heraldic existed, notably in Ancient Greece. There, divine figures painted on shields had an apotropaic function. However, these did not yet rely on a codified structure such as that developed during the Middle Ages.

It was during councils that Kings of Arms would compile coats of arms gathered from across the kingdom, correct those containing errors, and agree upon the establishment of heraldic rules. The art of heraldry is a true reflection of medieval society. The richness of its vocabulary, the variety of its motifs and forms, the prominent role of heralds, and its wide dissemination all help to revise the overly reductive and disparaging image some still hold of a supposedly "dark" Middle Ages. In fact, this same medieval heraldry even foreshadows certain modern practices such as visual communication, semantics, and data preservation methods.

Beyond emblematic and graphic design concerns, heraldry also had a practical function related to the battlefield: coats of arms displayed on shields, surcoats, horse trappings, and banners enabled the identification of belligerents amid the chaos of combat. The word "blazon" (coat of arms), synonymous with shields, came to acquire a conceptual meaning referring to the colours (metals and tinctures), shapes (ordinaries), and motifs (charges) arranged on a surface, regardless of the support.

The available colours, divided into categories based on light/dark contrast, are well distinguished, and the stylized figures are easily recognizable from afar to avoid misinterpretation. At least, that was the intention initially, some coats of arms eventually became so overloaded that they were indecipherable at a distance. The design style of heraldic figures was initially influenced by Romanesque art and the early Gothic style. Heralds created both imaginary and familiar elements to build a rich visual identity. As for heraldry's evolution in the face of socio-political changes: contrary to popular belief, coats of arms were not a privilege of the nobility. From the 13th century onward, coats of arms were created regardless of social status; guilds, corporations, and families could use personal armorial bearings, provided they respected the grammar of heraldry and did not appropriate an existing coat of arms.

Originally emerging in the regions between the Loire and the Rhine, coats of arms later spread to southern England, Switzerland, and Italy, eventually reaching all of Europe and even the borders of the East by the 14th century.

Numerous medieval texts contain anecdotes about heraldic motifs. Two particularly illustrate the emergence of this uniform and codified visual language in the late Middle Ages:

- The Bayeux Tapestry, dated to 1080, which depicts shield figures (dragons, crosses, etc.); however, due to the non-systematic association of these motifs, this remains a proto-heraldic era [92].
- In Chrétien de Troyes' *Lancelot, the Knight of the Cart* (written between 1164 and 1172), Lancelot, having set aside his shield to participate in a tournament anonymously, is recognized by a herald of arms who spreads the news. This suggests that coats of arms were already associated with knights, and that professional heralds existed to identify them.

The word "heraldry" derives from "herald," referring to the person appointed by a lord to deliver messages especially at the onset of conflict and announce tournaments. From messenger, the herald evolved into a heraldry specialist when one of his roles became describing knights' arms to the audience, since they were otherwise unrecognizable in full armour.

From the 12th century onward, the use of coats of arms painted on shields and embroidered on surcoats and horse trappings became systematic across Europe, both on battlefields and in tournaments. Heraldry was so successful that experts in this visual language were needed to safeguard and ensure the rules of heraldry were respected [92].

A few words on the profession of herald of arms: beyond their versatility as designers of armorial bearings, tournament commentators, emissaries, and ambassadors, heralds enjoyed significant respect. The most distinguished among them were promoted to the rank of King of Arms. During their inauguration, Kings of Arms wore royal garments and were crowned by their lord a ritual underscoring the true importance of their office.

Tradition held that every three years, these Kings of Arms would gather in a committee to establish, in the traditional formula:

“The knowledge of all nobles, each in his province, whether princes or lords and others among the living, and as is said, their names, surnames, coats of arms, crests, and noble fiefs, both through themselves and their wives, so that the King may be regularly informed of the nobility of his kingdom” [93].

The blazoning found in diplomatic documents and literary works can provide information on the evolution of heraldic vocabulary or evidence of lineage, considering the hereditary nature of coats of arms. These elements help to fill the gaps in the armorial records, which only begin to appear in the mid-13th century. Armorials and armorial seals remain the primary sources for historians.

A note for the reader of this chapter: heraldic language has its roots in French, which was largely adopted into English heraldic vocabulary, since Anglo-Norman French was the language of the nobility in England during the formative period of heraldry. This is why the vocabulary used in this chapter may seem unfamiliar, or even obscure.

2.2 Heraldry and Complexity

The reading of arms is called blazonry and allows for a description of the coat of arms, including the colours and elements that compose it. The language used to describe coats of arms is a specialized language. Some vocabulary elements come directly from everyday life in the Middle Ages, such as the naming of certain figures (e.g a sword). However, colours, for example, have symbolic names and there are two main families: tinctures and metals. For tinctures, we have azure (blue), gules (red), vert (green), and sable (black). For metal or (yellow) and argent (white) [91]. This use of language with strict syntax and rules developed to compile armorials using textual information rather than undertaking the laborious task of drawing each coat of arms. From a semantic perspective, this creation of a quasi-computer language allowed heralds to have a mental representation of the coat of arms by reading its description.

A coat of arms is composed of successive layers, so the blazonry always begins by stating the bottom layer before progressively moving up to the elements that are superimposed on it. Heraldry can be considered a 2.5D space (Figure 2.1), as it relies on a system of layered superposition that goes beyond simple bidimensionality. Each element of the coat of arms maintains its own existence, even when partially covered by another. Unlike a classic 2D image where shapes merge, heraldry functions as a system of layers in which the order of elements structures the composition. This implicit spatial hierarchy provides an organizational depth without introducing true three-dimensional perspective. Thus, heraldry follows a representational logic in which stratification plays a fundamental role, positioning its space between pure 2D and fully developed 3D. The author André Gide [94] would say, before the concept of fractals was developed by Benoît Mandelbrot:

"I rather like it when, in a work of art, one finds the subject of the work itself transposed to the scale of the characters, in comparison with the heraldic device of mise en abyme, which consists of placing the second within the first."

We hypothesize that heraldry is a multiscale structure, quite different from traditional fractal objects like the Koch Snowflake or the Sierpinski Triangle [95]. Indeed, the rule of self-similarity can appear in heraldry but is not common. However, the notion of informational complexity at different scales is fully present, with the theoretical possibility of an infinity of layers and elements within a finite space.

This fractality can be difficult to express, as a scaling law is hard to observe, as is self-similarity. Elements can, of course, repeat in reduced versions as the space of the shield is partitioned into various divisions, but the smaller scales can sometimes be simpler in terms of information than the larger scales. In essence, the lower layers can be left blank while the foreground phenomena a lion with multiple detailed elements in various colours, placing a significant amount of information in the foreground.

The notion of informational complexity in heraldry is correlated with its composition. A complex coat of arms composed of three elements, three colours, and ornaments will have a higher informational value than a simple coat of arms containing only one figure and two colours. Studies on the complexity of coats of arms are scarce; the only one to date is, in fact, more of a graphic design study than a true heraldic analysis. Indeed, the study by Miton and Morin [96] focuses on the graphical complexity of icons and geometric shapes (e.g., a lion is graphically more complex than a wheel, just as a cross is geometrically more complex than a pale). This assumption leads to an inversion of Zipf's law of abbreviation [97] in the occurrences observed within a corpus of 25,115 coats of arms.

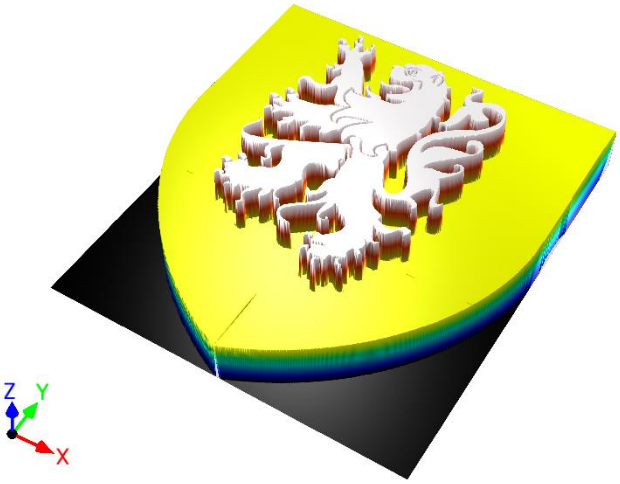

Figure 2.1 *2.5D representation of a coat of arms composed of two layers; the conversion to false colours related to height shows the superposition of the lion figure over the field*

Zipf's Law Of Abbreviations states that shorter signs are more frequent than longer ones. It is an empirical law observed in many human and non-human [98,99] communication systems. Regarding human systems, studies show that many languages follow Zipf's law; although this is not systematic, a high degree of redundancy can be observed [100,101]. In *The Psycho-Biology of Language* [102] he says: "In view of the evidence of the stream of speech we may say that the length of a word tends to bear an inverse relationship to its relative frequency. Footnote: Not necessarily proportionate; possibly some non-linear mathematical function."

We think that contrary of the article of Miton and Morin [96] Zipf's Law of Abbreviation is not related to the graphic complexity of the figures, but rather to laws intrinsic to heraldry itself: the more complex the composition, the greater the knowledge required to understand it. Complexity involves several variables that add up to one another: on the one hand, colours, the number of distinct elements on the coat of arms, the partitions, the details, and what we refer to as variations, that is, the deviations from a basic form toward auxiliary or derived forms.

These elements can be referred to as units of complexity, insofar as their accumulation increases the overall complexity of the coat of arms.

In this chapter, we aim to define what we mean by heraldic complexity and to calculate this complexity to establish a broader understanding of a unique communication system that was used for nearly a thousand years. Ultimately, this may allow us to explore whether heraldry follows a Zipf Law of Abbreviation.

2.3 Basic rules

Firstly, we must discuss the shield. The shape of the shield is not of interest as information in our mode of thought; it is simply the enclosed space in which the informational elements are found. Whether the shield is of an old French style, diamond-shaped, or Swiss style makes no difference (Figure 2.2). The representations in the history of heraldry can vary from one style to another without altering our logic.

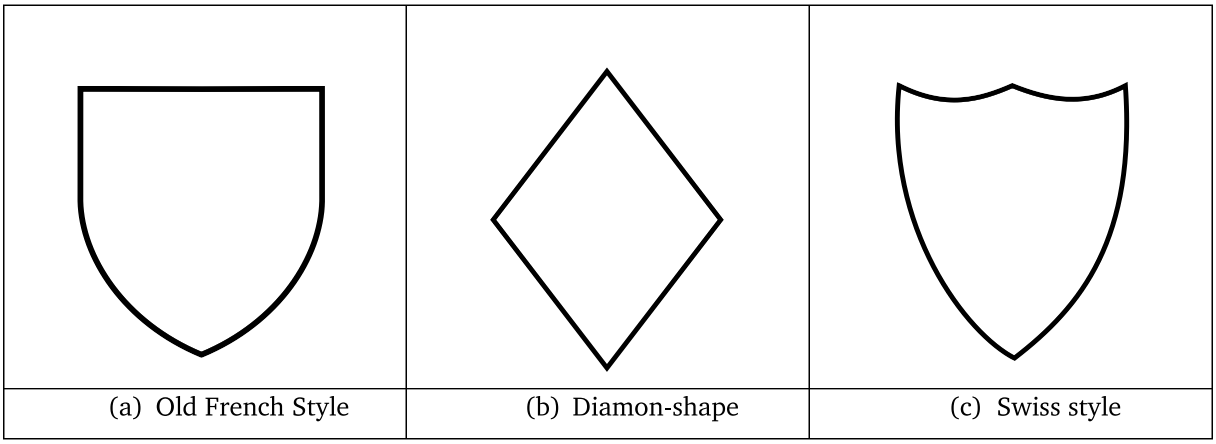

(a) Old French Style (b) Diamon-shape (c) Swiss style

Figure 2.2 *Different style of Shields as an example, we could also add Polish, German, British, Italian and so on.*

2.3.1 Partitions

The second element is what we call partitions, which involve dividing the coat of arms into two subdivisions that are part of the same system. This can occur during an alliance or marriage; in the Middle Ages, ladies had coats of arms that included both the arms of their husband and those of their father. The four basic partitions are 'party,' 'couped,' 'taillé,' and 'tranché' (Figure 2.3 and 2.4).

Two fundamental rules for the composition and interpretation of coats of arms are as follows:

1. It is forbidden to superimpose or juxtapose two colours from the same family (tinctures and metals). For example, the combination of white and yellow is not allowed (although there are exceptions, and unfortunately, they are numerous in heraldry).
2. The interpretation of the coat of arms always begins with the bottom layer, starting from the top left corner and progressively moving upwards.

These rules are essential for ensuring the clarity and distinctiveness of heraldic designs, which were originally intended to be easily recognizable from a distance, especially on the battlefield. The use of contrasting colours (tinctures and metals) helps to achieve this visibility, while the systematic approach to reading the coat of arms ensures that the design can be accurately described and understood.

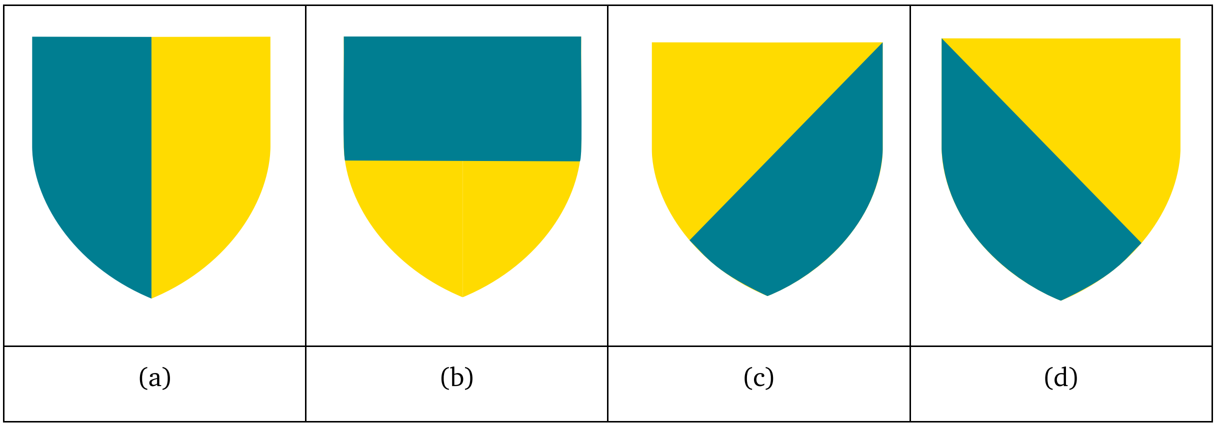

(a) (b) (c) (d)

Figure 2.3 *The four basic partition (a) Party per pale azure and or, (b) Couped per pale azure and or, (c) taillé per or and pale azure, (d) tranche per pale azure and or. N.B. Or is the heraldic term for yellow*

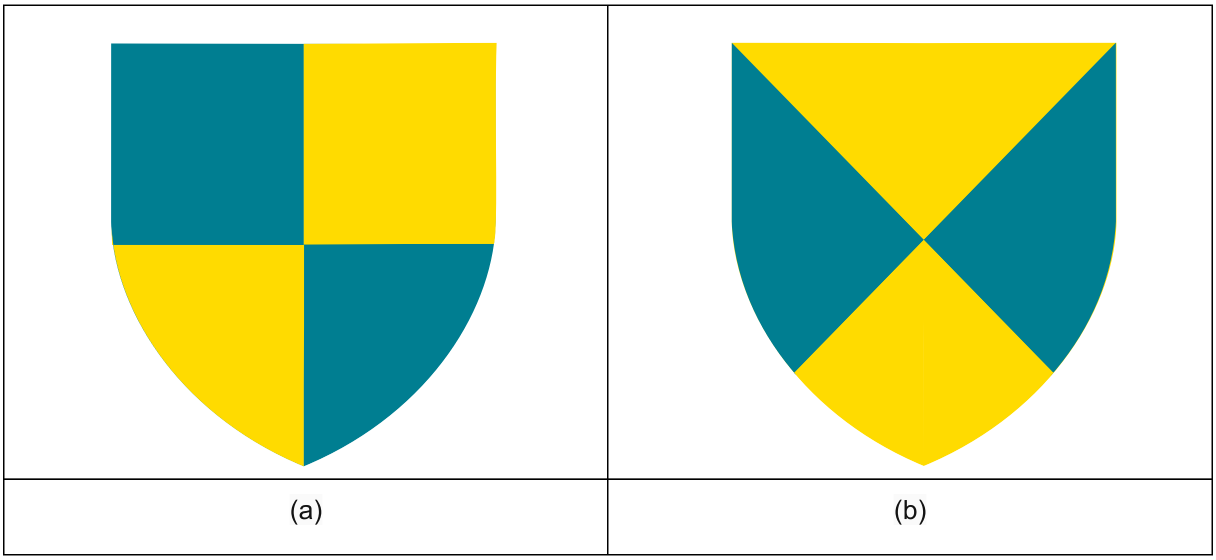

(a)

(b)

Figure 2.4 *(a) Quarterly azure and or (b) Quarterly per saltire azure and or*

2.3.2 Tinctures and ordinaries

The rule of tincture is a fundamental principle in heraldry, which states that metals (such as gold and silver) should not be placed on top of other metals, and colours should not be placed on top of other colours. This rule ensures that the elements of the coat of arms are clearly visible and distinguishable from one another. The rule of tincture is strictly adhered to in British coat of arms, with only rare exceptions, although it is generally observed in continental heraldry as well. In heraldry, the field of a shield can be divided into multiple tinctures, and the rule of tincture can be ignored for divisions of the shield. For example, a shield divided into azure (blue) and gules (red) would be acceptable.

The next step in these partitions is what is called the re-partition system, which involves creating an additional division that becomes another space in the heraldic complexity. After partitions and colours, the third important element in heraldic construction is the use of ordinaries. This involves structuring the surface of the shield, not by dividing it like partitions, but by overlaying it with ordinaries (also known as 'charges'), which are geometric figures. All ordinaries are identified by a noun. Some names refer to concrete realities, such as the pale (Figure 2.5.a) or the cross, for example. There are six very common and fairly large ordinaries that can be charged with other figures. These are then called 'honourable.' Additionally, these ordinaries extend to the edges of the shield, except when they are shortened or 'diminished' (Figure 2.5). Again, as in heraldry, there are types of ordinaries, but it would take too much time to enumerate them all, and it would not add significantly to our mathematical demonstration.

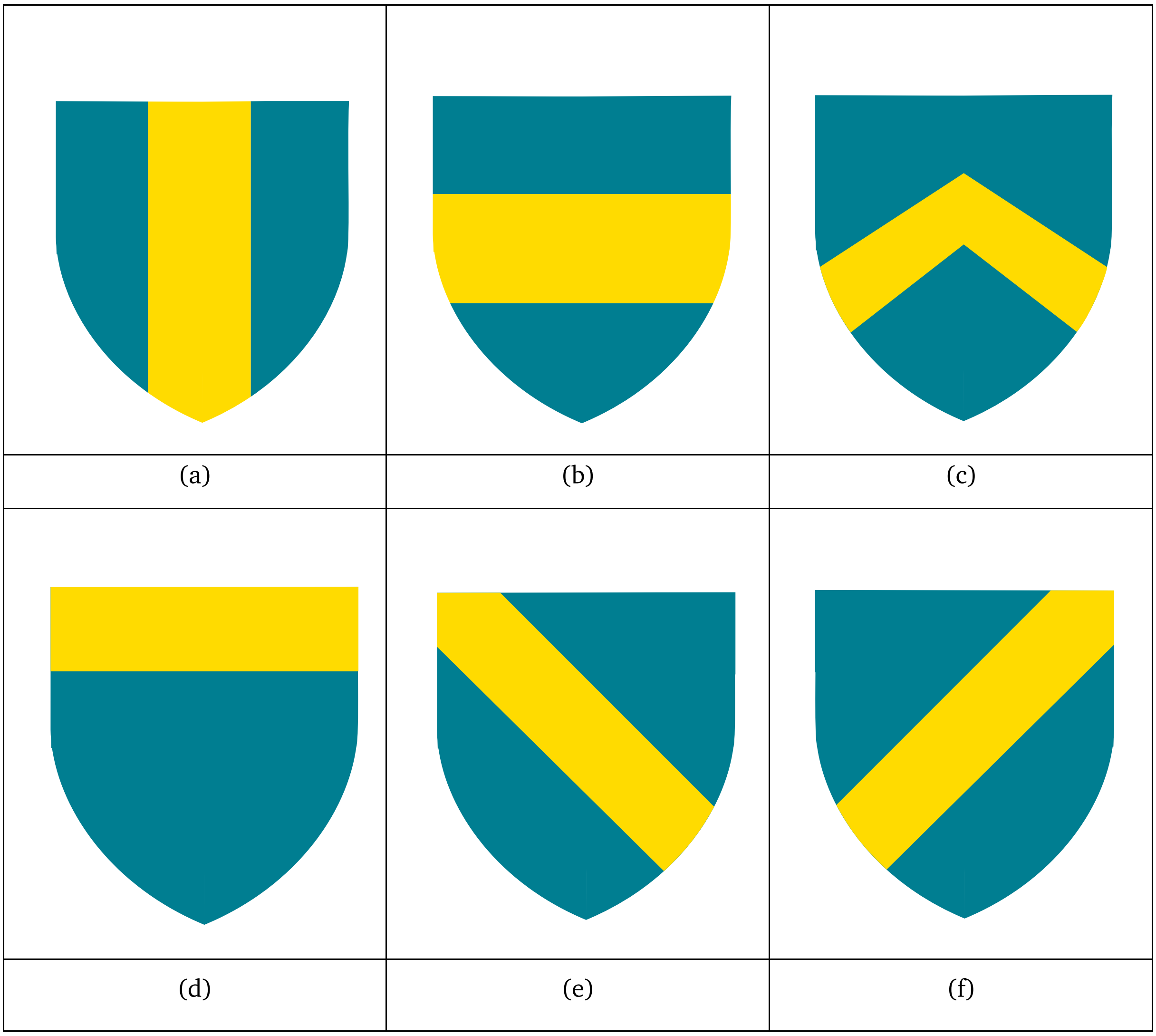

(a) (b) (c)

(d) (e) (f)

Figure 2.5 *(a) Azure, a pale or, (b) Azure, a fess or, (c) Azure, a chevron or, (d) Azure, a chief or, (e) Azure, a bar or, (f) Azure, a bend or*

The fourth function of heraldic syntax is constituted by what are commonly referred to as charges. Charges are elements that 'furnish,' or 'adorn,' the field of the coat of arms, whether there are ordinaries on it or not. The metaphorical names refer to concrete realities that can be various objects such as bezants, annulets, chains, mullets, etc., instruments of war, weapons or pieces of armour, constructions, often military, such as towers or castles, celestial bodies, plants such as flowers, trees, etc., animals of various kinds, and parts of the human body. These charges can be placed directly on a plain shield or on ordinaries, but it is also possible for some ordinaries to partially cover these charges; in such cases, they are said to be 'brochant' on something. We will only take a few examples, notably the lion, which has enough variants to be of interest (Figure 2.6). It should be noted that style does not affect the reading of a coat of arms. One may have a coat of arms with a lion in a very simple style offering few details, and the same representation of this coat of arms featuring a lion executed in a realistic style; both will be read in the same way. The style does not provide informational content. However, certain variants do provide information. For example, a lion described as 'rampant' is the default figure and must be depicted in a single colour. However, if 'armed' is added, it adds informational content because the claws must be of a different colour. Similarly, if 'lampassé' is added, the tongue will also be of a different colour. The size of charges in heraldry can vary from one coat of arms to another. It is logical that elements placed in subdivisions are smaller than when they are placed in the main field. If two charges are combined to form a single one, for example, an arm holding a sword, these two charges should be considered independently in terms of information.

Figure 2.6 *Azure, a lion or*

2.4 Information compression

In heraldry, there is a remarkable principle of compressing visually complex information into a single word, thereby reducing the informational load of a pattern. There are two cases for this: the simplest involves furs, which are heraldic representations of animal furs such as ermine and squirrel. In their simple form, these furs are represented with distinct colors: white and black for ermine, and white and blue for vair (squirrel fur). The second case is known as 'semy.' A semy is the repetition of a charge, reduced in size and without a specific count, to represent a pattern. For example, a bezant is a simple circle representing a gold or silver coin. If the shield is described as 'bezanty,' it means that it will be covered with small, countless bezants, cut off at the edges to convey a sense of infinite repetition. Semy patterns thus have a higher informational load than furs, as the semy must define the background color, the charge, and the colour of the charge (Figure 2.7).

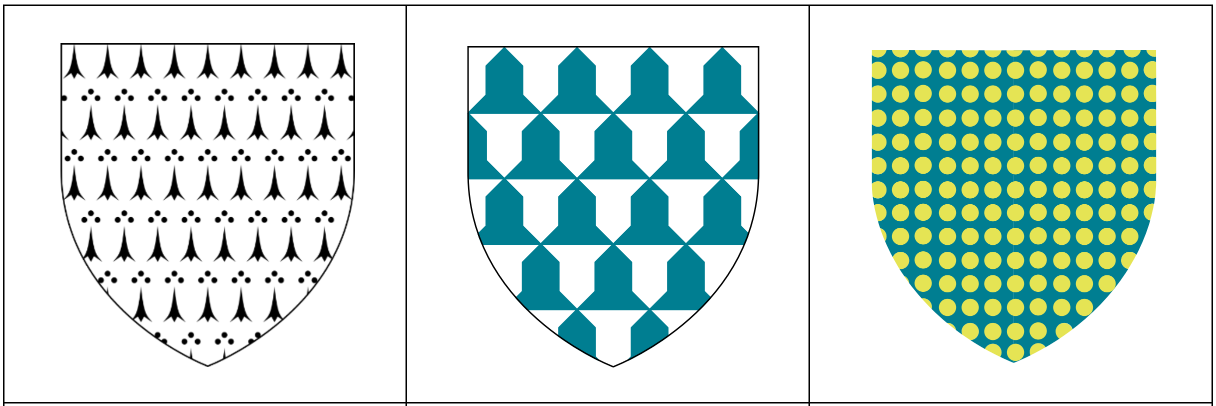

(a) (b) (c)

Figure 2.7 *(a) Ermine plain, (b) Vair plain, (c) Azure bezanty or*

Regarding the enumeration of elements, there are default positions and numbers that follow certain rules. Default positions require less information to be described. For example, three bezants by default are arranged with two at the top and one at the bottom. If the bezants are arranged in a specific way, this will be specified in the blazon, for example, 'three bezants in chief' or 'three bezants in bar (Figure 2.8).' Precisions and variants in heraldry carry a higher informational load.

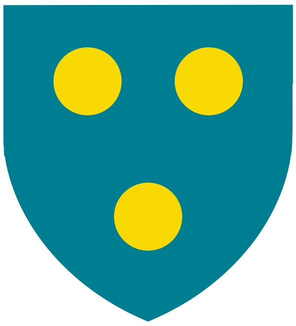	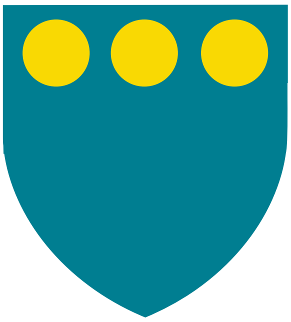	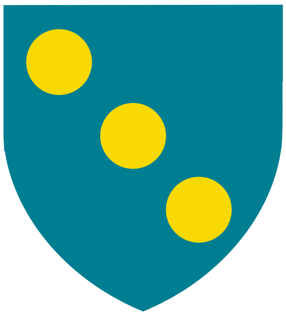
Default position	Variation	Variation
(a)	(b)	(c)

Figure 2.8 *(a) Azure, three bezants or, (b) Azure, three bezants or in chief, (c) Azure, three bezants or in bend*

The default enumeration rule applies to certain multiplications of parallel lines, which are usually in even numbers. There are four categories obtained from the basic partitions: pale, fess, bend, and bar. When the number is not specified, they are by default six pieces. When the pieces are four or twelve or other number, this must be specified. The default element here has a lower informational load than a graphically simpler variant, which can be confusing, but this is part of heraldic rules. Thus, adding additional information increases the descriptive entropy of the coat of arms even if the composition seems simpler. To make a compromise, we count the elements but add a factor for variants of standard figures. Thus, a barry of four pieces adds four units of information with an additional unit of detail, whereas a normal barry of six pieces will not have a factor (Figure 2.9).

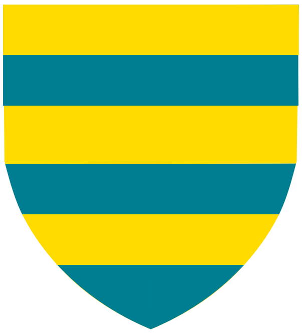	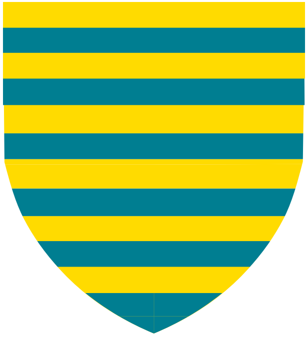	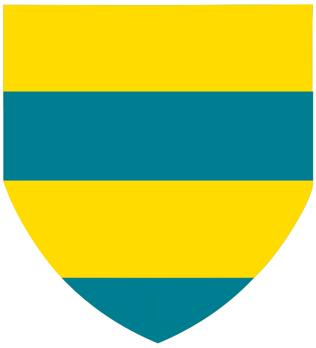
Default number	Variation with 12 elements	Variation with 4 elements
(a)	(b)	(c)

Figure 2.9 *(a) Barry or and azure, (b) Barry of twelve or and azure, (c) Barry of four or and azure*

2.5 Method for calculating the complexity of coats of arms

In studies verifying Zipf's Law of Abbreviation or brevity law, it is common to calculate the frequency of words in a corpus according to their length in characters or phonemes. It is a negative correlation between the frequency of a word and its size on a semi-log plot. A similar analysis applied to the textual data of heraldry, namely, the blazon or textual equivalent of the coat of arms image, would not be meaningful. At first glance, one might assume that a coat of arms containing more information would also have a longer blazon in terms of words or letters. However, this assumption proves false, as heraldic categories include words of varying lengths; a coat of arms described as *or and azure* would thus appear less complex than one described as *argent and purple*, which makes little sense. Moreover, heraldic vocabulary can compress information in ways that distort the relationship between word count and actual complexity. For instance, *Per pale gules and argent* describes a simple vertical division of the shield into two parts, whereas *Gyronny of gules and argent* refers to a much more complex geometric division, yet use a higher number of words for the simplest one.

In reality, the only viable way to calculate heraldic complexity must be a compromise that allows for automation across a large number of coats of arms. A continuous model could be a solution, but its computational complexity may hinder automation, and arbitrary choices of variables could lead to significantly different results for coats of arms with similar complexity and only minor variations. We therefore propose a simple discrete model that establishes levels of complexity on a scale, enabling distribution analysis (Table 2.1).

The challenge lies in creating a formula that allows for equivalences in complexity between different coats of arms. For example, a shield *per pale azure and argent* would have the same order of complexity as a shield *azure with a bend argent*, even though partitions and ordinaries belong to different categories. A shield *per pale azure and argent with a bend or* would have a complexity level of 4, according to equation 1.

$$L = n_{colors} + n_{partitions} + n_{figures} + n_{variations} \tag{1}$$

Order	Possibility of combinations
3	• 2 colours + 1 partition • 2 colours + 1 figure
4	• 2 colours + 1 partition + 1 variante • 3 colours + 1 partition • 2 colours + 1 figure + 1 variation
5	• 2 colours + 1 figure + 2 variations • 3 colours + 2 figures • 3 colours + 1 partition +1 figure • 3 colours + 1 partition + 1 variation • 1 colours + 1 figure + 3 variations • …

Table 2.1 *Example of possibility of combination for the different complexity order, the possibilities are increasing as the complexity*

Each element must be added together: additional colours count for 1, the number of partitions and charges as well. What is original in this approach are the variations, essentially, the details or variants that add extra information. For example, a standard lion would count as one figure, but a lion armed and langued in one or more colours can quickly add to the overall complexity. To study a corpus, the blazon descriptions must be formatted as lines of text in a cleaned CSV file, so that a Python script can be applied to extract term occurrences and count colours, partitions, etc., for each blazon. The lists are non-exhaustive but focus on the most common elements encountered in French and English (definitions of these terms are provided in Appendix B).

- For colours:

"argent","or","gold","silver","gules","azure","sable","vert","sinople","purpure","tenné","tenne", "sanguine","murrey","cendree","ermine","ermines","erminois","counter-ermine","hermine", "vair","counter-vair","potent", "counter-potent", "pean", "proper", "au naturel".

- For partition:

"per\\s+pale","per\\s+fess","per\\s+bend\\s+sinister","per\\s+bend","per\\s+chevron","per\\s+saltire","per\\s+pile","per\\s+pall","quarterly","tierced","gyronny","bendy","paly","barry"," chevronny","lozengy","fusilly","compony","countercompony","écartelé","parti","coupé","tranché" ,"taillé","gironné","burelé","fascé","palé","losangé","chaussé","barry\\s+wavy","tierced\\s+in\\s+pairle"

- For figure:

Ordinaries:
"chief","pale","bend","bend\\s+sinister","fess","bar","chevron","cross","saltire","pile","pall","orle", "bordure","escutcheon","canton", "inescutcheon",

Roundels

"bezant","plate","torteau", "hurt", "pellet", "roundel",

Animals and Creatures

"lion","leopard","eagle","falcon","hawk","dove","raven","martlet","merlette","griffin","wyvern"," dragon","unicorn","horse","ox","bull","cow","boar","bear","stag","hart","goat","ram","sheep","cat", "dog","wolf","fox","tiger","panther","serpent","snake",

Marina fauna

"fish","salmon","dolphin","whale",

Objects & Plants

"anchor","ship","castle","tower","church","house","tree","oak","pine","palm","branch","rose","lotus ","thistle","shamrock","trefoil","quatrefoil","cinquefoil","fleur[-\\s]?de[-\\s]?lys","mullet", "estoile","star","sun","moon","crescent","comet","billet","goutte","annulet","ring","escallop","shell

","book","sword","spear","arrow","bow","key","crozier","staff","sceptre","crown","coronet","mitre" ,"chalice","cup","hammer","axe","pick","sickle","scythe","harp","bagpipe","clarion","bugle"

- For variants:

Animal postures

"rampant","passant","passant\\s+guardant","statant","statant\\s+guardant","couchant","courant","salient","sejant","sejant\\s+erect","displayed","rising","volant","naiant","hauriant","addorsed","respectant","affront[eé]","contourn[eé]","regardant","dormant",

Qualifiers

"guardant","armed","langued","crowned","collared","gorged","winged","queuefourch[eé]e","couped","caboshed","noduled","enfiled","pierced","charged","holding","supporting","seized",

Line shapes

"engrailed","invected","indented","dancetty","embattled","raguly","dovetailed","wavy","nebuly"," flory","potenty","masoned",

Counter-variants

"counter-ermine","counter-vair","counter-potent","counter-changed",

Natural colour

"proper","au\\s+naturel"

N.B. The use of the colour *au naturel* means that an element is depicted in its natural, real-world colours, for instance, a tree *azure* is blue, whereas a tree *au naturel* has a brown trunk and green leaves. In our model, we count the colour *au naturel* (or *proper* in English) both as a colour, thus included in the colour count, and as a variation, adding an extra degree of complexity compared to standard heraldic colours. We retained 40 variation terms; other, rarer ones (such as *cléchée*, *ancrée*, etc.) were not included, which places some visually complex coats of arms into a moderate complexity order *L*. However, the rule is applied uniformly, so the relative distribution remains valid for testing the Zipf hypothesis. Considering this statement the non-exhaustiveness of the heraldic vocabulary used for the analysis is not a drawback.

2.6 Application of the calculation

To carry out the experiment, the author used two corpora:

- The first set of 4,611 blazons from the James Parker's glossary of terms used in heraldry Corpus from 1894 [103]. This British work contains approximately 95% British coats of arms and 5% French ones, which should not introduce any significant bias related to regional trends.
- The second set is the General Armory of England, Scotland and Ireland written by Burke et Burke in 1842 of over 60 000 coats of arms [104].

The first observation regarding our complexity levels is that we exclude coats of arms with complexity level 1, which corresponds to a shield bearing only one colour or a single field fur. Such coats of arms are referred to as *plain*. They are very rare due to their obvious simplicity. Two examples can be cited: the coat of arms of the city of Douai in northern France (*Gules plain*) and the coat of arms of Brittany (*Ermine plain*). We had to remove them due to the very high likelihood of overestimating their presence in our parsing. Indeed, many incomplete coats of arms, caused by data encoding errors, could be mistaken for complexity level 1, resulting in false positives. That said, it is important to keep this category in mind, as it plays a central role in our conclusion.

However, there is no category corresponding to complexity level 2. Indeed, coats of arms move directly from a simple field colour (category 1) to category 3, as this transition necessarily involves the addition of a charge or a partition, each of which introduces an additional colour.

Two complexity calculations were performed on each set. One counted similar charges or colour separately, adding additional units of information to the calculation (e.g., 4 lions would add 4 units of information), while the other did not, considering that a charge mentioned once, whether singular or multiple, adds only one unit of information. This distinction allows us to analyse whether counting individual repeated charges influences the overall complexity trend.

Out of the 4,611 blazons from set 1, only 4,317 were retained for analysis; the others contained encoding errors or were truncated, which could distort the results if an incomplete blazon includes occurrences of the target terms. Same observation from the second set where around 45000 were extracted from the 60000 original set.

The results of the analysis are shown in the graph (see Figure 2.10 and 2.11); the distribution is similar to those found in publications exploring the Zipf law of abbreviation in language, such as in the works of Sigurd et al. [101] or Tsizhmovska [105], to name just a few.

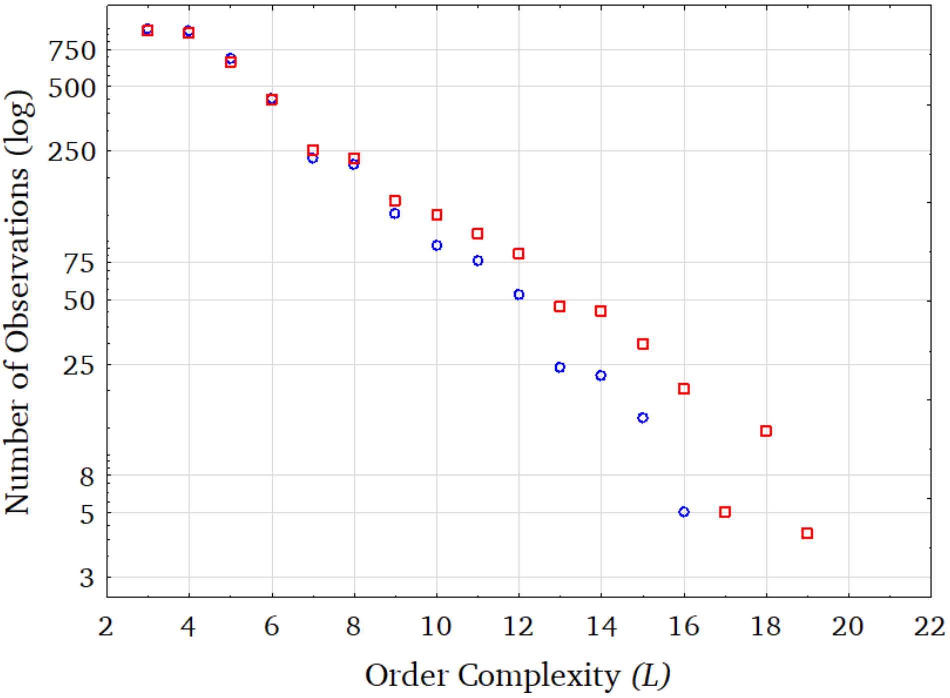

Figure 2.10 *Set 1 log of Number of coat of arms per complexity order, the red squares represent the coats of arms computed without counting repeated elements, while the blue circles represent those where each repeated element is counted individually*

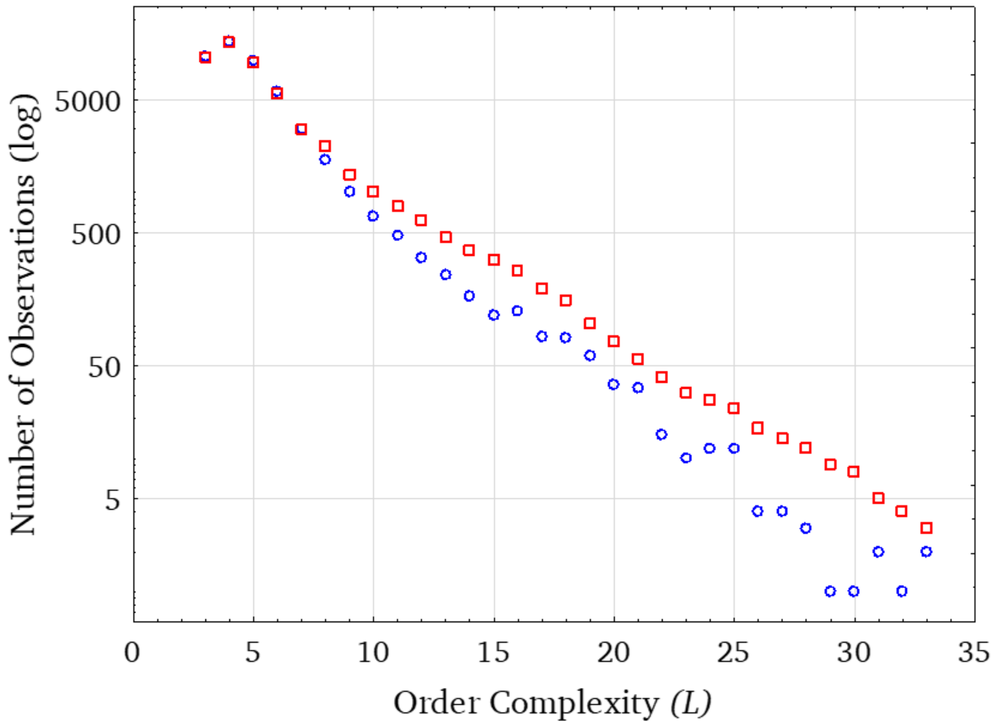

Figure 2.11 *Set 2 log of Number of coat of arms per complexity order, the red squares represent the coats of arms computed without counting repeated elements, while the blue circles represent those where each repeated element is counted individually*

The graphs (Figure 2.10 and 2.11) shows that the negative trend is notable, confirming that the simplest coats of arms according to our Equation 1 are the most numerous. Set 2 shows a greater number of complexity levels than Set 1 due to its larger size, which increases the likelihood of encountering highly complex coats of arms. Regarding the modelling of this complexity, Zipf did not explicitly provide a function describing the frequency-length relationship of words. Set 2, unlike Set 1, contains more coats of arms in order 4 than in order 3. However, the subsequent classes follow the same negative trend in both cases. Some researchers have explored the possibility of a formula that could model this relationship. Given the nature of our distribution, one may ask what best models the relationship between the complexity of a coat of arms and its frequency. One could therefore consider either an exponential distribution or a gamma distribution, as noted in the publication by Sigurd et al [101].

The formula of Gamma function is expressed following equation 2. The normalizing constant K is uniquely determined by the positive parameters α and β, as well as the requirement that the formula represents a valid probability distribution. The parameter α, known as the shape parameter, influences the presence and height of a peak in the function's graph. The parameter β, referred to as the scale parameter, controls the spread of the distribution.

$$f = K * L^{\alpha-1} * e^{\frac{-L}{\beta}} \tag{2}$$

The decreasing effect of coat of arms complexity is considered in the equation 3 suggested by the exponential factor C^L where $0 < \mathrm{c} < 1$. The complete formula with these two counteracting factors is then:

$$f(L) = a * L^b * c^L \tag{3}$$

Where b is equal to $\alpha - 1$ and c equal $e^{\frac{-L}{\beta}}$.

To characterize the relationship between the frequency of occurrence of coats of arms and their complexity L, we fitted three families of models:

- the discrete Gamma law: $f(L) = a * L^b * c^L$
- a simple exponential: $g(L) = k\ d^L$
- a power law: $h(L) = p\ L^q$

For each model, we estimated the parameters using least squares and compared the quality of fit using the coefficient of determination R^2 (Table 2.2). Each of these models corresponds to an underlying heraldic hypothesis. In the case of a gamma distribution, it may reflect the assumption of an information economy inherent to language systems: the more elements are added, the lower the probability becomes, but not in a purely exponential way. The combinatorial potential L^b is constrained by an economy factor c^L.

The exponential law $g(L) = k\ d^L$, assumes that with each unit increase in complexity L (such as the addition of a color, a charge, or a partition), the frequency decreases by a constant factor $d \in (0,1)$. In a heraldic context, this implies that each additional layer is discarded with the same fixed probability, regardless of the potential richness of the combination. The model uses only two parameters: k (scale) and d (decay rate). Its simplicity makes it a minimal reference point: if it were to perfectly describe the data, it would suggest that normative constraints (i.e., readability) completely dominate to the extent that they mask any combinatorial effect.

In contrast, the pure power law $h(L) = p\,L^q$ eliminates any exponential restraint; it assumes that frequency depends solely on unrestricted scalability: as L increases, the cost is paid only in terms of L^q (with $q > 0$). Applied to heraldry, this would correspond to an almost fractal universe in which the multiplication of partitions and charges is permitted without significant constraints, each new level of complexity would still occur with appreciable frequency.

	Determination coefficient R^2		
Set	Gamma	Exponential	Power law
Set 1 ND	0.991	0.962	0.891
Set 1 D	0.986	0.972	0.909
Set 2 ND	0.995	0.905	0.818
Set 2 D	0.987	0.916	0.835

Table 2.2 *Determination coefficients R^2 after calculation of Gamma model, Exponential and Power Law for every distribution Set 1 and 2 with and without counted repeated elements (ND = no doubles, D = doubles)*

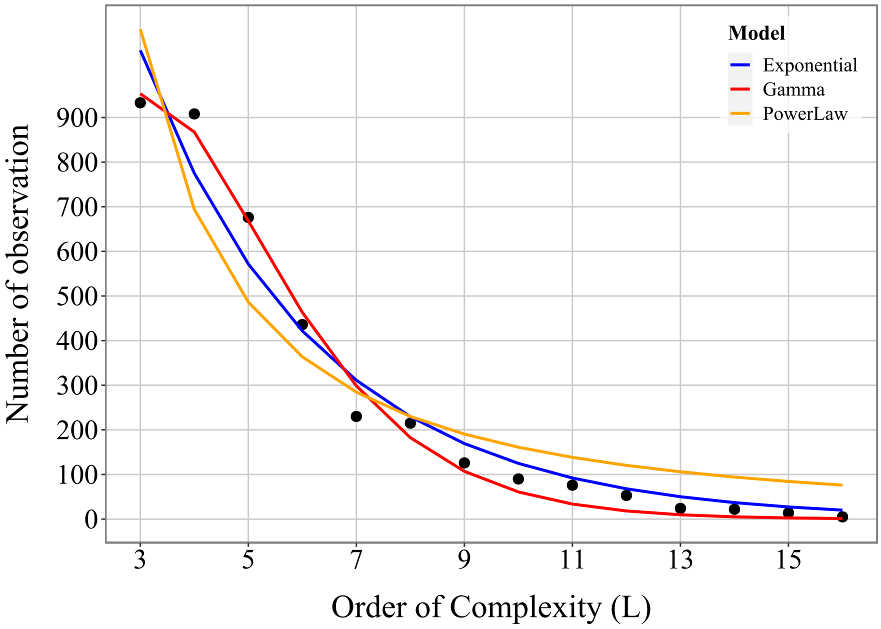

Figure 2.12 *Comparison of Models for the distribution of the Set 1 without counted repeated elements. The blue line is exponential model, the red line is Gamma model, and the yellow line is Power law model*

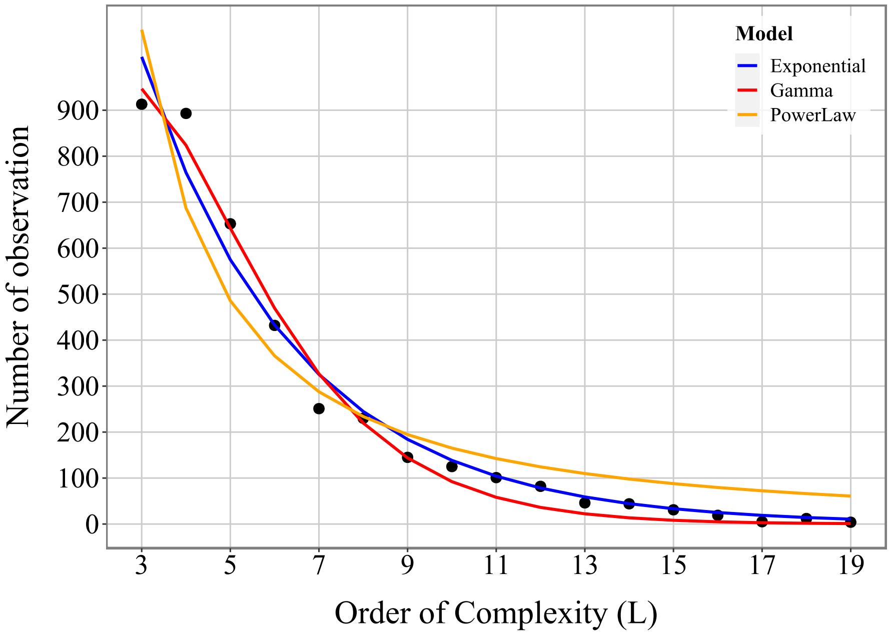

Figure 2.13 *Comparison of Models for the distribution of the Set 1 counted repeated elements. The blue line is exponential model, the red line is Gamma model, and the yellow line is Power law model*

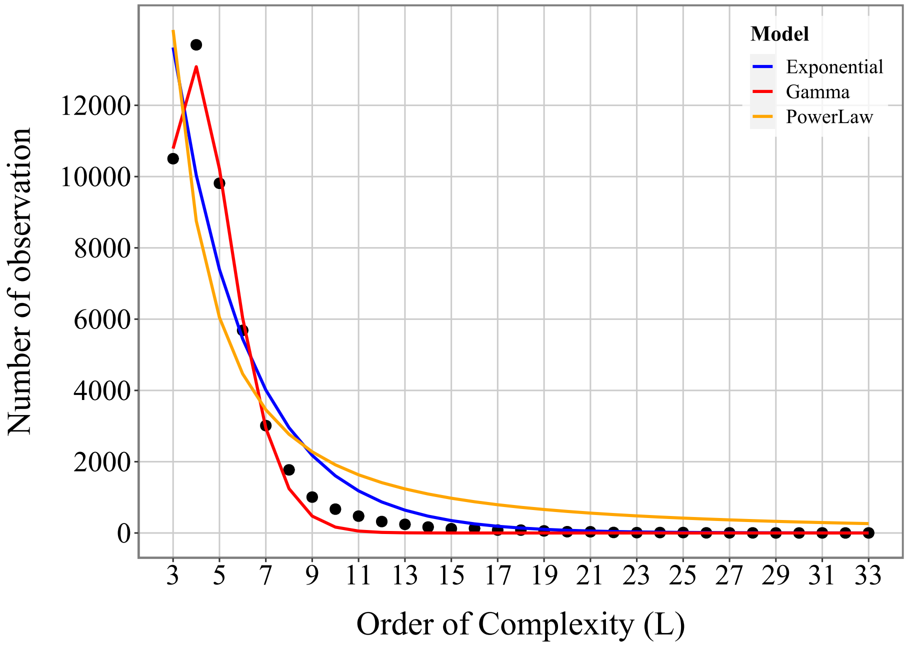

Figure 2.14 *Comparison of Models for the distribution of the Set 2 without counted repeated elements. The blue line is exponential model, the red line is Gamma model, and the yellow line is Power law model*

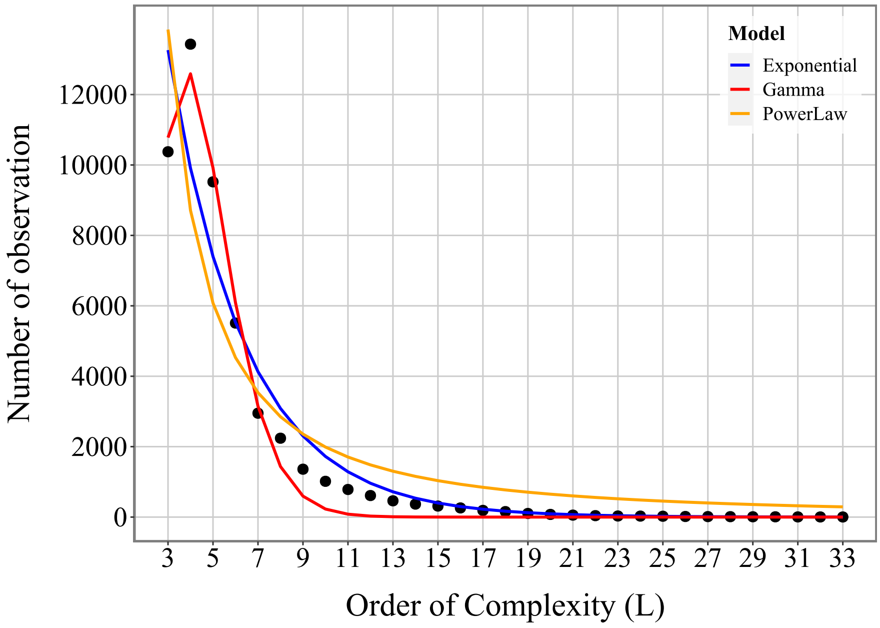

Figure 2.15 *Comparison of Models for the distribution of the Set 2 with counted repeated elements. The blue line is exponential model, the red line is Gamma model, and the yellow line is Power law model*

The table shows that the values for the gamma and exponential models are quite close, although the Gamma model consistently performs better. In our corpora, the power-law fit decreases too slowly: it overestimates the frequency of very high complexity levels (such as multiple partitioning) and fails to capture the steep drop observed beyond $L \approx 12$. This under-penalization confirms that an exponential damping factor, whether readability, heraldic tradition, or both, is essential to accurately model the reality. We can justify our choice of the gamma model for two reasons. The first is that complexity class 1, which was excluded from the datasets to avoid parsing errors, still exists, albeit rarely. We can perform a computation like that used in the figures to show that, when complexity level 1 is taken into account (i.e., a single colour on the field of the shield), the gamma law undeniably becomes the most appropriate model. To demonstrate this, we added a category 1 class composed of 12 elements (i.e., the 12 heraldic tinctures typically available for plain fields) to the distribution of Set 2, excluding repeated charges (see Figure 2.16

). It is worth noting that plain coats of arms can sometimes be attributed to multiple entities, meaning 12 is a conservative minimum. According to this graph, the gamma distribution maintains a high R^2 value of 0.98, while the other models drop significantly, to 0.51 for the exponential and 0.33 for the power law.

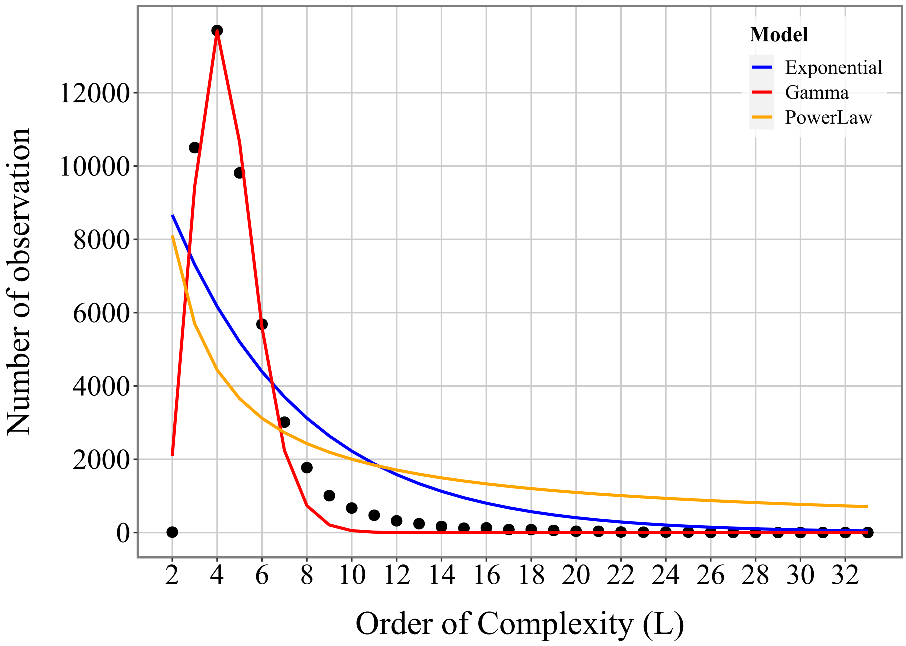

Figure 2.16 *Comparison of Models for the distribution of the Set 2 without counted repeated elements (plus order of complexity 1 here noted 2 on the scatterplot). The blue line is exponential model, the red line is Gamma model, and the yellow line is Power law model*

Across the four datasets the parameter patterns (Table 2.3) are consistent with an "economy-of-information" view:

- Gamma

  The shape pair (b, c) becomes steeper as the corpus grows: in Set 2 with doubles counting the combinatorial term is strongest ($b \approx 6.1$) while the damping factor is lowest ($c \approx 0.20$), indicating that once a very large palette of heraldic options is available, usage is curbed more aggressively. In the smaller or de-duplicated sets b settles around 5 and c rises toward 0.27, reflecting a milder trade-off between variety and readability.

- Exponential

  With only one form parameter (d) the exponential captures the heavy head but falls away too fast beyond L≈10; the best-fit decay rates cluster near 0.43–0.50 yet still undershoot the empirical tail in every corpus.

- Power-law

  Exponents ($q < -2$) are required to counterbalance the very large counts in classes 3–4, but the resulting curve declines too slowly, over-predicting high-complexity arms. This confirms that a free-scale (fractal) model alone cannot explain heraldic practice.

Overall, the discrete gamma accommodates both extremes: it reproduces the pronounced peak at $L = 3 - 5$ via the L^b term and enforces the observed drop-off through c^L. As soon as relative weighting or logarithmic scales are applied, its ability to track the long tail surpasses that of the exponential, while remaining far more realistic than a pure power law

Data set	γ : a	γ : b	γ : c	Exp : k	Exp : d	Power : p	Power : q
Set 1 ND	4.1 x 10^2	5.3	0.247	1 x 10^3	0.472	1.1 x 10^6	-2.54
Set 1 D	1.1 x 10^2	4.7	0.269	3.2 x 10^2	0.501	3.2 x 10^5	-2.33
Set 2 ND	1.61 x 10^3	6.1	0.202	1.2 x 10^5	0.429	8.7 x 10^7	-2.82
Set 2 D	5.2 x 10^2	5.5	0.226	2.8 w 10^4	0.453	2.1 x 10^7	-2.60

Table 2.3 *Parameter values for the Gamma, Exponential and Power Law for every distribution*

To conclude the analysis and generalize the Gamma model, a Bootstrap replication with replacement was performed on the residuals of the distributions to compute many coefficients R^2, both for the Gamma model and for the exponential model, with the goal of determining a distribution of ΔR^2 (Table 4) between Gamma and exponential. The Bootstrap replication is further explained in Chapter 4 and serves as a solid foundation for our statistical analyses. Bootstrapping the residuals allows us to capture the data's inherent variability and to generate synthetic regressions for analysing the behaviour of the distributions.

	$\boldsymbol{\Delta R^2}$		
	P5	P50	P95
Set 1 ND	0.02	0.03	0.05
Set 1 D	0.005	0.01	0.03
Set 2 ND	0.08	0.10	0.11
Set 2 D	0.06	0.08	0.10

Table 2.4 *Results of the different between the two distributions of R^2 noted ΔR^2 for set 1 and 2 with counted repeated elements (D) and not counted repeated elements (ND). The percentile 5, 50 (median) and 95 are showed.*

Regardless of the armorial source or the counting method, the gamma law consistently maintains an advantage, ranging from +1 to +5 points of R^2 on our small corpus, and from +6 to +11 points on the larger one. While these differences are modest in the first dataset, they become decisive as the sample size increases and the tail of the distribution becomes denser, highlighting the importance of the combinatorial factor L^b. The smaller difference observed in Set 1 can be explained by the fact that complexity level 3 slightly exceeds level 4, an observation that is not consistent, as shown by Set 2 and by the theoretical presence of a level 1 class. Moreover, the gamma distribution tends to fit the head of the data well but then falls below the observed values around levels 8 to 10 across all distributions. This pattern matches the findings reported by Sigurd et al. [101].

2.7 Discussion of the chapter

It is difficult to objectively quantify the complexity of a system whose everyday use is known to us only through medieval texts (i.e., with respect to daily rather than purely decorative use, as is mostly the case today). Nevertheless, heraldry does contain quantifiable units, colours, partitions, and so on. As for the repetition of a single motif, we regard each occurrence as adding extra degrees of complexity; however, applying a weighting scheme in the future could help reduce the informational impact of a figure that appears several times.

Granularity in corpus analysis is crucial: heraldry is meant, in theory, to be readily interpreted, and a coarse level of granularity would mean defining our complexity tiers in relation to a more common or core heraldic vocabulary. Experiments at different granularities can be carried out to see whether incorporating more frequent or less frequent heraldic terms changes the distribution. Priority should be given to the head of the distribution while minimizing the tail of the distribution as the number of complexity orders can vary from one armorial to another.

Our analyses rely on corpora whose data are already indexed in CSV format, a rarity in heraldry given the difficulty of automating manuscript extraction. Our hypothesis must be tested on additional corpora of coats of arms from different periods and provenances to assess whether the results truly remain consistent.

Finally, Heraldry may not form a fractal universe considering the power law is not working here, but, if our model for synthesising its elements is correct, it obeys the same rules as a language.

2.8 Conclusion of the chapter

The results of the analysis suggest that heraldry follows a statistical tendency consistent with the principle of economy as expressed by Zipf's law of brevity. This study reopens a strand of heraldic research previously deemed unproductive, as noted in the introduction. In the future, it may be possible to address related questions, for instance, why heraldry has succeeded as a panchronic and quasi-universal identification system. Having shown in Chapter 2 that heraldic complexity can be captured by quantitative descriptors, thus completing the “visual-syntax” tier of the Surface Information Acquisition Spectrum (SIAS), we must now ensure that these descriptors remain trustworthy when a surface is no longer an ideal graphic like heraldry but a digitised geometry (i.e fractal geometry). Chapter 3 therefore shifts to a synthetic yet analytically tractable model, the Koch snowflake, to probe how pixel size, sampling density and mesh topology distort or preserve intrinsic complexity. By isolating such discretisation effects in a controlled setting, we secure a calibrated bridge from visual syntax to numerical evaluation, paving the way for the fully metrological fractal analysis developed in Chapter 4

Chapter 3

Von Koch Complexity

Methods to Compute Fractal Dimensions of Fractal Curves

Prolegomena of chapter 3

Occupying the interface between “visual syntax” and “quantitative evaluation” within the Surface Information Acquisition Spectrum (SIAS), Chapter 3 investigates how geometric complexity is distorted, or preserved, when an ideal curve becomes a digital object. Using the classic Koch snowflake as a didactic test case, we compare successive discretisation’s, vector, raster and point-cloud, to separate intrinsic fractality from mesh-induced artefacts. This analysis extends the syntactic insights of heraldry (Chapter 2) into the numeric realm: where the coat of arms revealed how formal rules generate complexity, the snowflake shows how sampling rules can *hide or fabricate* it. By modelling error propagation in estimated fractal dimension as a function of node density and indentation angle, the chapter delivers a calibrated filtering protocol that safeguards the evaluation tier of the SIAS. The protocol will be pivotal in Chapter 4, ensuring that the fractal metrics extracted from real surfaces reflect genuine morphology rather than artefacts of visualisation.

3.1 On Fractals

The relevance of using the principles of fractal geometry is now beyond question. From the moment Benoit Mandelbrot was able to leverage the foundations of this approach, a paradigm shift occurred in the characterization of complex geometric objects. The book "*Fractal Geometry of Nature*" [106] has become a must-read for scientists in all fields who wish to analyse the correlation between the complexity of structures and systems and physical phenomena. But this work is a highly in-depth exploration of previous studies and an analysis of mathematical objects whose properties had previously challenged mathematicians. The emergence of fractal calculation methods begins with simple problems, such as measuring areas and lengths of geometrically complex objects. The development of thought on fractals begins with paradoxes related to the limitations of Euclidean geometry. Notably, long before Mandelbrot, there was the mathematician Steinhaus. He was the first to introduce in modern scientific paper the paradox of length, particularly in relation to geographical measurements, as early as 1954 [107]. When measuring the left bank of the Vistula on a school map, the length is much shorter than on a 1:2,000,000 scale map. Similarly, comparing the length of the current Poland's borders with those from the year 963 is difficult due to the lack of accurate maps from that time. This issue also applies to measuring the contours of leaves or tree cross-sections, where the results vary depending on the precision of the tools used. Shortly afterward, the paradox of calculating area also arose, this time addressed by the mathematician Richardson. The relationship between area and perimeter is a mathematical concept explored well before the advent of fractal theory. British mathematician Lewis F. Richardson, renowned for his work in weather prediction, also studied the connection between the length of a country's border and its likelihood of engaging in conflict with neighbouring nations. Richardson discovered that by altering the measurement scale, for example, using a 200 km ruler instead of a 100 km ruler to measure the British coastline and gradually decreasing this length, one could theoretically obtain an infinite length within a finite area. Although these results were published posthumously in a work that initially attracted little scientific attention [108], they were later revisited by Benoit Mandelbrot in his renowned 1967 study, "How Long is the Coast of Britain?" [109]. In this context, D represents the fractal dimension. According to the formula $L(G)=MG^{1-D}$, D reflects the complexity or irregularity of the boundary. A fractal dimension of $D = 1$ corresponds to a boundary that appears smooth, whereas a higher fractal dimension, such as $D = 1.25$, indicates a more irregular and complex boundary, like the western coast of Great Britain [4].

Thus, the fractal dimension serves as a measure of the boundary's roughness or fragmentation at various scales. It is interesting to note that this cartometric concept developed by Richardson not only inspired Mandelbrot but also other scientists in their quest for measurement precision. The Mating's article [110], in particular, discusses the Richardson's method of measurement using dividers, which was also studied alternatively developed by Soviet scientists. We can also mention the Hakanson's method [111], which, instead of using dividers of different sizes, employs grids of different sizes made from transparent tracing paper.

From this point, it becomes challenging to list all the application areas that have used fractals to characterize the geometry of elements. It is more practical to refer to the relevant reviews for each field rather than individual studies. For example, one can mention Cross's review on microscope image analysis [112], which summarizes a non-exhaustive set of fields studied using fractals. Other more comprehensive reviews focus on specific fields such as medicine [113], fluid mechanics [114], and biomechanics [115].

However, the question arises regarding computer algorithms for calculating fractal dimension, given the fundamental difference between the theoretical infinite fractal object and the finite object of observation. Numerous algorithms have been reported in the literature for measuring the length of a profile and calculating its fractal dimension. For self-similar patterns, these algorithms are often validated using Von Koch islands, whose fractal dimension is precisely known. However, a major problem arises when the ruler length does not exactly match a segment of the snowflake. For the method to be fully effective, each segment measured by the ruler should perfectly coincide with the segments that make up the curve. If not, the perimeter measurement will inevitably be incorrect. One of the main artefacts in applying Richardson's method to the Von Koch snowflake is the systematic underestimation of the length $L(\epsilon)$ when the ruler does not perfectly align with the fractal segments. When the ruler size is slightly shorter or longer than the length of a segment of the snowflake, the ruler "jumps" over certain details of the curve, thereby missing some of the fractal structure. For instance, if the ruler is slightly longer than the shortest segments, it will "cut across" the peaks of the snowflake without precisely following the contours, leading to an underestimation of the true curve length. This underestimation is exacerbated by the self-similar nature of the Von Koch snowflake. Since each segment is itself composed of increasingly smaller sub-segments, any approximation in measurement propagates and amplifies as the ruler size decreases. As a result, instead of obtaining an accurate measurement, one systematically underestimates the actual length.

This problem is not unique to the Von Koch snowflake but is inherent to any application of the Richardson's method where the fractal structure is composed of specific segment lengths.

The result is a systematic underestimation of the fractal perimeter, which can skew the calculation of the fractal dimension and affect the interpretation of the structure complexity.

Despite the extensive research, some critical aspects of the problem remain unresolve [116–118]. While extensive research has focused on fractal dimension calculations, the practical limitations of digital images have been largely overlooked. Digital images, being two-dimensional representations of three-dimensional objects, are composed of individual pixels and can be generated by various imaging technologies.

Fractals are crucial in numerical simulations, particularly for modelling complex phenomena such as turbulence, diffusion, or surface morphology. Their ability to represent structures with details at all scales makes them extremely useful in various applications, from civil engineering to biology and materials science. Simulations based on fractals allow the generation of surfaces and volumes that reflect the complexity of natural objects. For example, in mechanical engineering, fractals are used to model surface roughness, which is essential for understanding friction and wear between materials. The Von Koch snowflake can be used in simulations to study the effect of various physical processes, such as erosion, substance diffusion, or crystal growth. These simulations can modify the fractal structure of the snowflake, either by smoothing certain parts or by introducing new details. For example, an erosion simulation applied to the Von Koch snowflake might smooth out the shortest segments, which would affect the fractal dimension. By analysing changes in $L(\epsilon)$ versus ϵ before and after the simulation, it is possible to quantify how the structure has been altered at different spatial scales [31].

These studies are particularly useful in fields like geomorphology, where natural shapes are often modified by physical processes over long periods. Simulation allows testing different scenarios and better understanding how these processes influence the fractal structure of the objects studied.

The objective of this study is to analyse the artifacts created by the Richardson's method when its used to calculate the fractal dimension of the Von Koch snowflake [119]. In our study, we propose eight methods for calculating the fractal dimension on a digitized Von Koch snowflake. These methods are applied to a variety of snowflake-like fractals, with fractal dimensions ranging from 1.1 to 1.9, including a stochastic Von Koch snowflake. The methods are designed to address both deterministic and stochastic variations of the fractal dimension. Some techniques leverage specific properties of the Von Koch snowflake, such as its self-similarity and iterative construction, making them highly accurate when these properties are known. However, other methods are more generic and can be applied without requiring detailed knowledge of the fractal underlying properties. This approach allows for a broader range of application, particularly when dealing with fractals that do not follow strict deterministic rules.

Our exploration of different methods allows us to assess their effectiveness across various types of fractals, from more regular, deterministic snowflakes to irregular, stochastic versions. This is critical for understanding how different computational approaches interact with fractal structures and for determining which methods provide the most reliable results in varying contexts.

3.2 Self-similarity dimension and fractal dimension of the Von Koch Island

The Koch snowflake, introduced by Swedish mathematician Helge von Koch in 1904 [119], emerged during a period of profound exploration in mathematics, particularly in the foundations of geometry. At the turn of the 20th century, mathematicians were increasingly interested in concepts that challenged the traditional Euclidean framework. The work of figures like Karl Weierstrass [120], who introduced functions that were continuous but nowhere differentiable, set the stage for the Von Koch’s creation. The Koch snowflake was not merely a mathematical construction; it represented a direct challenge to classical notions of dimension and curves. By creating a shape that was continuous but infinitely jagged, Von Koch demonstrated that curves could possess properties far more complex than those explained by classical geometry. This exploration of "pathological" objects or “monster curves” [121] mathematical entities that defied intuition was part of a broader movement to push the boundaries of existing mathematical theory.

The Von Koch's work was driven by a geometric curiosity: the desire to create a shape with a finite area but an infinite perimeter, a concept that seemed paradoxical in classical terms. Although fractal geometry did not formally exist during his time, the Koch snowflake would later become a cornerstone in this field, particularly through the work of Benoît Mandelbrot in the 1970s. Mandelbrot recognized the Koch snowflake as an early example of a fractal, a shape that exhibits self-similarity at different scales and has a non-integer dimension. The Von Koch curves are part of a significant class of fractal curves generated by Iteration Function Systems [122,123] and lack any analytical mathematical expression. As a result of factors such as discretization, resolution limitations, and mathematical or statistical issues, accurately estimating the fractal dimension from data produced during experiments presents challenges. To better understand the effects of these errors, it is beneficial to first analyse artifacts in the well-known Von Koch curves before calculating the fractal dimension of experimental curves. The use of the Von Koch snowflake has been demonstrated not only in the analysis of fractal objects but also in art [124], antenna design for signal transmission [125], and various scientific fields [126]. In 1984, Barcellos [127] created variations of the Koch curve by dividing the initiator into four equal segments, producing curves with a fixed fractal dimension. In 2002, Vinoy, Jose, and Vardan [128] expanded on this by adjusting the indentation angle of the Koch curve to develop new antenna shapes and provided a formula to calculate their fractal dimensions.

3.3 Evaluating the fractal pattern of the Von Koch Island using Richardson's method

fractal and fractional

Article

Evaluating the Fractal Pattern of the Von Koch Island Using Richardson's Method

Maxence Bigerelle [1], François Berkmans [1,2,3] and Julie Lemesle [4,5,*]

[1] Univ. Polytechnique Hauts-de-France, CNRS, UMR 8201—LAMIH—Laboratoire d'Automatique de Mécanique et d'Informatique Industrielles et Humaines, UMR CNRS 8201, Université Polytechnique Hauts-de-France, 59313 Valenciennes, France; maxence.bigerelle@uphf.fr (M.B.); francois.berkmans@uphf.fr (F.B.)
[2] Univ. Polytechnique Hauts-de-France, INSA Hauts-de-France, LARSH—Laboratoire de Recherche Sociétés & Humanités, 59313 Valenciennes, France
[3] Institute of Mechanical Technology, Poznan University of Technology, Plac Marii Sklodowskiej-Curie 5, 60−965 Poznan, Poland
[4] Valutec, Univ. Polytechnique Hauts-de-France, 59314 Valenciennes CEDEX 9, France
[5] U.R Concept, 59300 Valenciennes, France
* Correspondence: julie.lemesle@uphf.fr

Abstract

The principles of fractal geometry have revolutionized the characterization of complex geometric objects since Benoit Mandelbrot's groundbreaking work. Richardson's method for determining the fractal dimension of boundaries laid the groundwork for Mandelbrot's later developments in fractal theory. Despite extensive research, challenges remain in accurately calculating fractal dimensions, particularly when dealing with digital images and their inherent limitations. This study examines the numerical artifacts introduced by Richardson's method when applied to the Von Koch Island, a classic fractal curve, and proposes a novel approach for computing fractal dimensions in image analysis. The Koch snowflake serves as a key example in this analysis; it serves to assess the algorithm of fractal dimension calculation as his theoretical one is known. However, there is a fundamental difference between the theoretical calculation of fractal dimension and the actual calculation of the fractal dimension from digital images with a given resolution undergoing discretization. We propose eight different calculation methods based on Richardson's area–perimeter relationship: the Self-Convolution Patterns Research (SCPR) method accurately estimates the fractal dimension, as the 95% confidence interval includes the theoretical dimension.

Keywords: fractal dimension; Von Koch; Mandelbrot; Richardson

check for updates

Academic Editor: Riccardo Caponetto

Received: 20 May 2025
Revised: 14 July 2025
Accepted: 18 July 2025
Published: 24 July 2025

Citation: Bigerelle, M.; Berkmans, F.; Lemesle, J. Evaluating the Fractal Pattern of the Von Koch Island Using Richardson's Method. *Fractal Fract.* **2025**, *9*, 483. https://doi.org/10.3390/fractalfract9080483

1. Introduction

1.1. About Fractal Geometry

In the field of image analysis and pattern recognition, the study of fractal geometry has emerged as a critical approach for characterizing complex structures. Since Benoît Mandelbrot's seminal work "The Fractal Geometry of Nature" [1], fractal geometry has provided a framework for analyzing natural and artificial patterns that exhibit self-similarity across multiple scales. The fractal dimension, a key parameter within this framework, captures the complexity of these structures by quantifying how details change with scale. This makes it an invaluable tool for applications such as image analysis [2] and feature extraction [3]. Pattern recognition, as a discipline, relies on the accurate identification and classification of features within images [4]. Fractals are used in the target separation branch to enhance the distinction between the object and the background as presented in Zhu et Guo [5]. By constructing a self-similar fractal structure, the model can analyze details at multiple scales, enabling precise capture of complex boundaries. These saliency features with expanded boundaries amplify differences at the edges, thereby improving the complete and accurate separation of the object from the background. The fractal method used by most pattern recognition studies is a variant of the box-counting method, also known as the Minkowski–Bouligand dimension [6]. This variant estimates the fractal dimension by dilating an object at different scales and measuring the area covered at each step. The measurements are obtained using a cost map calculated with the IFT (Image Foresting Transform) algorithm [7]. A logarithmic curve is plotted to show how the area varies with dilation, and the slope of this curve allows the calculation of the fractal dimension. This method is effective for analyzing real and digital objects with partial or complex fractality such as plant leaf structures [8], shoeprint [9], video images [10], and others. Another method was proposed by Plotze et al., stating that a single non-integer number is insufficient to capture the full complexity of an object. The Multi-Scale Fractal Dimension (MSFD) overcomes this by using the derivative of the log–log curve, linking changes in object complexity to visualization scale changes. Unlike traditional fractal dimension, which relies on linear interpolation, MSFD offers more effective object discrimination. It accounts for irregular growth in the degree curve, often due to shape peculiarities, by applying the derivative of the log of the degree with respect to the distance. The Fourier Transform is used for derivative calculation, and a Gaussian low-pass filter is applied to reduce noise and high-frequency information [11].

However, an interesting example appears in the article by Torres [12], using a fractal dimension calculation based on the modified Minkowski–Bouligand dimension mentioned earlier, on a Koch snowflake. The Koch snowflake is a repetition of the Koch curve, which appeared in a 1904 paper titled “On a Continuous Curve Without Tangents, Constructible from Elementary Geometry” [13] by the Swedish mathematician Helge Von Koch. The fractal dimension of the snowflake given by the algorithm is 1.23, while the theoretical fractal dimension is 1.26 [12]. With its known theoretical fractal dimension, the Koch snowflake is used to assess the robustness of a fractal dimension calculation algorithm [14]. The shape of the Koch curve has also been applied to model the shape of fractal antenna [15].

A well-known challenge in calculating fractal dimensions for real structures is the strong dependency of the estimated dimension on the chosen algorithm [16,17]. As a result, each estimate is only directly comparable to those obtained using the same method. Additionally, different algorithms exhibit varying sensitivities to the fractal dimension they aim to estimate ideally, an algorithm should accurately determine the fractal dimension across the entire range. Moreover, the estimation process can be influenced by the resolution of the image and the number of pixels. These issues have been known by mathematicians since the 1990s. Numerous studies have examined the reliability of fractal dimension estimation by applying different algorithms to various fractal functions. These comparisons reveal that different estimation methods produce biased results, complicating their interpretation [18,19]. A key reason for these discrepancies is that real-world data sets are finite, whereas true fractals exhibit infinite resolution. Although mathematical studies have established error bounds for fractal dimension estimation [20,21] they often overlook practical issues, such as the inconsistencies between different estimators.

In this study, we propose eight new different methods to more accurately calculate the fractal dimension of a complex object such as the Koch snowflake. These methods are not based on those presented in the introduction but rather on an approach that is rarely used in pattern recognition yet widely applied in surface topography characterization [22]. This is the Yardstick method, theorized by the mathematician Richardson and later revisited by Mandelbrot in the article "How long is the coast of Britain" [23]. It involves using a fixed-length segment (the "yardstick") to measure the curve. As the size of the yardstick decreases, the measured length increases, as it captures more details. By plotting the relationship between the measured length and the yardstick size on a log–log graph, the resulting slope allows for the calculation of the fractal dimension [24].

1.2. The Definition of the Koch Curve

The Von Koch snowflake is constructed using an initiator and a generator. The initiator is a triangle (with internal angles of 60°) and side length L_0. At each step of the construction, every side of the triangle is replaced by the generator, a segment with a length one-third of the original segment. We are taking the construction formula from the paper from Bigerelle and Iost. [25]. This iterative process is repeated infinitely. The length of the Von Koch Island (perimeter P) is first determined by the following procedure: The Von Koch snowflake is a fractal constructed mathematically by starting with a triangle of side length L_0. At each iteration, each side of the triangle is divided into three segments of equal length $L_0/3^n$, where n is the iteration number. The middle segment is replaced by two segments forming a new triangle "peak", thus increasing the number of segments by a factor of 4 in each iteration. After n iterations, the curve consists of 3×4^n segments. The fractal dimension D of the Von Koch snowflake is given by $D = \frac{\ln(4)}{\ln(3)} \approx 1.26$, indicating that it is more complex than a line (dimension 1) but does not fully occupy the plane (dimension 2). The resulting shape has an infinite perimeter yet encloses a finite area, a hallmark of fractal geometry. By eliminating n from the above equations, Equation (1) is obtained.

$$P_n = P_0^D \left(\varepsilon_n\right)^{1-D} \tag{1}$$

where $D = \ln 4/\ln 3$ is the self-similarity dimension.

The von Koch curve is a fractal where the apex angle "α" of the peaks added at each iteration determines its shape and complexity (Figure 1). In fact, when α is different from 60°, similar reasoning leads to Equation (2).

$$D = \ln 4/\ln\left[2(1+\cos\alpha)\right] \tag{2}$$

For $\alpha = 60°$, representing the classic von Koch curve, $D \approx 1.2619$. When $\alpha = 90°$, the curve is highly complex with $D = 2$, while for $\alpha = 0°$, the curve becomes a straight line with $D = 1$. As α decreases, the curve becomes smoother and less complex, whereas the α values increase the sharpness of the peaks and the fractal complexity of the curve.

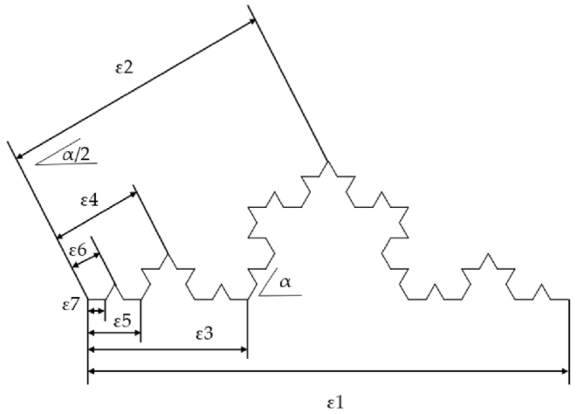

Figure 1. The fluctuations observed on the Richardson curve are related to geometrical relations between the yardstick and generator lengths: we obtain $\alpha' = \alpha/2$ and then $\eta_2 = \eta_1/2\cos(\alpha/2)$, and recursively we obtain $\eta_n = \eta_{n-1}/2\cos(\alpha/2)$.

2. Materials and Methods

2.1. Richardson's Method and Perimeter-Based Fractal Dimension Estimation

The estimation of fractal dimension from geometric contours often relies on the principle originally described by L.F. Richardson [26] as the Richardson–Mandelbrot scaling law. This approach, commonly referred to as Richardson's method or the compass method, is based on the observation that the measured length $\mathrm{P}(\eta)$ of a complex curve depends on the yardstick size η used to measure it. Specifically, for a self-similar curve, the perimeter scales as in Equation (3) where D is the fractal dimension. Taking logarithms yields a linear relation as in Equation (4) from which D can be estimated as the slope of a linear regression in a log–log plot.

$$\mathrm{P}(\eta) \propto \eta 1 - \mathrm{D} \tag{3}$$

$$\log \mathrm{P}(\eta) = (1 - \mathrm{D}) \log \eta + \mathrm{const} \tag{4}$$

In the present study, several of the eight tested methods are either direct implementations or digital adaptations of this principle. These include variations in how the measuring yardsticks are applied (fixed vs. sliding), how curvature is handled (straight-line vs. adaptive compass), and how regression is performed (global vs. piecewise). Other methods, such as box-counting or Fourier analysis, use different underlying models but often converge with similar estimates of boundary complexity. To maintain terminological clarity throughout the manuscript, we reserve the term "Richardson's method" to denote this classical perimeter-scaling approach and explicitly indicate which of our tested algorithms are derived from it. A summary of the computational steps is also provided as a schematic flowchart in Appendix B.

2.2. Computer Software and Statistical Estimation

To investigate Richardson's method, two original computer programs were especially developed to construct the fractal curves and to calculate their related fractal dimension. The reasons for creating our own computer programs are as follows:

1. Images as large as possible are needed to analyze the properties of the fractal curves. The application we developed allows creating images without size limits (except for the RAM memory of the computer).
2. Some of the fractal's properties require a special implementation that will not be found in the usual software.
3. As reported in the literature, some results could depend on the implementation such as error discretization or statistical methods. No doubt must remain about numerical implementation to analyze the efficiency of Richardson's method, and therefore all parts of the software must be controlled without any assumptions about the implementation or the algorithm used.

2.3. Fractal Curve Generation Software (FCGS)

The Iterated Function System (IFS) is the system allowing us to create fractal curves. This process needs two steps to create a curve: 1- defining the coordinates of the initiator and the generator; 2- defining the number of iterations to generate the curve. The Von Koch curve is then created using vector notation. Thanks to the vector representation, the curve is constructed without errors of discretization (except for numerical representation). The total number of coordinates for the Von Koch snowflake, based on a p-sided polygon initiator, is given by $\mathrm{p} \times 4^{\mathrm{i}}$, where i is the number of iterations. A resolution of export must be selected for the software to connect coordinates with line segments, during this process the discretization errors can appear. The images are then saved in the PCX version 5 graphic format (as a widely used and versatile format).

2.4. Fractal Analysis System Software

The program created for the study decodes all PCX images. In our case, we shall analyze only the simulated curves given by the F.C.G.S. The binary images are shown in two colors (white and black), and the black one is considered as matter we shall call Islands. First, for each island, the perimeter is detected, and each point of the perimeter is numerated depending on the connexity used C8D or C4D. We then construct the polygon of pixels and calculate the coordinates (x, y) of each center of the pixels. In this step, the fractal island is defined as a polygon described by a list of pointers. This list points onto the properties of the considered island. A measuring unit of size η then recovers the polygon. Let P_0 be the arbitrary origin (Figure 2) of the covering files, P_1 and P_2, the first successive points of data list such that $d_1 < \eta < d_2$ with $d_1 = \overline{P_0P_1}$ and $d_2 = \overline{P_0P_2}$, and let P_x be the final point such that $\eta = \overline{P_0P_x}$. The coordinates of P_x are the intersections of the circle with center P_0 and radius η with the segment $\overline{P_1P_2}$. This operation is repeated until $P_x = P_0$ and we can then count the number of yardsticks of size η that allows us to recover the perimeter. This operation is then repeated for a yardstick of size $\eta + \delta\eta$ and so on. To construct the data bank of yardsticks [size-perimeters], noted $\left[\eta, P_{(\eta)}\right]$, we choose a minimal yardstick size (in pixel), a maximal one and an increment. However, many algorithm parameters will lead to different estimations of $P(\eta)$ and statistical artifacts can lead to different estimations of the fractal dimension that will be discussed in the Section 3.3. As regards all the parameters that will change the calculated fractal dimension, it will clearly appear that Richardson's method must be processed on Personal Software.

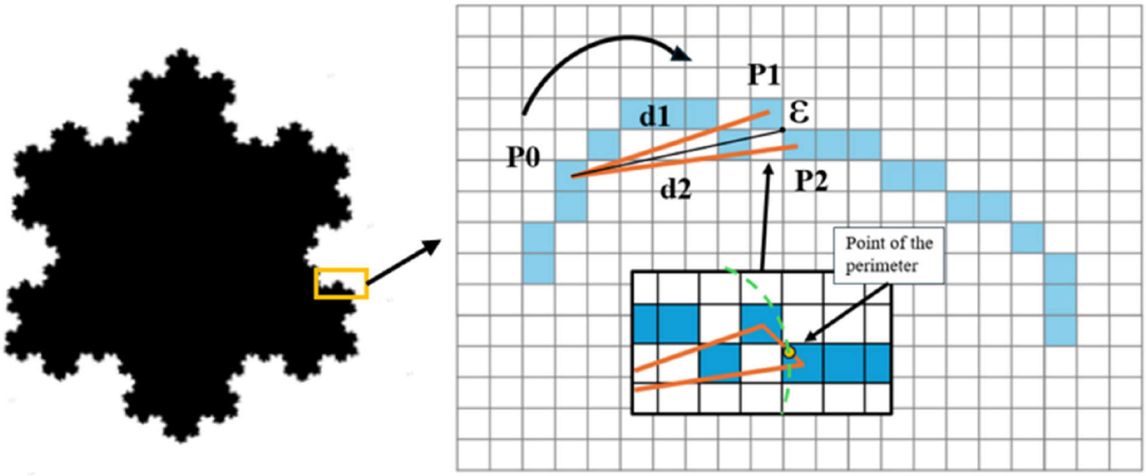

Figure 2. Numerical methods used to measure the perimeter with a yardstick of size η centered on the points P0. The dot represents the new points in the perimeter. The blue squares refer to the pixels during discretization, and the orange lines represent the distances (d1, d2) calculated from one pixel (P0) in relation to two other pixels (P1 and P2).

In this study, all the analyzed curves are defined by a resolution of 2048 × 2048 pixels, matching the current resolution of the CCD camera used to capture material morphology through optical microscopy.

A resolution of 2048 × 2048 pixels was defined for all the generated curves, as it is like the resolution of the CCD sensor equipped to most of the optical microscopy apparatus.

2.5. Statistical Estimation of the Fractal Dimension

To calculate the fractal dimension, we first choose the range of variation and one of the following incremental laws for the yardstick:

1. The yardstick linear variation (YLV): $\eta_n = \eta_{n-1} + \Delta\eta$, where $\Delta\eta$ is the linear increment,

2. The yardstick geometrical variation (YGV): $\eta_n = q\eta_{n-1}$, where q is a geometrical increment.

As the fractal dimension is calculated by the slope of the linear range obtained by the least square method plotting values of $F = \{\log P(\eta_1), \log P(\eta_2), \ldots, \log P(\eta_n)\}$ versus $E = \{\log \eta_1, \log \eta_2, \ldots, \log \eta_n\}$, the distribution of the values of the E-set modifies the estimation of the fractal dimension. If the YLV is used, then the E-set will present a lognormal distribution since $\eta_1, \eta_2, \ldots, \eta_n$ are regularly spaced. The lower the yardstick, the higher the number of $\log \eta_i$ terms. This means that the calculated fractal dimension is more influenced by the perimeter calculated by the lower yardstick than by the higher ones. Consequently, the evaluation of the fractal dimension will include image errors in discretization. In other cases, by using the YGV method then the E-set presents a uniform distribution, and the yardstick range does not influence Δ. To calculate analytically the error made on the determination of the fractal dimension, we suppose that the noise in the determination of the perimeter is independent of the yardstick size (no discretization error) and therefore the standard deviation of the fractal dimension calculated by both YGV and YLV is given, respectively, by Equations (5) and (6).

$$\sigma_{\mathrm{YGV}} = \frac{s\sqrt{12}}{\delta\eta\sqrt{(n-1)}(n-1)} \tag{5}$$

$$\sigma_{\mathrm{YLV}} = \frac{s}{\sqrt{(n-1)\left(\frac{\eta_{\max}\left(\ln^2 \eta_{\max} - 2\ln \eta_{\max} + 2\right) - \eta_{\min}\left(\ln^2 \eta_{\min} - 2\ln \eta_{\min} + 2\right)}{\eta_{\max} - \eta_{\min}} - \left(\frac{\eta_{\max}(\ln \eta_{\max} - 1) - \eta_{\min}(\ln \eta_{\min} - 1)}{\eta_{\max} - \eta_{\min}}\right)^2\right)}} \tag{6}$$

where n is the number of yardsticks, $\delta\eta = \log \eta_i - \log \eta_{i-1}$, $\eta_{\max} - \eta_{\min} = (n-1)\delta\eta'$ (with $\delta\eta' = \eta_i - \eta_{i-1}$) the yardstick increment for, respectively, the YGV and the YLV model, and s the standard deviation for the regression residuals.

At this stage, three remarks can be stated:

1. It can be proved than $\sigma_{\mathrm{YLV}} > \sigma_{\mathrm{YGV}}$, then the YGV method is always the more appropriate to calculate Δ with a good accuracy.
2. Using the YLV method, the experimental weight is not uniform and Δ is more influenced by the estimated perimeter for large yardstick rather than for smaller one. The higher $\eta_{\max} - \eta_{\min}$, the higher the perimeter for large yardsticks.
3. As we shall see in the next paragraph, discretization errors can lead to an erroneous measurement of the perimeter for large yardsticks, consequently the YLV method could overestimate or underestimate the fractal dimension of the image.

3. Curve Analyses

We shall then test our methods on Von Koch Island and the stochastic Von Koch Island.

3.1. Analyses on the Von Koch Flake

The fractal dimension of the Von Koch flake is calculated by the following method:

1. A 1.2 fractal dimension Von Koch flake with $\alpha = 54°$ instead of 60° is computed with a resolution of 2048 × 2048 pixels (we use this dimension on purpose to compare with the Von Koch flake since it is impossible to construct a Stochastic flake defined in Section 4 without recovering). Seven iterations are carried out to construct the flake.
2. The origin of the yardstick is chosen at random.
3. The fractal dimension is calculated by the YGV method and the perimeter's length is computed by Method 4 (floating number of yardstick).

Figure 3 represents the variation in the perimeter versus the yardstick length in log–log coordinates. The upper line corresponds to the true perimeter (same origin for the yardstick and the initiator), and the broken line is the result of the calculation. It is shown that the calculated perimeter's length is shorter than the true one except if the origin of the yardstick corresponds to the origin of the initiator and if the yardstick's length is $L_0/3^i$. From simple geometrical relation (Figure 1), it is obvious that the distance between the maxima is $\log[2\cos(\alpha/2)] = 0.25$. An interesting discovery can be stated in relation with the serrated variation since a systematic departure from linearity is always observed in real microstructural features such as surface rupture of Titanium alloys and steel [3,4], rock mechanics [5], or wear processes [6]. Such variations may be related to grain diameter or other microstructural parameters to give information on the physical process involved.

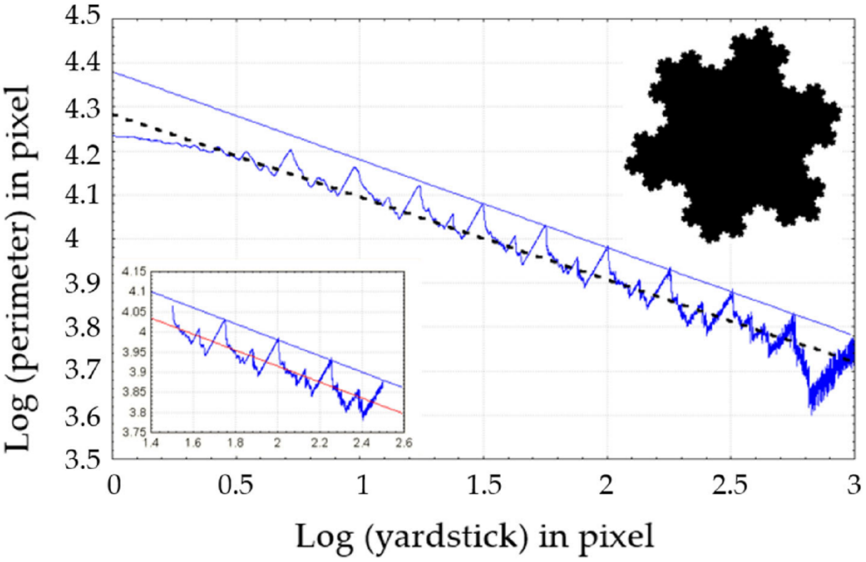

Figure 3. Variation in the perimeter length versus the yardstick size (in log–log coordinates) for a triadic Von Koch Island with a Self-similarity dimension D = 1.2. The upper line represents the theoretical perimeter according to Equation (1). The Dotted line represents the linear regression and gives the values of Δ = 1.188. The red line of the detail represents the linear regression.

From Figure 3, the regression line is parallel to the theoretical one and gives $\Delta = 1.188_{\pm 0.002}$. If we consider that when $\eta < 30$ pixels the peak does not match with the upper line due the errors in discretization and when $\eta < 10$ pixels the undulations are lost in the discretization noise, a new regression performed for $30 < \eta < 300$ pixels gives $\Delta = 1.198_{\pm 0.002}$. By analyzing the computed perimeter, we can observe that this perimeter is more and more underestimated when the size of the yardstick increases. This can be explained away as follows: if the size of the yardstick matches with the length of the initiator, the perimeter will be underestimated except if we choose as origin the origin of the Koch construction. When the size of the yardstick increases, the probability that the yardstick has the same origin as the initiator decreases dramatically. Let us note this probability $\Pr(\eta)$ defined by Equation (7).

$$\Pr(\eta) = \delta\eta/\eta \tag{7}$$

where $\delta\eta$ is the constant size of the elementary pixel.

Then, Equation (10) shows that the probability to estimate the true perimeter decreases logarithmically with the size of the yardstick. Moreover, for large yardsticks, the curves are noisier and noisier since the variance of the measure of the perimeter increases with the size of the yardstick. Postulating that the variance decreases with the probability that the yardstick has the same origin as the Von Koch initiator becomes obvious.

We can also remark that the graph itself achieves a self-affinity multifractal structure meaning that the fractal dimension depends on the scale [7,8]. Figure 3 shows that some parts of the plot present successive segments with slope 1 meaning that the local fractal dimension is null and not 1.2.

To minimize all these artifacts, the result can be improved by the following averaged method:

1. The starting point for the first yardstick is chosen at random.
2. A second iteration is carried out taking the previous origin + 1 pixel.
3. The operation is repeated for δ varying from 1 to 500 pixels.
4. Then the following statistics are built:
    - The computed perimeter is the mean of these 500 perimeters.
    - The computed perimeter is the maximum of these 500 perimeters.
    - The standard deviation is computed.

Figure 4 represents the evolution of mean and maximal perimeters versus the yardstick length. For a long yardstick, a set of computed perimeters is equal to the theoretical one using the maximal value, but using the mean value, the perimeter will always be underestimated. This simulation confirms the hypothesis we state about the underestimation of the perimeter that could then be avoided using the maximal perimeter that approaches the true fractal dimension ($\Delta = 1.19965_{\pm 0.00035}$) with much accuracy although the mean perimeter gives $\Delta = 1.22_{\pm 0.02}$. The standard deviation of the perimeter versus the yardstick's length follows a linear relation $\sigma[\mathrm{P}(\varepsilon)] = 0.8\varepsilon$ and confirms the hypothesis that the measurement of the perimeter is less precise as the size of the yardstick increases.

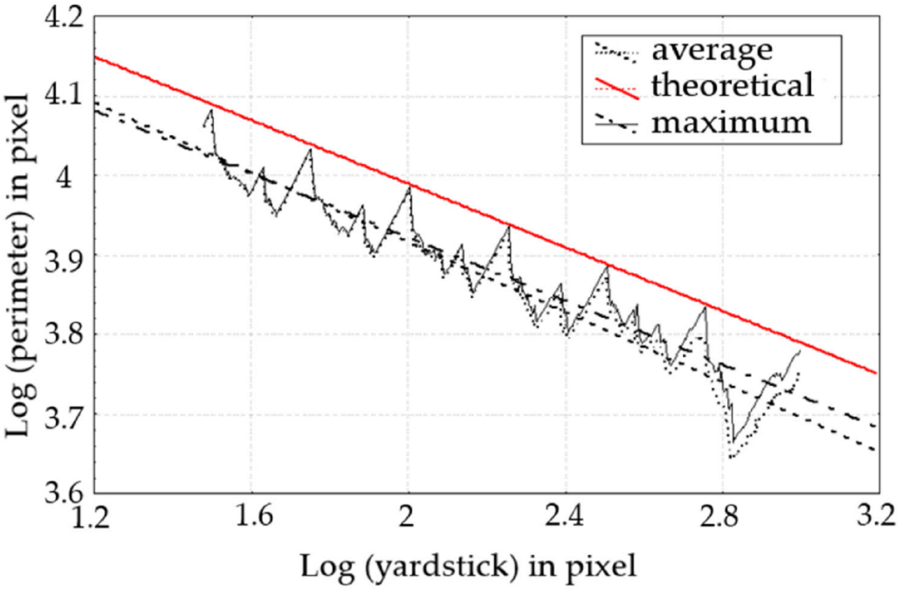

Figure 4. Variation in the perimeter length versus the yardstick size (in log–log coordinates) for a triadic Von Koch island with a Self-similarity dimension D = 1.2. The island is defined on a 2048 × 2048 pixel grid on the border of the graph. The upper line represents the theoretical perimeter according to Equation (1). For a fixed yardstick, 10 perimeter measures are performed by choosing the initial point at random. The Dotted line represents the average perimeter and gives the values of $\Delta = 1.22$. The other dotted line represents the maximal values of the ten perimeter measures and gives a fractal dimension of $\Delta = 1.19965$.

Series of curves from dimensions 1.1 to 1.9 are now created and discretized at a resolution of 2048 × 2048 pixels with a stick from 1 to 800 pixels. Figure 5 shows the variability of length for the perimeter depending on the stick size for fractal dimensions of 1.1, 1.5 and 1.9. We can draw some insight about those graphs:

1. For smaller sticks, the perimeter is increasingly underestimated as the fractal dimension grows and the underestimating range increases critically. This phenomenon is related to the length of the initiator that makes the fractal dimension grows with the smallest size of ε_n in the Koch construction. Let ε_n represent the length of the last stick after n iterations of the Koch construction. With similar principles as in Equation (1), we can lead eventually to Equation (7).

$$\varepsilon_n = L_0/10^{\frac{n \log 4}{\Delta}} \tag{8}$$

2. The critical value ε_c, defined by the first significant variation in the log–log representation is plotted versus ε_5 in Figure 6 (n = 5 means that five iterations are performed to construct the Von Koch Island). The very good correlation shows that the underestimation of the perimeter is a consequence of the size of the lowest initiator met in the construction of the Von Koch flake.

The maxima observed in Figure 5 exist with a path depending on the geometry of the generator. The errors of discretization imply that log P does not vary linearly versus log η and presents a cross-over at a critical value, t. To estimate the influence of this cross over when computing the fractal dimension, Δ is calculated with $t < \eta < 300$ pixels for all the Von Koch islands. Figure 7 shows that the fractal dimensions vary and present oscillations whose maxima fit well with the theoretical value. According to Equations (2) and (7), if we noted d, the distance between two adjacent peaks, as $\cos\ \alpha/2 = \sqrt{(1 + \cos\alpha)/2}$, we finally obtain Equation (8).

$$\Delta = \frac{\log 2}{d} \tag{9}$$

3. The variance in the estimation of the perimeter rises with the fractal dimension.
4. For a given yardstick, the perimeter is undervalued as the dimension increase.

From all these remarks, seven methods were developed to calculate the slope of the log–log plot.

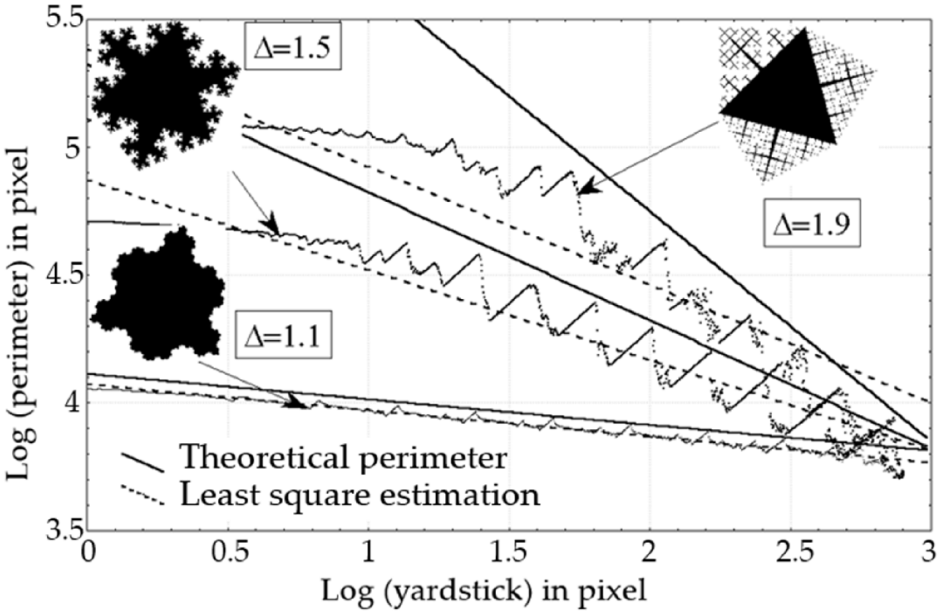

Figure 5. Variation in the perimeter length versus the yardstick size (in log–log coordinates) for a triadic 3 Von Koch Island with a self-similarity dimension D = 1.1, 1.5 and 1.9. The island is defined on a 2048 × 2048 pixel grid shown on the graph. The continued line represents the theoretical perimeter and the doted one the regression line [25].

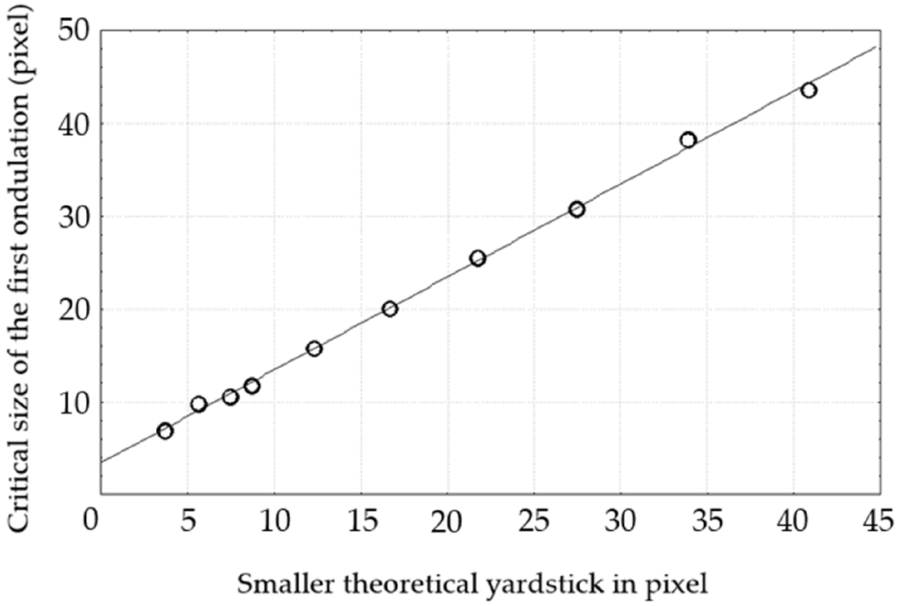

Figure 6. Correlation between ε_5 from Equation (10) and ε_c corresponding to the first significant undulation of the log–log plot of Figure 5.

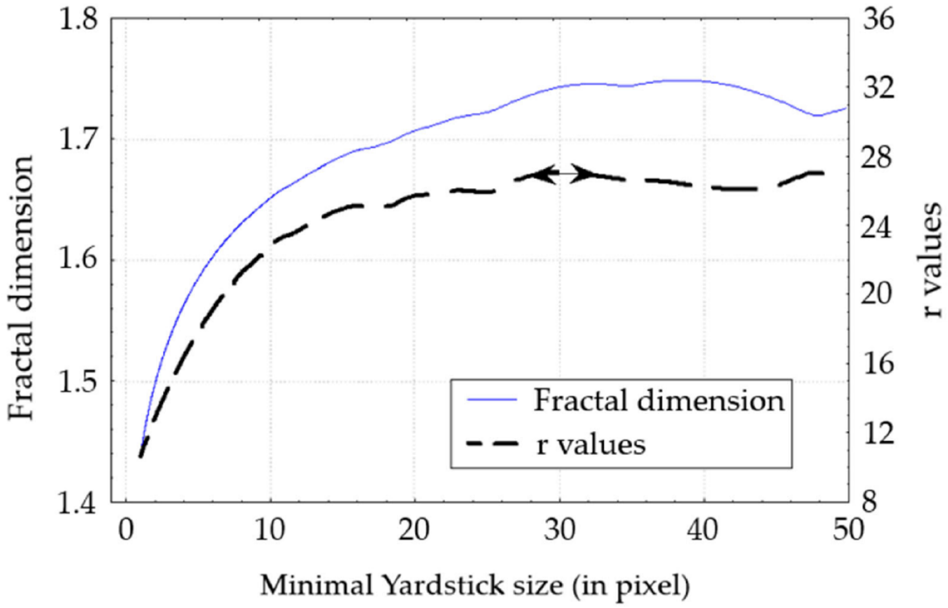

Figure 7. Values r_j and Δ_i versus the minimal size of η_i (in pixel) for the Von Koch of theoretical fractal dimension of 1.8. We obtain $r_{max} = 27.5$ that gives a fractal dimension of $\Delta_{max} = 1.74$.

3.2. Method 1: All Range of the Yardstick Variation (ARYV)

The ARYV and MSMV methods are the same as those used in the publication by Bigerelle and Iost, [25] showing similar results. The aim of this study is to include these methods in the general comparison of seven methods. We provide a summary of the ARYV and MSMV methods, as too much detail on previous results would automatically result in plagiarism. This method involves plotting the relationship between area and yardstick length on a log–log scale. It uses the area covered by the curve as a function of yardstick size to estimate the fractal dimension. Calculations show that smaller yardsticks tend to underestimate the fractal dimension, as they do not capture fine details of the curves, leading to a reduced slope in the log–log plot and thus indicating a lower dimension estimate. As presented in Table 1, the method increasingly underestimates the fractal dimension as it grows. This occurs because ε_5 increases with the fractal dimension, which in turn lowers the slope in the log–log plot due to perimeter underestimation. The result of the calculation of the fractal dimension (1.5) shows that the method is ineffective for accurately determining higher fractal dimensions.

Table 1. Fractal dimension values using the different methods of computation (ARYV to TRROFD). Δ_t is the theoretical dimension as Δ_c is the dimension calculated using the range of sticks size (η_{min} and η_{max}).

	1 **ARYV**		**2** **IEMMV**		**3** **MSMV**		**4** **TMSMV**		**5** **FTPR**	**6** **SCPR**	**7** **RROFD**	**8** **TRROFD**	
Δ_t	Δ_c	η_{min} η_{max}	Δ_c	η_{min} η_{max}	Δ_c	η_{min} η_{max}	Δ_c	η_{min} η_{max}	Δ_c	Δ_c	η_{min} η_{max}	Δ_c	η_{min} η_{max}
1.1	1.102	1 800	1.101	4 580	1.099	1 580	1.102	1 800	1.141	1.096	27 187	1.098	37 172
1.2	1.181	1 800	1.188	6 573	1.183	2 573	1.189	2 800	1.244	1.197	69 712	1.187	37 172
1.26	1.224	1 800	1.241	8 609	1.231	2 609	1.243	3 800	1.244	1.255	53 724	1.260	37 172
1.3	1.248	1 800	1.275	9 619	1.267	4 619	1.285	9 800	1.244	1.295	38 259	1.318	37 172
1.4	1.306	1 800	1.368	13 645	1.352	5 645	1.359	5 800	1.348	1.396	44 362	1.367	37 172
1.5	1.352	1 800	1.459	17 672	1.438	7 672	1.457	10 800	1.452	1.480	59 343	1.444	37 172
1.6	1.389	1 800	1.555	22 681	1.537	14 691	1.543	13 800	1.555	1.581	64 380	1.583	37 172
1.7	1.417	1 800	1.647	28 717	1.644	24 717	1.652	24 800	1.659	1.671	75 408	1.692	37 172
1.8	1.439	1 800	1.738	34 737	1.737	30 737	1.743	30 800	1.763	1.786	40 179	1.792	37 172
1.9	1.462	1 800	1.816	41 755	1.826	35 755	1.825	35 800	1.866	1.901	36 187	1.893	37 172

3.3. Method 2: Initiator Epsilon Min-Max Variation (IEMMV)

The slope is calculated as follows. The yardstick varies between the size of the initiator ε_1 (between 580 and 755 pixels) and the smallest size of the iterator after five iterations, i.e., ε_5 (between 4 and 41 pixels). When choosing the yardstick range, we obtain (Table 1) a better estimation of the fractal dimension, and errors vary between 0.01 and 0.09. The best results obtained by Method 2 mean that

- The yardstick's size must be higher than a critical value corresponding to the beginning of the fractal regime.
- The yardstick's size must be lower than a critical size depending on the support of the fractal.

In our case, these critical sizes are determined from the values ε_1 and ε_5 related to the Von Koch flake construction. However, the fractal dimension is not well evaluated by this method because the perimeter is underestimated for short yardsticks even if the yardstick size is higher than ε_5. This is since the fractal curve is discretized in a highly anisotropic matrix and then it is not possible for ε_5 to be confounded for each segment with the Von Koch flake even with a high number of randomly distributed origins. This effect is amplified for high fractal dimensions, which increase the anisotropy of the discretized image.

This method which requires the knowledge of both ε_1 and ε_5 (the way to construct the fractal curve and therefore its fractal dimension) is not relevant to calculate the fractal dimension of unknown curves.

3.4. Method 3: Maximal Slope with Minimal Variation (MSMV)

This method, also presented in detail in Bigerelle and Iost [25], measures the mean square variation in the fractal dimension as a function of yardstick size. To evaluate the set of perimeters that is significantly less than the expected one, A linear method on a log–log plot is used to estimate the fractal dimension Δ_j. To avoid errors related to small scales, an estimator $r_j = \frac{\Delta_j}{S_j}$ is defined, where S_j is the standard deviation of the residuals.

The best estimate of the fractal dimension Δ_{max} is obtained at the highest value of r_j. This method allows estimation of the smallest meaningful scale (ε_5) without knowing the construction parameters, but it requires prior knowledge of the largest scale (ε_1).

3.5. Method 4: Total Maximal Slope with Minimal Variation (TMSMV)

This method is the same as the MSMV method except for the largest yardstick which is not given by ε_1 but is equal to 800 (the maximal yardstick size used in our simulations). The results are nearer than those obtained by Methods 3 and 2 in which parameters of the fractal were completely or partially known. Moreover, this method does not require any hypothesis on the flake constructor and can then be applied to any fractal curve and then to any experimental image.

3.6. Method 5: Fourier Transform Patterns Research (FTPR)

A periodicity in the representation of log(P) versus log(η) related to the self-similarity dimension of the Von Koch construction by $D = \log 2/d$ is shown in Figures 4 and 5. To estimate d with this relation, we first calculated the fractal dimension by Method 1. Secondly the signal is straightening up on by keeping only the residuals of the least square regression line to avoid lower frequencies related to the slope of the log–log plot which leaves unchanged the d value. Thirdly we processed a Discrete Fourier Transform. Figure 8 represents the spectra of the log–log plot for Δ = 1.2. As it can be observed, the fundamental peak appears on d = 0.242 and two harmonic peaks at d/2 = 0.126 and d/4 = 0.063. However, even if the border effects are neglected (in our cases we used the Hamming window to process to the weighted moving average transformation), the lowest frequencies are not defined very precisely. In our experiment, the two adjacent periods for d = 0.242 are 0.223 and 0.263. This lower resolution is intrinsic to the Fourier transform and can only be increased by taking a higher number of points, which means increasing dramatically the image size and then the calculation time. However, according to Equation (11) and a fractal dimension varying between one and two, the d-range lies in the [$\log\sqrt{2}$, log 2] interval, i.e., [0.1505, 0.3010]. Consequently, using the Fourier analysis, the precision on Δ cannot exceed 0.2. In Figure 8, we obtain Δ = 1.24 which lies in the interval [1.14, 1.35]. This procedure is repeated for the different fractal dimensions and the results with their confidence intervals are shown in Table 2. As can be observed, the uncertainty on the determination of the fractal dimension is around 0.2, which represents an error of 20%. However, the theoretical fractal dimension always lies in the confidence interval determined by this spectrum method, proving that the research pattern method is adequate but that its precision must be improved. The next method will present an original technique to better estimate d.

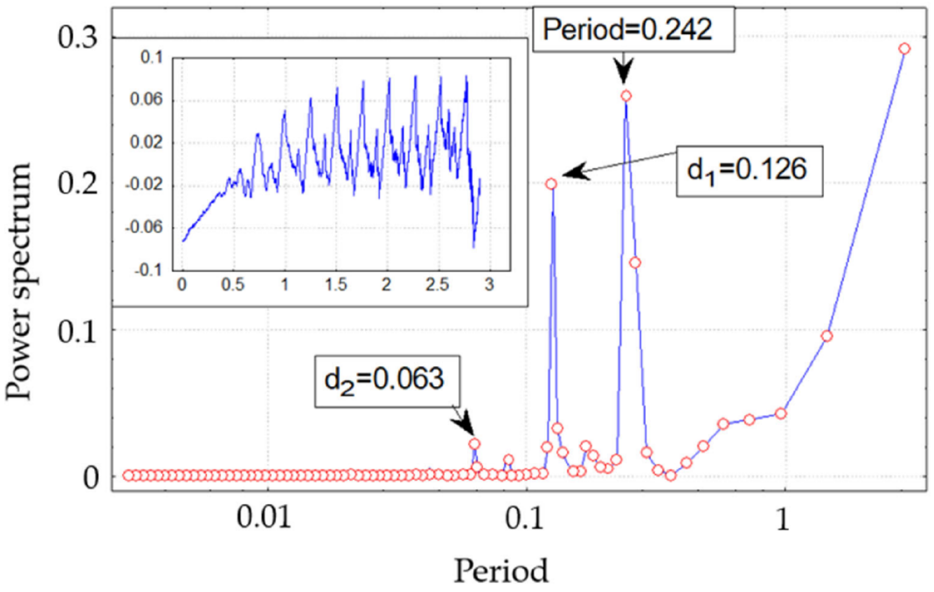

Figure 8. Discrete Fourier Transform of the log–log plot shows the border of the figure, which is the residuals from the regression of Figure 3. The theoretical fractal dimension is 1.2. The harmonics give the value of d = 0.242 and give Δ = 1.24.

Table 2. Results of the Discrete Fourier Transform. d_{theo} represents the period of the log–log plot of the Richardson graph according to Equation (11). d_{mean}, d_{inf} and d_{sup} represents the statistics of the adjacent points of the higher harmonics (period) (see Figure 8). The fractal dimension could be calculated from these D values and give an interval of variation $\Delta_c \in [\Delta_{min}, \Delta_{max}]$.

Δ	d_{theo}	d_{mean}	d_{inf}	d_{sup}	Δ_c	Δ_{inf}	Δ_{sup}
1.10	0.274	0.264	0.242	0.290	1.14	1.04	1.24
1.20	0.251	0.242	0.223	0.264	1.24	1.14	1.35
1.26	0.239	0.242	0.223	0.264	1.24	1.14	1.35
1.30	0.232	0.242	0.223	0.264	1.24	1.14	1.35
1.40	0.215	0.223	0.207	0.242	1.35	1.24	1.45
1.50	0.201	0.207	0.193	0.223	1.45	1.35	1.56
1.60	0.188	0.194	0.181	0.207	1.56	1.45	1.66
1.70	0.177	0.181	0.171	0.194	1.66	1.56	1.76
1.80	0.167	0.171	0.161	0.181	1.76	1.66	1.87
1.90	0.158	0.161	0.153	0.171	1.87	1.76	1.97

3.7. Method 6: Self-Convolution Patterns Research (SCPR)

This method aims at determining d precisely and then, according to Equation (11), the fractal dimension. As could be proved for the FTPR method, the resolution of all methods based on the mathematical basis of the Fourier transform is insufficient to calculate the fractal dimension. For this reason, we use an autocorrelation function by calculating the coefficient of regression $R(\delta\eta)$ between the points $\log P(\eta)$ and $\log P(\eta + \delta\eta)$. By taking the mean of all values for different profiles, we obtain Equation (10).

$$R(\delta\eta) = \frac{1}{\sigma^2}\frac{1}{\eta_{max} - \eta_{min} - \delta\eta}\int_{\eta_{min}}^{\eta_{max}-\delta\eta} \log(P^*(\eta))\log(P^*(\eta+\delta\eta))d\eta \quad (10)$$

where σ^2 is the variance of $\log(P^*(\eta))$ with $\log(P^*(\eta)) = \log(P(\eta)) - \mu$ and μ the mean of $\log P(\eta)$.

As we have used the yardstick geometrical variation (YGV) method, each distance between discretized adjacent points is constant and the integral can be discretized by Equation (11).

$$\mathrm{R(i)} = \frac{1}{\sigma^2(\mathrm{N}-\mathrm{i})}\sum_{\mathrm{j}=1}^{\mathrm{N}-\mathrm{i}} \log\left(\mathrm{P}^*(\mathrm{j})\right)\log(\mathrm{P}^*(\mathrm{j}+\mathrm{i})) \tag{11}$$

where N is the number of discretized points $\log(\mathrm{P}^*(\mathrm{j}))$.

To find d, $\delta\eta$ is calculated such that the functional $\mathrm{R}(\delta\eta)$ is maximal with $\delta\eta \in \left[\log\sqrt{2}, \log 2\right]$, $\mathrm{R}(\delta\eta)$ is plotted versus $\Delta(\delta\mathrm{n}) = \frac{\log 2}{\delta\eta}$ (Figure 9) for all the Von Koch curves whose fractal dimension varies from 1.1 to 1.9. The maximum of each curve gives the fractal dimension calculated by the SCPR method with an error lower than 0.03 (Table 1). This method can estimate the highest fractal dimension and is more precise than the previous ones. Moreover, this original method allows us to calculate the angle of the constructor α (with the relation $\mathrm{d} = \log[2\cos(\alpha/2)]$) without estimation of the regression slope. Figure 5 shows that if m is the number of maxima met in the log–log plot and i the number of iterations for the snowflake, the relation $\mathrm{m} = 2\mathrm{i} - 1$ is obtained. Consequently, all the odd peaks represent the value of ε_n used in the construction of the flake.

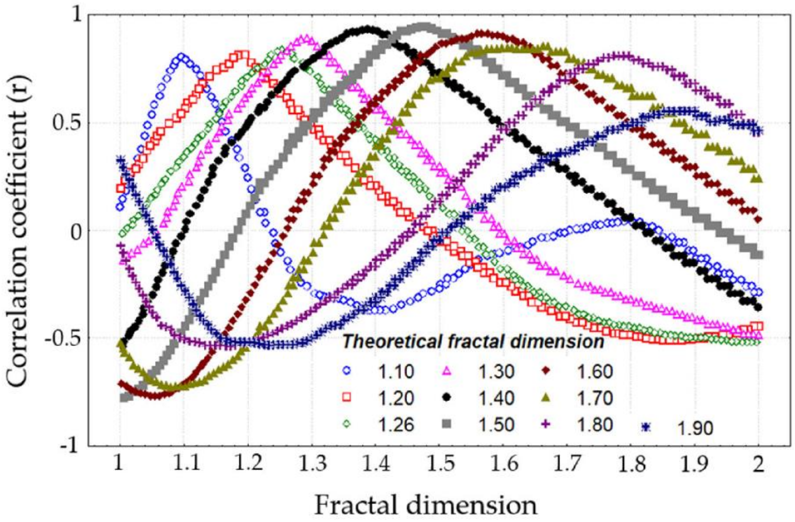

Figure 9. Values of $\mathrm{R}(\delta\eta)$ versus $\frac{\log 2}{\delta\eta}$ for all the different Von Koch curves with fractal dimension varying from 1.1 to 1.9. The maximum of each curve gives the fractal dimension calculated by the SCPR method.

As the relation $\varepsilon_\mathrm{n} = \mathrm{L}_0/[2(1+\cos\alpha)]^\mathrm{n}$ holds, by plotting $\log\varepsilon_\mathrm{n}$ versus $\log \mathrm{n}$ and by the least square linear regression, the values of the ordinate give the values of L_0. Then it becomes very simple to reconstruct all the parameters of the initial fractal curve without restriction. The SCPR method becomes an inverse method that could be used to find the beginning of a fractal process and its origin. However, it can only be used to calculate the fractal dimension of fractal curves constructed by Linear Iterative Function System (LIFS) and cannot be applied to other forms.

3.8. Method 7: Range Research of Optimized Fractal Dimension (RROFD)

RROFD is not a method to calculate the fractal dimension, but it allows us to find the optimal range of $[\eta_{\min}, \eta_{\max}]$ on which the calculated fractal dimension corresponds to the theoretical one (Table 1). To find this interval, we calculate the fractal dimension from the set of points

$$\mathrm{E}_{\mathrm{i,j}} = \left\{(\log\eta_\mathrm{i}, \log\mathrm{P}(\eta_\mathrm{i})), (\log\eta_{\mathrm{i}+1}, \log\mathrm{P}(\eta_{\mathrm{i}+1})), \ldots, (\log\eta_{\mathrm{j}-1}, \log\mathrm{P}(\eta_{\mathrm{j}-1})), (\log\eta_\mathrm{j}, \log\mathrm{P}(\eta_\mathrm{j}))\right\}$$

noted $\Delta_{i,j}$.

We retain the values (i, j) that give the functional $\left|\Delta_{i,j} - \Delta_{theoretical}\right|$ minimal. It is then possible to plot the surface response of the error $\left|\Delta_{\eta_{min},\eta_{max}} - \Delta_{theoretical}\right|$ versus the minimal and maximal sizes of the pixel η_{min} and η_{max} used to estimate the fractal dimension. The main problem is that the surface on which optima are found does not consist of valleys, making the optima not very stable, particularly for higher dimensions. Moreover, each optimum depends on the fractal dimension and is quite different. Therefore, all methods used to calculate the fractal dimension must be tested on curves with different fractal dimensions and must lead to robust minima.

3.9. Method 8: Total Range Research of Optimized Fractal Dimension (TRROFD)

This method is close to Method 7 (RROFD) but its aim is to find the unique optimal range $[\eta_{min}, \eta_{max}]$ on which all calculated fractal dimensions correspond to the theoretical ones. The research algorithm described in Method 6 is used to retain the shortest size of the pixel η_{min} and the largest one η_{max} used to estimate the fractal dimension which minimizes the functional $\frac{1}{n}\sum_{i=1}^{n}\left|{}^{i}\Delta_{\eta_{min},\eta_{max}} - {}^{i}\Delta_{theoretical}\right|$ where $1.1 < {}^{i}\Delta < 1.9$ represents the fractal dimension for the ith Koch flakes between n curves. The surface response of the mean error for $\eta_{min} = 37$ and $\eta_{max} = 172$ gives a fractal dimension with an error lower than 0.016 (Table 1). Note that changing the previous functional by $\sqrt{\frac{1}{n}\sum_{i=1}^{n}\left({}^{i}\Delta_{\eta_{min},\eta_{max}} - {}^{i}\Delta_{theoretical}\right)^2}$ does not affect $\boldsymbol{\eta}_{min}$ and $\boldsymbol{\eta}_{max}$ proving that the optimization problem is well stated.

3.10. Influence and Optimization of Yardstick Ranges

The accuracy of fractal dimension estimation using Richardson's method strongly depends on the selection of the yardstick range, defined by $\boldsymbol{\eta}_{min}$ and $\boldsymbol{\eta}_{max}$. Each of the eight methods described in this study adopts a different strategy for choosing or optimizing this interval. Table 3 summarizes how these values are defined or computed in each method, whether they are fixed, derived from the fractal geometry, statistically optimized, or indirectly determined through signal analysis.

Table 3. Definition of η min **and** η max **in the eight methods**.

Method	Full Name	$\boldsymbol{\eta}_{min}$	$\boldsymbol{\eta}_{max}$	Description
1. ARYV	All Range of the Yardstick Variation	Fixed (e.g., 1 pixel)	Fixed (e.g., 800 pixels)	Full range arbitrarily chosen; prone to errors due to discretization (low η) or oversmoothing (high η).
2. IEMMV	Initiator Epsilon Min-Max Variation	ε_5 = smallest segment of the generator (iteration 5)	ε_1 = initial segment of the initiator	Requires knowledge of the fractal's construction parameters; not usable on unknown curves.
3. MSMV	Maximal Slope with Minimal Variation	Selected to minimize slope variance	Selected to minimize slope variance	Searches for stable intervals with low slope fluctuation, without relying on explicit geometric knowledge.
4. TMSMV	Total Maximal Slope with Minimal Variation	Like MSMV	Fixed at 800 pixels	More general version of MSMV that can be applied to unknown or experimental fractals.
5. FTPR	Fourier Transform Pattern Research	Implicit (derived from residuals)	Implicit (derived from residuals)	No explicit η range; analysis is based on the periodicity of residuals in the log–log perimeter plot.
6. SCPR	Self-Convolution Patterns Research	Determined automatically via autocorrelation	Determined automatically via autocorrelation	Peak lag r_{max} defines the periodicity; $\boldsymbol{\eta}_{min}$ and $\boldsymbol{\eta}_{max}$ are implicit from the correlated signal.

Table 3. *Cont.*

Method	Full Name	$\eta_{\min}$	$\eta_{\max}$	Description
7. RROFD	Range Research of Optimized Fractal Dimension	Explored by grid search	Explored by grid search	Optimized per curve to find the best $[\eta_{\min}, \eta_{\max}]$ interval with minimal deviation from theoretical D.
8. TRROFD	Total Range Research of Optimized Fractal Dimension	$\eta_{\min}$ = 37 pixels	$\eta_{\max}$ = 172 pixels	Globally optimized range that minimizes average error across all tested fractal dimensions; provides stable and general recommendation.

4. Analyses of the Stochastic Von Koch Flake

We shall now introduce the stochastic construction of the Von Koch flake (size 2048 × 2048 with five iterations) (Figure 10). All the steps of the iterative construction are the same as in the deterministic case, but the direction of the initiator is chosen at random, with a probability ½, (these operations leave unchanged the theoretical fractal dimension). These fractal curves presenting a stochastic structure met in nature are more appropriate to test Richardson's method (Figure 11) and introduce a stochastic measure for the fractal dimension that was impossible for deterministic curves. However, during the construction, some recovering may appear that diminishes the fractal dimension of the curves leaving unchanged the self-similarity dimension. We have shown that when using a fractal dimension lower than 1.2, no recovering appears and then the fractal dimension of the flake equals its self-similarity dimension (Δ = D). It is to be noticed that some analytical models applied to calculate the fractal dimension of ruptured surfaces do not take this fact into account and give overestimated values of Δ.

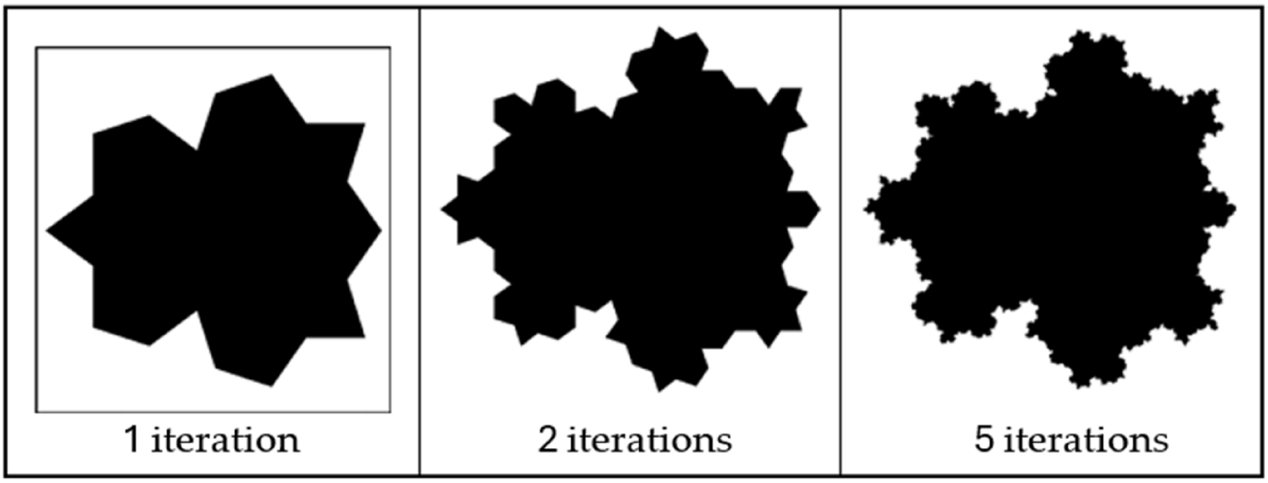

Figure 10. The Stochastic triadic Von Koch Island construction with D = 1.2: first, second and fifth iterations.

To estimate the fractal dimension of the stochastic Von Koch flake, the following scheme is applied:

1. 100 stochastic Von Koch flakes are constructed with five iterations and a resolution of 2048 × 2048 pixels.
2. The fractal dimensions are calculated by the six different methods (ARYV, IEMMV, MSMV, TMSMV, SCPR, and TRROFD (taking the range obtained by the nearer optimization, i.e., $\eta \in [37, 172]$) as indicated by Method 8.
3. Statistics on the 100 fractal dimensions are performed (mean, standard deviation, standard error, min, max, median, 95% confidence level for the mean) (Table 4).

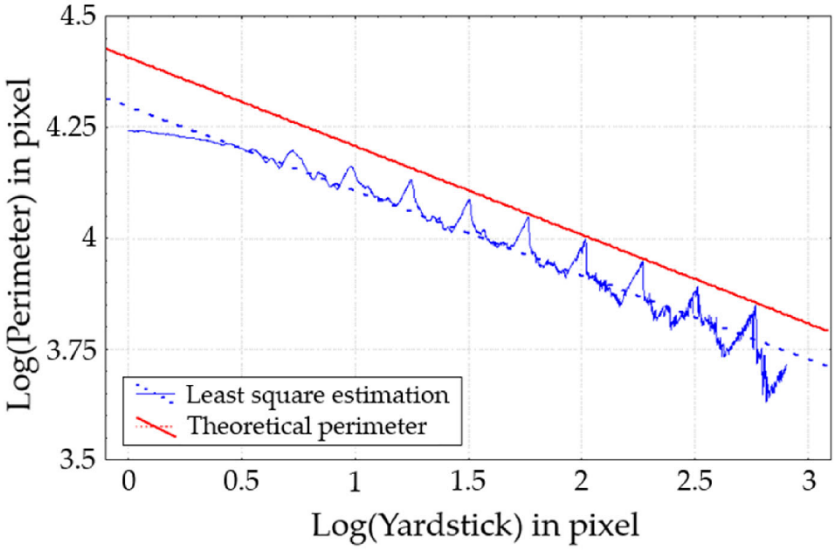

Figure 11. Variation in the perimeter length versus the yardstick size (in log–log coordinates) for a triadic Stochastic von Koch Island with a self-similarity dimension D = 1.2. The island is defined on a 2048 × 2048 pixel grid as illustrated in Figure 10. The upper line represents the theoretical perimeter according to Equation (1). The dotted line represents the linear regression and gives the values of $\Delta = 1.19$.

Table 4. Descriptive statistics on the calculation of the fractal dimension (theoretical fractal dimension 1.2) shown in Figure 10 for 100 Stochastic Von Koch flakes built with five iterations on a resolution of 2048 × 2048. Fractal dimension is calculated by the six different methods: ARYV, IEMMV, MSMV, TMSMV, SCPR, and TRROFD. IC 95% represents the 95% confidence interval of means, and Std. dev the standard deviation.

Method	Mean	−IC 95%	+ IC 95%	Median	Minimum	Maximum	Std Dev
ARYV	1.186945	1.186567	1.187322	1.186793	1.182414	1.192838	0.001892
TMSMV	1.197857	1.197272	1.198442	1.197949	1.191600	1.207049	0.002932
SCPR	1.199980	1.198943	1.201017	1.198000	1.191000	1.212000	0.005200
TRROFD	1.197210	1.195674	1.198745	1.196271	1.180984	1.214840	0.007698
IEMMV	1.196716	1.196080	1.197351	1.196651	1.190029	1.207746	0.003184
MSMV	1.180796	1.180464	1.181128	1.180775	1.177221	1.185031	0.001665

The SCPR Method perfectly estimates the fractal dimension because the 95% confidence interval includes the theoretical dimension. On stochastic curves, the results obtained by this original method are also very accurate. The TRROFD method also speaks for itself, confirming the fact that the range on which the yardstick is chosen plays an important role in giving a precise determination of the fractal dimension. Moreover, this method helps to determine the yardstick range. The methods ARYV and IEMMV underestimate Δ, proving once more that the yardstick range cannot be chosen arbitrarily. Because of the lack of precision on the measure of the fractal dimension, the MSMV method is not appropriate for stochastic curves. Finally, the TMSMV method is accurate and can be applied both to stochastic and deterministic curves.

A promising avenue for future work is the extension of the He–Liu formulation [27], originally developed for porous materials, to partially fractal geometries such as the stochastic Von Koch curve as shown in Appendix A. By treating the probability p of recursive refinement as a proxy for geometric porosity, we derive in Appendix A, a heuristic dimension $\alpha(p,n)$ that captures the progressive loss of complexity. This model enables a continuous transition between linear and fully fractal regimes and defines a critical threshold $p_{\text{transition}}$ where the structure reaches the classical Koch dimension. These results suggest that the He–Liu approach could bridge geometric and physical perspectives in fractal analysis.

5. Conclusions

This study highlights both the strengths and limitations of using Richardson's method for estimating the fractal dimension of self-similar structures. A key strength of our approach is the development and comparison of multiple computational methods, allowing for a more robust and precise estimation of fractal dimensions, particularly when applied to digital images. Methods such as the Self-Convolution Patterns Research (SCPR) technique demonstrated high accuracy, with confidence intervals including the theoretical fractal dimension. Additionally, our findings emphasize the importance of selecting an appropriate yardstick range, as arbitrary choices can significantly bias results. However, certain limitations persist. The dependency of the estimated fractal dimension on the chosen algorithm remains a challenge, making cross-method comparisons difficult. Discretization errors introduce artifacts, particularly for large yardstick sizes, affecting the precision of the perimeter estimation. Moreover, while our approach is effective for deterministic fractals such as the Koch snowflake, its applicability to more complex, naturally occurring fractals or stochastic fractal structures requires further investigation. Future research could extend these findings by integrating physical simulation models to explore how characteristic scales of interface modification emerge under specific physical mechanisms, such as erosion, diffusion, or mechanical stress. Additionally, refining computational techniques to mitigate discretization errors and improve cross-method comparability will be crucial for advancing fractal analysis in various scientific and engineering applications.

In conclusion, this study demonstrates the effectiveness of Richardson's method for estimating the fractal dimension of self-similar structures. Our analyses underscore the emergence of artifacts when the condition of self-similarity is not strictly met, highlighting the critical role of selecting appropriate parameters for accurate analysis. We observed that the fractal dimension is influenced by various morphological factors in the Koch curve construction, suggesting a potential link between shape parameters and underlying physical processes.

Using an innovative approach, we analyze the perimeter as a function of yardstick size, enabling the extraction of key parameters for constructing fractal curves. This inverse method proves valuable in identifying critical experimental features. Furthermore, our findings confirm that specific methods, such as Self-Convolution Patterns Research (SCPR), provide accurate fractal dimension estimations, whereas methods like All Range of the Yardstick Variation (ARYV) and Initiator Epsilon Min-Max Variation (IEMMV) reveal the sensitivity of results to the chosen yardstick range. This study also highlights the suitability of certain methods for either stochastic or deterministic curves, offering robust tools for fractal analysis.

Looking ahead, this work opens promising avenues for leveraging physical simulation models on fractal constructions such as the Von Koch curve. These models could explore how characteristic scales of interface modification emerge under specific physical mechanisms. For instance, simulations of erosion, deposition, or diffusion along a fractal interface could help identify critical points of interaction, while models of mechanical stress or adhesion could elucidate the role of fractality in fracture propagation. Moreover, dynamic simulations involving fluid–structure interactions, growth processes, or thermal ablation could reveal how external forces alter the geometry of fractal structures. By combining these simulations with a quantification approach based on morphological indicators, such as fractal dimension or specific roughness parameters, it would be possible to systematically study the interplay between fractal geometries and physical phenomena. These methodologies may provide new insights into interface dynamics, enabling the identification of characteristic features and scales relevant to applications in materials science, surface engineering, and even biological systems.

Author Contributions: Methodology, M.B.; Data curation, M.B.; Writing—original draft, M.B. and F.B.; Writing—review & editing, F.B. and J.L.; Visualization, M.B. All authors have read and agreed to the published version of the manuscript.

Funding: This research received no external funding.

Data Availability Statement: Data are contained within the article.

Conflicts of Interest: Author Julie Lemesle was employed by the company U.R Concept. The remaining authors declare that the research was conducted in the absence of any commercial or financial relationships that could be construed as a potential conflict of interest.

Appendix A. Toward the Application of He–Liu Formulation in Partially Fractal Structures: The Case of the Stochastic Von Koch Curve

In the field of fractal analysis, it is essential to distinguish between two major categories of structures: boundary (or contour) fractals and mass fractals. The former, such as the classical Von Koch curve, are one-dimensional geometric objects embedded in a higher-dimensional space. They are characterized by complex boundaries but occupy zero area or volume. The latter, by contrast, include porous solids or granular media, which exhibit a hierarchically distributed occupation of space. In these cases, the notion of mass density at multiple scales becomes central. These two families of fractals rely on fundamentally different measurement logics: boundary fractals are analyzed via perimeters or lengths, while mass fractals require volumetric or areal evaluations.

The Lacunar Stochastic Von Koch curve constitutes a particularly intriguing intermediate case. It generalizes the deterministic Koch curve by introducing a probability $p \in [0,1]$ of adding the triangular protuberance at each iteration step. As a result, only a fraction of the segments undergoes fractal refinement at each stage, yielding a partially fractal structure marked by local lacunarity. Some zones remain smooth (non-iterated), which introduces a measurable loss of geometric complexity. Conceptually, this reduction can be likened to porosity in mass fractals, where expected structure is absent.

In this context, it becomes relevant to question whether the formulation first proposed by Kong [27] and improved by He and Liu [28] to quantify the fractal dimension of porous materials based on the ratio of preserved to missing matter, could be extended to partially fractal geometries. Their two-scale approach relies on the relationship between a total reference domain of size L and a fractally occupied subdomain C, given by the following:

$$\alpha = \frac{\ln \frac{L^2}{L^2 - C^2}}{\ln \frac{L}{C}} \tag{A1}$$

where L^2 is the bounding area (or total volume in 3D), and C^2 the effective area occupied by structure. In porous media, $L^2 - C^2$ represents voids. Analogously, in the stochastic Koch curve, this difference may be interpreted as a geometric porosity, reflecting the absence of local fractal development.

The average fractal dimension of the stochastic Koch curve can be explicitly derived by modifying the classical deterministic model. In the standard Von Koch curve, each segment is replaced by four segments of one-third the original length, leading to a dimension $D = \ln 3/\ln 4 \approx 1.2619$.

In the stochastic variant (Table A1, Figure A1), only a proportion p of the segments undergo refinement. On average, a single segment yields 1+3p new segments: the base segment is divided into three, and the triangular "bump" is added with probability p, contributing two additional segments. Hence, the mean fractal dimension becomes $D(p) = \ln(1+3p)/\ln(3)$.

This formulation behaves intuitively:

- When p = 1, we recover the classical dimension D = ln4/ln3,
- When p = 0, no refinement occurs, and D = 0, corresponding to a straight line (minimal complexity).

Table A1. Grid of stochastic Von Koch snowflakes generated at recursion level 10, for decreasing values of the probability p (from 1.0 to 0.0) applied to each segment. Each column represents a distinct p, while each row shows an independent random realization. Geometric complexity decreases with lower p, leading to smaller estimated fractal dimensions.

p = 1	**p = 0.9**	**p = 0.8**	**p = 0.7**	**p = 0.6**	**p = 0.5**	**p = 0.4**	**p = 0.3**	**p = 0.2**	**p = 0.1**	**p = 0**
D = 1.264 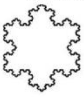	D = 1.263 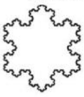	D = 1.254 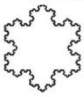	D = 1.176 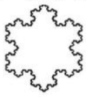	D = 1.222 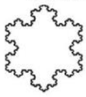	D = 1.158 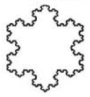	D = 0.917 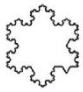	D = 0.910 	D = 0.442 	D = 0.248 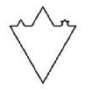	D = 0 
D = 1.264 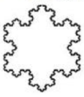	D = 1.263 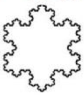	D = 1.250 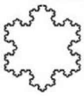	D = 1.247 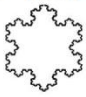	D = 1.197 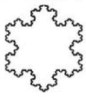	D = 1.027 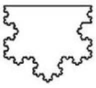	D = 0.877 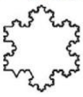	D = 0.896 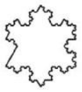	D = 0.726 	D = 0.146 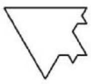	D = 0 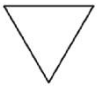
D = 1.264 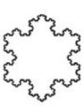	D = 1.262 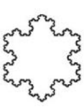	D = 1.258 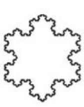	D = 1.232 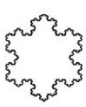	D = 1.215 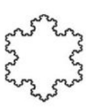	D = 1.102 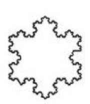	D = 0.996 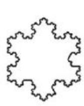	D = 0.905 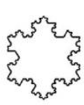	D = 0.401 	D = 0.378 	D = 0 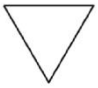
D = 1.264 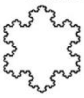	D = 1.263 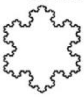	D = 1.257 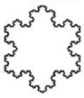	D = 1.239 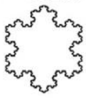	D = 1.197 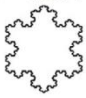	D = 1.130 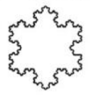	D = 0.885 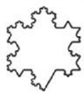	D = 0.826 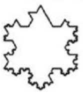	D = 0.686 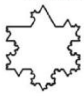	D = 0.352 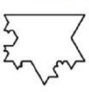	D = 0 
D = 1.264 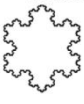	D = 1.263 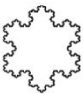	D = 1.253 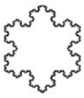	D = 1.241 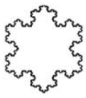	D = 1.029 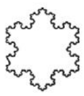	D = 1.100 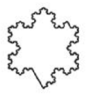	D = 1.021 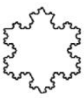	D = 0.806 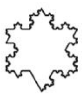	D = 0.435 	D = 0.459 	D = 0 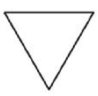

To explore the applicability of the He–Liu method in this context, we propose the following heuristic argument. At iteration n, the effective area developed by the stochastic Koch curve is reduced relative to the fully deterministic version by a factor of p^n, corresponding to the fractal density. We may thus approximate the occupied area as $C^2 \approx A_n p^n$, where A_n is the area in the classical case. Assuming L = 1, the fractal dimension is shown in Equation (A2).

$$\alpha(p,n) = \frac{\ln \frac{1}{1-p^n}}{\ln \frac{1}{\sqrt{p^n}}} \tag{A2}$$

This expression decreases with p, aligning with the intuition that greater lacunarity (lower p) results in reduced fractal complexity. Therefore, the He–Liu formulation can capture both the scale-dependent behavior and the local fractal density in structures that are only partially developed.

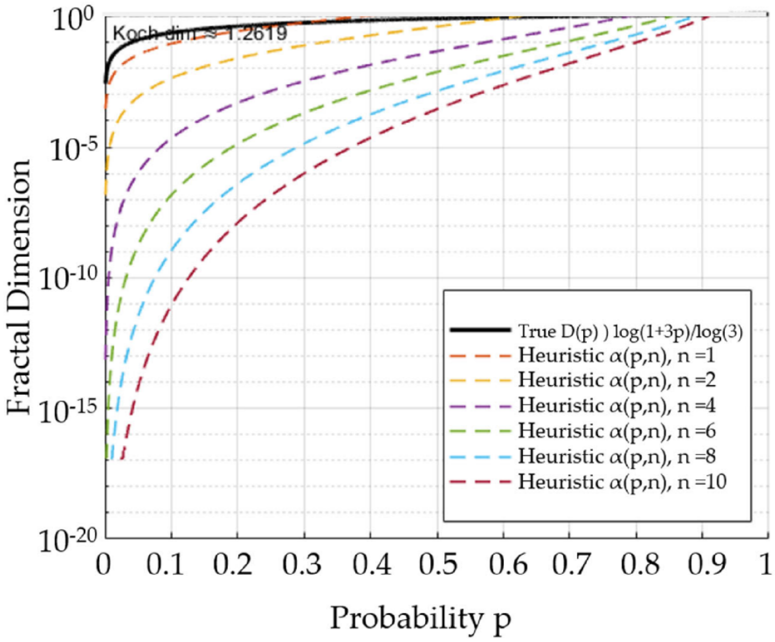

Figure A1. Plot of the heuristic fractal dimension α(p,n) as a function of the stochastic activation probability p, for various iteration depths n. The exact dimension D(p) is shown in black. For each n, the heuristic formula α(p,n) overestimates the dimension for high p and is truncated at 1.2619 to reflect the deterministic Koch curve limit.

This expression decreases with p, aligning with the intuition that greater lacunarity (lower p) results in reduced fractal complexity. Therefore, the He–Liu formulation can capture both the scale-dependent behavior and the local fractal density in structures that are only partially developed.

The expression of α(p,n) provides a useful heuristic interpretation of effective fractal complexity in partially developed structures. However, it diverges as p→1, unlike the true fractal dimension of the deterministic Koch curve. Therefore, this formulation should be interpreted as an approximation valid for $p < 1$. Interestingly, the heuristic formulation α(p,n) derived in analogy to the He–Liu model does more than approximate local complexity—it also provides a continuous description of the transition between geometrical regimes. For each iteration depth n, a critical probability $p_{\text{transition}}$ can be defined by the condition of Equation (A3).

$$\alpha(p_{\text{transition}}, n) = \frac{\ln 4}{\ln 3} \tag{A3}$$

This transition point separates two regimes (see Figure A2):

- For $p < p_{\text{transition}}$, the structure behaves as a partially fractal boundary, with lower geometric complexity.
- For $p \geq p_{\text{transition}}$, the effective fractal dimension saturates to that of the deterministic Koch curve, indicating full geometric development.

Thus, the heuristic α(p,n) serves as a phase-function interpolating between linear and fully fractal contours. This offers a geometric counterpart to the original He–Liu formulation applied to mass–void systems and suggests a broader conceptual framework in which fractal completeness is governed by parameters such as p, scale n, or material porosity. Although the He–Liu model was originally conceived for physical systems with hierarchical porosity, its underlying logic, quantifying structural information loss across scales, makes it relevant for geometric objects with incomplete or randomly distributed fractality. When applied to the stochastic Von Koch curve, the model yields an effective fractal dimension interpretable as a measure of complexity density. This transposition opens a promising avenue for bridging geometric and physical approaches to fractal analysis, and for comparing deterministic methods (Richardson, SCPR, etc.) with scale-integrated techniques from material science, thus moving toward a unified framework for fractal quantification across scientific domains.

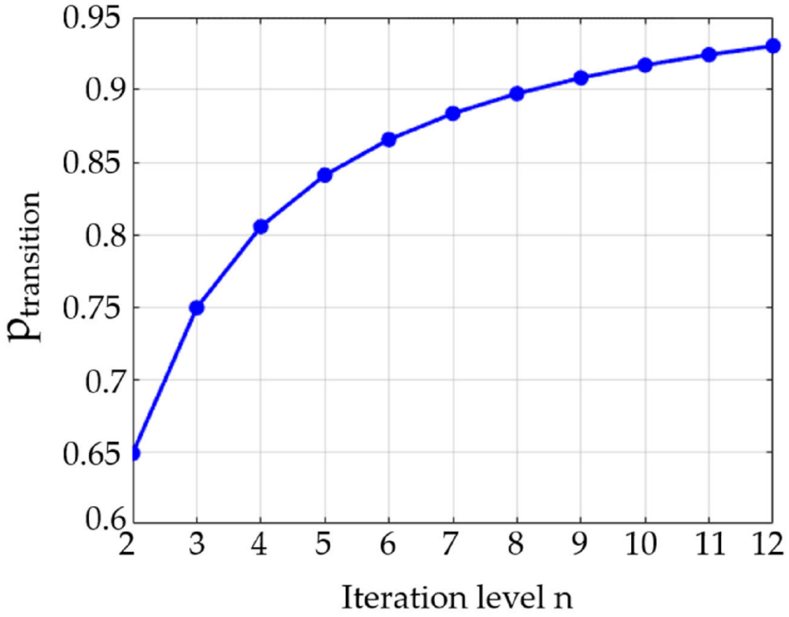

Figure A2. Critical probability $p_{transition}$ at which the effective dimension α(p,n) reaches that of the deterministic Koch curve.

Appendix B. Algorithmic Schema of Richardson's Method

This appendix provides a step-by-step schematic description of the Richardson–Mandelbrot method for estimating the fractal dimension of planar curves. The method is based on measuring the perimeter of an object at various scales using yardsticks of decreasing size.

We provide below a generalized version of the algorithm applicable to digital images or parametric curves.

Appendix B.1. Algorithm: Richardson–Mandelbrot (Compass) Method

The process of estimating the fractal dimension of a two-dimensional boundary begins with the input of either a binary image or a parametric curve representing the contour to be analyzed. A set of yardstick sizes η_i within a specified range [η_min, η_max], expressed in pixels or normalized units, is then applied. By measuring the boundary's length at each scale and observing how this length changes with respect to the yardstick size, one can estimate the fractal dimension D, which quantifies the geometric complexity of the contour across scales (Figure A3).

Step-by-step procedure:

1. Preprocessing
    - Extract the boundary or contour of the object (e.g., via edge detection or marching squares).
    - Represent the contour as a sequence of ordered points $\{x_k\}_{ik=1}^{N}$
2. Select yardstick sizes
    - Define a set of scales $\eta_1, \eta_2, \ldots, \eta_n$, typically logarithmically spaced.
    - Ensure η_{min} is above image resolution noise, and η_{max} below the object size.
3. Traverse the contour with each yardstick

   - For each η_i, walk along the curve using a ruler of fixed length η_i, placing steps of this size end to end.
   - Count the number of steps $N(\eta_i)$ needed to traverse the full contour.
4. Compute effective perimeter
   - Approximate the perimeter as $P(\eta_i) = N(\eta_i).\eta_i$.
5. Log–log regression
   - Fit a linear regression of $\log P(\eta_i)$ vs. $\log(\eta_i)$.
   - The slope s yields the fractal dimension: $D = 1 - s$

The Figure A4 presents five realizations of the Von Koch snowflake, constructed through recursive subdivision of an equilateral triangle using the classical deterministic algorithm. At each iteration, every segment is replaced by four smaller segments forming a triangular "bump," which is consistently applied when the probability parameter is set to $p = 1$. As expected, all realizations are geometrically identical, since the probabilistic mechanism is inactive in this configuration. This scenario represents the theoretical limit of maximal fractal development, where the expected fractal dimension reaches 1.2619. The Figure A5 displays perimeter measurements obtained from multiple realizations of the same underlying geometry, with each point in the plot corresponding to a distinct realization. The data reveal a clear power-law relationship across several orders of magnitude, from which the fractal dimension is estimated using linear regression, following the relation $D = 1 - \text{slope}$. In this case, the estimated fractal dimension slightly exceeds the theoretical value of the Koch curve ($D = \log(4)/\log(3) \approx 1.2619$), with observed values around $D \approx 1.31$—likely attributable to resolution and discretization effects.

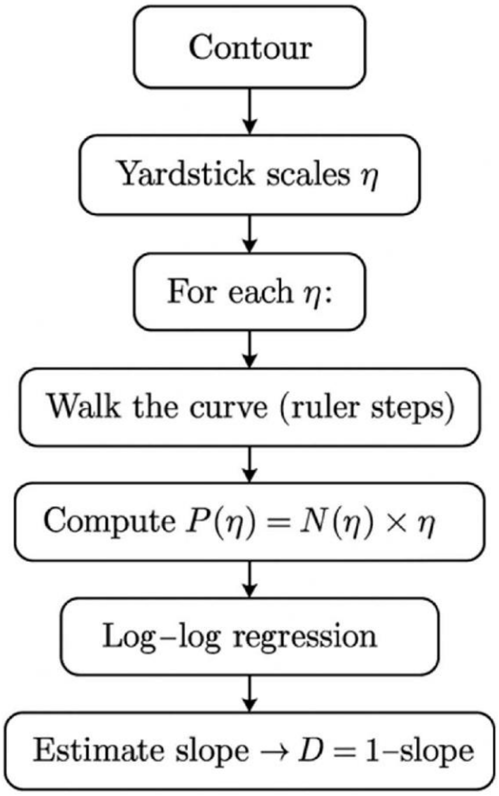

Figure A3. Algorithmic schema of Richardson's method.

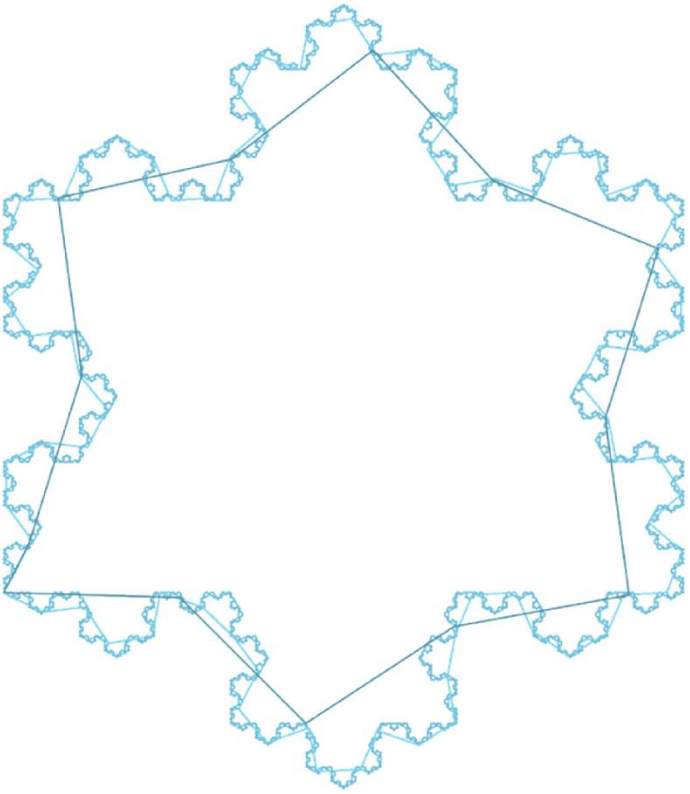

Figure A4. Deterministic construction of the Von Koch snowflake at successive iterations.

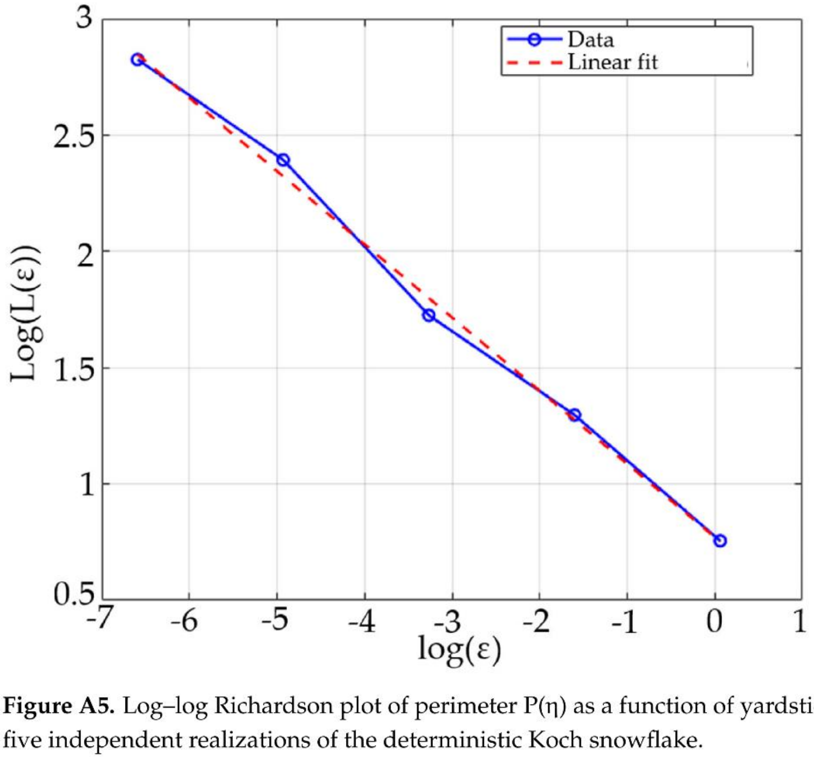

Figure A5. Log–log Richardson plot of perimeter P(η) as a function of yardstick size η, measured on five independent realizations of the deterministic Koch snowflake.

References

1. Mandelbrot, B.B. *The Fractal Geometry of Nature*; WH Freeman: New York, NY, USA, 1982; Volume 1.
2. Li, J.; Du, Q.; Sun, C. An Improved Box-Counting Method for Image Fractal Dimension Estimation. *Pattern Recognit.* **2009**, *42*, 2460–2469. [CrossRef]
3. Zhang, Z.; Wu, W.; Sun, C.; Wang, C. Seizure Detection via Deterministic Learning Feature Extraction. *Pattern Recognit.* **2024**, *153*, 110466. [CrossRef]

4. Theodoridis, S.; Koutroumbas, K. *Pattern Recognition*; Elsevier: San Diego, CA, USA, 2006; ISBN 978-0-08-051361-4.
5. Zhu, G.; Li, J.; Guo, Y. Separate First, Then Segment: An Integrity Segmentation Network for Salient Object Detection. *Pattern Recognit.* **2024**, *150*, 110328. [CrossRef]
6. Tricot, C. *Courbes et Dimension Fractale*; Springer Science & Business Media: Berlin/Heidelberg, Germany, 1999.
7. Falcão, A.X.; Stolfi, J.; de Alencar Lotufo, R. The Image Foresting Transform: Theory, Algorithms, and Applications. *IEEE Trans. Pattern Anal. Mach. Intell.* **2004**, *26*, 19–29. [CrossRef] [PubMed]
8. Plotze, R.D.O.; Falvo, M.; Pádua, J.G.; Bernacci, L.C.; Vieira, M.L.C.; Oliveira, G.C.X.; Bruno, O.M. Leaf Shape Analysis Using the Multiscale Minkowski Fractal Dimension, a New Morphometric Method: A Study with *Passiflora* (Passifloraceae). *Can. J. Bot.* **2005**, *83*, 287–301. [CrossRef]
9. Bouridane, A.; Alexander, A.; Nibouche, M.; Crookes, D. Application of Fractals to the Detection and Classification of Shoeprints. In Proceedings of the 2000 International Conference on Image Processing (Cat. No.00CH37101), Vancouver, BC, Canada, 10–13 September 2000; Volume 1, pp. 474–477.
10. Shivakumara, P.; Wu, L.; Lu, T.; Tan, C.L.; Blumenstein, M.; Anami, B.S. Fractals Based Multi-Oriented Text Detection System for Recognition in Mobile Video Images. *Pattern Recognit.* **2017**, *68*, 158–174. [CrossRef]
11. Backes, A.R.; Bruno, O.M. Shape Classification Using Complex Network and Multi-Scale Fractal Dimension. *Pattern Recognit. Lett.* **2010**, *31*, 44–51. [CrossRef]
12. Torres, R.d.S.; Falcão, A.X.; Costa, L.d.F. A Graph-Based Approach for Multiscale Shape Analysis. *Pattern Recognit.* **2004**, *37*, 1163–1174. [CrossRef]
13. Koch, H.V. Sur Une Courbe Continue sans Tangente, Obtenue Par Une Construction Géométrique Élémentaire. *Ark. Mat. Astr. Fys.* **1904**, *1*, 681–704.
14. Meisel, L.V.; Johnson, M.A. Convergence of Numerical Box-Counting and Correlation Integral Multifractal Analysis Tech-niques. *Pattern Recognit.* **1997**, *30*, 1565–1570. [CrossRef]
15. Mathur, V.; Gupta, M. Morphology of Koch Fractal Antenna. *J. Int. J. Comput. Technol.* **2014**, *13*, 4157–4163. [CrossRef]
16. Arqub, O.A.; Abo-Hammour, Z. Numerical Solution of Systems of Second-Order Boundary Value Problems Using Continuous Genetic Algorithm. *Inf. Sci.* **2014**, *279*, 396–415. [CrossRef]
17. Abo-Hammour, Z.; Arqub, O.A.; Momani, S.; Shawagfeh, N. Optimization Solution of Troesch's and Bratu's Problems of Ordinary Type Using Novel Continuous Genetic Algorithm. *Discrete Dyn. Nat. Soc.* **2014**, *2014*, 401696. [CrossRef]
18. Carr, J.R.; Benzer, W.B. On the Practice of Estimating Fractal Dimension. *Math. Geol.* **1991**, *23*, 945–958. [CrossRef]
19. Russ, J.C. *Fractal Surfaces*; Springer Science & Business Media: Berlin/Heidelberg, Germany, 2013; ISBN 1-4899-2578-3.
20. Dubuc, B.; Dubuc, S. Error Bounds on the Estimation of Fractal Dimension. *SIAM J. Numer. Anal.* **1996**, *33*, 602–626. [CrossRef]
21. Taylor, C.C.; Taylor, J. Estimating the Dimension of a Fractal. *J. R. Stat. Soc. Ser. B Methodol.* **1991**, *53*, 353–364. [CrossRef]
22. Brown, C.A. Areal Fractal Methods. In *Characterisation of Areal Surface Texture*; Leach, R., Ed.; Springer: Berlin/Heidelberg, Germany, 2013; pp. 129–153. ISBN 978-3-642-36458-7.
23. Mandelbrot, B. How Long Is the Coast of Britain? Statistical Self-Similarity and Fractional Dimension. *Science* **1967**, *156*, 636–638. [CrossRef]
24. Berkmans, F.; Lemesle, J.; Guibert, R.; Wieczorowski, M.; Brown, C.; Bigerelle, M. Two 3D Fractal-Based Approaches for Topographical Characterization: Richardson Patchwork versus Sdr. *Materials* **2024**, *17*, 2386. [CrossRef]
25. Bigerelle, M.; Iost, A. Perimeter Analysis of the Von Koch Island, Application to the Evolution of Grain Boundaries during Heating. *J. Mater. Sci.* **2006**, *41*, 2509–2516. [CrossRef]
26. Richardson, L.F. The Problem of Contiguity: An Appendix to Statistics of Deadly Quarrels. *Gen. Syst. Yearb.* **1961**, *6*, 139–187.
27. Kong, H.-Y. Research on Principle of Bubble Electrospinning and Morphologies Controlling and Applications of Bubble Electrospun Nanofibers. Ph.D. Thesis, Soochow University, Suzhou, China, 2015. [CrossRef]
28. He, C.-H.; Liu, H.-W.; Liu, C. A Fractal-Based Approach to the Mechanical Properties of Recycled Aggregate Concretes. *Facta Univ. Ser. Mech. Eng.* **2024**, *22*, 329–342. [CrossRef]

3.4 Conclusion of the chapter

By dissecting the Koch snowflake, an ideal curve with a known analytical dimension, we have shown that sampling density, indentation angle and mesh topology each introduce systematic bias into estimated fractal metrics. The error model derived here yields two practical outcomes. First, it defines a *safe-resolution envelope*: a minimum of 12 nodes per indentation cycle keeps the relative error on the fractal dimension below 2 %, regardless of curve depth. Second, it validates a Gaussian low-pass pre-filter as the most effective way to suppress aliasing without erasing scale information.

With these calibrations in hand, the thesis can now advance from synthetic geometry to real, textured surfaces. Chapter 4 will embed the Gaussian filter inside a multi-scale Sdr protocol, applying it to turned and blasted metal so that the complexity measured reflects intrinsic morphology rather than discretisation artefacts. In SIAS terms, we are crossing the threshold from the *visual-syntax* tier, where complexity is first recognised, to the *quantitative-evaluation* tier, where that complexity becomes a reliable numerical descriptor usable across engineering and heritage domains.

Chapter 4

New Fractal-based Method

Using the Sdr parameters from ISO 25178-2 and Gaussian filter

Prolegomena of the chapter 4

Standing firmly on the “quantitative-evaluation” tier of the Surface-Information Acquisition Spectrum (SIAS), Chapter 4 forges the methodological bridge between the thesis’s two preceding chapters: the heraldic study that formalised visual complexity (Chapter 2) and the Koch-snowflake investigation that quantified sampling-induced bias (Chapter 3). Here, we translate those theoretical lessons into an operational protocol for *real* surfaces, coupling the ISO-25178-2 Sdr extension parameter with a multi-scale Gaussian filter to generate a scale-dependent relative area analysis. By calibrating filter bandwidth with the error model established for synthetic curves, the chapter ensures that the dimensional estimates reflect genuine morphology rather than discretisation artefacts. Bootstrap uncertainty analysis positioning it as the core quantitative tool that the subsequent case studies, Van Gogh’s impastos will exploit to unify artistic perception and metrological rigour.

4.1 Bootstrap methodology

One of the statistical methods used to process measurement results is called Bootstrap. Introduced by Efron in the field of statistics in 1979 [129,130], this method quickly became widely applied in many fields. The Bootstrap method relies on treating the available sample data as a proxy for the population to approximate the sampling distribution of a statistic. This is achieved by resampling with replacement from the original dataset, generating numerous Bootstrap samples (typically in the thousands). A statistical measure is then calculated for each of these samples, and the distribution of these values, visualized as a histogram, is known as the Bootstrap distribution of the statistic (Figure 4.1).

Let q be a population parameter to be estimated, and $\hat{q}$ the estimator computed from a sample of size n, such as the median or the mean. According to the Central Limit Theorem (CLT), when n is large, the distribution of $\hat{q}$ is approximately normal, centred at q, with a standard error of the form $\frac{\alpha}{\sqrt{n}}$, where α depends on the population and the estimator. However, when q is complex (e.g., median, correlation), the standard error is difficult to compute analytically. The Bootstrap overcomes this issue by generating multiple Bootstrap samples from the observed data and recalculating $\hat{q}B$ for each of them. The distribution of the obtained $\hat{q}B$, known as the Bootstrap distribution, converges to the theoretical distribution of $\hat{q}$, thus validating the Bootstrap CLT. Moreover, if we consider the standardized statistic $(\hat{q} - q)/SE$ where SE is the standard error, the Bootstrap allows for a second-order correction, providing a more accurate approximation of the limiting distribution, especially for small samples. Finally, in the specific case of the mean $\hat{q} = \overline{X}$, the Bootstrap variance $\hat{\sigma}_B^2 = \frac{1}{B}\sum_{i=1}^{B}(\bar{X}_i - \bar{X})^2$ offers a robust estimation of the standard error, making this method particularly useful in practice.

In surface topography characterization, the Bootstrap method is used in multiple ways. One approach is to resample with replacement the roughness parameter values obtained from surface measurements. This allows for a better estimation of statistical uncertainties, the stability of roughness descriptors, and the confidence intervals associated with the measured parameters. It should be noted that Bootstrap can be applied not only to simple distributions but also to pairs and residuals.

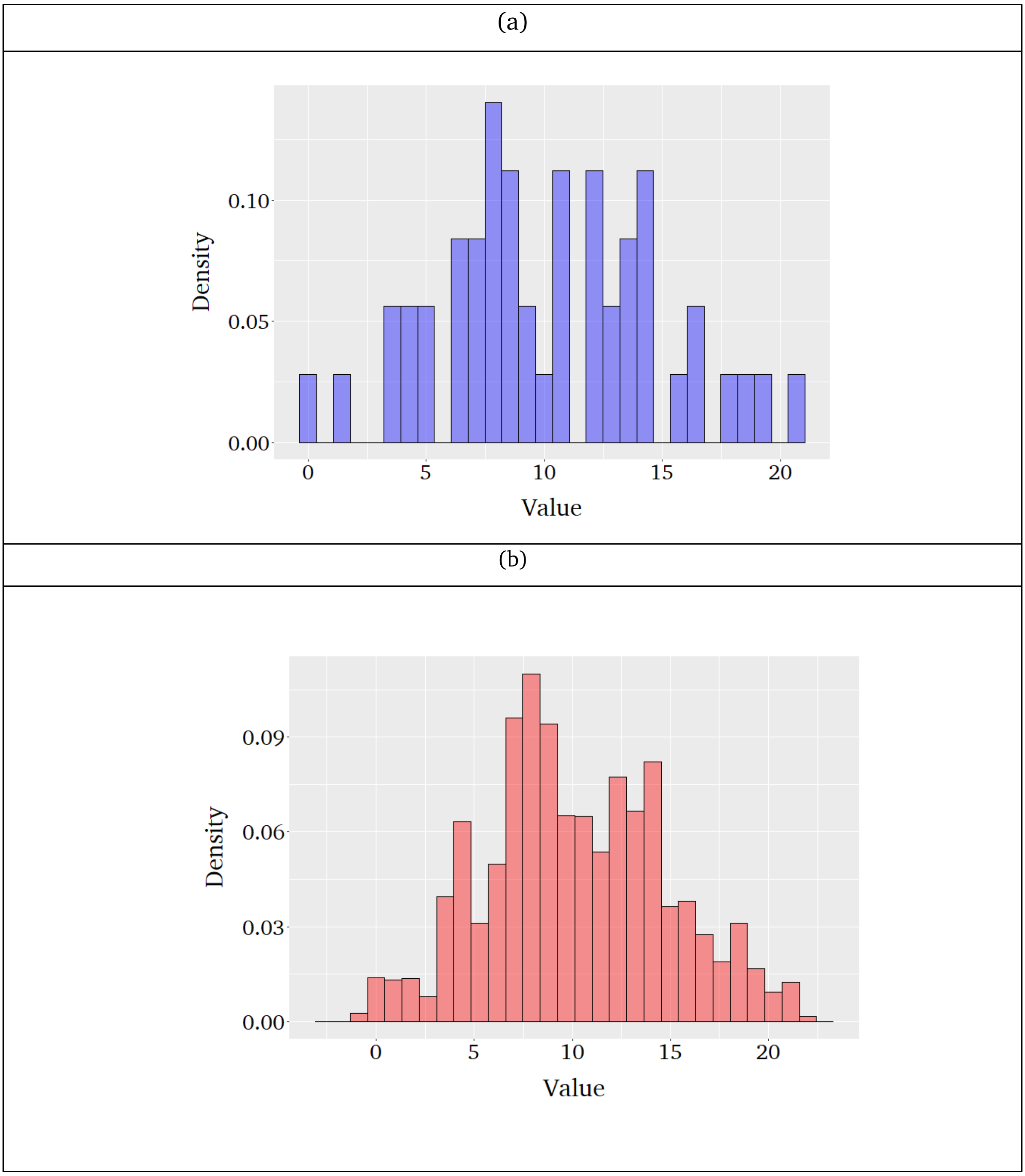

Figure 4.1 *(a) Original distribution of 50 random values from a variable with a mean of 10 and standard deviation of 5. (b) distribution of 100000 Bootstrap replications based on the original distribution*

4.2 Analysis of Variance (ANOVA)

When analysing surface roughness, there are quantity of parameters that geometrically describe the topography termed by Whitehouse as “parameter rash” [131]. It is necessary to find the most discriminating parameter that best differentiates between groups of surfaces. ANOVA is a statistical analysis method used to compare the means of several groups to determine if at least one mean is different from the others. It evaluates the effect of one or more qualitative variables (factors) on a quantitative variable (dependent variable). The qualitative variables are called factors, and each factor can have multiple levels (or modalities). ANOVA allows for the study of the main effects of these factors as well as the interactions between them.

For example, in a surface study, one can analyse the evolution of a parameter based on the blasting media of a surface, with three modalities: small glass beads (70-150 μm), large glass beads (150-250 μm), and fragments of crystallized alumina also known as corundum (200-300 μm). The factor 'blasting media' is considered a qualitative variable, and its effect on a quantitative surface parameter, such as roughness (Sa), can be studied.

In this case, a one-factor ANOVA is used to analyse the dependence of the quantitative variable (surface parameter) on the factor 'blasting media'. The test involves verifying whether the mean of the quantitative variable is homogeneous across the different modalities of the factor. The F-test of Fisher compares the inter-group variance (between groups) to the intra-group variance (within groups). If the ratio of these variances (F-ratio) is significantly different from 1, the null hypothesis of equal means is rejected, indicating that at least one group mean is different from the others. The analysis of variance thus determines whether the studied dependence is significant for the factor considered. To better understand the ANOVA process, we can visualize it through several key graphs using our example of sandblasted samples. First, a box plot can be created to display the distribution of roughness values (Sa) for each type of blasting media (Figure 4.2). This plot helps to identify the median, quartiles, and any outliers within the data, providing a clear overview of how the roughness values vary across different media types. Next, we can enhance the visualization by adding error bars to the box plot, which represent the standard deviation (Figure 4.3). These error bars provide additional insight into the variability of the roughness values for each media type, allowing us to assess the consistency and reliability of the measurements. By examining the error bars, we can determine if there are significant differences in roughness values between the different media types.

Finally, to ensure the validity of our ANOVA results, we can visualize the residuals (Figure 4.4). This involves plotting the residuals to check for homogeneity of variances and normality. By analysing the residual plot, we can identify any patterns or deviations that might indicate violations of the ANOVA assumptions. A well-distributed residual plot with no clear patterns suggests that the variances are homogeneous, and the residuals are normally distributed, confirming the robustness of our ANOVA findings.

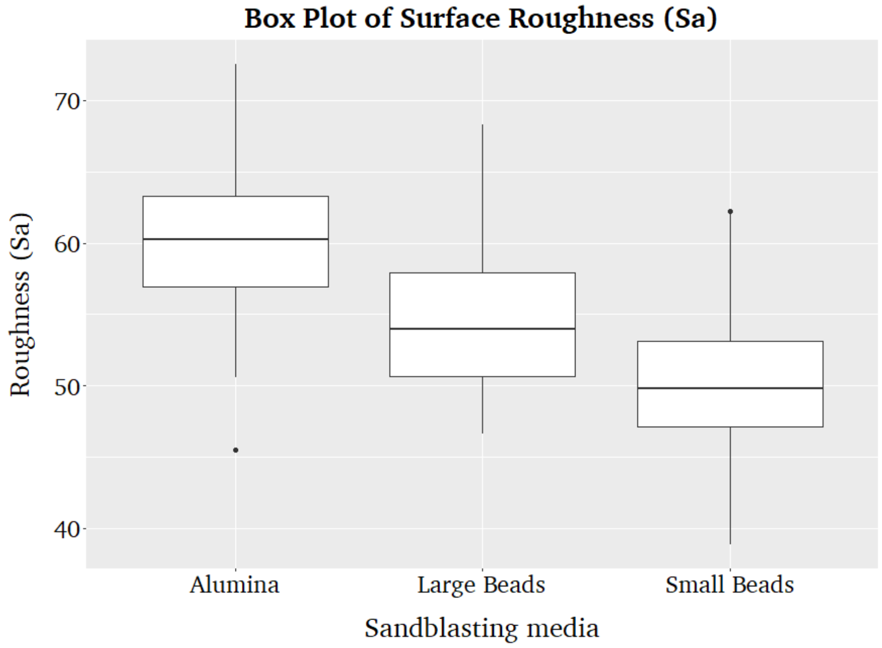

Figure 4.2 *Distribution of roughness values (Sa) for each type of media*

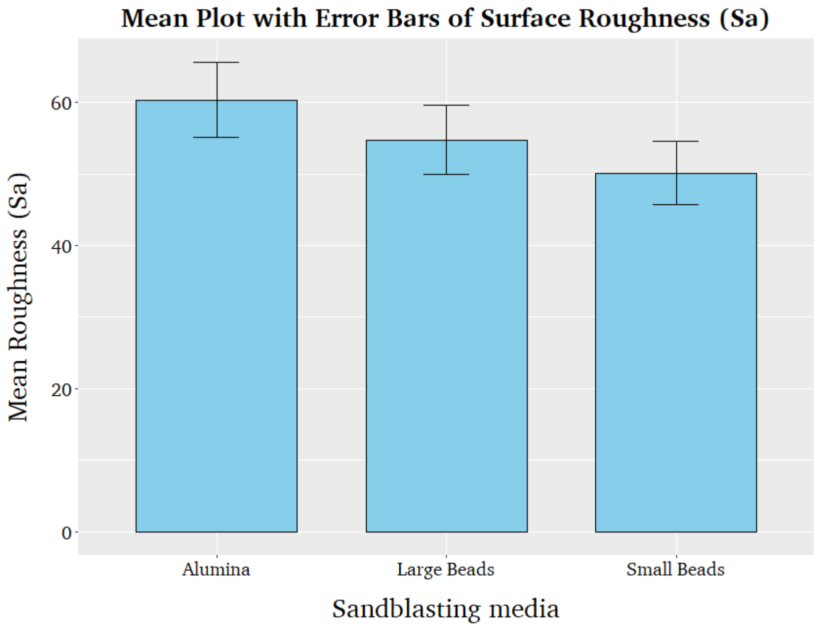

Figure 4.3 *Mean of roughness values for every type of media with error bars*

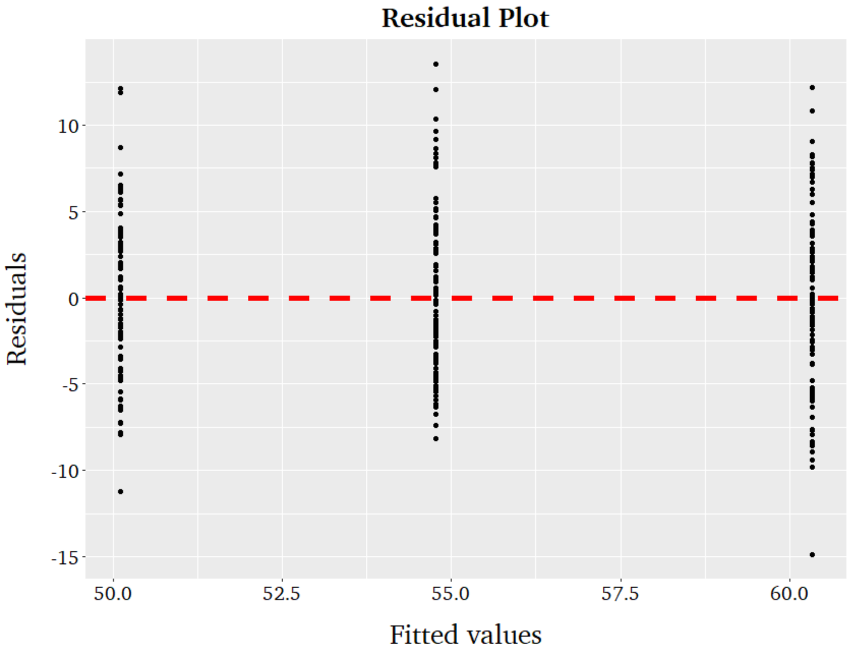

Figure 4.4 *Distribution of the residuals*

Although considered a discriminating parameter, the question remains whether the Sa parameter, present in the ISO 25178-2 standard, is the most discriminating for characterizing the morphological difference between surfaces. Indeed, other parameters such as Sdq or Sdr may be good candidates for better characterizing the difference between the various modalities of the factor(s). Therefore, it will be necessary to perform ANOVA tests, taking each parameter one by one as the dependent variable, and then compare the results of the Fisher tests. The higher the F-value, the more significant the difference between the groups will be.

4.3 Two 3D fractal-based approaches for topographical characterization: Richardson Patchwork versus Sdr

materials

MDPI

Article

Two 3D Fractal-Based Approaches for Topographical Characterization: Richardson Patchwork versus Sdr

François Berkmans [1,2,3], Julie Lemesle [4,5], Robin Guibert [1], Michał Wieczorowski [2], Christopher Brown [6] and Maxence Bigerelle [1,*]

[1] CNRS, UMR 8201-LAMIH-Laboratoire d'Automatique de Mécanique et d'Informatique Industrielles et Humaines, University Polytechnique Hauts-de-France, F-59313 Valenciennes, France; francois.berkmans@uphf.fr (F.B.); robin.guibert@uphf.fr (R.G.)
[2] Institute of Mechanical Technology, Poznan University of Technology, Plac Marii Sklodowskiej-Curie 5, 60-965 Poznan, Poland; michal.wieczorowski@put.poznan.pl
[3] LARSH—Laboratoire de Recherche Societes & Humanites, INSA Hauts-de-France, University Polytechnique Hauts-de-France, F-59313 Valenciennes, France
[4] VALUTEC, University Polytechnique Hauts-de-France, CEDEX 9, F-59314 Valenciennes, France; julie.lemesle@uphf.fr
[5] U.R Concept, 59300 Valenciennes, France
[6] Surface Metrology Laboratory, Worcester Polytechnic Institute, Worcester, MA 01609, USA; brown@wpi.edu
* Correspondence: maxence.bigerelle@uphf.fr

Abstract: Various methods exist for multiscale characterization of surface topographies, each offering unique insights and applications. The study focuses on fractal-based approaches, distinguishing themselves by leveraging fractals to analyze surface complexity. Specifically, the Richardson Patchwork method, used in the ASME B46.1 and ISO 25178 standards, is compared to the Sdr parameter derived from ISO 25178-2, with a low-pass Gaussian filter for multiscale characterization. The comparison is performed from the relative area calculated on topographies of TA6V samples grit blasted with different pressures and blasting materials (media). The surfaces obtained by grit blasting have fractal-like characteristics over the scales studied, enabling the analysis of area development at multiple levels based on pressure and media. The relative area is similar for both methods, regardless of the complexity of the topographies. The relevance scale for each calculation method that significantly represents the effect of grit blasting pressure on the increased value of the relative area is a tiling of 7657.64 µm² of triangle area for the Patchwork method and a 124.6 µm cut-off for the low-pass Gaussian filter of the Sdr method. These results could facilitate a standard, friendly, new fractal method for multiscale characterization of the relative area.

Keywords: multiscale analysis; surface topography; fractal-based analysis; Sdr parameter

check for updates

Citation: Berkmans, F.; Lemesle, J.; Guibert, R.; Wieczorowski, M.; Brown, C.; Bigerelle, M. Two 3D Fractal-Based Approaches for Topographical Characterization: Richardson Patchwork versus Sdr. *Materials* **2024**, *17*, 2386. https://doi.org/10.3390/ma17102386

Academic Editor: Silvio Genna

Received: 18 April 2024
Revised: 8 May 2024
Accepted: 13 May 2024
Published: 16 May 2024

1. Introduction

Multiscale characterization enables the analysis of surface features present at different scales and facilitates a functional understanding of the relationships between the processing and performance of a surface and its topography. Considering that geometric properties of rough surfaces can differ considerably, there are several multiscale calculation methods [1]. For each method, the application and insights regarding a surface can vary. The use of different multiscale characterization methods depends on several factors. Firstly, the geometry of surface topography may favor one approach over another, as in the case between isotropic and anisotropic surfaces [2,3]. Furthermore, the variety of research domains reflects specific needs that may influence the choice of multiscale calculation methods, i.e., the nature of the geometric characterization should be pertinent to the application [4]. Lastly, choices may be related to algorithmic complexity, which can significantly lengthen characterization depending on the method used. Guibert et al. [5] provided a comparison between three of these methods, discussing the advantages and disadvantages of each method for characterizing polymer abrasion. Multiscale characterization methods, based on fractals or not, employ different mathematical principles to analyze phenomena at various scales. Wavelets, Fourrier series decompositions, power spectral densities and bandpass filters are some examples of non-fractal methods as summarized in the review written by Brown et al. [1]. In this paper, fractal-based methods [6,7] are specifically studied.

The term 'fractal', introduced by Mandelbrot in 1975, is used to describe surface topographies that are continuous but not differentiable, with a self-similar or self-affine structure relative to scale [8]. Fractals have shapes or features that can be iterated at different scales. The surfaces of objects can be described mathematically using classical geometry formulas. However, at finer scales, the surface microgeometries can become stochastic and self-similar, like collections of littler scratches on bigger ones, suggesting characterizations through recipes or recursive algorithms. To model and characterize stochastic surfaces, it is necessary to use fractal models to determine the fractal dimensions of topographies. The fractal dimension is used to characterize the complexity of surface topographies. Different methods have been developed to determine different kinds of fractal dimensions [9–11]. Fractal methods have been used to simulate chaotic surfaces and to characterize measured surfaces. These models are used to model surface interactions. One method is based on the Weierstrass–Mandelbrot function [12–15]. This function provides a simulated surface with adjustable parameters, allowing for the desired complexity in applications modeling the size and number of multiscale contacts [13]. In surface analysis, it is possible to analyze the fractal dimensions of surfaces in the forms of 2D or 3D profiles. The methods for analyzing 2D profiles are called length–scale, Richardson or coastline analyses, and it is possible to calculate the relative length. Richardson's study on the coastlines of Britain, later expanded upon by Mandelbrot [16], is a well-known example. In summary, relative lengths depend on the scale of the observation or calculation. To calculate the relative length of a 2D surface profile, the scale is determined by the size of compasses or dividers that follow the surface profile (Figure 1). The smaller the size of these dividers, the greater their number becomes, allowing them to calculate more details on the profile. The relative length is the ratio of the measured to the nominal length. Relative lengths can be represented on a log–log plot against scale (Figure 2). As the scale decreases, the relative lengths begin to deviate from unity. This deviation occurs when the line segments become short compared to the topographical features, causing significant tilting when they land on the valleys and peaks of the profile. When the profile exhibits self-similarity across a range of scales, the logarithm of the relative length shows a linear increase as the logarithm of the scale decreases. The length–scale fractal dimension is determined by subtracting the slope of the length–scale plot from the unity, as specified in ASME B46.1.

To understand the difference between the length scale and area scale, we can conduct a similar study to that of the coastlines of Britain, but this time trying to calculate the area of a mountain land. Area scale analysis involves calculating the areas of surfaces at various scales. Following Richardson's and Mandelbrot's methods, Brown developed a method for calculating the relative area using a 3D triangular tiling with the same philosophy as the relative length with scale variation. Area scale analysis is a type of fractal multiscale analysis. Surfaces containing chaotic elements exhibit scale-dependent variations in their surface areas. The importance of area in understanding performance is emphasized by the fact that many interactions that impact physical functionality are area-dependent. This observation emphasizes the potential of area scale analysis in distinguishing surfaces with different behaviors and in correlating with performance and behavior. The characterization of surface topographies nowadays leans more towards an areal analysis of the surface [17]. Industrial requirements necessitate a deeper understanding of surface features for effective analysis. This goes beyond the limited use of a straight axis for characterizing 2D profiles. To define the development of the relative area of a complex surface (e.g., after sandblasting), where craters may nest within larger craters in a self-similar manner, the fractal area scale method is well suited.

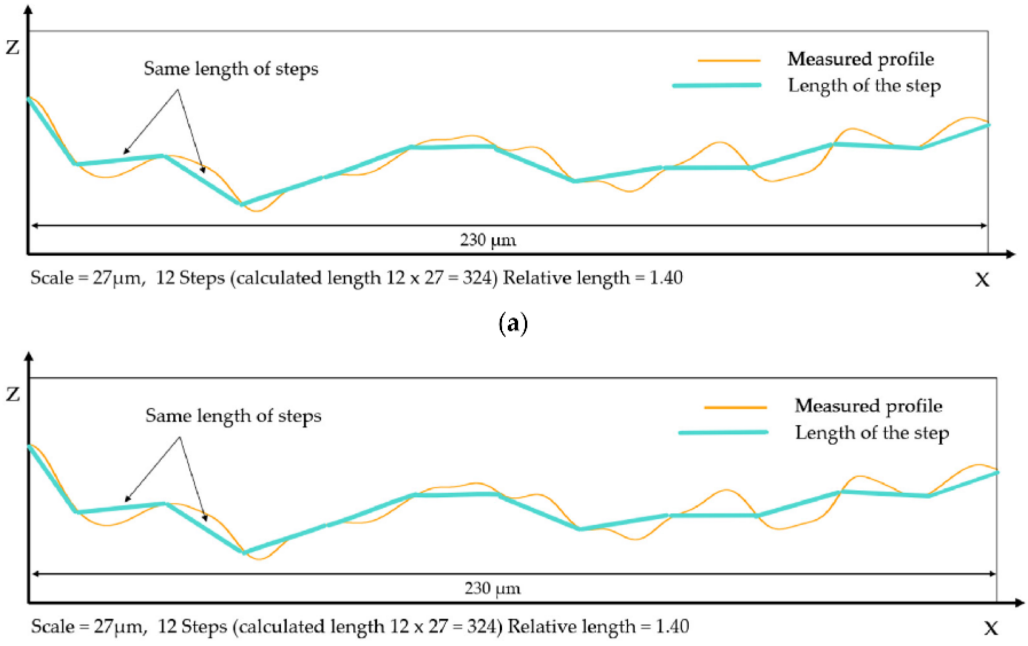

(**a**)

(**b**)

Figure 1. Two calculations of the relative length for two different scales. (**a**) Calculation from a profile view with 4 steps. (**b**) Calculation from a profile view with 12 steps. The calculated length is the sum of the step length multiplied by the number of steps. The nominal length is 230 μm.

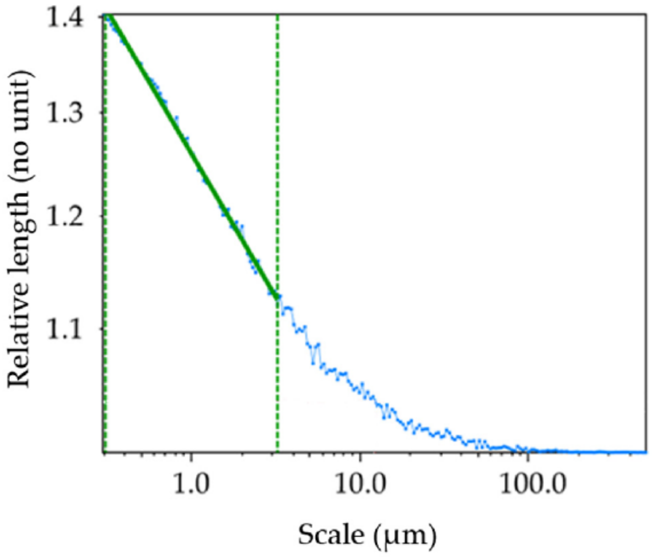

Figure 2. Length–scale plot. The self-similarity over some range of scales is emphasized by the regression line in green. According to ASME B.46, the fractal dimension based on the length scale is 1.095 (no unit). The blue line is the interpolation between the values for the calculation of the relative length on every scale. The dashed green corresponds to the fractal domain, which is the range where the surface is self-similar on different scales.

This study will present two methods for calculating the relative area, in line with the fractal philosophy of area scale computation from Richardson to Mandelbrot: the developed interfacial area ratio (Sdr) parameter (ISO 25178-2 [18]) using a low-pass Gaussian filter (ISO 16610-61 [19]) and the triangular tiling method or Patchwork method. The aim is to introduce a technique for computing the relative area, which leverages two elements commonly found in standards: the Sdr parameter as defined in ISO 25178-2 and a set of low-pass Gaussian filters. The idea is to iterate the calculation of the Sdr parameter using filters to change the scale of calculation. The advantage would be to increase the calculation speed of the relative area for multiscale characterization and to use elements already present in existing surface processing software such as MountainsMap® version 9. This new method would allow for an expansion of the scope of application, as multiscale characterization methods depend on the nature of the surfaces, i.e., a certain method is more suitable for a given surface.

2. Materials and Methods

2.1. Materials

Considering that these characterization methods (Patchwork and Sdr) serve to quantify the developed area of a surface topography, it was necessary to find a way to control the topography using the same process to avoid introducing bias into our further statistical methods. The manufacturing process of the samples and the increasing developed area needed to be correlated to ensure control over the experiment. For this reason, this study presents grit-blasted TA6V logs. Using two factors, namely the grit-blasting media and the pressure of the blaster, it was possible to create a wide range of surfaces and to influence the areal increase due to surface work hardening.

The dimensions of the TA6V logs were a 30 mm diameter and 20 mm height, and they were ground with SiC papers from grit 80 to 4000 before grit blasting. An indentation test was performed on this material to determine its mechanical properties. Ground TA6V surfaces were therefore grit blasted using the Guyson Euroblast 6SF system. Three grit materials were used to blast the TA6V logs:

- two types of micro balls of glass silico–soda–calcium (G 100 (particle size of 70–150 µm) and G 250 (150–250 µm)) from ARENA;
- one abrasion material, named C 300 50/80 (particle size of 100–630 µm) from Semanaz, which was composed of hard, sharp, abrasive crystals manufactured from molten glass mass whose material composition was silicate, alumina and iron oxide.

For each grit material, seven pressures were applied from 2 to 8 bar. A total of 35 TA6V logs were blasted, one set for C 300, one set for G 100 and three sets for G 250, to study the repeatability of the grit blasting process. During grit blasting, the blasting gun/log distance was around 10 cm. The grit materials were shot perpendicularly to the TA6V surface during around 30 s for the pressures from 3 to 8 bar and around one minute for the 2 bar pressure to homogeneously blast the whole surface. The grit materials were shot according to a back-and-forth movement (left to right) from the top to bottom of the surface. The 7 grit blasting pressures allowed for a wide variation in relative surface area. The question of the relevant scale for analyzing this process helped in determining which calculation method presented in this study best discriminated the pressure during the grit blasting.

2.2. Topographical Measurement and Data Post-Processing

Each blasted TA6V surface was measured by white light interferometry with Bruker ContourGT™ (San Jose, CA, USA). A 50× lens was used which corresponded to an elementary image of 127 × 94.9 µm, and 50 zones of 1 × 1 mm^2 (5059 × 5058 pixels, 0.198 µm X/Y resolution) were measured randomly on each surface using stitching (540 elementary images, i.e., 27 rows × 20 columns). A total of 1750 measurements were obtained for the 35 surfaces. The surfaces were post-processed and filtered with the software MountainsMap® (Digital Surf™, Besançon, France). Figure 3 shows the measurements of surface topographies. We exhibit a sample of 3 different pressures out of the 7.

(**a**) (**b**) (**c**)

(**i**) **G 100**

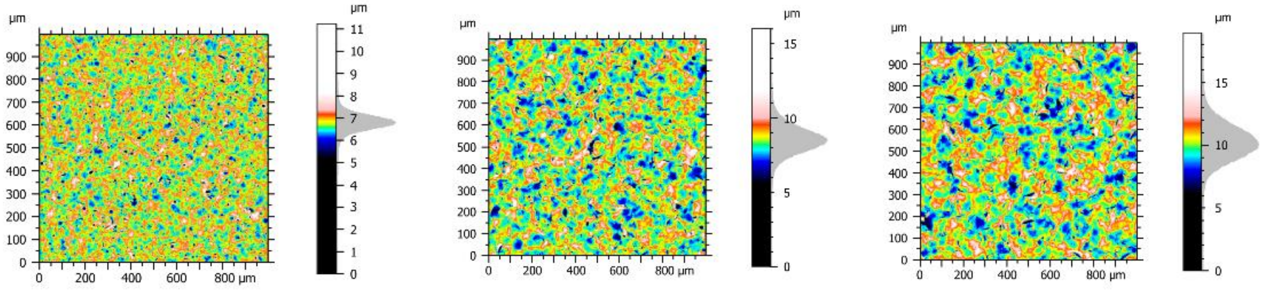

(**ii**) **G 250**

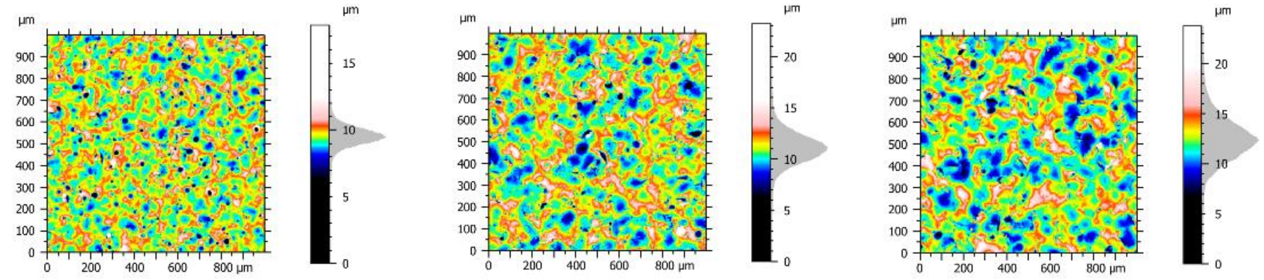

(**iii**) **C 300**

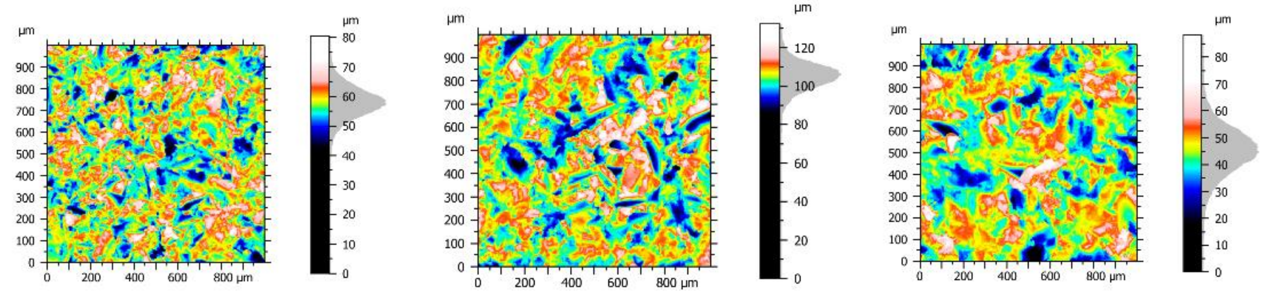

Figure 3. Selection of surface topographies classified by pressure of grit blasting (**a**–**c**) and blasting material (**i**–**iii**). The topographies for the media G 100 (**i**) and G 250 (**ii**) have more circular features considering the spherical nature of the glass beads. The topographies of the C 300 medium (**iii**) have more sharply edged indents due to the angular nature of the corundum.

2.3. Fractal Multiscale Characterization Methods

2.3.1. Method n°1: Patchwork

The first method based on the principle of a developed area is the triangular tiling method, also known as the Patchwork method, which was developed by Brown in the early 1990s [20]. The area, as a function of scale, is determined through a virtual tiling algorithm, such as the one employed in the length–scale analysis (i.e., the coast of Britain). Unlike the length–scale analysis however, which focuses on tiles with line segments, area scale analysis utilizes triangles. Each triangle area serves as a representation of the scale of the calculation. In each tiling instance, all virtual triangles used for tiling have the same area in three dimensions. This places this technique among the methods of fractal analysis based on areal scale. However, when projected onto a datum or nominal XY-plane, the area of these triangles will vary depending on their inclination. The tiling algorithm used in these examples aligns the vertices on the tiling triangles with one of two active rows or columns of heights. These active rows or columns are separated in the *X* or *Y* directions by a distance which is the square root of two times the area of the tiling triangle (Figure 4).

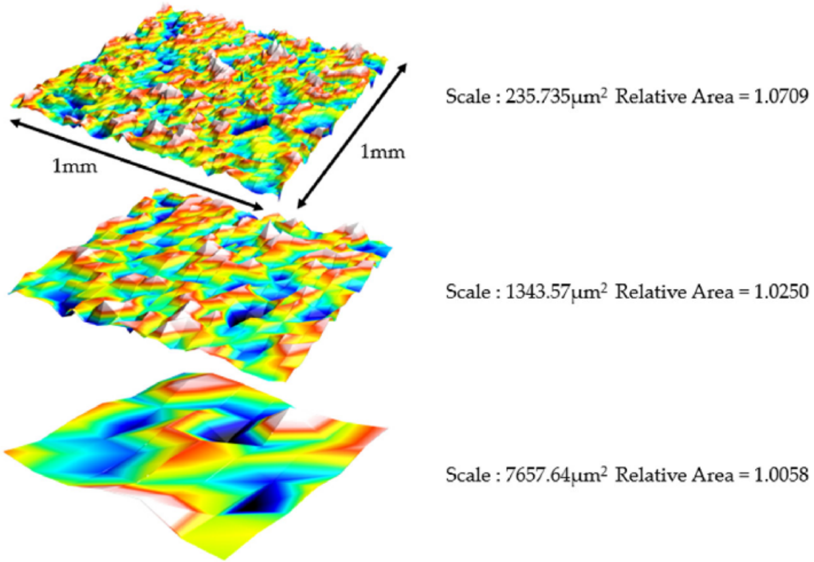

Figure 4. Triangular tiling at three different scales of a TA6V surface grit blasted with the C300 medium and a pressure 8 bar. The scale is the area of the triangular tiles, which have the same area but different projected areas, depending on the inclination.

The Patchwork method uses linear interpolation to precisely position vertices along rows or columns, enabling the creation of triangles with desired areas in a 3D tiling process. It begins by setting initial heights for the first triangle and then interpolates the remaining vertices on a similar scale for subsequent triangles within rows or columns. This tiling process can commence from any corner and progress along rows or columns. The outcomes can then be averaged. At larger scales, this method results in the use of more of the measured heights, thereby potentially offering a more accurate representation of the area at that scale. In 2002, the Patchwork method was introduced into the US standards for defining surface textures, ASME B46.1 [21]. Subsequently, in 2012, area scale analysis was incorporated into ISO 25178-2. However, Brown recommends prioritizing using the method presented in ASME B46 [6]. These methods have been applied in several cases, but it is possible to summarize this by two studies: the complexity of the surface (i.e., fractal dimension) of food impacts how the frying process will occur, as shown by Moreno et al. [22], and the fractality of chocolate using the Patchwork method [19].

2.3.2. Method n°2: Sdr Parameter

Developed Area Principle

The two calculation methods presented in this study are two approaches that initially allow for quantifying roughness through its correlation between the topography of the surface measured with a microscopy system and the projected surface. This ratio is called the developed area (Rs). The principle is summarized in the study of Lange et al. [23], and it is a foundation for quantifying roughness. To calculate a surface area, one must first compute the sum of the areas of elements defined by four adjacent pixels over an entire measurement. To find the parameter Rs, one must divide the sum of the areas of the elements by the projected area. The parameter Rs can be calculated using Equation (1).

$$\mathrm{Rs} = \frac{\text{actual surface area}}{\text{projected surface area}} \tag{1}$$

Plane geometry is employed to determine the surface area of each element. A representative element of area is depicted in Figure 5. The height levels (z) of four adjacent pixels are labeled Z_1–Z_4. The line segments between points are designated as S_{12}, S_{23}, S_{34}, S_{41} and S_{13}. These line segments constitute the sides of two triangles, the areas of which can be calculated. The sum of the two triangular areas offers an approximation of the actual surface bounded by the four adjacent pixels.

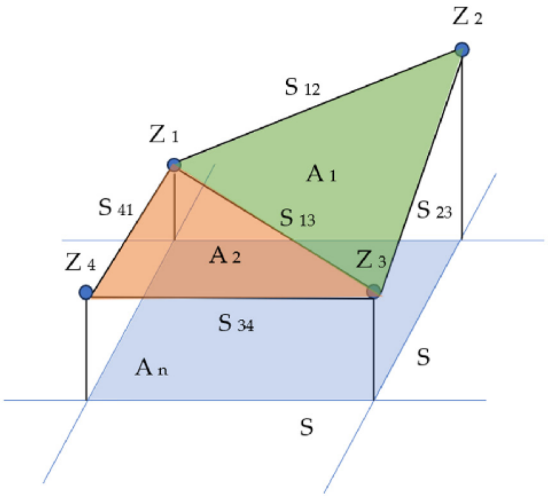

Figure 5. Representation of the four neighboring pixels (Z_1 to Z_4) of the surface topography used to create two triangular areas (A_1 in green and A_2 in orange) with segments (S_{12}, S_{23}, S_{34}, S_{13}, S_{41}) and a comparison on the projected area (A_n in blue).

Sdr Calculation

The Sdr parameter used in this study is a hybrid parameter from the standard ISO 25178-2 [18]. Hybrid parameters use both information present in elevations and their positions to a similar extent. Examples of such hybrid parameters include the arithmetic mean slope, the root mean square slope, the arithmetic mean summit curvature and the area ratio. Hybrid parameters are highly sensitive to scale and their values are influenced by the data resolution [24]. The Sdr parameter calculates the ratio of the incrementation of the developed surface to the sampled surface. The ratio of the developed interfacial area reflects the combined characteristics of surfaces. A high value of this parameter indicates the importance of either the amplitude, spacing or both [25]. The analysis of the Sdr parameter is relevant for studies on wettability, coating and conductivity in the electronics industry. For wettability, according to the study of Werb et al. [26], since the relative increase in total surface area is closely linked to wetting energy, it is expected that this parameter can effectively differentiate between biofilm variants. Initially, the Sdr parameter (ISO 25178-2) is calculated according to Equation (2).

$$\mathrm{Sdr} = \frac{1}{A}\left[\iint_A \left(\sqrt{\left[1+\left(\frac{\partial z(x,y)}{\partial x}\right)^2+\left(\frac{\partial z(x,y)}{\partial y}\right)^2\right]}-1\right)dxdy\right] \tag{2}$$

The Sdr parameter can be expressed as a dimensionless positive number or as a percentage. For instance, a flat and smooth surface would have a value of zero. Essentially, the parameter serves as an indicator of a surface's complexity and is particularly valuable for tracking surface changes across different processing stages. This characteristic also makes it beneficial for adhesion applications. It is important to mention that the parameter is significantly affected by the sampling scheme, including the number of points and the spacing in the X and Y axes [27]. However, a comment needs to be made as the following: the formula presented in the standard implies that the surface is differentiable everywhere, which is not the case with fractal surfaces, as they may exhibit singularities and abrupt variations that are not represented by differentiable functions.

The calculation of Sdr shows a similarity with Equation (1) for calculating the Rs but the difference is that Sdr uses the mean value of two triangulations (Figure 6) and not only one as for the Rs [25] (Equation (3)). The provided equation calculates a representative value, denoted as $A_{i,j}$, for a specific cell in a grid or matrix. In this formula, the distances between the points A, B, C and D in a quadrilateral are computed using vectors. Subsequently, the average lengths of the quadrilateral sides are calculated to obtain the final value. This average is detailed in an expression utilizing the coordinates (x, y) of each point to compute the Euclidean distance between them.

$$\begin{aligned} A_{i,j} &= \frac{1}{2}\left[\left(\frac{1}{2}\left|\overrightarrow{AB}\cdot\overrightarrow{AD}\right| + \frac{1}{2}\left|\overrightarrow{CB}\cdot\overrightarrow{CD}\right|\right) + \left(\frac{1}{2}\left|\overrightarrow{BA}\cdot\overrightarrow{BC}\right| + \frac{1}{2}\left|\overrightarrow{DA}\cdot\overrightarrow{DC}\right|\right)\right] \\ &= \frac{1}{4}\left(\left|\overrightarrow{AB}\right| + \left|\overrightarrow{CD}\right| + \left|\overrightarrow{AD}\right| + \left|\overrightarrow{BC}\right|\right) \\ &= \frac{1}{4}\left\{ \begin{array}{l} \left(\left[\Delta y^2 + \left(z(x_i, y_j) - z(x_{i,}y_{j+1})\right)^2\right]^{\frac{1}{2}} + \left[\Delta y^2 + \left(z(x_{i+1}, y_{j+1}) - z(x_{i+1,}y_j)\right)^2\right]^{\frac{1}{2}}\right). \\ \left(\left[\Delta x^2 + \left(z(x_i, y_j) - z(x_{i+1,}y_j)\right)^2\right]^{\frac{1}{2}} + \left[\Delta y^2 + \left(z(x_i, y_{j+1}) - z(x_{i+1,}y_{j+1})\right)^2\right]^{\frac{1}{2}}\right) \end{array} \right\} \end{aligned} \tag{3}$$

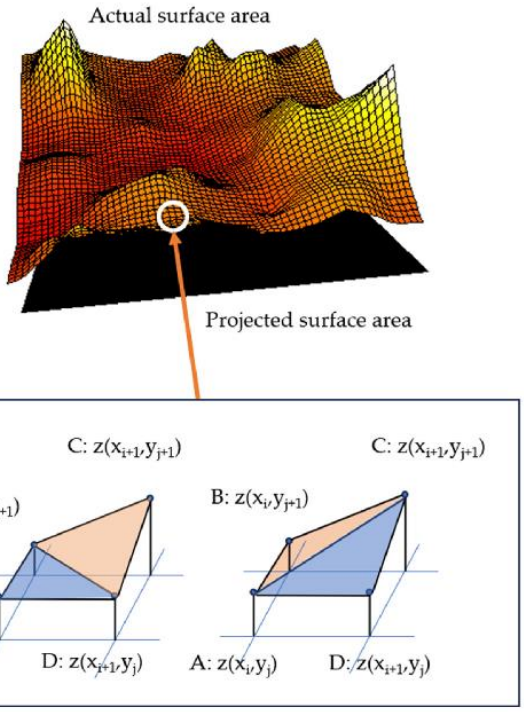

Figure 6. Actual surface area as topography on a given scale (color) on the projected surface area (black). The topography is represented as squares of 4 pixels. The magnification is representing the calculation of the area between four adjacent points (A–D) calculated from the mean value of two triangulations (blue triangles) [25].

The calculation of the developed interfacial area ratio, Sdr, is derived directly from the digitized measured dataset, exclusively at the scale of the sampling interval. It is not initially suitable for estimating a fractal dimension. In essence, it does not represent the genuine developed area since this concept is meaningful only when it is associated with the scales of measurement and computation. Given that the calculation of the Sdr parameter does not currently allow it to be used as a multiscale calculation method, modifications were made. The particularity of this study consisted of varying the scale of the topography during the calculation of Sdr by using a low-pass Gaussian filter, in compliance with the ISO 16610-61 [19] standard. Appendix A presents some filtered surfaces used to visualize the topographical changes according to the cut-off length of the low-pass filtering. The difference between the developed area and relative area is semantic. The developed area expresses the ratio of the Sdr parameter taken at a single scale, whereas as we vary the calculation scales of this ratio, this area becomes relative.

2.3.3. Differences between Both Methods

For a more comprehensive understanding of this study, it is important to highlight the major differences between these two methods. This could be achieved by simplifying and schematizing the comparison, not calculating an area on a 3D profile but rather a length on a 2D profile. The calculation of the developed length for Sdr (Figure 7) was performed by following the sampling rate and summing the length between each point. This method is therefore at a constant pace (kΔx). On the other hand, the Patchwork method operates at a constant length; it is possible to modify the number of steps by reducing their size, thereby better fitting the measured profile.

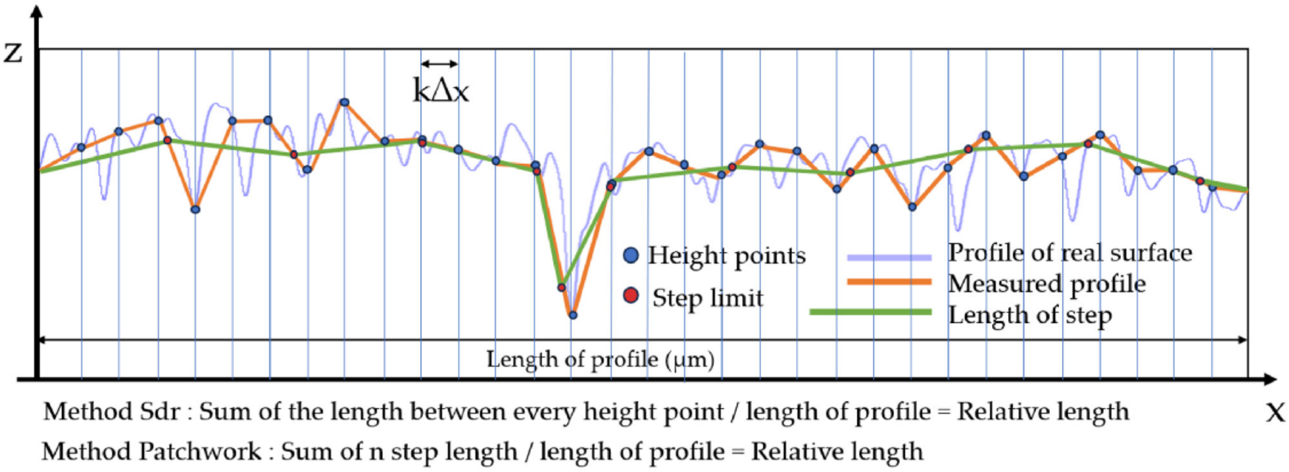

Figure 7. Diagrams of the two calculation methods used in this study for the developed length. The blue line is a representation of a real surface. The orange line is a linear interpolation between measured height points which is our measured profile (the Sdr method was used for computing the relative length at the sampling scale). The green line is a representation of the Patchwork method following the measured profile using the same length steps and sometimes interpolating between measured height points.

2.4. Statistical Analysis

Given the complexity of our factors (pressure, media, scale), directly comparing the means of distributions whose nature was unknown would have been both lengthy and risky. To compare the two methods of the relative area calculation, a robust statistic is required such as the mean and the standard deviation. A bootstrap sampling protocol was therefore used to quantify the variation in distributions of both methods. Bootstrapping is a resampling method that involves drawing repeated samples with replacements from a given dataset to estimate its distribution and assess data variability [28,29]. We replicated the value of the relative area 1000 times for the 50 measurements on all of the TA6V logs. Employing bootstrapping in statistical analysis can offer significant advantages, particularly when one aims to circumvent assumptions about the underlying data distribution, especially in cases where this distribution deviates from a normal distribution. Only based on these assumptions can the correspondence between the Sdr and Patchwork prove to be reliable.

3. Results

The relative area values were calculated from the two methods. The first part of the results aims to establish the reliability of our data, and the second part aims to define a relevance scale to measure the impact of sandblasting on surface geometry. Figure 8 presents the relative areas calculated by both methods on the surfaces obtained with the highest pressure (8 bar) and the hardest material (C 300). It can be observed that at large scales, the relative areas are unified regardless of the method. Whether it was tiling or Gaussian filtering, it did not compute the details of the topography at large scales and resulted in minimal or null changes.

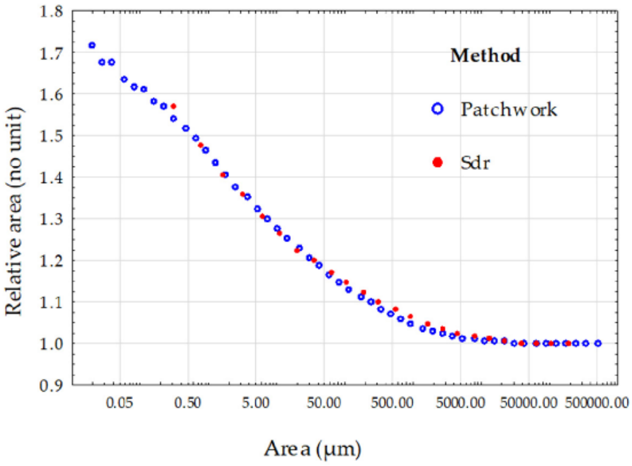

Figure 8. Comparison of the two methods, Sdr and Patchwork, for the calculation of the relative area on the surface topographies created with the C 300 grit-blasting material and a pressure of 8 bar (these are the most aggressive conditions of our material/pressure experimentation). The blue rings represent the values of the relative area calculated by the Patchwork method depending on the size of the triangle tiling (patch area). The red dots represent the calculation of the relative area related to one of the 24 cut-off lengths of the low-pass filter.

To analyze the data distribution, a bootstrapping replication was performed, consisting of 50 measurements on a sample grit blasted with C 300 at 8 bar. Since the results of the relative area varied depending on the size of the triangular area of the tiling, this procedure was repeated three times on different sizes as shown in Figure 9.

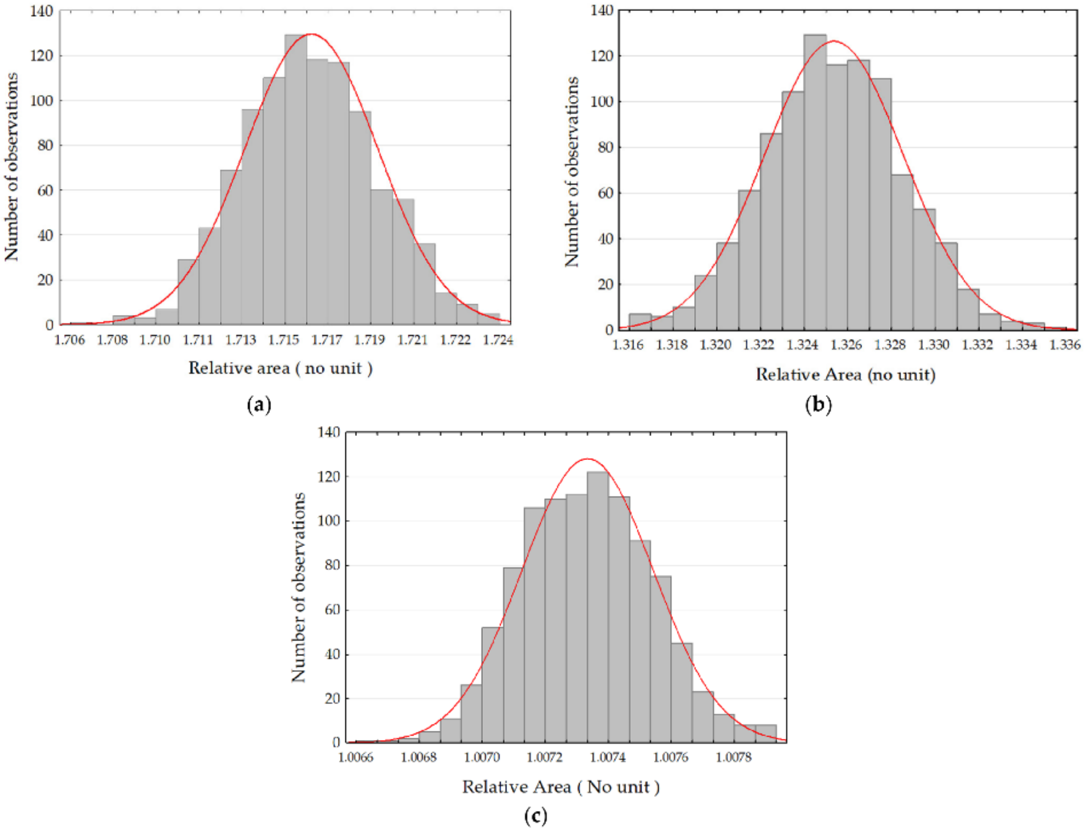

Figure 9. Density probability distributions obtained after applying the bootstrapping protocol to the relative area measurement data. The area of the tiling triangles corresponds to (**a**) 0.02 µm^2, (**b**) 5.124 µm^2 and (**c**) 10,845 µm^2.

The histograms of Figure 9 do not show bias considering the distribution of values for the relative area. It was then possible to analyze the measurement data behavior across all tile sizes. The plot presented in Figure 10a shows the relative area values across all scales of the 50 measurements on the surface obtained by grit blasted with C 300 at 8 bar. The points were replaced by a line to analyze the distribution of each measurement. It can be observed, firstly, that the distribution follows the same trend for each measurement. In Figure 10b, a bootstrap replication was conducted, this time on the relative area measurement values of the 50 measurements, each at every tile scale, echoing the histograms presented in Figure 9. It can be noted that the distribution follows the same trend as Figure 10a, indicative of the stability of the Patchwork method at all scales (i.e., no fundamental changes in the distribution). Figure 10c depicts the average of the curves presented in Figure 10a, compared with Figure 10d, which represents the average of the bootstraps. Both curves are similar, which may indicate that the bootstrapping replication did not significantly alter the mean of the original data. Therefore, it can be assumed that the distribution can give a robust mean.

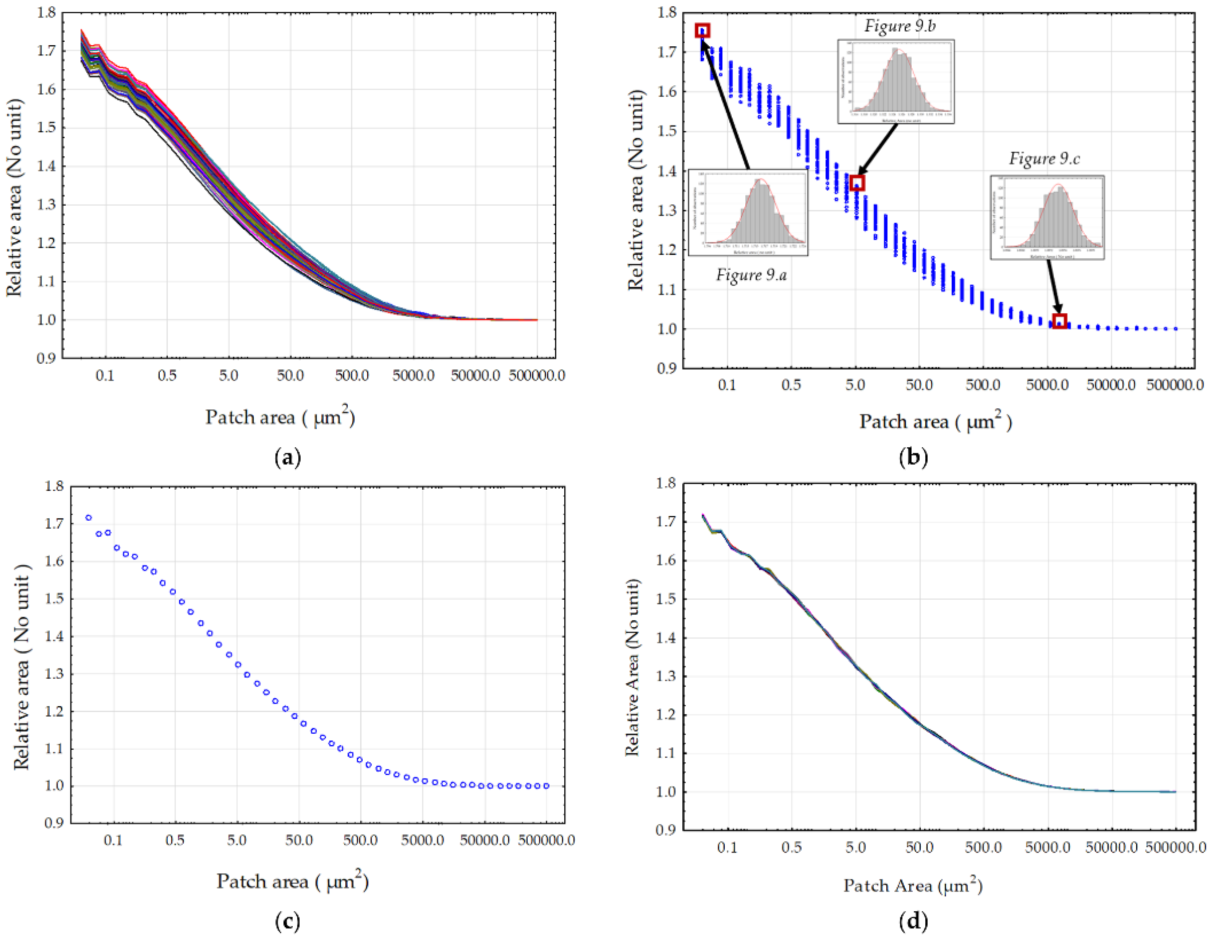

Figure 10. Distributions of the relative area values calculated by the Patchwork method from the 50 measurements of the sample sandblasted at 8 bar with C 300: (**a**) the lines of the 50 sample measurements, (**b**) the values after resampling by bootstrapping, (**c**) the averages of the original measurements and (**d**) the averages of the bootstrapped values.

Finally, a comparison was performed by studying the medians of the distribution values across the 50 measurements by categorizing the calculation method and the pressure (Figure 11). By selecting the medians for each category, it was possible to compare the central tendency among them without being affected by extreme values or differences in dispersion. The first observation drawn from analyzing Figure 11 is the difference in trend regarding material change. There is a greater dispersion of distributions noted for G 100

(Figure 11a) compared to other materials. This is due to the size of the abrasion material G 100 (70–150 µm) which will have a minimal impact on surface topography modification, i.e., the relative area, at low pressures. Conversely, more aggressive materials more easily reach the hardness limit of TA6V due to work hardening, explaining the closer distributions for G 250 (Figure 11b) and even more so for C 300 (Figure 11c). The second observation derived from these graphs (Figure 11) is the systematic correlation between the values calculated using the two methods. The smallest value of the Gaussian filtering cut-off length is about 0.8 µm, which is why the curves of the Sdr method always start from this value. However, the values are still correlated with those of the Patchwork method. The reason why the relative area value at 8 bar (Figure 11b,c) pressure is lower at smaller scales with less pressure is that the work-hardening rate will flatten the surface up to a certain limit, making it a smaller relative area value at smaller scales.

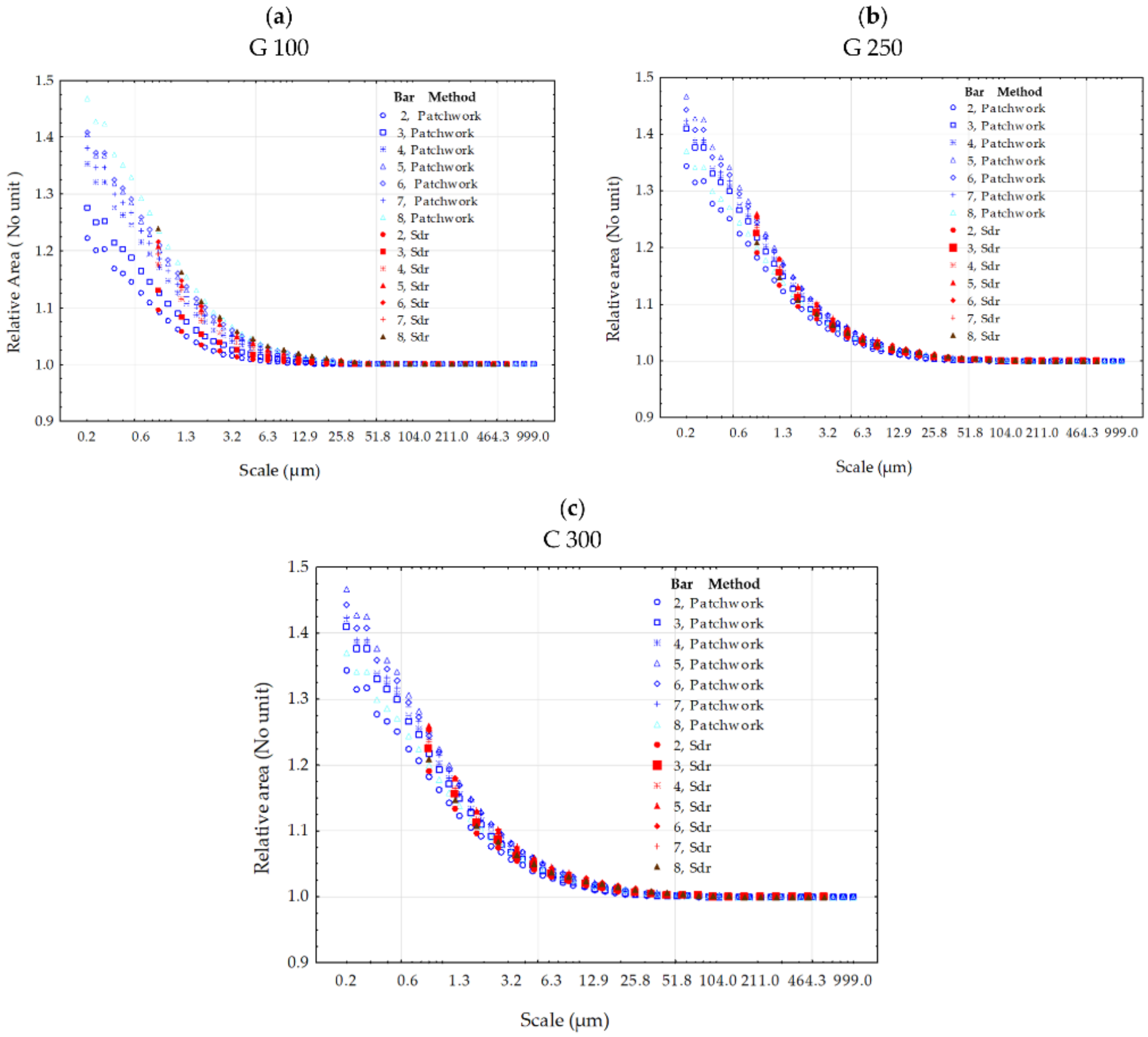
(**a**) G 100
(**b**) G 250
(**c**) C 300

Figure 11. Comparison of the two methods, Sdr and Patchwork, for the calculation of the relative area of the surface topographies created with the grit-blasting materials G 100 (**a**), G 250 (**b**) and C 300 (**c**). The points represent the medians of the distribution of the relative area values, categorized by the calculation method and pressure. The blue symbols represent the median points for the Patchwork method and the red symbols correspond to the Sdr method. The scale references the cut-off length for the low-pass Gaussian filter applied for the Sdr calculation. In this scale, the tiling size in µm^2 for the Patchwork method is equal to the square of the cut-off length divided by 2.

The analysis of the relationship between the blasting pressure and the value of the relative area is consistent. Figure 12 indicates that the distribution of the relative area values varies according to the applied pressure. The higher the pressure, the more complex the surface becomes, and its relative area increases. The distributions between the two calculation methods can be compared at the same scale: the distributions follow the same trends for both methods except for the G 100 media at 7 and 8 bar, but both methods invent for G 250 at 7 and 8 bar. Upon examining the mean and standard deviation values for media G 100 (Table 1a), the means vary slightly across the calculation methods up to bar 7. However, for measurements taken on the sandblasted sample at a pressure of 7 bar, the values differ significantly and are closer at bar 8. The means calculated across all media are slightly lower for the Patchwork method than for the Sdr method, although some exceptions confirm that this is not systematic. The Patchwork method generally exhibits a greater dispersion of data around the mean, which is reflected in slightly higher standard deviations.

Table 1. Means and standard deviations of the relative area from distributions of Figure 12, by media (G 100, G 250, C 300), pressure (2 to 8 bar) and method of calculation (Patchwork, Sdr).

(a) G 100

Pressure (bar)	Relative area			
	Method: Patchwork		Method: Sdr	
	Mean	Standard deviation	Mean	Standard deviation
2	1.000023	1.17×10^{-6}	1.000008	6.67×10^{-7}
3	1.000071	2.51×10^{-6}	1.000061	1.40×10^{-6}
4	1.000112	2.83×10^{-6}	1.000104	5.52×10^{-6}
5	1.000178	4.49×10^{-6}	1.000174	2.30×10^{-6}
6	1.000224	4.61×10^{-6}	1.000242	3.10×10^{-6}
7	1.000250	7.44×10^{-6}	1.000352	1.49×10^{-6}
8	1.000286	6.15×10^{-6}	1.000346	6.64×10^{-6}

(b) G 250

Pressure (bar)	Relative area			
	Method: Patchwork		Method: Sdr	
	Mean	Standard deviation	Mean	Standard deviation
2	1.00018	6.97×10^{-6}	1.00017	5.79×10^{-6}
3	1.00024	8.43×10^{-6}	1.00024	3.64×10^{-6}
4	1.00036	1.16×10^{-5}	1.00045	8.36×10^{-6}
5	1.00045	1.42×10^{-5}	1.00059	1.45×10^{-5}
6	1.00053	1.21×10^{-5}	1.00074	1.16×10^{-5}
7	1.00060	1.97×10^{-5}	1.00087	1.20×10^{-5}
8	1.00058	1.52×10^{-5}	1.00086	1.52×10^{-5}

(c) C 300

Pressure (bar)	Relative area			
	Method: Patchwork		Method: Sdr	
	Mean	Standard deviation	Mean	Standard deviation
2	1.0038	7.22×10^{-5}	1.0053	9.72×10^{-5}
3	1.0054	1.16×10^{-4}	1.0081	1.41×10^{-4}
4	1.0057	1.69×10^{-4}	1.0091	1.68×10^{-4}
5	1.0078	2.11×10^{-4}	1.0127	3.19×10^{-4}
6	1.0082	2.40×10^{-4}	1.0135	3.17×10^{-4}
7	1.0093	2.35×10^{-4}	1.0151	3.65×10^{-4}
8	1.0100	2.94×10^{-4}	1.0156	3.64×10^{-4}

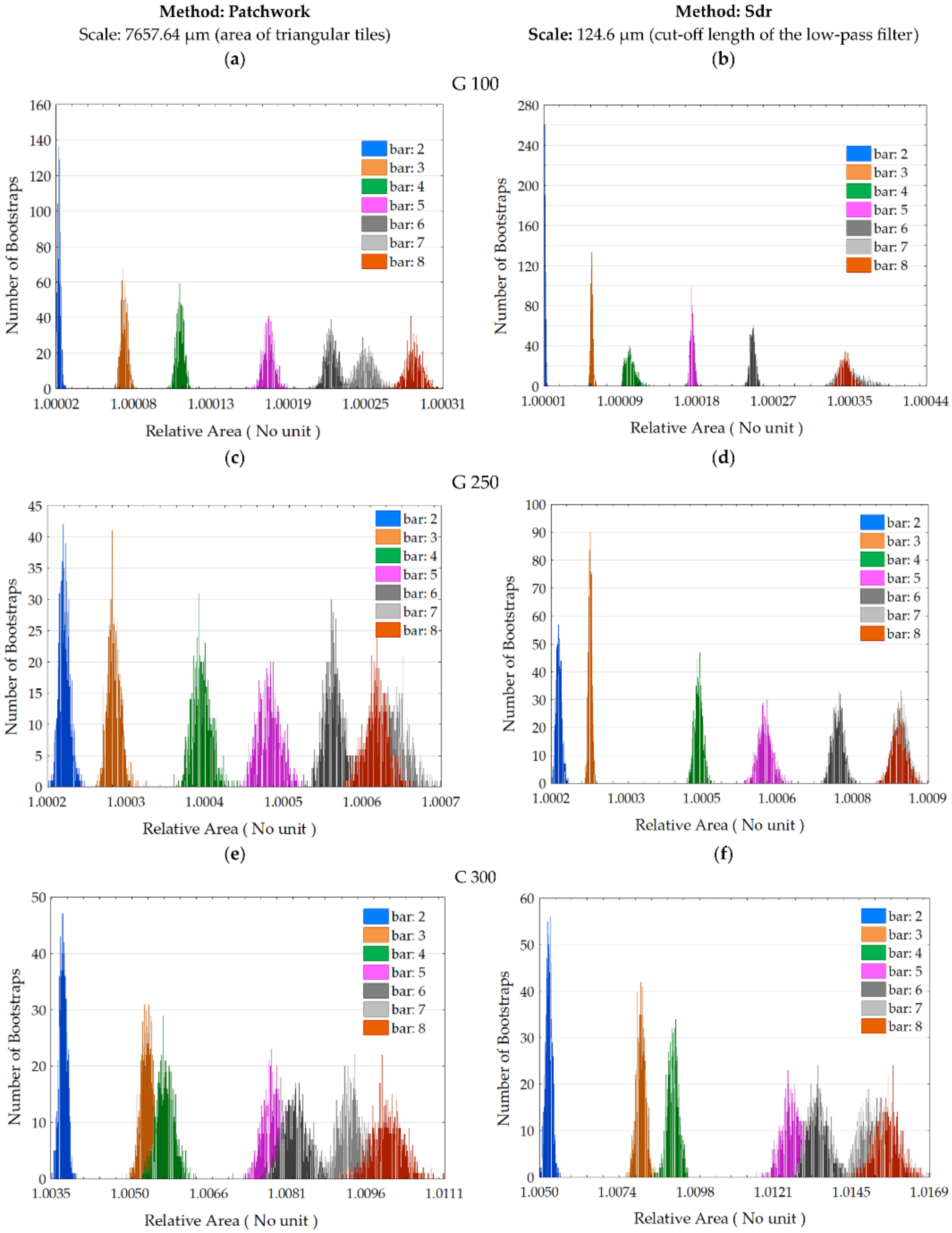

Figure 12. Distributions of the relative area values by method of calculation (Patchwork (**a**,**c**,**e**) and Sdr (**b**,**d**,**f**)), media (G 100 (**a**,**b**), G 250 (**c**,**d**) and C 300 (**e**,**f**)) and pressure.

4. Discussion

The results demonstrate a strong correlation between the two methods of calculating the relative area. However, to express the limitations of this study, we can focus on two aspects. The Patchwork method introduces measurement uncertainties at very small scales. This can potentially be explained when the triangle size for tiling falls below the sampling interval. During the experimentation, no S-Filter was applied to remove microroughness associated with measurement noise, as recommended by ISO 25178-3 [30]. Following the calculation philosophy of the Patchwork method, we believe that triangular tiling at very small scales amplifies measurement noise because it interpolates between measured points. This phenomenon can be observed in Figure 8, where the third tiling exercise indicates a higher relative area value than the previous one, which logically should not be the case. One of our assumptions is that the Patchwork method acts as a low-pass Gaussian filter by removing details at each surface tiling scale. This initial point leads to the second, which concerns measurement uncertainties in general. The fluctuations in heights can be estimated through multiple topographical measurements at the same location, as demonstrated by Lemesle et al. [31,32]. The authors argue that the largest measurement fluctuations correspond to regions with significant plastic deformations, namely from grit blasting. In Appendix B of Lemesle's study, two graphs depict the fluctuations of the Sdr parameter on surfaces blasted at 3 and 6 bar, measured 100 times. These results indicate that the Sdr parameter fluctuates over time when the surface exhibits a certain level of complexity, suggesting a significant variation in fractal surfaces. Another trend is that the graphs generally show an increase in the relative area as a function of pressure, as indicated in Figure 11. However, in the distributions at 7 and 8 bar in Figure 12b–d, an overlap or even exceeding of the histogram is observed for 7 bar compared to 8 bar. The hypothesis for this is that the grit blaster struggled to maintain a pressure of 8 bar, which was its maximum capacity, and it is possible that the TA6V logs were grit blasted at a lower pressure. If we consider this hypothesis, we can still observe that the rest of the grit blasting process is consistent in the relationship between the relative area and the pressure.

5. Conclusions

From the results of the comparison between the Patchwork method and the Sdr method using a low-pass Gaussian filtering, it is possible to observe a strong similarity between the two methods for calculating the relative area. The Sdr method offers several advantages: its computation time is shorter and its components are derived from ISO standards (i.e., computation and filtering). The relevance scale for each calculation method that significatively represents the effect of grit blasting pressure on the increased value of the relative area is a tiling of 7657.64 μm^2 of triangle area for the Patchwork method and a 124.6 µm cut-off for the low-pass Gaussian filter of the Sdr method. Moreover, these components are already implemented in surface processing software solutions, making them easily accessible to researchers. These findings are important as they demonstrate the robustness and reliability of both approaches for calculating the relative area, providing researchers and practitioners with flexibility in choosing the appropriate method based on the specific needs of their study or application. However, it is important to note that despite the similarity in results, each method has its own advantages and limitations, which should be considered when using them. Therefore, it is recommended for researchers and practitioners to carefully consider the specific characteristics of their samples and the objectives of their study before choosing the appropriate measurement method.

Author Contributions: Software, R.G.; Validation, M.W.; Formal analysis, C.B.; Investigation, F.B. and C.B.; Data curation, F.B. and J.L.; Writing—original draft, F.B.; Writing—review & editing, F.B. and J.L.; Supervision, M.B.; Project administration, M.B All authors have read and agreed to the published version of the manuscript.

Funding: This research received no external funding.

Institutional Review Board Statement: Not applicable.

Informed Consent Statement: Not applicable.

Data Availability Statement: Data are contained within the article.

Conflicts of Interest: The authors declare no conflict of interest.

Appendix A. Visualization of Filtered Surfaces

The 24 values of the cut-off length of the low-pass Gaussian filter used in this study were the following: 0.8, 1.2, 1.8, 2.5, 3.5, 4.7, 6.3, 8.4, 11.2, 14.7, 19.3, 25.3, 33.1, 43.2, 56.3, 73.4, 95.7, 124.6, 162.1, 211.0, 274.5, 357.0, 464.3, 603.8 µm. In this appendix, the original surfaces (a) and some surfaces filtered at different cut-off lengths (b–d) for the three grit-blasting media at 8 bar (Figures A1–A3) are presented to observe topographical changes. The relative area was calculated for each filtered surface topography.

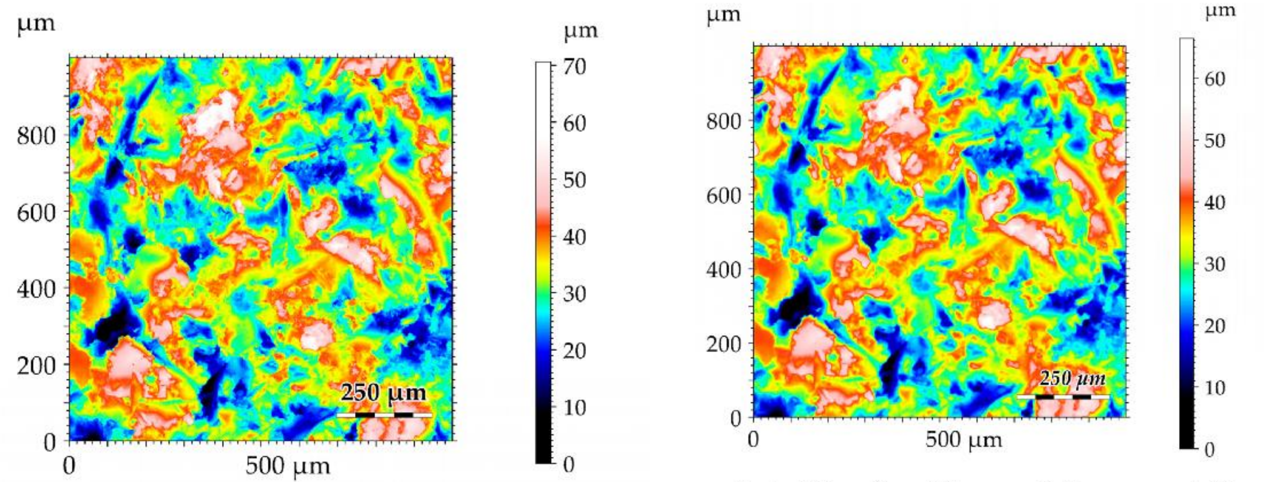

(**a**)

Cut-off length = 8.4 µm, relative area = 1.19

(**b**)

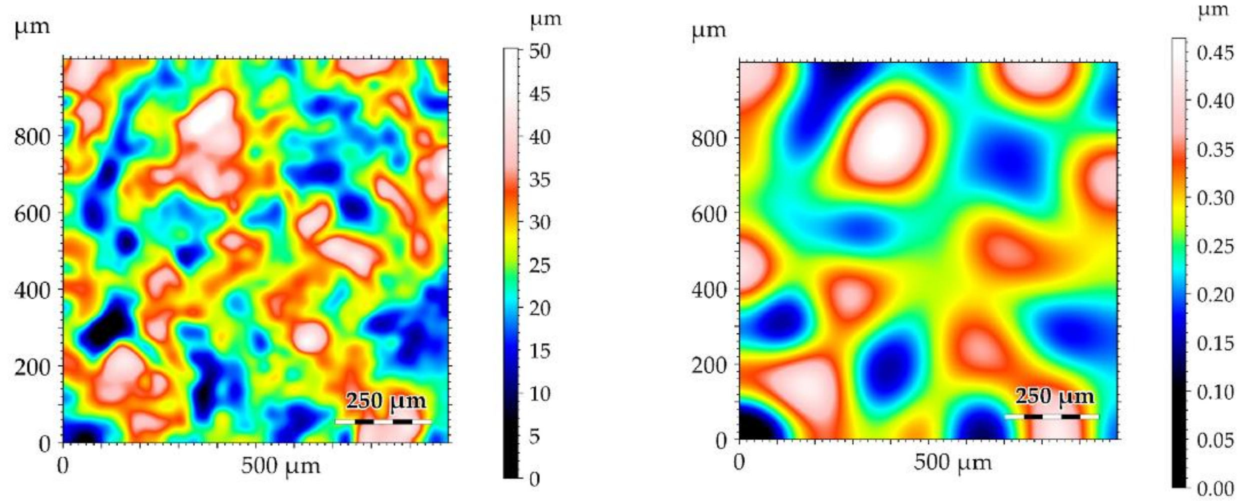

Cut-off length = 73.4 µm, relative area = 1.03

(**c**)

Cut-off length = 603.8 µm, relative area = 1.0003

(**d**)

Figure A1. Original and filtered surfaces grit blasted by C 300 at 8 bar. The surfaces were, respectively, unfiltered (**a**) and filtered at 8.4 µm (**b**), 73.4 µm (**c**) and 603.8 µm (**d**). The relative area was calculated after filtering.

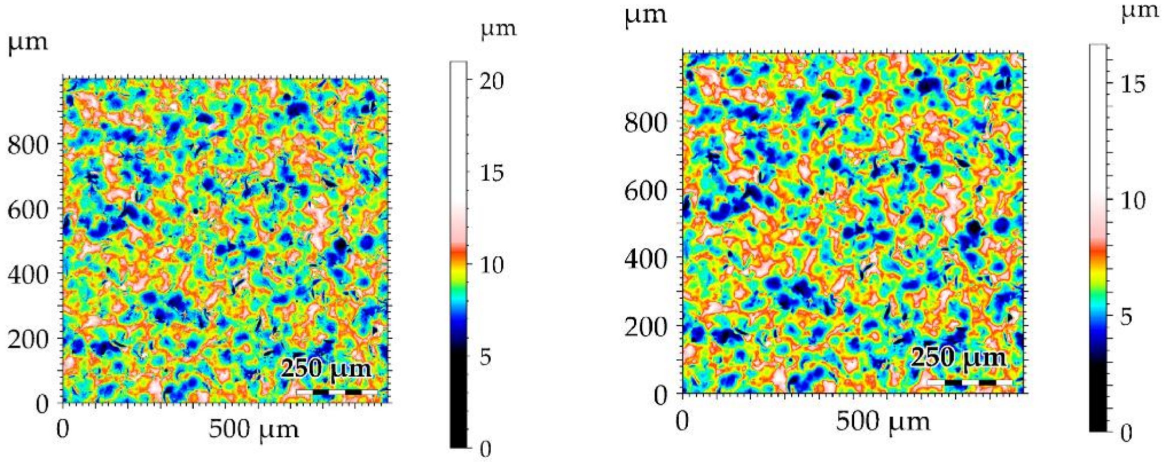

(**a**)

Cut-off length = 8.4 µm, relative area = 1.02

(**b**)

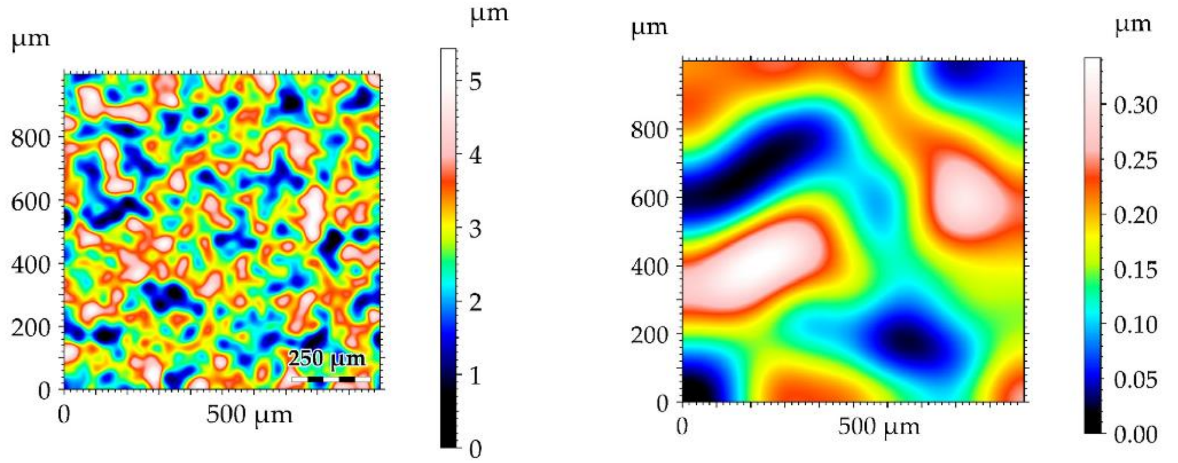

Cut-off length = 73.4 µm, relative area = 1.001

(**c**)

Cut-off length = 603.8 µm, relative area = 1.00000008

(**d**)

Figure A2. Original and filtered surfaces grit blasted by G 100 at 8 bar. The surfaces were, respectively, unfiltered (**a**) and filtered at 8.4 µm (**b**), 73.4 µm (**c**) and 603.8 µm (**d**). The relative area was calculated after filtering.

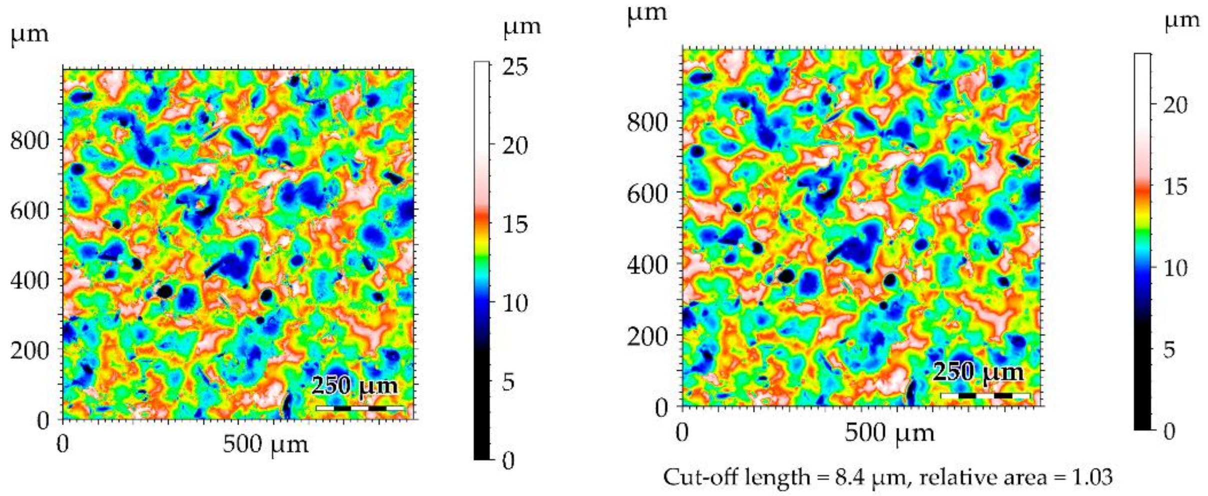

(**a**)

Cut-off length = 8.4 µm, relative area = 1.03

(**b**)

Figure A3. *Cont.*

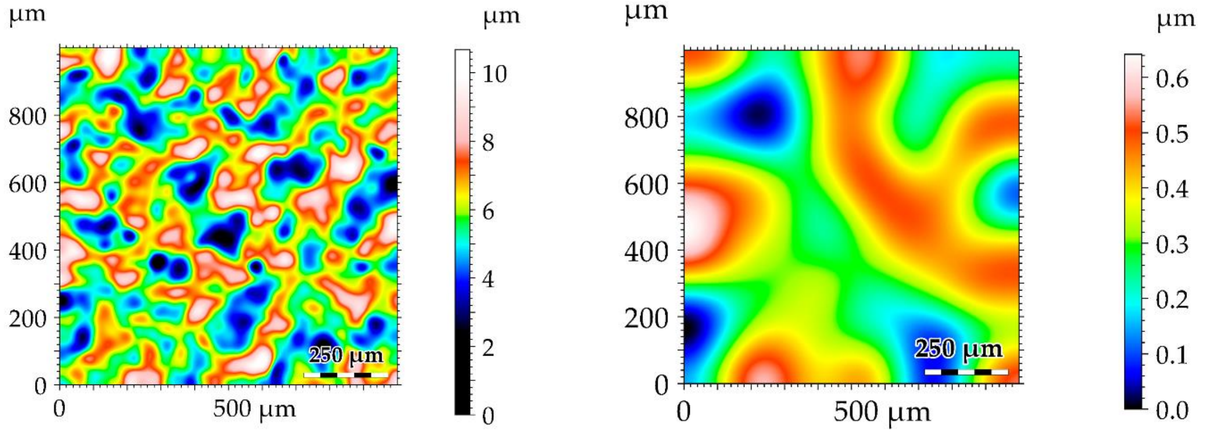

Cut-off length = 73.4 μm, relative area = 1.002
(**c**)

Cut-off length = 603.8 μm, relative area = 1.0000003
(**d**)

Figure A3. Original and filtered surfaces grit blasted by G 250 at 8 bar. The surfaces were, respectively, unfiltered (**a**) and filtered at 8.4 μm (**b**), 73.4 μm (**c**) and 603.8 μm (**d**). The relative area was calculated after filtering.

References

1. Brown, C.A.; Hansen, H.N.; Jiang, X.J.; Blateyron, F.; Berglund, J.; Senin, N.; Bartkowiak, T.; Dixon, B.; Le Goïc, G.; Quinsat, Y.; et al. Multiscale s and Characterizations of Surface Topographies. *CIRP Ann.* **2018**, *67*, 839–862. [CrossRef]
2. Majumdar, A.; Tien, C.L. Fractal Characterization and Simulation of Rough Surfaces. *Wear* **1990**, *136*, 313–327. [CrossRef]
3. Bartkowiak, T.; Berglund, J.; Brown, C.A. Multiscale Characterizations of Surface Anisotropies. *Materials* **2020**, *13*, 3028. [CrossRef] [PubMed]
4. Brown, C.A. Surface Metrology Principles for Snow and Ice Friction Studies. *Front. Mech. Eng.* **2021**, *7*, 753906. [CrossRef]
5. Guibert, R.; Hanafi, S.; Deltombe, R.; Bigerelle, M.; Brown, C.A. Comparison of Three Multiscale Methods for Topographic Analyses. *Surf. Topogr. Metrol. Prop.* **2020**, *8*, 024002. [CrossRef]
6. Brown, C.A. Areal Fractal Methods. In *Characterisation of Areal Surface Texture*; Leach, R., Ed.; Springer: Berlin/Heidelberg, Germany, 2013; pp. 129–153. ISBN 978-3-642-36458-7.
7. De Chiffre, L.; Lonardo, P.; Trumpold, H.; Lucca, D.A.; Goch, G.; Brown, C.A.; Raja, J.; Hansen, H.N. Quantitative Characterisation of Surface Texture. *CIRP Ann.* **2000**, *49*, 635–652. [CrossRef]
8. Mandelbrot, B.B.; Mandelbrot, B.B. *The Fractal Geometry of Nature*; WH freeman: New York, NY, USA, 1982; Volume 1.
9. Thomas, T.R. *Rough Surfaces*, 2nd ed.; World Scientific: London, UK, 1998; ISBN 978-1-78326-236-6.
10. Russ, J.C.; Russ, J.C. Modeling Fractal Profiles and Surfaces. *Fractal Surf.* **1994**, 149–190.
11. Kaye, B.H. *A Random Walk through Fractal Dimensions*; John Wiley & Sons: Hoboken, NJ, USA, 2008; ISBN 3-527-61598-9.
12. Whitehouse, D.J. *Handbook of Surface and Nanometrology*, 2nd ed.; CRC Press: Boca Raton, FL, USA, 2010; ISBN 978-0-429-14069-3.
13. Zahouani, H.; Vargiolu, R.; Loubet, J.-L. Fractal Models of Surface Topography and Contact Mechanics. *Math. Comput. Model.* **1998**, *28*, 517–534. [CrossRef]
14. Majumdar, A.; Bhushan, B. Fractal Model of Elastic-Plastic Contact between Rough Surfaces. *J. Tribol.* **1991**, *113*, 1–11. [CrossRef]
15. Berry, M.V.; Lewis, Z.V.; Nye, J.F. On the Weierstrass-Mandelbrot Fractal Function. *Proc. R. Soc. London. A. Math. Phys. Sci.* **1980**, *370*, 459–484.
16. Mandelbrot, B. How Long Is the Coast of Britain? Statistical Self-Similarity and Fractional Dimension. *Science* **1967**, *156*, 636–638. [CrossRef] [PubMed]
17. Jiang, X.; Scott, P.J.; Whitehouse, D.J.; Blunt, L. Paradigm Shifts in Surface Metrology. Part II. The Current Shift. *Proc. R. Soc. A Math. Phys. Eng. Sci.* **2007**, *463*, 2071–2099. [CrossRef]
18. ISO 25178-2:2021. Available online: https://www.iso.org/fr/standard/74591.html (accessed on 16 April 2023).
19. ISO 16610-61:2015. Available online: https://www.iso.org/standard/60813.html (accessed on 7 April 2024).
20. Brown, C.A.; Charles, P.D.; Johnsen, W.A.; Chesters, S. Fractal Analysis of Topographic Data by the Patchwork Method. *Wear* **1993**, *161*, 61–67. [CrossRef]
21. Kelechava, B. ASME B46.1-2019: Surface Texture (Roughness, Waviness, Lay). *The ANSI Blog*. 2020. Available online: https://blog.ansi.org/2020/08/asme-b46-1-2019-surface-texture-roughness/ (accessed on 5 March 2024).
22. Moreno Constenla, M.C.; Brown, C.A.; Bouchon Aguirre, P.A. Effect of Food Surface Roughness on Oil Uptake by Deep-Fat Fried Products. *J. Food Eng.* **2010**, *101*, 179–186. [CrossRef]
23. Lange, D.A.; Jennings, H.M.; Shah, S.P. Analysis of Surface Roughness Using Confocal Microscopy. *J. Mater. Sci.* **1993**, *28*, 3879–3884. [CrossRef]

24. Lonardo, P.M.; Trumpold, H.; De Chiffre, L. Progress in 3D Surface Microtopography Characterization. *CIRP Ann.* **1996**, *45*, 589–598. [CrossRef]
25. Blunt, L.; Jiang, X. *Advanced Techniques for Assessment Surface Topography: Development of a Basis for 3D Surface Texture Standards "Surfstand"*; Elsevier: Amsterdam, The Netherlands, 2003.
26. Werb, M.; Falcón García, C.; Bach, N.C.; Grumbein, S.; Sieber, S.A.; Opitz, M.; Lieleg, O. Surface Topology Affects Wetting Behavior of Bacillus Subtilis Biofilms. *NPJ Biofilms Microbiomes* **2017**, *3*, 1–10. [CrossRef] [PubMed]
27. Tsigarida, A.; Tsampali, E.; Konstantinidis, A.A.; Stefanidou, M. On the Use of Confocal Microscopy for Calculating the Surface Microroughness and the Respective Hydrophobic Properties of Marble Specimens. *J. Build. Eng.* **2021**, *33*, 101876. [CrossRef]
28. Efron, B.; Tibshirani, R. Bootstrap Methods for Standard Errors, Confidence Intervals, and Other Measures of Statistical Accuracy. *Stat. Sci.* **1986**, 54–75. [CrossRef]
29. Najjar, D.; Bigerelle, M.; Iost, A. The Computer-Based Bootstrap Method as a Tool to Select a Relevant Surface Roughness Parameter. *Wear* **2003**, *254*, 450–460. [CrossRef]
30. ISO 25178-3:2021. Available online: https://www.iso.org/fr/standard/42895.html (accessed on 10 May 2023).
31. Lemesle, J.; Moreau, C.; Deltombe, R.; Martin, J.; Blateyron, F.; Bigerelle, M.; Brown, C.A. Height Fluctuations and Surface Gradients in Topographic Measurements. *Materials* **2023**, *16*, 5408. [CrossRef] [PubMed]
32. Lemesle, J.; Moreau, C.; Deltombe, R.; Blateyron, F.; Martin, J.; Bigerelle, M.; Brown, C.A. Top-down Determination of Fluctuations in Topographic Measurements. *Materials* **2023**, *16*, 473. [CrossRef] [PubMed]

The first study, “Two 3D fractal-based approaches for topographical characterization: Richardson Patchwork versus Sdr” [132] ,served as a methodological shoot-out, demonstrating that a Gaussian-filtered multi-scale Sdr curve delivers a smoother cumulative profile and a more stable fractal dimension than the classical Richardson patchwork. Building directly on that verdict, the second study : “Uncertainty-based scale identification and process-topography interaction analysis via Bootstrap: application to grit blasting” [133], elects Sdr as its core metric, augments it with a residual-Bootstrap routine to map confidence bands at every cut-off, and deploys the enhanced toolset to reveal how grit-blasting parameters steer surface complexity. Together, the two articles trace a logical arc from choosing the most reliable fractal descriptor to harnessing its full statistical robustness for real-process diagnostics, thus laying the technical foundation for the protocol advanced in the remainder of Chapter 4.

4.4 Uncertainty based scale Identification and Process-Topography interaction Analysis via Bootstrap: Application to Grit Blasting

fractal and fractional

Article

Uncertainty-Based Scale Identification and Process–Topography Interaction Analysis via Bootstrap: Application to Grit Blasting

François Berkmans [1,2,3], Julie Lemesle [4,5], Robin Guibert [1], Michal Wieczorowski [2], Christopher Brown [6] and Maxence Bigerelle [1,*]

[1] Univ. Polytechnique Hauts-de-France, CNRS, UMR 8201 - LAMIH - Laboratoire d'Automatique de Mécanique et d'Informatique Industrielles et Humaines, F-59313 Valenciennes, France; francois.berkmans@uphf.fr (F.B.)
[2] Institute of Mechanical Technology, Poznan University of Technology, Plac Marii Sklodowskiej-Curie 5, 60-965 Poznan, Poland; michal.wieczorowski@put.poznan.pl
[3] Univ. Polytechnique Hauts-de-France, INSA Hauts-de-France, LARSH - Laboratoire de Recherche Sociétés & Humanites, F-59313 Valenciennes, France
[4] Valutec, Univ. Polytechnique Hauts-de-France, 59314 Valenciennes CEDEX 9, France; julie.lemesle@uphf.fr
[5] U.R Concept, 59300 Valenciennes, France
[6] Surface Metrology Laboratory, Worcester Polytechnic Institute, Worcester, MA 01609, USA; brown@wpi.edu
* Correspondence: maxence.bigerelle@uphf.fr

Abstract: Finding the relevant scale to observe the influence of a process is one of the most important purposes of multiscale surface characterization. This study investigates various methods to determine a pertinent scale for evaluating the relationship between the relative area and grit blasting pressure. Several media types were tested alongside two different methods for calculating the relative area and three bootstrapping approaches for scale determination through regression. Comparison with the existing literature highlights innovations in roughness parameter characterization, particularly the advantages of relative area over traditional parameters like Sa. This study also discusses the relevance of different media types in influencing surface topography. Additionally, insights from a similar study on the multiscale Sdq parameter and blasting pressure correlation are integrated, emphasizing a scale relevance akin to our Sdr method's 120 μm cut-off length. Overall, our findings suggest a pertinent scale of 10,000 μm^2 for the Patchwork method and a 120 μm cut-off length for the Sdr method, derived from bootstrapping on residual regression across all media. At the relevant scale, every value of R^2 inferior to 0.83 is not significant with the threshold of 5% for the two methods of calculation of the relative area. This study enhances the understanding of how media types and blasting pressures impact surface topography, offering insights for refining material processing and surface treatment strategies.

Keywords: surface topography; multiscale analysis; grit blasting; fractal analysis

Academic Editor: Carlo Cattani

Received: 13 November 2024
Revised: 5 January 2025
Accepted: 13 January 2025
Published: 17 January 2025

Citation: Berkmans, F.; Lemesle, J.; Guibert, R.; Wieczorowski, M.; Brown, C.; Bigerelle, M. Uncertainty-Based Scale Identification and Process–Topography Interaction Analysis via Bootstrap: Application to Grit Blasting. *Fractal Fract.* **2025**, *9*, 48. https://doi.org/10.3390/fractalfract9010048

1. Introduction

1.1. Grit Blasting and Surface Metrology

One of the primary challenges of multiscale characterization studies is to model the relationship between a manufacturing process and its influence on surface topography [1,2]. These studies on the relationships between manufacturing techniques and surface condition aim at establishing a cause-and-effect relationship. Grit blasting stands out as a widely employed surface treatment technique, traditionally used for surface cleaning and rust elimination. In contemporary applications, it finds extensive use in altering surface roughness to achieve complex functionality. Grit blasting alters the surfaces of zirconium ceramics in dental applications, where blasted surfaces enhance the biaxial strength and reliability by inducing compressive residual stresses [3]. One could also mention other applications such as improving cell adhesion [4] and increasing wettability or super hydrophobicity [5,6]. Grit blasting process variables affect blasted surface states. These process variable factors include grit blasting times, which influence the coverage, the nozzle orientation relative to the workpiece surface, the type of blasting material (including silica sand), as well as the workpiece material, and the blasting pressure.

Studies that investigate the relationship between the surface condition and the grit blasting process conduct the following:

- Examine the impact of changing a single factor in the process on roughness;
- Consider multiple factors and their interactions;
- Focus on surface analysis to select relevant characterization roughness parameters and observation scales;
- Concern the fractal dimensions of sandblasted surfaces.

Bouzid and Bouaouadja [7] argued that the maximum height of the profile (Rt) increases with the angle and blasting duration, while the Ra is found to only increase with blasting duration [8]. Regarding the size of the materials, several studies agree that roughness increases when the surface is blasted with finer materials. The study of Su et al. [9] compares powders of 50 μm and 110 μm on zirconia. The geometry of the blasting grit significantly affects the surface topography: smaller grit sizes result in more homogeneous surface textures and lower Sa and Ra values compared to larger grits. As expected, the Ra values of the surfaces of the TA6V alloy increase with higher blasting pressure for both 20/40 (300–850 μm)- and 180 (53–90 μm)-mesh garnet particles [10].

The study by Su et al. [11] presents the results of a comparison between all these factors on dental zirconia. The volume and height loss increased with higher grit blasting pressure and longer treatment duration but decreased with larger grit powder size. The Substrate Bonding Strength (SBS), which refers to the strength of adhesion between an applied layer and the underlying material, known as the substrate, significantly increased with longer grit blasting durations and larger alumina powder sizes. However, the SBS values did not differ significantly among different grit blasting pressures. The previous article does not express its results in terms of standards such as ISO 25178-2 [12] (roughness parameters), which are nonetheless crucial for the geometric characterization of surface topographies. On the other hand, the study by Valverde et al. [13] presents an investigation on a titanium alloy, providing the values of the roughness parameters as the results. Statistical analyses revealed that the Sa, Sq, and Sdr values were influenced significantly by the blasting media, velocity, and surface coverage (all $p < 0.001$). Moreover, the media velocity, the media coverage, and the interaction between the media and velocity, as well as the interaction between the media and coverage, significantly impacted the Sa, Sq, and Sdr values ($p < 0.002$).

Surface metrology focuses on characterizing surfaces using relevant parameters that best represent changes in geometry in a comparative study [14]. Previous studies merely discriminate between blasted surfaces using overly general parameters (e.g., Ra, Rt) to describe surface geometries. Relevant roughness parameters must also be analyzed at a pertinent scale which best isolates the features characteristic of the process, i.e., those influencing the surface topography. According to Ho et al. [15], the parameter that characterizes significant changes in morphologies in the grit blasting process is the Sdq from ISO 25178-2; Sdq describes a correlation between the blast pressure and surface roughness. Sdq represents the root-mean-square value of the surface slope within the sampling area. Sdq is computed using a Lagrangian polynomial with seven points in orthogonal directions [16,17]. The pertinent filtering scale for the Sdq parameter (i.e., the one that best describes the change in topography induced by grit blasting) is a 120 µm low-pass filter in the study by Ho et al. [15] using 150–250 µm silicon carbide particles as the blasting medium for pressures from 1 to 7 bar.

1.2. Fractal Philosophy

Blasted surfaces are also studied using fractal dimension analysis, which is another method of multiscale characterization. Fractal structures and advanced material characterization are pivotal in enhancing the functional properties of materials and surfaces. Recent advances, such as the work of Yan et al. [18], have demonstrated the potential of engineered multilayer nanocomposites to overcome trade-offs between a high breakdown strength and the dielectric constant, achieving significant performance gains. This emphasis on multiscale strategies highlights the importance of advanced methodologies, including fractal-based approaches, in addressing challenges in surface and material characterization. Advanced material characterization plays a crucial role in bridging the gap between fundamental research and technological applications. For instance, O. Barros et al. [19] investigated the dielectric properties of $ZnNb_2O_6$ (ZNO) combined with $CaTiO_3$ (CTO), highlighting the impact of crystalline phase interactions on thermal stability and electromagnetic performance. Such studies underscore the importance of multiscale approaches and precise characterization techniques, which are also critical in understanding and optimizing surface properties across different domains.

Blasted surfaces exhibit self-affinity, meaning they have a structure that is similar at different scales. Persson's work [20] provides a kinetic model to understand how sandblasting generates a fractal surface, combining theoretical and experimental aspects. Blasting operates on the principle of transferring the kinetic energy of high-velocity particles to a target surface. Upon impact, the particles' energy is dissipated through multiple mechanisms, including plastic deformation, elastic rebound, and minor losses (e.g., noise and vibrations). Hutchings [21] suggested that 80% of the energy is converted into heat for metals, but the experimental work by Gillstrom and Jarl [22] estimated this fraction to be closer to 39% for steels, challenging prior assumptions. The energy balance during impact shows that only the energy associated with plastic work in the workpiece contributes to heat generation. Elastic energy causes rebound, which can be quantified using the coefficient of restitution. The rebound effect depends on the material properties, such as the hardness and elastic modulus. As shown in prior studies, softer materials absorb less energy as heat due to their higher hardness-to-modulus ratio, which enhances elastic recovery. The contact mechanics are described using the Hertz contact theory, as discussed by Timoshenko [23] for elastic contact time and Chaudri and Walley [24] for plastic contact time. The contact radius and time depend on the particle's velocity, size, and material properties. Maeda et al. [25] assumed the contact area to be the particle's projected area. However, numerous shot-peening and sandblasting experiments have demonstrated that the penetration depth during impact is significantly smaller than the particle radius. Studies on materials highlighting the effect of heat on titanium alloys indicate that the morphology can become unstable when exposed to a constant temperature of 400 °C for a certain period [26]. The localized heat generated by the impact of sandblasting is insufficient to cause such changes, particularly during a brief blasting of a few seconds like in our study [27].

In general, blasted surfaces are extensively studied for their fractal complexity because the grit blasting conditions vary the complexities of the surface topography [28–30].

This study builds on the study of Berkmans et al. [31] in which two methods of fractal-based characterization calculation were compared to determine the relative area with respect to scale. In summary, the Richardson Patchwork method, from the ASME B46.1 [32], was compared with the Sdr parameter derived from ISO 25178-2 (Equation (1)) [12], using a low-pass Gaussian filter for multiscale characterization. Filtering methods are widely used in roughness analysis, providing a reliable and simple way to process 2D or 3D signals depending on how the surface profile is studied. Common methods include Gaussian [33–35], robust [36,37], and spline filters. Gaussian filters, standardized under ISO 16610-21 [38], are the most commonly used method [39].

$$Sdr = \frac{1}{A}\left[\iint_A \left(\sqrt{\left[1+\left(\frac{\partial z(x,y)}{\partial x}\right)^2+\left(\frac{\partial z(x,y)}{\partial y}\right)^2\right]}-1\right)dxdy\right] \tag{1}$$

The comparison is based on the relative area calculated from topographies of TA6V samples that were grit-blasted with different pressures and blasting materials (media). The surfaces produced by grit blasting exhibit fractal-like characteristics over the scales studied, allowing for the analysis of area development at multiple levels based on pressure and media. Both methods yield similar relative area results across a wide range of scales for a given blasting condition. The Patchwork method is clearly sensitive to complexities and to differences in pressure. The Sdr method, with our proposed protocol, is easier to implement with some conventional roughness software. This could make Sdr more practical for some analyses. The results of this study present the calculations of the relative area at different computation scales. Increasing the blasting pressure causes a work-hardening phenomenon on the surface, making it less rough at high pressures (8 bar) compared to intermediate pressures (5 bar) when using media such as glass beads. This results in a smaller relative area at 8 bar compared to 5 bar at the smaller scales for both methods (Figure 1).

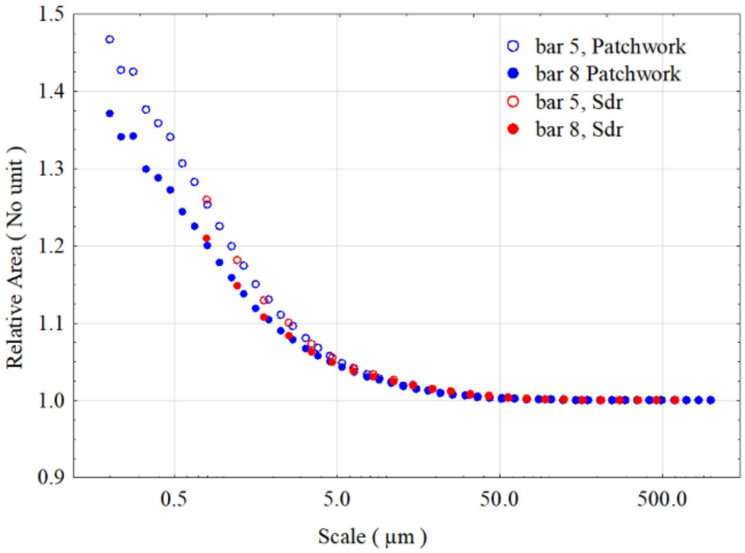

Figure 1. Comparison of two methods, Sdr (ISO 25178-2) and Patchwork, for calculating relative areas of surface topographies created by blasting with glass beads. The points represent the median of the relative area values, categorized by calculation method and pressure. Blue symbols indicate the median points for the Patchwork method, while red symbols correspond to the Sdr method. The scale refers to the cut-off length of the low-pass Gaussian filter applied in the Sdr calculation. For the Patchwork method, the tile size in µm^2 is equal to half the square of the cut-off length.

It should be noted that the equation of the Sdr parameter (Equation (1)) is inconsistent with fractal theory, as a fractal curve is non-differentiable.

The objective of this work is to propose a method to calculate the scale in the calculation of the relative area pertinent to the pressure of grit blasting. Based on the previous results, this method will contribute to improving the precision and reliability of surface area calculations, leading to more effective control and optimization of blasting processes in various applications. The method would allow for better characterization of the grit blasting process, as well as other manufacturing processes that create fractal surfaces with modifiable intensities, such as electrical discharge machining [40] and laser manufacturing [41].

2. Materials and Methods

2.1. Creation of the Blasted TA6V Surfaces

The data used in this publication come from the study by Berkmans et al. [31]. To control surface topography and avoid bias in subsequent statistical analyses, this study utilized grit-blasted TA6Vsurfaces. The workpiece cylinders, measuring 30 mm in diameter and 20 mm in height, were ground with SiC papers ranging from grit 80 to 4000 before grit blasting.

The TA6V surfaces were grit-blasted using the Guyson Euroblast 6SF system (Guyson S.A, Skipton, North Yorkshire, UK). Three types of grit materials were used: two types of glass silico-soda–calcium microbeads (G 100 with particle size of 70–150 µm and G 250 with particle size of 150–250 µm) from ARENA (Marquette-lez-Lille, France) and an abrasive material named C 300 50/80 (particle size of 100–630 µm) from Semanaz (Bray-Saint-Aignan, France), composed of hard, sharp, abrasive crystals manufactured from molten glass mass with a composition of silicate, alumina, and iron oxide.

Seven blasting pressures, ranging from 2 to 8 bar, were applied for each grit material, resulting in a total of 35 blasted TA6V samples. The specimens were divided into sets, one set for C 300, one set for G 100, and three sets for G 250, to study the repeatability of the grit blasting process. In preliminary experiments, 1 bar was included, but challenges were encountered in achieving a consistent and uniform surface topography, leading its exclusion from the main study.

During grit blasting, the distance between the blasting gun and the workpiece surfaces was maintained at approximately 10 cm. The grit materials were blasted perpendicularly to the TA6V surface for about 30 s for pressures ranging from 2 to 8 bar, ensuring a homogeneous blast across the entire surface. The blasting was performed with a back-and-forth motion (left to right) from the top to the bottom of the surface. This method provided a wide variation in the relative surface areas.

2.2. Topographical Measurements of the Blasted Surfaces

White-light interferometry (Bruker ContourGT™, San Jose, CA, USA) was used to measure the blasted surface topographies (Figure 2). Fifty 1 × 1 mm^2 regions, corresponding to stitching maps of 5059 × 5058 pixels (540 elementary maps), were measured randomly on each surface with a 50× lens (elementary map size of 127 × 94.9 µm for a 0.198 µm X/Y resolution). A total of 1750 measurements were obtained from the 35 surfaces. Post processing, filtering and fractal calculations were performed on the dataset of the 1750 measurements (50 zones × 35 blasted surfaces) using the software MountainsMap 8® (Digital Surf, Besançon, France).

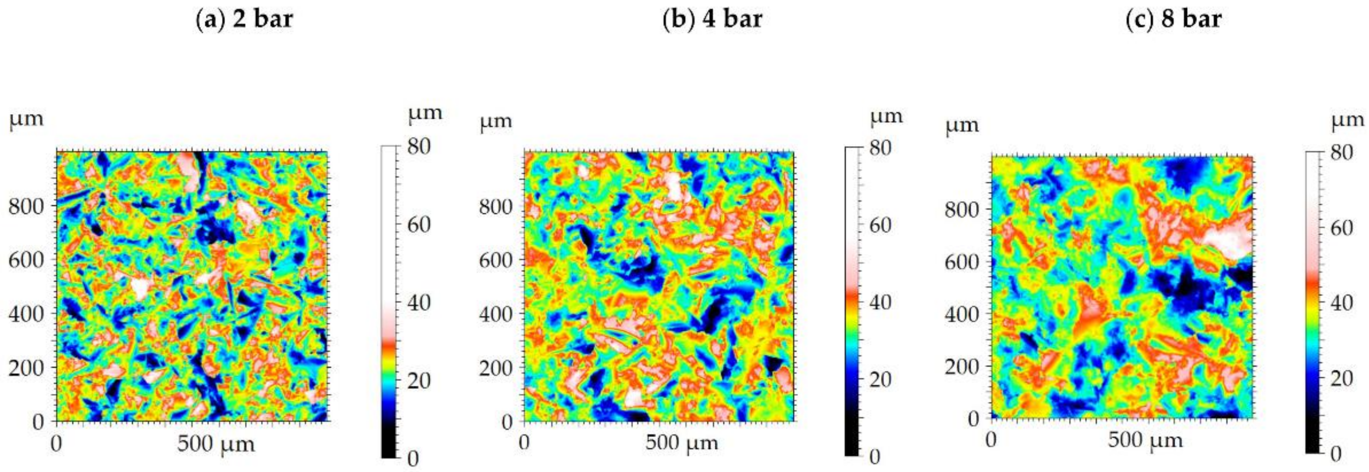

Figure 2. Surface topographies of TA6V surfaces grit-blasted at 2 bar (**a**), 4 bar (**b**), and 8 bar (**c**) with the C300 medium. The aggressiveness of the medium can make it difficult to assess visually the gradation in blasting intensity. More surface topographies are shown in Appendix A.

2.3. Methods of Relative Area Calculation

The methods used to calculate the relative surface area are fractal methods known as area-scale analyses. The first method is called the Patchwork method, developed by Brown in the 1990s [42]. The second is a method derived from the Sdr parameter of the ISO 25178-2 standard, with the addition of a low-pass Gaussian filter for the multiscale approach [31]. Brown's Patchwork method and the Sdr (Surface Area Ratio) method are both used to analyze surface roughness and topography, but they differ in how they define and calculate relative area. In the Patchwork method, the surface is divided into small triangular patches of constant size (Figure 3). These patches are created through interpolation between the regularly spaced measured heights on the surface. As a result, each triangular patch has a fixed, uniform area across the entire surface, regardless of the spacing or density of the measurement points. This constancy in patch size enables a local analysis of surface roughness or texture. The strength of this method lies in its ability to capture local variations in texture and provide a fine-grained statistical view of the surface irregularities. It is particularly useful for studies requiring multiscale characterization or the analysis of complex functional surfaces. On the other hand, in the Sdr method, the patches are not of constant size. They are defined by the sampling intervals on the surface, and their area varies depending on the height differences between these points. The Sdr measures the ratio between the real surface area of a topography, accounting for its features, and the projected surface (Figure 3). Thus, unlike the Patchwork method, the patch area in the Sdr calculation is variable and directly reflects the surface topographical complexity. The more pronounced the irregularities between the sampled points, the larger the patch area becomes, leading to a higher Sdr value. The Sdr is expressed as a percentage and is used to quantify the relative roughness of a surface compared to a flat reference surface. The key difference between these two methods lies in the areas of the triangular patches. In the Patchwork method, the area is constant, ensuring uniform and regular analysis, even if the vertices of the triangular patches are spread unevenly. In the Sdr method, the patch area is variable, influenced directly by the distribution of sampled heights and local asperities, providing an equally accurate representation of a measured surface. Formally, the Patchwork method is more closely related to fractal theory, as introduced by Benoît Mandelbrot in his study of the coastline of Great Britain, based on Richardson's data [43]. The fractal nature of the method lies in its ability to handle different scales, making it particularly suited to analyzing surfaces with varying roughness.

However, the Patchwork method has certain challenges. One difficulty can be the potential distortion of the patch shapes, which could lead to the Schwartz area paradox, if this is not controlled for. Correcting this deformation is straightforward, and the algorithms needed to address this issue are computationally simple. The Sdr method is easier to implement computationally, as it directly computes the ratio based on the sampled heights, without concerns about patch deformation; however, it depends on the filtering algorithm, which distorts the measured topography. Despite these differences, we can expect convergence between the two methods when dealing with surfaces that are not too rough, i.e., complex, at the scales being investigated. The distinction between these two calculation methods is presented in 2D form in Figure 3.

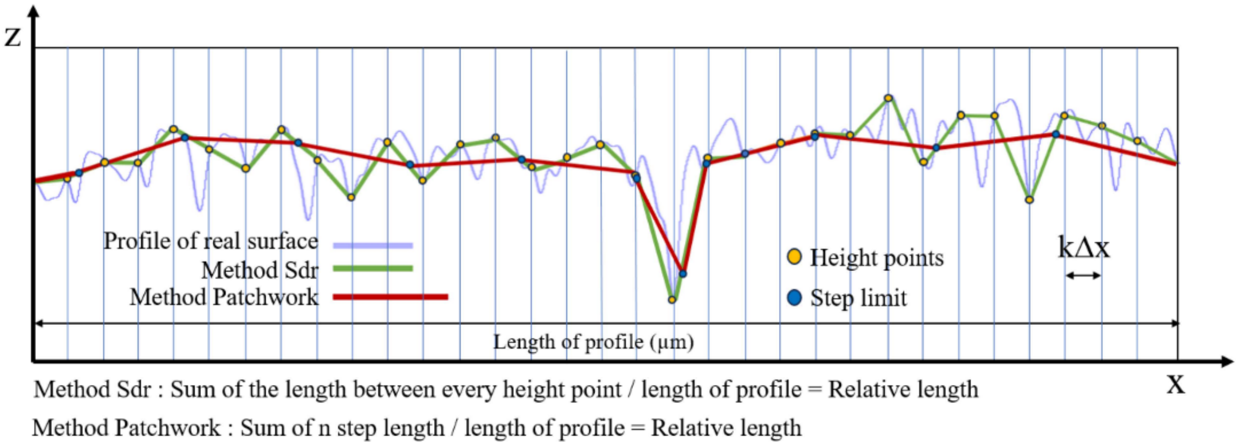

Method Sdr : Sum of the length between every height point / length of profile = Relative length

Method Patchwork : Sum of n step length / length of profile = Relative length

Figure 3. Diagram of the two calculation methods used in this study, shown in terms of relative length. The blue continuous line represents a real surface. The green line, a linear interpolation between measured height points, represents our measured profile (the Sdr method calculates the relative length at the sampling scale). The red line illustrates the profile obtained by the Patchwork method.

2.4. Statistical Analysis Based on Bootstrapping

2.4.1. Description of the Adopted Methodology

The results of linear regressions as a function of the scale used to calculate the relative area are used to evaluate the relevant scale for analyzing the relative area based on the pressure used; we present the results of linear regressions as a function of the scale used to calculate the relative area. The study presented here uses the principle of multiscale analysis for surface characterization. The principle is to examine the surface across multiple scale ranges and to associate findings or calculations with different scales [44]. In addition, a bootstrapping protocol is used to obtain robust results. Bootstrapping is a statistical method used to estimate the distribution of a sample statistic by repeatedly resampling with replacement from the original data. This technique helps assess the accuracy and variability of estimates, providing robust results even with small or non-normally distributed datasets [45]. The linear regressions in Figure 4 use replicated data (10 values of the relative area for each pressure are randomly selected out of the 1000 bootstrapped values) and were computed at the smallest scale of calculation for both methods. This provides us with initial information regarding the relevance of the scale. Indeed, for both calculation methods, the scale, where the relation of the relative area value depending on the pressure is high, is not the smallest scale that should be observed. The smallest reasonable tile size for the Patchwork method is one-half the square of the sampling interval (Figure 4a), while the cut-off length is 0.789 µm for the filtering used for the Sdr method (Figure 4b). Here, with very low determination coefficients R^2 (0.04 for the Patchwork method and 0.05 for Sdr), one can consider that analyzing the surface in maximum detail does not show the influence of pressure on the relative area. This could be due to the work-hardening phenomenon and media size [46], which flattens the surface and makes it less complex as pressure increases.

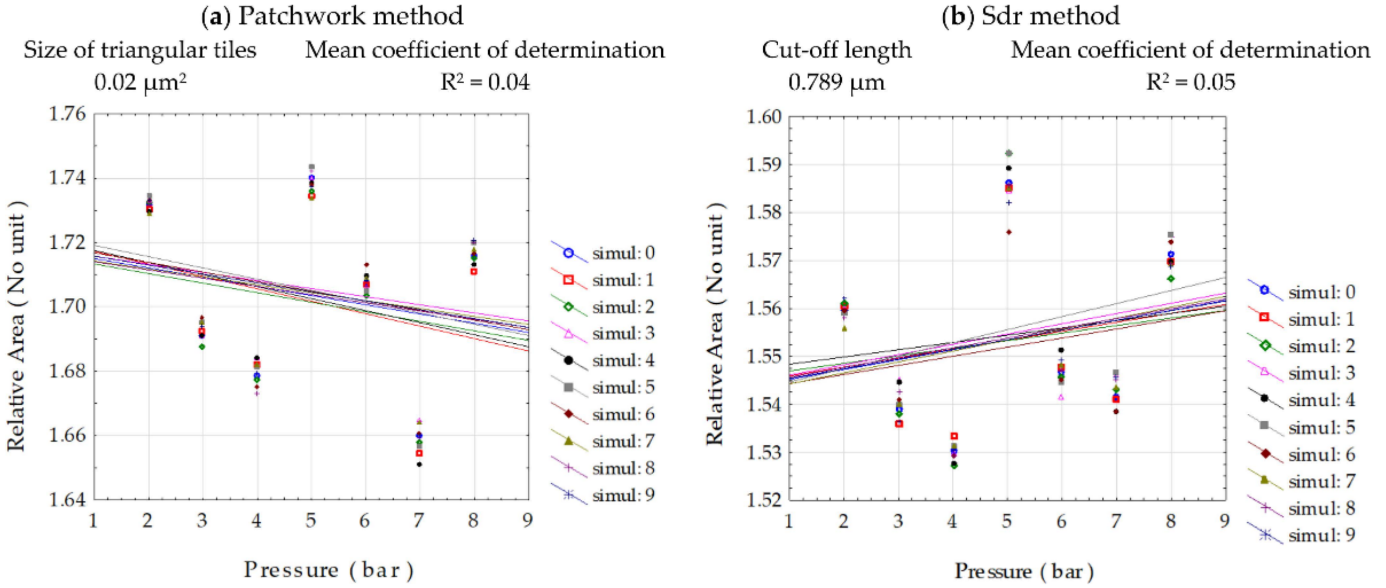

Figure 4. Results of the linear regressions of the relative area as a function of pressure for the two calculation methods. Simulations from 0 to 9 are obtained from bootstrapping replication of the real data and then averaged. The results come from measurements performed on surfaces blasted with the C 300 medium (corundum). Each simulation corresponds to an R^2 value, which is then averaged.

In this study, two statistical hypotheses are formulated to test the effect of blasting pressure on the relative area of surfaces. The null hypothesis (H0) states that there is no significant relationship between the blasting pressure and the relative area of the surfaces, implying that any observed variation may be attributed to random chance. In contrast, the alternative hypothesis (H1) proposes that a significant relationship exists between these two variables, suggesting a measurable impact of pressure on surface topography. These hypotheses are statistically tested to determine whether the data provide sufficient evidence to reject H0 and accept H1.

For H0, the data were permuted to represent the distribution of regression coefficients if there was no real relationship between the pressure and the relative area. This means that for each combination of the relative area (RA) and pressure, there are 7 pairs of data. In the bootstrapping for H0, the seven values of relative area are randomly permuted. This means that instead of using the actual order of the relative area on every scale, such as X_1 to X_7, and the 7 pressure values Y_1 to Y_7, we create new combinations of pairs to calculate the coefficient of regression by performing a random permutation of Y_1 to Y_7. The goal is to generate a distribution of R^2 that could be obtained if pressure and relative area were not correlated. Although this method can eliminate any apparent correlation between pressure and relative area, it is important to note that the regression coefficients obtained will not be exactly equal to zero.

To compare these hypotheses robustly, three bootstrapping protocols have been defined: simple bootstrap, double bootstrap based on pairs, and double bootstrap based on residuals.

2.4.2. Simple Bootstrap

The relationship between the blasting pressures (independent variable) and the developed surface area (dependent variable) using 50 topography measurements for each of the seven different pressures (ranging from 2 to 8 bar) is investigated. Our goal is to assess how well the variation in pressure explains the variation in the developed surface area, which will be quantified using the regression coefficient R^2.

Data Preparation and Bootstrapping Sampling

We have seven blasting pressures (e.g., 2, 3, 4, 5, 6, 7, 8 bar). For each pressure, there are 50 measurements of relative area. For each measurement, a bootstrapping is performed as follows:

1. For each pressure level (2, 3, . . ., 8 bar), conduct the following:
   - Draw 50 random samples with replacement from the 50 original measurements for that pressure level;
   - Calculate the mean relative area for that resample;
   - Repeat this process multiple times (e.g., 1000 times) to obtain a distribution of bootstrapping means for each pressure.
2. For each of the 7 pressures, end up with a set of means from the bootstrapping means.

Regression Analysis for Each Resampling

With a set of bootstrapping means for each pressure level, conduct the following:

- Perform a linear regression between the pressure (independent variable) and the corresponding bootstrapping mean surface relative area (dependent variable).
- Calculate the coefficient of determination R^2 for this regression. The R^2 value will tell us how much the variation in the developed surface area is explained by the variation in the grit blasting pressure.
- Repeat the entire bootstrapping resampling process many times (e.g., 1000 times).

Each time, a new set of regression results and a new R^2 value are obtained. By repeating this process, a distribution of R^2 values is created.

Analysis of the R^2 Distribution

Once the distribution of R^2 values is obtained, conduct the following:

- Calculate the mean or median of the R^2 values to obtain an overall sense of the fit;
- Estimate confidence intervals (e.g., 95% CI) for R^2, giving a range in which the true relationship between the pressure and the surface area likely lies;
- Assess the stability of the relationship by looking at the variability in the R^2 values across the bootstrapped samples.

2.4.3. Double Bootstrap Based on Pair Replication

The relationships between the blasting pressure and the developed surface area are analyzed by using a two-stage bootstrapping approach. In the first stage, the surface area measurements for each pressure are resampled, and in the second stage, a pairwise bootstrap on the resulting bootstrapping means is performed. The goal is to explore the statistical distribution of the regression coefficient R^2, providing a more robust understanding of the relationship. In this extended approach, we perform two levels of bootstrapping:

1. A first bootstrap on the individual surface area measurements for each pressure level;
2. A second bootstrap on the pairs [pressure, surface area means] derived from the first bootstrap.

By incorporating the second bootstrap, the variability is determined not only within each pressure group but also in the overall relationship between the pressure and the developed surface area.

Data Preparation

As previously specified, we have seven grit blasting pressures, each with 50 topography measurements of developed surface area. Two bootstrapping levels are performed.

First-Level Bootstrap

For each pressure, a simple bootstrap is performed, resulting in a set of bootstrapping means for each of the 7 pressure levels whose means are input for the next stage.

Second-Level Bootstrap: Bootstrap on Pairs

Once we have the bootstrapping means for each pressure, we introduce the second bootstrap step, where we resample pairs [pressure, bootstrapping means]:

1. Resample pairs: for each iteration, randomly sample pairs [pressure, bootstrapping mean] from the set of 7 pressure levels (with replacement). For example, a bootstrap sample might be [2 bar, mean2], [3 bar, mean3], . . ., [8 bar, mean8].
2. Perform a linear regression: perform a linear regression on the resampled pairs, with pressure as the independent variable and the corresponding bootstrapping mean surface area as the dependent variable.
3. Calculate R^2: for each resampled pair, calculate the regression coefficient R^2, which measures how much the variation in surface area is explained by the variation in pressure.
4. Repeat: repeat this entire second-level resampling process many times (e.g., 1000 times) to build a distribution of R^2 values.

2.4.4. Double Bootstrap Based on Residuals

This is also a two-level bootstrapping method. This time, instead of performing a bootstrap on pairs [pressure, surface area mean], a bootstrap on residuals in the second stage is used. The two methods are similar in concept, but they differ in the way they handle resampling in the second stage. The bootstrap on residuals focuses on the variability captured by the regression model errors, while the bootstrap on pairs resamples the entire dataset. The main difference between the two methods lies in the resampling approach:

- The bootstrap on pairs resamples all the pairs [pressure, surface area mean], which can distort the relationship between the independent (pressure) and dependent (surface area) variables;
- The bootstrap on residuals preserves the structure of the data by resampling only the errors (residuals) of the model, ensuring that the overall relationship between the pressure and the surface area is maintained while introducing variability based on the model accuracy.

First-Level Bootstrap

The first stage remains identical in both approaches, i.e., the following is a simple bootstrap:

1. The surface area measurements within each pressure group (e.g., 50 samples with replacement) are resampled;
2. For each pressure level (2 to 8 bar), the bootstrapping mean is computed;
3. This process is repeated (e.g., 1000 times) to obtain a distribution of bootstrapping means for each pressure level.

After this first step, there is a set of bootstrapping means for each pressure level, just like in the bootstrap on pairs method.

Second-Level Bootstrap: Bootstrap on Residuals

In the bootstrap on pairs method previously described, the following is true:

- All the pairs of pressure and bootstrapping means are resampled;
- For each iteration, the pairs from the set of pressure levels and their corresponding bootstrapping means are sampled randomly (with replacement);
- Then, a new linear regression is calculated, and the regression coefficient R^2 is determined.

In the bootstrap on residuals method, instead of resampling pairs, the following steps are performed:

1. Fit an initial regression: After calculating the bootstrapping means for each pressure level, we fit a linear regression between the pressure (independent variable) and these bootstrapping means (dependent variable). We then calculate the residuals, which represent the differences between the actual bootstrapping means and the predicted values from the regression model.
2. Resample residuals: Instead of resampling pairs, the residuals are resampled with replacement. These residuals capture the variability in the relationship between the pressure and the surface area.
3. Generate new data: For each pressure level, we create new bootstrapping means by adding the resampled residuals to the predicted values from the original regression model (Equation (2)). This step maintains the core structure of the original regression model, ensuring that the relationship between the pressure and the surface area remains intact, while introducing variability based on the residuals.

$$new\ mean = predicted\ value + resampled\ residua \tag{2}$$

4. Perform regression and calculate R^2: We fit a new linear regression to the original pressure values and the newly generated bootstrapping means. The regression coefficient R^2 for this resampled dataset is calculated.
5. Repeat the process (e.g., 1000 times) to generate a distribution of R^2 values, just as we performed in the bootstrap on pairs method.

3. Results

After generating the data with our three bootstrapping protocols, the best protocol for finding the relevant scale to characterize the relationship between relative area and grit blasting pressure can be identified.

Figure 5 presents the results of the R^2 distributions as a function of the scale for the relative area calculation, for the three bootstrapping methods previously described. The bootstrapping methods indicate that regardless of the calculation method or the medium used, the relevance of the R^2 values at scales is given.

For the three bootstrapping methods (Figure 5i–iii), regardless of the media (Figure 5c,e,g), the maximum relevance which highlights the influence of pressure is obtained for a tile size of around 10,000 μm^2 for the Patchwork method and a cut-off length of around 120 μm for the Sdr method (Figure 5a). The choice of this specific cut off is directly tied to the analysis in Figure 5. The box plots included in these graphs allow us to directly observe the variation in the R^2 values with changes in the cut-off parameter. Consequently, a 120 μm cut off and 10,000 μm^2 triangular tile size were chosen as a balance between capturing relevant surface features and minimizing noise while ensuring comparability between the two methods. To determine if the R^2 values associated with this relevance are significant to validate H1, we must look at the distribution of the R^2 values under H0 (Figure 5b).

Figure 6 presents a visualisation of the surface topography after being filtered on the relevant scale for the Sdr Method (120 µm cut off length). Surface are smoother than the original ones but have differences depending on the pressure, the surface blasted at 2 bar is more homogeneous than the two other ones.

The distributions under H0 (Figure 7b) indicate that at a 95% threshold, the R^2 values are located at different points depending on the bootstrapping method used. For the simple bootstrap (Figure 7i), the threshold value is 0.59, indicating that 95% of the values must be below this to invalidate H0. For the paired bootstrap (Figure 7ii), the threshold value is 0.91, and for the residual bootstrap (Figure 7iii), it is 0.83. This assumption is valid for both methods of calculation. These checks under H0 are necessary because the H1 hypothesis alone is not sufficient, considering that the values are correlated if we assume that the surfaces are the same at different filtering scales. For H1, the graphs clearly indicate that the values generally approach 1 regardless of the bootstrapping method used (Figure 7a).

(**a**) H1 (**b**) H0

(**i**) R^2, simple bootstrap

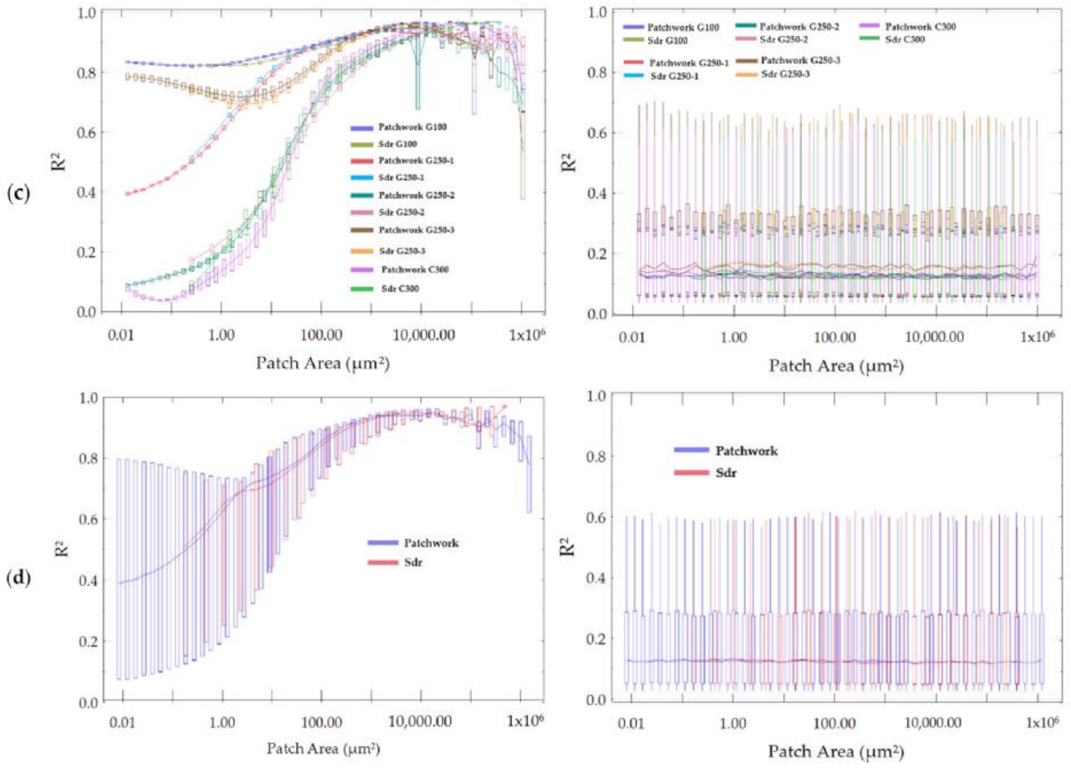

(**ii**) R^2, bootstrap based on pairs

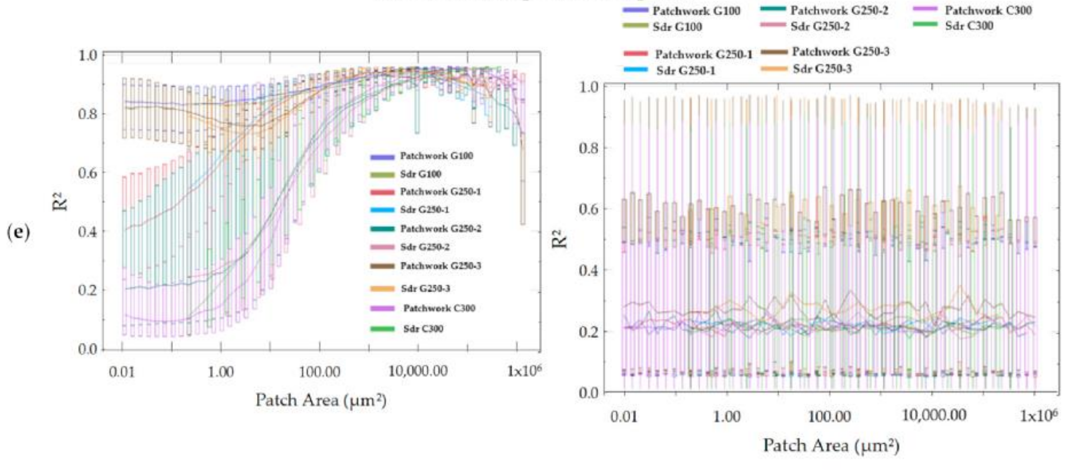

Figure 5. *Cont.*

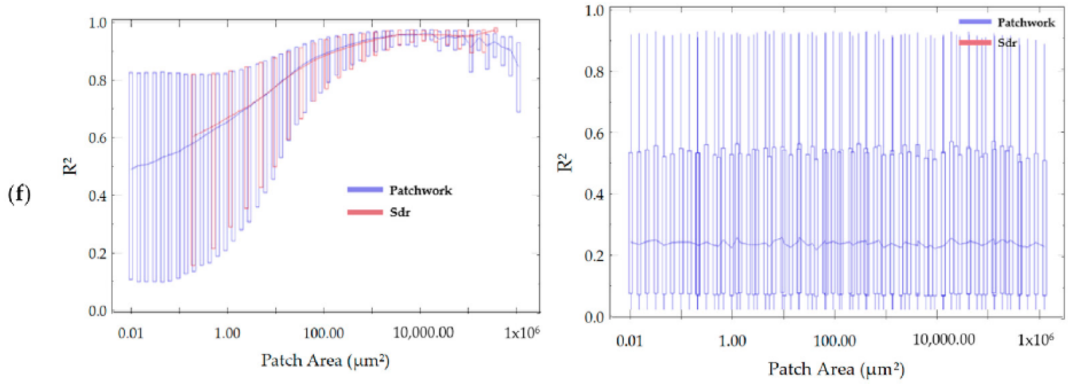

(iii) R², bootstrap based on residuals

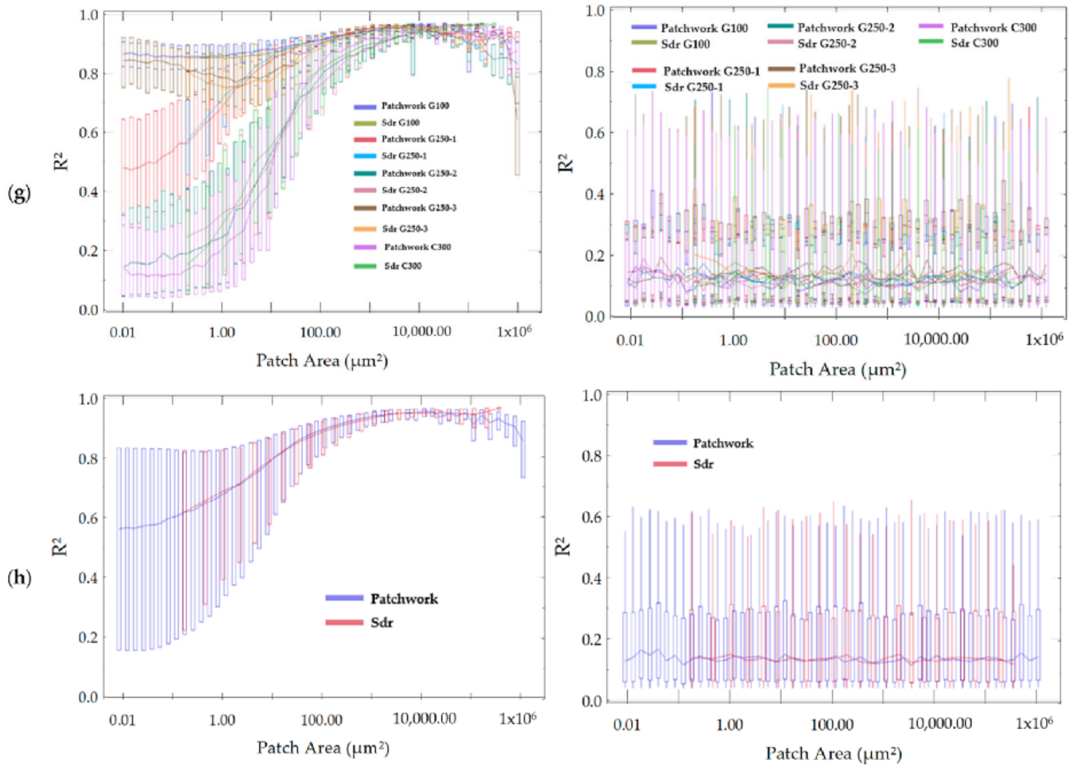

Figure 5. Analysis of the R^2 distributions according to the scale of calculation for relative area under hypotheses H1 (**a**) and H0 (**b**) for the three bootstrapping methods: simple bootstrap (**i**), bootstrap based on pairs (**ii**), and bootstrap based on residuals (**iii**). The tile size of the Patchwork method (in μm^2) is equal to half the square of the cut-off length of the Sdr method. Two plots are proposed for each bootstrapping method: the first one based on the media (**c**,**e**,**g**) and the second one based on the method of the relative area calculation, Sdr or Patchwork (**d**,**f**,**h**).

To continue the analysis, the choice was made to use bootstrapping on residuals as a promising method. Indeed, the threshold for the simple bootstrap, equal to 0.59, is too low under H0 to be helpful to validate significance. Additionally, to capture the variations in the initial model and gain a better view of the uncertainties, the bootstrap based on pairs is too high with a threshold of 0.91. The bootstrap on residuals preserves the original regression structure by resampling residuals, maintaining the relationship between grit pressure and relative area, unlike the paired bootstrap, which may introduce noise or trends. It captures variability from model errors without distorting the data, ensuring that subtle roughness variations are not overshadowed. Moreover, narrower confidence intervals and more stable R^2 estimates are provided, closely aligning with physical observations, making it the most suitable method for identifying relevant scales.

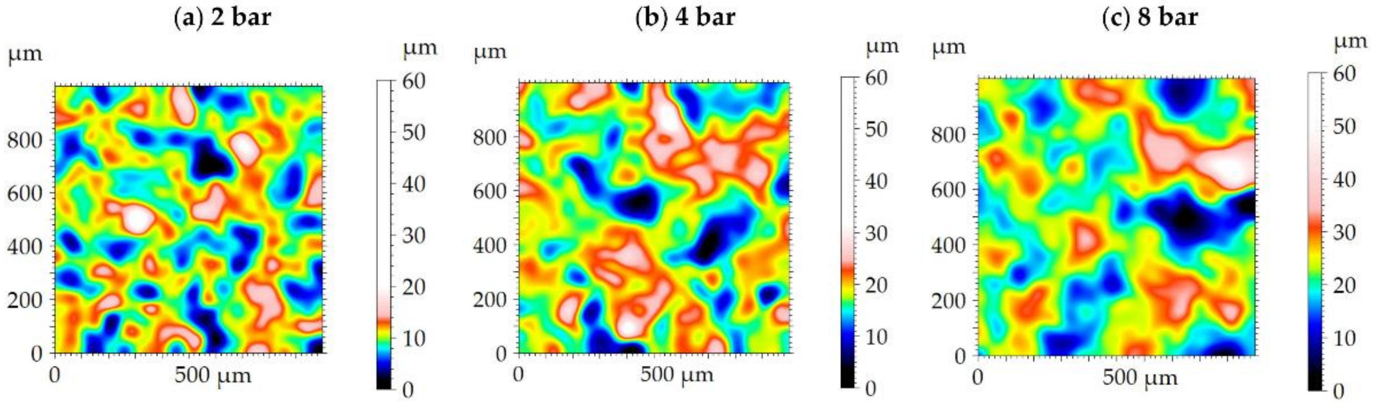

Figure 6. Surface topographies of TA6V samples grit-blasted at 2 bar (**a**), 4 bar (**b**), and 8 bar (**c**) with the C300 medium. The range of height varies significantly. The surfaces are the same as those presented in Figure 2 but this time filtered with a low-pass Gaussian filter at a 120 µm cut off (the relevance scale).

In Figure 8, the slopes (Figure 8i) and intercepts (Figure 8ii) of the bootstrapping model based on residuals for the two methods of calculation (Patchwork and Sdr) are analyzed. For G 100, the relationship between slope stability and initial roughness (Figure 8(ai)) is relatively stable, with smoother and more homogeneous surfaces showing lower variability in slope values. In contrast, for C 300, the relationship is more variable, with higher initial roughness leading to increased unstable slope values due to the angular particles' sharp edges. The variations stabilize at the same scale as in the comparison of the bootstrapping models in Figure 5 under H1. The results of the slope and intercept variations show a distinct behavior for the C 300 blasting medium (corundum). For this aggressive medium, at small calculation scales, there is little variation in the surface area developed relative to pressure. The high intercept at small scales indicates that even at the lowest pressure, the surface is already rougher compared to other media. The results of all the distributions of slopes and intercepts can be found in Appendix B.

After selecting our bootstrap on residuals model, the analysis of the R^2 distribution at the relevant scale using this method shows disparities among the media and methods of calculation (Figure 9). Surprisingly, the trend is reversed for the R^2 values compared to the methods of calculation of the relative area. The Patchwork method (Figure 9i) shows numerous values close to 1 for G 100, the third series of G 250, and C 300 media, whereas the Sdr method (Figure 9ii) shows values close to 1 for series 1 and 2 of the G 250 medium (Figure 9a). While both methods yield high R^2 values, there are notable differences between them. The Patchwork method produces smoother histograms, which may be advantageous for certain analyses. However, in the case of the triple repetition for the same medium G 250, the results differ between the two methods, making it challenging to establish a definitive strategy for selecting one method over the other. To address this, the method yielding the highest correlation (the best R^2 value) could be prioritized. This strategy combines the strengths of both methods while ensuring the most robust correlation for each specific case.

(**a**) H1 (**b**) H0

(**i**) Simple bootstrap

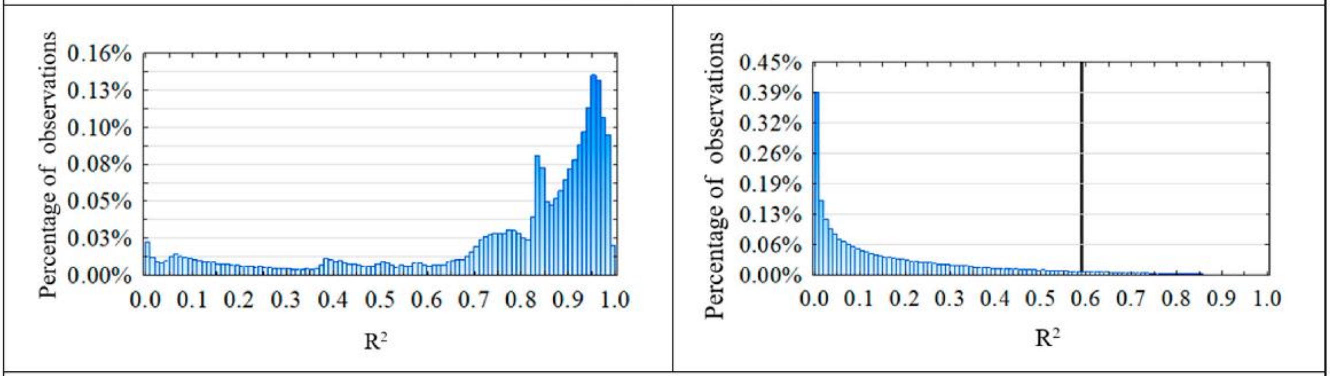

(**ii**) Bootstrap based on pairs

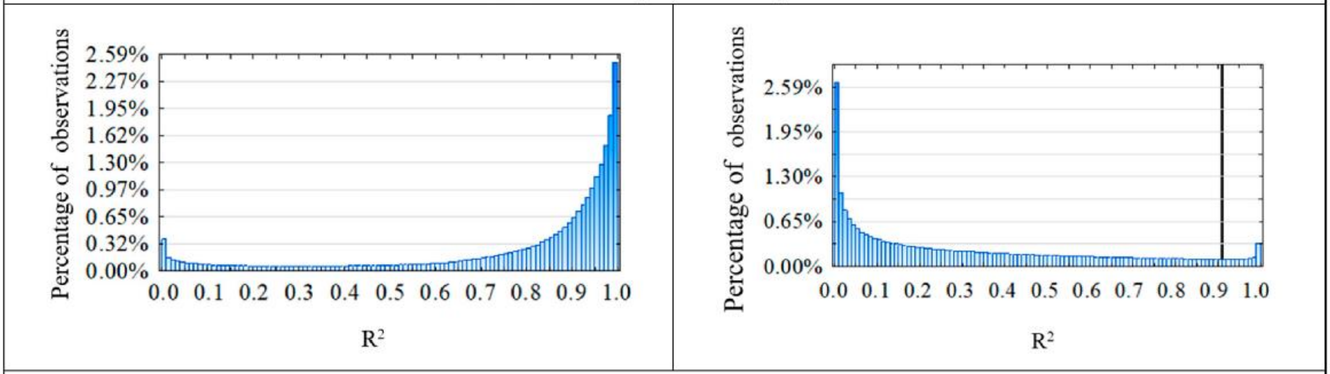

(**iii**) Bootstrap based on residuals

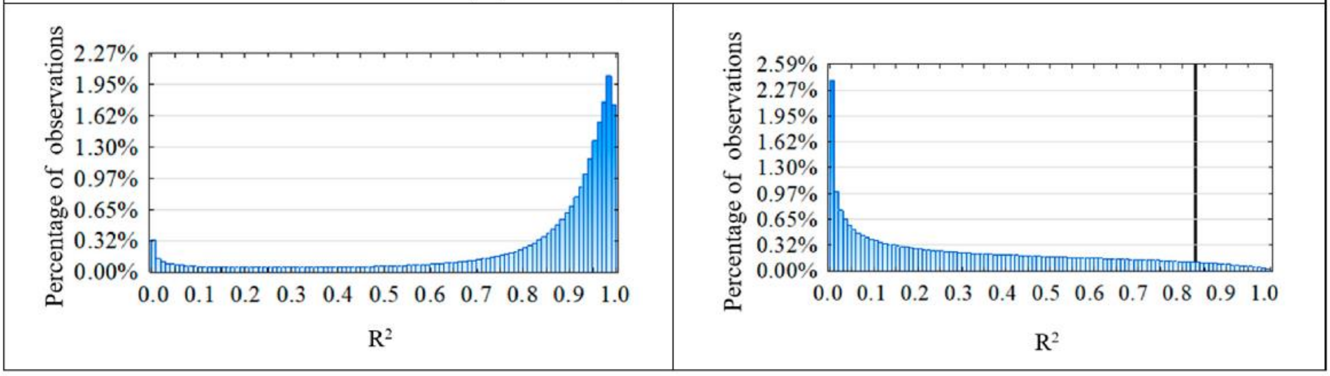

Figure 7. Distributions of the R^2 values at all scales under H1 (**a**) and H0 (**b**) for every method of bootstrapping computation: simple bootstrap (**i**), paired bootstrap (**ii**), and bootstrap based on residuals (**iii**). The black lines on the H0 plots are the threshold value at 95% of the R^2 distribution: 0.59 (**bi**), 0.91 (**bii**), and 0.83 (**biii**).

To conclude this analysis, the results of the relationship between relative area and pressure were plotted at the optimal pertinence scale (Figure 9), encompassing all media (Figure 10a–e) and both relative area calculation methods (Figure 10i,ii). The relevance scale ranges between 10,000 μm^2 and 14,000 μm^2 for the Patchwork method (Figure 10i).

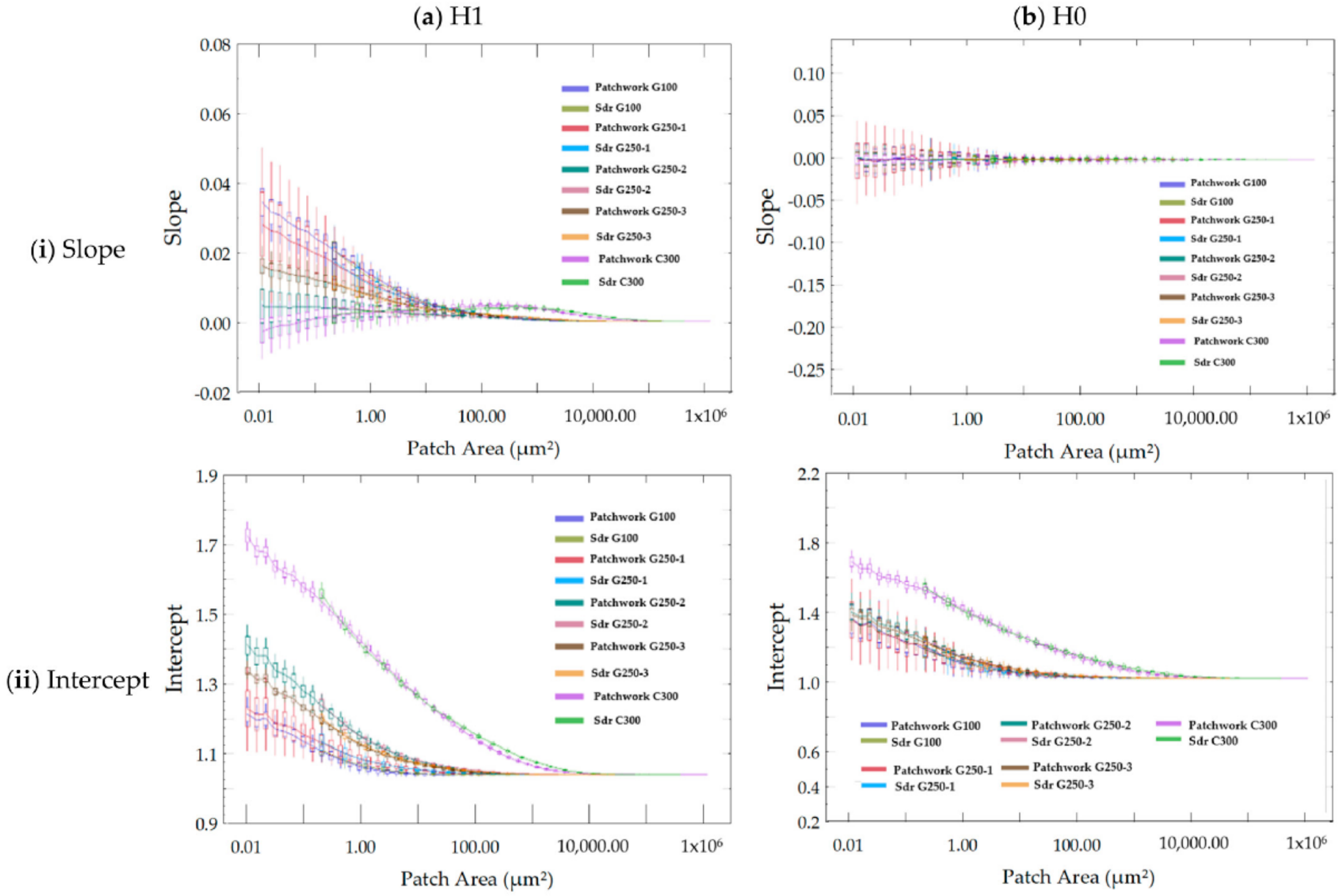

Figure 8. Evolution of the slope (**i**) and intercept (**ii**) as a function of scale for H1 (**a**) and H0 (**b**) using bootstrap based on residuals.

The study of the distribution of the intercepts according to the slopes at the relevant scale can be added to these insights (Figure 11). Besides the fact that the glass beads (G100, G250) are grouped together, there are three types of distributions of these points. The first one is a rather oblique distribution of intercepts for the fine glass beads (G 100). The slightly oblique distributions of this material indicate that the intercept is relatively constant, while the slope varies, suggesting that the initial roughness is quite stable, but the effect of pressure varies. While the points form a nearly vertical distribution for the angular medium (C 300), the effect of the pressure on the relative area (slope) is quite stable for this medium, but the initial roughness varies significantly. This type of distribution could indicate that the medium had a uniform relation to the pressure but with variable starting conditions. These findings suggest that using an angular medium like C 300 might be optimal for applications requiring high stability in response to varying pressures. The variability in surface roughness across the different media (e.g., G 100, G 250, C 300) can be attributed to the intrinsic properties of each medium, including particle hardness, size, and morphology. For instance, the corundum-based C 300 medium, characterized by its higher hardness and angular morphology, induces more aggressive impacts on the surface, resulting in a higher intercept at small scales. It indicates a rougher initial surface even at lower pressures compared to the softer and more spherical glass beads (e.g., G 100 and G 250). In contrast, the glass beads, due to their lower hardness and smoother shape, tend to cause more gradual surface roughening, leading to lower initial roughness and a more pronounced dependency on pressure, as seen in their slope distributions. The differences in particle size also play a role: larger particles (e.g., G 250) can create broader indentations, contributing to different scaling behaviors compared to smaller particles like G 100. These intrinsic properties directly influence the interaction mechanisms between the blasting media and the surface, which are captured in the variations in the slope and intercept distributions, reflecting the distinct roughness evolution patterns for each medium. However, the two methods of calculation, Patchwork and Sdr, lead to the same three clusters in Figure 11, which means that both methods characterize the relevant scale for studying the relative area depending on the pressure of blasting.

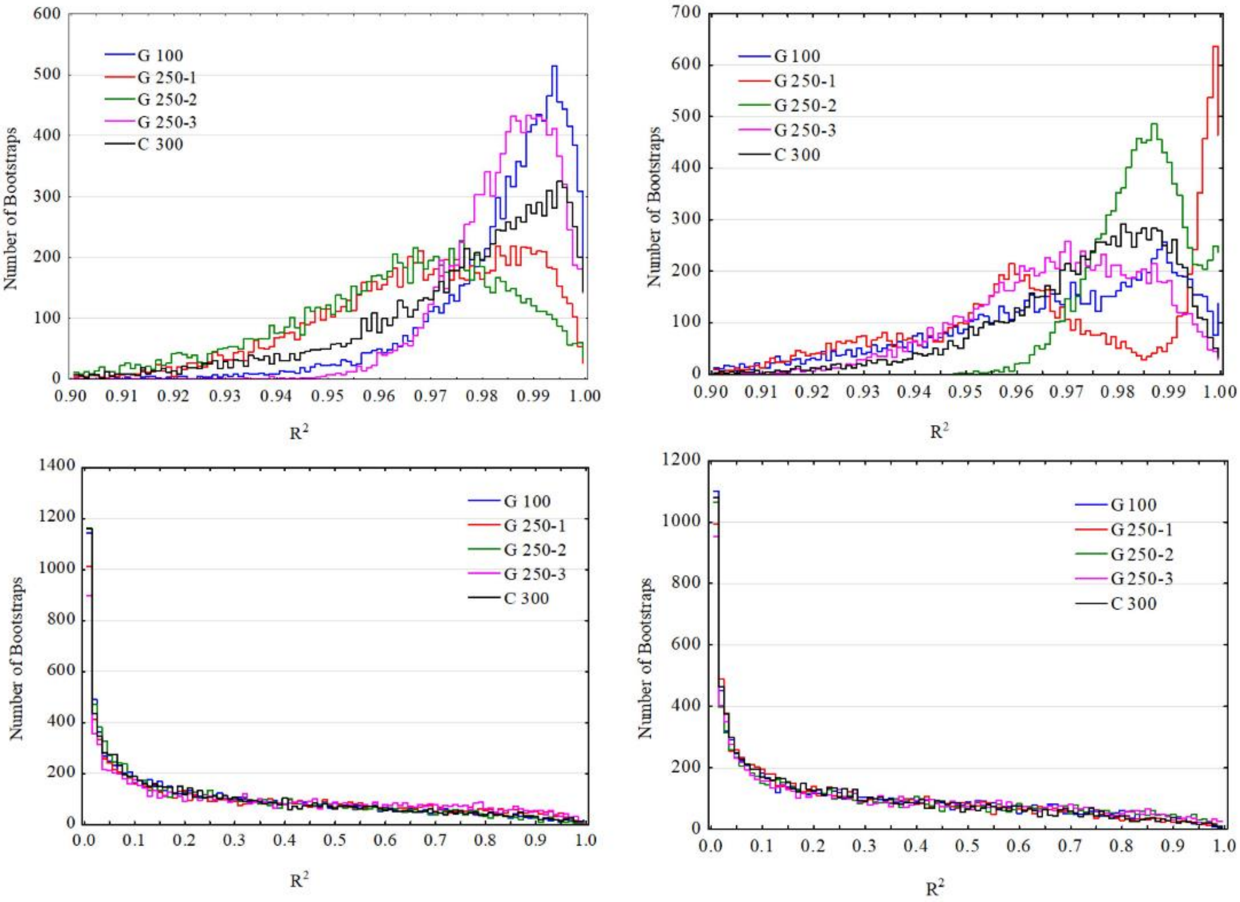

(**i**) Patchwork method

(**ii**) Sdr method

(**a**) H1

(**b**) H0

Figure 9. Distribution of the R^2 values by medium at the relevant scale for the Patchwork (**i**) and Sdr (**ii**) methods and for H1 (**a**) and H0 (**b**). The digits after 250 indicate the blasting series (e.g., G 250-1 = first series of the G250 medium).

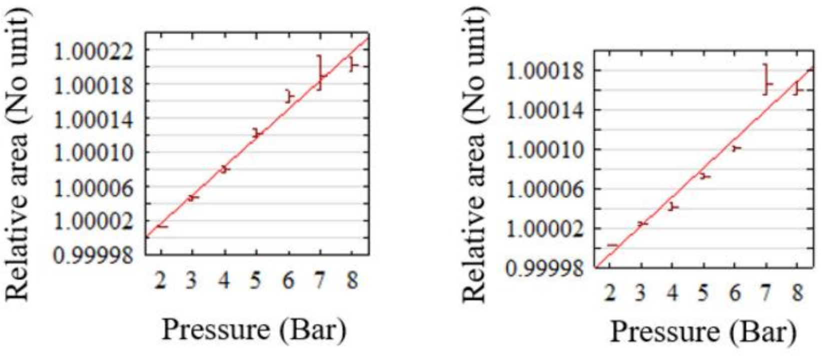

(**i**) Patchwork method

(**ii**) Sdr method

(**a**) G 100

Figure 10. *Cont.*

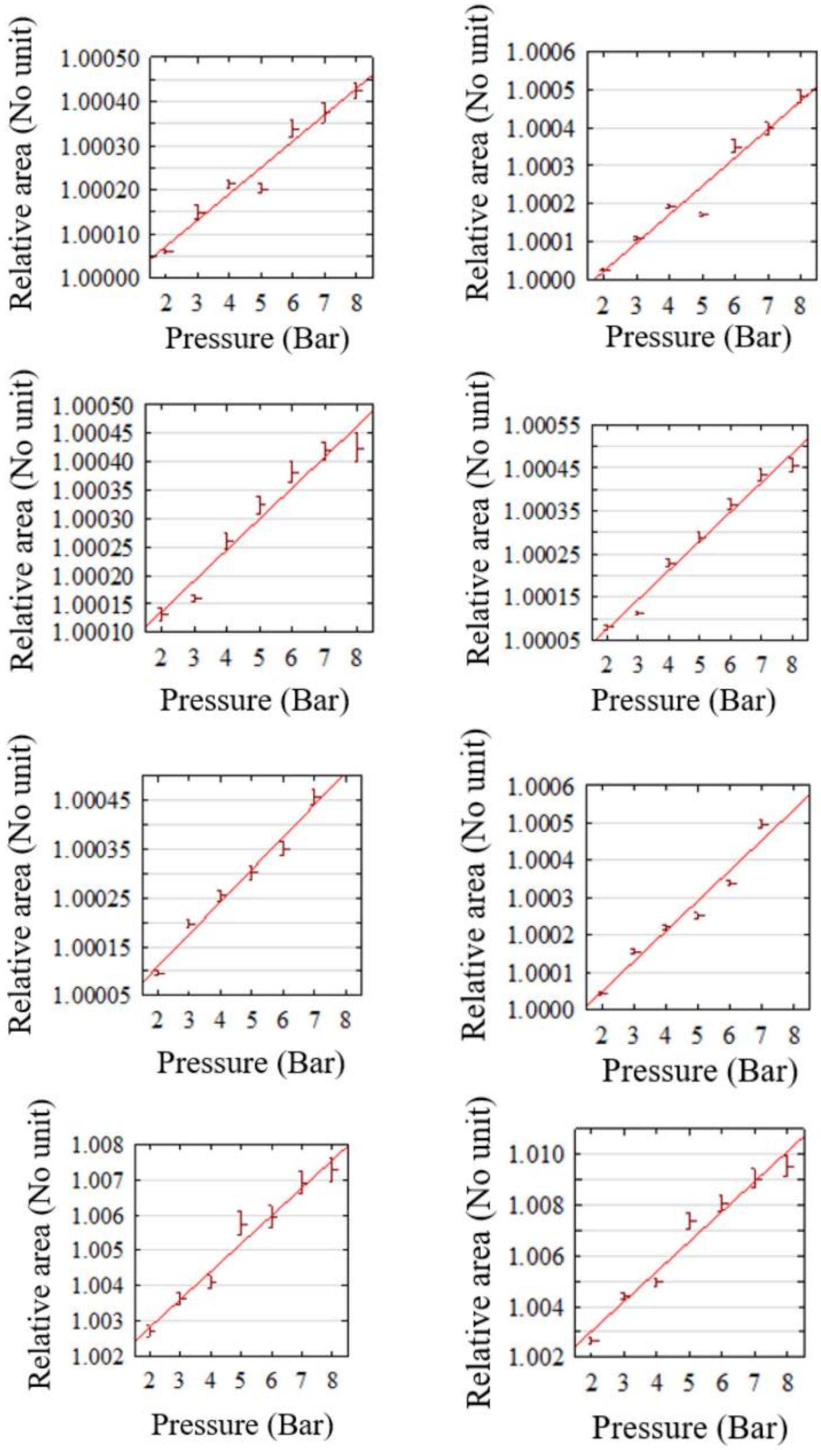

(**b**) G 250-1

(**c**) G 250-2

(**d**) G 250-3

(**e**) C 300

Figure 10. Box plots of the relative area values by pressure at the relevance scale (tile size between 10,000 μm^2 and 14,000 μm^2 for the Patchwork method and cut-off length of 120 μm for the Sdr method). The results are presented by medium (**a**–**e**) and calculation method (**i**,**ii**).

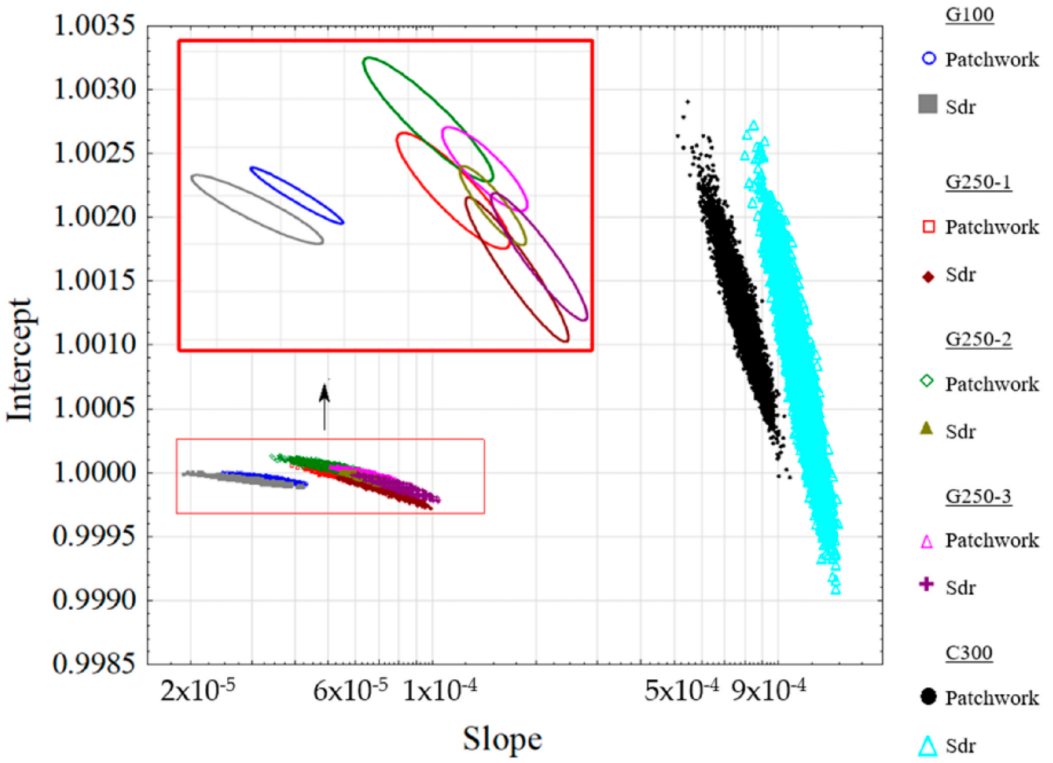

Figure 11. Bivariate density (intercept, slope) of the linear regression at the relevant scale between relative area for the three media of grit blasting and the two methods of relative area calculation (Patchwork, Sdr) obtained by bootstrap on residuals. The red frame is a zoom with ellipses of confidence at 95%.

4. Discussion

The analysis results indicate that the bootstrapping method based on residuals is the best choice for characterizing the relevance scale to highlight the influence of the grit blasting pressure on the relative area. In this study, we have several aspects that warrant comparison with the existing literature. These aspects pertain to roughness parameters, specifically how our method is innovative compared to the grit blasting characterization parameters already presented in the literature and the scale used to characterize the surface. This also concerns the different media and how their nature influences surface topography.

The use of the Sa parameter to characterize the influence of blasting on materials is documented in the literature [10]. However, the methods of calculation of the relative area proposed in this study is considered more suitable because the relative area captures surface irregularities at different scales and is sensitive to large-scale features such as deep recesses and significant local variations. The Sdq parameter is discussed in the study of Ho et al. [15]. Impact craters are generated by SiC particles striking the surface of the substrate. The repetitive impacts can lead to the development of a plastically deformed layer and the formation of additional craters on top of existing ones. This process results in the creation of a series of small peaks and valleys with sharp edges, whose slopes can be characterized using Sdq. This study, which is very similar to ours, gives a scale of relevance for characterizing the relationship between the value of the multiscale Sdq parameter and the blasting pressure. The filtering uses a low-pass filter with a cut off of 120 µm, which also corresponds to our relevance scale with the Sdr method. This result is interesting because the pressures used for this study changed slightly, ranging from 1 to 7 bar, whereas our samples were blasted from 2 to 8 bar. This comparison gives an argument for the generalization of our results.

It is essential to address two critical aspects in the discussion part: the influence of surface modification during the experiment on the results and the impact of the chosen Gaussian filtering method on fractal surfaces. Below, we provide detailed considerations regarding these aspects. Factors such as humidity and temperature can disrupt measurements by introducing uncertainties. The room where the measurements were conducted is a temperature-controlled environment with an automatic regulation system maintaining a constant temperature of 20 °C. Regarding humidity, the air circulation provided by the ventilation system helps regulate condensation and the humidity density in the measurement room. Neither the temperature of the metal during blasting nor the humidity altered the surface appearance during the experiment due to the excellent mechanical properties of TA6V, which is resistant to heat and corrosion [26,27,47]. Regarding the use of Gaussian filtering, two remarks can be made. This surface filtering method is the most common in surface processing; it is well documented, and its limitations are well known. However, we acknowledge that for fractal surfaces, such as those generated by blasting, distortions may be introduced by the Gaussian filter on the sharpest features. The chapter on the use of filters in the book by Blunt and Jiang [36] clearly explains the difference between robust and Gaussian filters on a plateau-honed surface. However, the robust filter requires a longer computation time, which explains our choice in this study. A comparison between both is necessary.

The results indicate that the relationship between pressure and roughness evolution is not strictly linear for some blasting media such as C300, as initially hypothesized. At lower pressures (e.g., 2 bar), roughness increases are moderate and uniform, reflecting gradual material erosion. In contrast, at higher pressures (e.g., 8 bar), the changes become pronounced, with deeper asperities and irregular textures, likely due to enhanced impact energy and its effects on asperity deformation and void formation.

Given these results, a nonlinear model such as $Y = aP^b + c$ may better capture the relationship between pressure and roughness, where Y represents a roughness parameter, P is the pressure, and a, b, c are the model parameters. Notably, the model converges to the linear approximation $Y = aP + c$, as discussed earlier in this article, when b is statistically equal to 1. Significant deviations from $b \approx 1$ could reveal transitions in the dominant mechanisms of surface modification with different materials and process conditions.

To test if $b < 1,\ b = 1\ or\ b > 1$, the bootstrapping techniques proposed in this paper (simple, paired, or residual bootstraps) could assess the statistical significance of parameters a, b, and c, providing insights into the interplay between the pressure, media type, and substrate response. However, implementing such a nonlinear model would require solving a regression problem through iterative optimization algorithms, ensuring convergence to a unique global minimum. This added complexity would extend beyond the current study's scope. We plan to apply this framework to further research on the nonlinear effects of contact pressure and media type on surface topography.

The grit blasting process is known to exhibit inherent variability, which can contribute to the inconsistencies observed in the G 250 medium series. Factors related to the sandblasting equipment itself, such as nozzle wear or inconsistent abrasive flow, can further contribute to variations in surface preparation. These variations lead to fluctuations in the surface roughness and texture of materials treated with G 250, as the process may not consistently achieve the intended surface finishing across different batches or applications. Therefore, the lack of reliability in the grit blasting process is likely a significant factor contributing to the variability observed in the G 250 series.

The results of this study may encourage further research to continue determining the reference scale of complex surfaces created by different processes that allow for varying intensities of surface modification. Thus, it is possible that the results could be compared with acid etching, electric discharge machining, and shot peening (i.e., steel bead blasting) on titanium alloys like in this study. By varying parameters such as the type of filament used and the electrical intensity [48] for electric discharge machining, it is possible to modify the surface topography and study the relevant scale for this process. The same applies to soaking time in acid during chemical etching [49]. Some studies on functional optimization already exist and aim to identify a relevant scale for process analysis. For instance, one study highlights the sensitivity of hMSC cells to topographical features at different scales (Ra, Sm) on surfaces generated by EDM (electric discharge machining) [50].

5. Conclusions

In this study, the results of different bootstrapping methods are presented in order to find a relevant scale for determining the relationship between the relative area and blasting pressure. Three types of media were tested with seven pressures. Two methods for calculating the relative area (Patchwork and Sdr) and three bootstrapping methods (simple bootstrap, double bootstrap based on pair replication, and double bootstrap based on residuals) for determining the relevant scale associated with the regression are studied. Several factors already presented in other studies were considered to generalize our results, such as the influence of different media or different pressures. The scale of pertinence corresponds to a tile size of 10,000 μm^2 for the Patchwork method and a filtering cut-off length of 120 µm for the Sdr method using low-pass filtering. Using the regression results of the bootstrap on residuals method, the R^2 value required to characterize the area/pressure link has to be higher than 0.83 to be significant at the threshold of 5%. In addition, to determine pertinent scales and the R^2 values, our study contributes to the understanding of how different media types and blasting pressures influence surface topography, providing insights that can inform more effective material processing and surface treatment strategies.

Author Contributions: Conceptualization, M.B.; methodology, C.B.; software, R.G.; validation, M.B. and M.W.; formal analysis, M.B. and F.B.; investigation, F.B. and J.L.; data curation, J.L. and F.B.; writing—original draft preparation, F.B.; writing—review and editing, J.L. and F.B.; visualization, M.B. and F.B.; supervision, M.B. All authors have read and agreed to the published version of the manuscript.

Funding: This research received no external funding.

Data Availability Statement: The data are available on demand.

Conflicts of Interest: Author Julie Lemesle was employed by U.R Concept. The remaining authors declare that the research was conducted in the absence of any commercial or financial relationships that could be construed as a potential conflict of interest.

Appendix A

The original unfiltered blasted surface topographies with the three materials used in this study are presented at different pressures (in bar) to represent the differences between topographies.

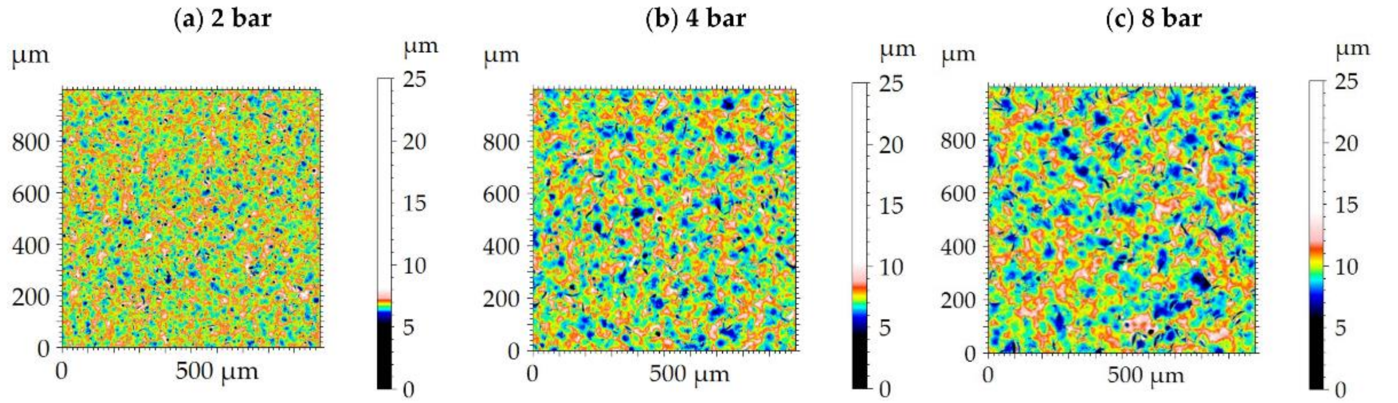

Figure A1. Surface topographies of blasted surface using the medium G 100 at (**a**) 2 bar of pressure, (**b**) 4 bar of pressure, and (**c**) 8 bar of pressure.

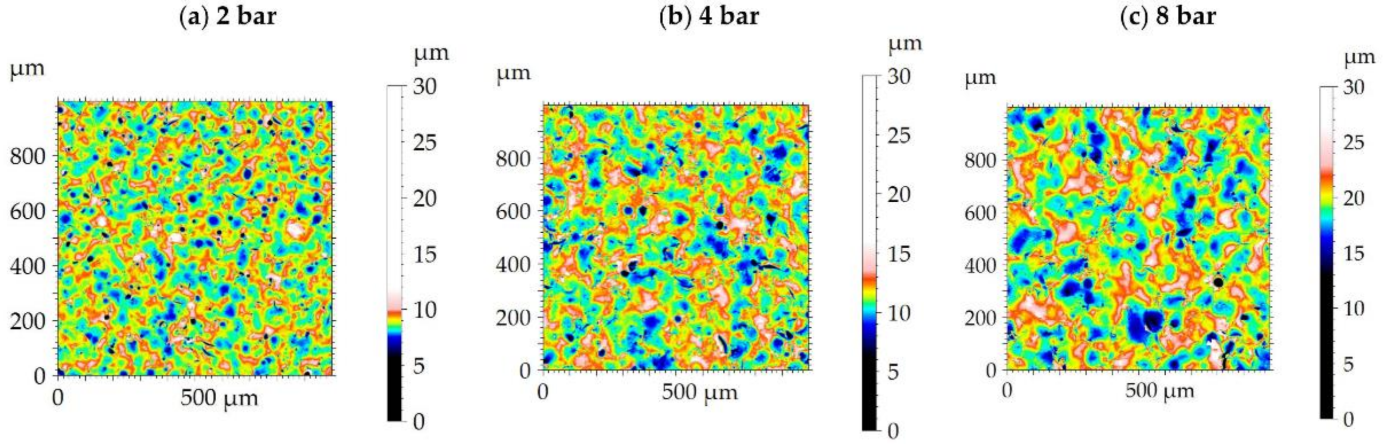

Figure A2. Surface topographies of blasted surface using the medium G 250 at (**a**) 2 bar of pressure, (**b**) 4 bar of pressure, and (**c**) 8 bar of pressure.

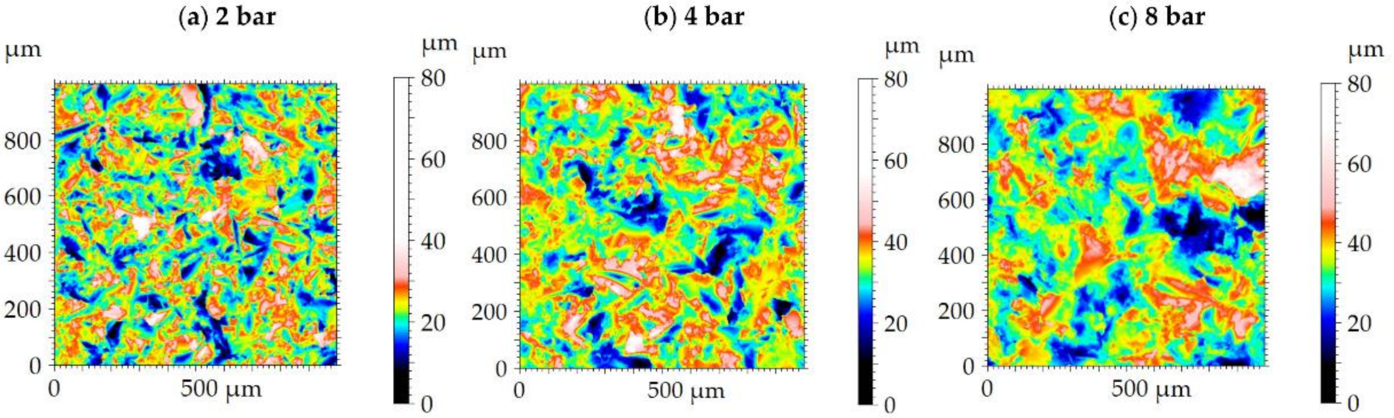

Figure A3. Surface topographies of blasted surface using the medium C 300 at (**a**) 2 bar of pressure, (**b**) 4 bar of pressure, and (**c**) 8 bar of pressure.

Appendix B

This section presents tables containing the results of linear regressions according to each hypothesis and each bootstrapping method.

Table A1. Results of the linear regression distributions according to hypothesis H1 for the simple bootstrap method. For the G 250 medium, the last digit represents the series, e.g., G 250-1 corresponds to the first series of this medium.

Media	Intercept P5	R^2 P5	Slope P5	Intercept P50	R^2 P50	Slope P50	Intercept P95	R^2 P95	Slope P95
				Patchwork method					
G 100	0.99994346	0.9605421	3.1964×10^{-5}	0.99994994	0.98024554	3.3521×10^{-5}	0.99995545	0.99069454	3.5564×10^{-5}
G 250-1	0.99994265	0.93998527	5.6607×10^{-5}	0.99995483	0.95741298	5.9307×10^{-5}	0.99996718	0.97144593	6.2193×10^{-5}
G 250-2	1.00001458	0.91216793	5.0771×10^{-5}	1.00002897	0.94877385	5.4101×10^{-5}	1.00004328	0.97272786	5.7609×10^{-5}
G 250-3	0.99996649	0.96296679	6.356×10^{-5}	0.99997767	0.97724731	6.6341×10^{-5}	0.99998741	0.98845025	6.9056×10^{-5}
C 300	1.00101778	0.93252007	0.00074162	1.00123208	0.96675567	0.00079234	1.00145402	0.98623911	0.00083841
				Sdr method					
G 100	0.99993077	0.91114478	2.8109×10^{-5}	0.99993543	0.95429143	2.9207×10^{-5}	0.99993925	0.97222884	3.0678×10^{-5}
G 250-1	0.99986366	0.94674398	7.2577×10^{-5}	0.99987231	0.95471517	7.4832×10^{-5}	0.99988003	0.95981093	7.7251×10^{-5}
G 250-2	0.99993112	0.96827255	6.6163×10^{-5}	0.99994013	0.97783397	6.8047×10^{-5}	0.99994774	0.98597727	7.0285×10^{-5}
G 250-3	0.99987676	0.94419689	7.9193×10^{-5}	0.99988505	0.95428896	8.1181×10^{-5}	0.99989356	0.96350047	8.3368×10^{-5}
C 300	1.00045608	0.93746278	0.00112675	1.00067672	0.96254004	0.0011778	1.00088318	0.97971935	0.00123367

Table A2. Results of the linear regression distributions according to hypothesis H0 for the simple bootstrap method. For the G 250 medium, the last digit represents the series, e.g., G 250-1 corresponds to the first series of this medium.

Media	Intercept P5	R^2 P5	Slope P5	Intercept P50	R^2 P50	Slope P50	Intercept P95	R^2 P95	Slope P95
				Patchwork method					
G 100	0.99998005	0.00074667	-2.59889×10^{-5}	1.00011303	0.0998969	7.95122×10^{-7}	1.00024542	0.57852645	2.8049×10^{-5}
G 250-1	1.00000187	0.00099695	−0.00005105	1.00024848	0.09622853	5.4433×10^{-7}	1.0004976	0.58899767	4.9761×10^{-5}
G 250-2	1.00006342	0.00116497	-4.19153×10^{-5}	1.00028471	0.09044521	2.79673×10^{-6}	1.00051083	0.55888993	4.5329×10^{-5}
G 250-3	1.00003625	0.00088057	-4.96151×10^{-5}	1.00028404	0.12048242	-1.49483×10^{-6}	1.0005359	0.64680814	4.8274×10^{-5}
C 300	1.0021071	0.0005601	−0.000653803	1.00525864	0.08550533	-1.08371×10^{-5}	1.00840518	0.55558088	0.00063065
				Sdr method					
G 100	0.99996117	0.00153102	-2.35362×10^{-5}	1.00007958	0.10014213	5.07146×10^{-7}	1.00020192	0.58251626	2.3917×10^{-5}
G 250-1	0.99993002	0.00103109	-6.52164×10^{-5}	1.00026373	0.08679445	-3.912×10^{-6}	1.00057789	0.58270044	6.2492×10^{-5}
G 250-2	0.99999004	0.00129898	-5.41773×10^{-5}	1.00029743	0.10132161	-3.3893×10^{-6}	1.00055961	0.56778929	5.7678×10^{-5}
G 250-3	0.99994349	0.00151227	-6.60741×10^{-5}	1.00027356	0.12006613	-4.5955×10^{-6}	1.00057745	0.64192854	6.2393×10^{-5}
C 300	1.00188342	0.00087451	−0.000933592	1.00663373	0.09388461	-1.4159×10^{-5}	1.01112943	0.56925084	0.00091395

Table A3. Results of the linear regression distributions according to hypothesis H1 with the paired bootstrap method. For the G 250 medium, the last digit represents the series, e.g., G 250-1 corresponds to the first series of this medium.

Media	Intercept P5	R^2 P5	Slope P5	Intercept P50	R^2 P50	Slope P50	Intercept P95	R^2 P95	Slope P95
				Patchwork method					
G 100	0.99992846	0.93651857	2.97081×10^{-5}	0.99994992	0.98765361	3.34376×10^{-5}	0.99996945	0.99933642	3.9465×10^{-5}
G 250-1	0.99991799	0.85158765	5.13625×10^{-5}	0.99995367	0.96156467	5.92575×10^{-5}	0.99999982	0.99606657	6.6725×10^{-5}
G 250-2	0.99997389	0.88291308	4.23452×10^{-5}	1.00002549	0.96352655	5.4452×10^{-5}	1.00010307	0.99502698	6.745×10^{-5}
G 250-3	0.99994599	0.94350252	5.19333×10^{-5}	0.99997793	0.98176962	6.61776×10^{-5}	1.00004143	0.99932267	7.3596×10^{-5}
C 300	1.00073813	0.88411381	0.000691077	1.00119264	0.97430649	0.000793964	1.00180254	0.99803303	0.00091091
				Sdr method					
G 100	0.99990288	0.89934141	2.43914×10^{-5}	0.99993617	0.96513054	2.91411×10^{-5}	0.9999516	0.99813461	3.5923×10^{-5}
G 250-1	0.99981818	0.83799507	6.65061×10^{-5}	0.99987617	0.95563311	7.46588×10^{-5}	0.999907	0.99924201	8.2506×10^{-5}
G 250-2	0.9998916	0.95753257	5.96684×10^{-5}	0.99993774	0.98344327	6.85639×10^{-5}	0.99998996	0.99888513	7.859×10^{-5}
G 250-3	0.99982669	0.90361156	5.85351×10^{-5}	0.99988662	0.96528469	8.15432×10^{-5}	0.99997794	0.99853208	9.2672×10^{-5}
C 300	0.99986501	0.90528018	0.001002537	1.00060315	0.97048401	0.001182872	1.00176586	0.99498155	0.00138857

Table A4. Results of the linear regression distributions according to hypothesis H0 with the paired bootstrap method. For the G 250 medium, the last digit represents the series, e.g., G 250-1 corresponds to the first series of this medium.

Media	**Intercept P5**	**R^2 P5**	**Slope P5**	**Intercept P50**	**R^2 P50**	**Slope P50**	**Intercept P95**	**R^2 P95**	**Slope P95**
Patchwork method									
G 100	0.9999	0.00162	−0.000039	1.0001	0.18	−0.0000034	1.0003	0.89	0.000034
G 250-1	0.9998	0.00219	−0.00007	1.0002	0.25	−0.0000005	1.0006	0.89	0.000081
G 250-2	0.9999	0.0022	−0.000071	1.0003	0.22	−0.00000234	1.0006	0.89	0.000067
G 250-3	0.9998	0.00144	−0.000082	1.0002	0.27	0	1.0006	0.96	0.000085
C 300	0.9993	0.00198	−0.001029	1.0052	0.26	0	1.0104	0.91	0.001068
Sdr method									
G 100	0.9999	0.00161	−0.000036	1	0.21	0.0000005	1.0002	0.9	0.000035
G 250-1	0.9997	0.00158	−0.000092	1.0002	0.21	−0.0000014	1.0004	0.89	0.00009
G 250-2	0.9998	0.0014971	-8.77189×10^{-5}	1.0002971	0.2115413	-3.20292×10^{-6}	1.00074429	0.9	0.000083
G 250-3	0.9997	0.0018004	−0.000108688	1.0002212	0.2687166	4.18523×10^{-6}	1.00076864	0.95	0.0001
C 300	0.9991	0.0018053	−0.001491175	1.0071597	0.2177582	−0.000103172	1.0141841	0.8828032	0.001440755

Table A5. Results of the linear regression distributions according to hypothesis H1 with the bootstrap on residuals method. For the G 250 medium, the last digit represents the series, e.g., G 250-1 corresponds to the first series of this medium.

Media	**Intercept P5**	**R^2 P5**	**Slope P5**	**Intercept P50**	**R^2 P50**	**Slope P50**	**Intercept P95**	**R^2 P95**	**Slope P95**
Patchwork method									
G 100	0.999932	0.9565443	3.00899×10^{-5}	0.9999498	0.9874099	3.3551×10^{-5}	0.99996783	0.997883	3.72897×10^{-5}
G 250-1	0.9999097	0.9310252	5.07515×10^{-5}	0.9999556	0.970523	5.93189×10^{-5}	0.99999789	0.9946046	6.75171×10^{-5}
G 250-2	0.9999837	0.9172058	4.52646×10^{-5}	1.0000289	0.9653095	5.42804×10^{-5}	1.00007403	0.992669	6.2665×10^{-5}
G 250-3	0.9999418	0.9660482	5.87297×10^{-5}	0.9999777	0.9854348	6.63596×10^{-5}	1.00001188	0.9970392	7.37881×10^{-5}
C 300	1.0007119	0.9295922	0.000684518	1.0011989	0.9806584	0.000793258	1.00181321	0.9973577	0.000898461
Sdr method									
G 100	0.9999143	0.910487	2.50086×10^{-5}	0.9999348	0.9705346	2.90556×10^{-5}	0.99995929	0.9959154	3.37325×10^{-5}
G 250-1	0.9998133	0.9205808	6.38924×10^{-5}	0.9998784	0.9650501	7.46952×10^{-5}	0.99992171	0.9989289	8.52443×10^{-5}
G 250-2	0.999903	0.9680796	6.14229×10^{-5}	0.9999401	0.9845218	6.83071×10^{-5}	0.99997368	0.9979556	7.49173×10^{-5}
G 250-3	0.9998274	0.9370731	6.85729×10^{-5}	0.9998864	0.9694675	8.09004×10^{-5}	0.9999449	0.9928928	9.30415×10^{-5}
C 300	0.9999004	0.9376534	0.001023062	1.0006449	0.9760935	0.001181016	1.00150702	0.9940184	0.001328685

Table A6. Results of the linear regression distributions according to hypothesis H0 with the bootstrap on residuals method. For the G 250 medium, the last digit represents the series, e.g., G 250-1 corresponds to the first series of this medium.

Media	**Intercept P5**	**R^2 P5**	**Slope P5**	**Intercept P50**	**R^2 P50**	**Slope P50**	**Intercept P95**	**R^2 P95**	**Slope P95**
Patchwork method									
G 100	0.9999299	0.0020084	-3.11653×10^{-5}	1.0001127	0.202859	9.53073×10^{-7}	1.00028281	0.7994261	3.65729×10^{-5}
G 250-1	0.9999497	0.0023251	-7.31388×10^{-5}	1.0002654	0.2443196	-2.80214×10^{-6}	1.00061606	0.8626616	6.14137×10^{-5}
G 250-2	1.0000079	0.001991	-5.11685×10^{-5}	1.000287	0.1917183	2.84894×10^{-6}	1.00056674	0.78524	5.6151×10^{-5}
G 250-3	0.9999356	0.0029693	-6.35342×10^{-5}	1.0002779	0.288483	-6.62178×10^{-7}	1.00059524	0.8713916	6.56124×10^{-5}
C 300	1.0006622	0.0018682	−0.00086555	1.0049848	0.1982778	4.17098×10^{-5}	1.00951576	0.8162126	0.000857372
Sdr method									
G 100	0.9999363	0.0019827	-3.1144×10^{-5}	1.0000939	0.2274792	-2.54905×10^{-6}	1.00024402	0.8072309	2.78718×10^{-5}
G 250-1	0.9998456	0.0026152	-7.49781×10^{-5}	1.0002684	0.2167074	-5.68906×10^{-6}	1.00064383	0.800484	7.44384×10^{-5}
G 250-2	0.999928	0.0022781	-7.96435×10^{-5}	1.0003079	0.2371843	-5.22383×10^{-6}	1.00069378	0.8569223	6.86005×10^{-5}
G 250-3	0.9998214	0.0029229	-7.80835×10^{-5}	1.0002386	0.2563251	1.99542×10^{-6}	1.00066272	0.8536141	8.14062×10^{-5}
C 300	1.0004782	0.0020249	−0.001196388	1.0067009	0.2076762	-2.27189×10^{-5}	1.01303065	0.7983381	0.001178235

References

1. Whitehouse, D.J. *Handbook of Surface Metrology*; Routledge: New York, NY, USA, 2023; ISBN 978-0-203-75260-9.
2. Leach, R. (Ed.) *Characterisation of Areal Surface Texture*; Springer: Berlin/Heidelberg, Germany, 2013; ISBN 978-3-642-36457-0.
3. Chintapalli, R.K.; Rodriguez, A.M.; Marro, F.G.; Anglada, M. Effect of Sandblasting and Residual Stress on Strength of Zirconia for Restorative Dentistry Applications. *J. Mech. Behav. Biomed. Mater.* **2014**, *29*, 126–137. [CrossRef] [PubMed]

4. Anselme, K.; Bigerelle, M. Topography Effects of Pure Titanium Substrates on Human Osteoblast Long-Term Adhesion. *Acta Biomater.* **2005**, *1*, 211–222. [CrossRef] [PubMed]
5. Kim, S.-J.; Kim, T.-H.; Kong, J.-H.; Kim, Y.; Cho, C.-R.; Kim, S.-H.; Lee, D.-W.; Park, J.-K.; Lee, D.; Kim, J.-M. Dual-Scale Artificial Lotus Leaf Fabricated by Fully Nonlithographic Simple Approach Based on Sandblasting and Anodic Aluminum Oxidation Techniques. *Appl. Surf. Sci.* **2012**, *263*, 648–654. [CrossRef]
6. Shen, Y.; Tao, J.; Tao, H.; Chen, S.; Pan, L.; Wang, T. Nanostructures in Superhydrophobic Ti6Al4V Hierarchical Surfaces Control Wetting State Transitions. *Soft Matter* **2015**, *11*, 3806–3811. [CrossRef]
7. Bouzid, S.; Bouaouadja, N. Effect of Impact Angle on Glass Surfaces Eroded by Sand Blasting. *J. Eur. Ceram. Soc.* **2000**, *20*, 481–488. [CrossRef]
8. Zhou, J.; Ai, N.; Wang, L.; Zheng, H.; Luo, C.; Jiang, Z.; Yu, S.; Cao, Y.; Wang, J. Roughening the White OLED Substrate's Surface through Sandblasting to Improve the External Quantum Efficiency. *Org. Electron.* **2011**, *12*, 648–653. [CrossRef]
9. Su, N.; Yue, L.; Liao, Y.; Liu, W.; Zhang, H.; Li, X.; Wang, H.; Shen, J. The Effect of Various Sandblasting Conditions on Surface Changes of Dental Zirconia and Shear Bond Strength between Zirconia Core and Indirect Composite Resin. *J. Adv. Prosthodont.* **2015**, *7*, 214–223. [CrossRef]
10. Yetik, O.; Koçoğlu, H.; Yıldıran Avcu, Y.; Avcu, E.; Sınmazçelik, T. The Effects of Grit Size and Blasting Pressure on the Surface Properties of Grit Blasted Ti6Al4V Alloy. *Mater. Today Proc.* **2020**, *32*, 27–36. [CrossRef]
11. Wang, H.-Y.; Zhu, R.-F.; Lu, Y.-P.; Xiao, G.-Y.; He, K.; Yuan, Y.F.; Ma, X.-N.; Li, Y. Effect of Sandblasting Intensity on Microstructures and Properties of Pure Titanium Micro-Arc Oxidation Coatings in an Optimized Composite Technique. *Appl. Surf. Sci.* **2014**, *292*, 204–212. [CrossRef]
12. *ISO 25178-2:2021*; Geometrical Product Specifications (GPS)—Surface Texture: Areal—Part 2: Terms, Definitions, and Surface Texture Parameters. International Organization for Standardization: Geneva, Switzerland, 2021. Available online: https://www.iso.org/fr/standard/74591.html (accessed on 16 April 2023).
13. Valverde, G.B.; Jimbo, R.; Teixeira, H.S.; Bonfante, E.A.; Janal, M.N.; Coelho, P.G. Evaluation of Surface Roughness as a Function of Multiple Blasting Processing Variables. *Clin. Oral Implant. Res.* **2013**, *24*, 238–242. [CrossRef]
14. Bobrovskij, I.N. How to Select the Most Relevant Roughness Parameters of a Surface: Methodology Research Strategy. *IOP Conf. Ser. Mater. Sci. Eng.* **2018**, *302*, 012066. [CrossRef]
15. Ho, H.S.; Bigerelle, M.; Vincent, R.; Deltomb, R. Correlation Modeling between Process Condition of Sandblasting and Surface Texture: A Multi-scale Approach. *Scanning* **2016**, *38*, 191–201. [CrossRef]
16. Dong, W.P.; Sullivan, P.J.; Stout, K.J. Comprehensive Study of Parameters for Characterising Three-Dimensional Surface Topography: III: Parameters for Characterising Amplitude and Some Functional Properties. *Wear* **1994**, *178*, 29–43. [CrossRef]
17. Chetwynd, D.G. Slope Measurement in Surface Texture Analysis. *J. Mech. Eng. Sci.* **1978**, *20*, 115–119. [CrossRef]
18. Guo, Y.; Zhou, D.; Li, D.; Zhao, W.; Wang, Y.; Pang, L.; Shi, Z.; Zhou, T.; Sun, S.; Singh, C.; et al. Improved Energy Storage Performance of Sandwich-Structured P(VDF-HFP)-Based Nanocomposites by the Addition of Inorganic Nanoparticles. *J. Mater. Chem. C* **2023**, *11*, 6999–7009. [CrossRef]
19. Barros, H.D.O.; Abreu, R.F.; Abreu, T.O.; de Sousa, W.V.; Nogueira, F.E.A.; do Carmo, F.F.; de Morais, J.E.V.; do Nascimento, J.P.C.; da Silva, M.A.S.; da Silva, R.S.; et al. High Thermal Stability of the Microwave Dielectric Properties of $ZnNb_2O_6$ with $CaTiO_3$ Addition. *Phys. B Condens. Matter* **2024**, *695*, 416547. [CrossRef]
20. Persson, B.N.J. On the Fractal Dimension of Rough Surfaces. *Tribol. Lett.* **2014**, *54*, 99–106. [CrossRef]
21. Hutchings, I.M. A Model for the Erosion of Metals by Spherical Particles at Normal Incidence. *Wear* **1981**, *70*, 269–281. [CrossRef]
22. Gillström, P.; Jarl, M. Replacement of Pickling with Shot Blasting for Wire Rod Preparation. *Scand. J. Metall.* **2004**, *33*, 269–278. [CrossRef]
23. Ma, H.M.; Gao, X.-L.; Reddy, J. A Microstructure-Dependent Timoshenko Beam Model Based on a Modified Couple Stress Theory. *J. Mech. Phys. Solids* **2008**, *56*, 3379–3391. [CrossRef]
24. Chaudhri, M.M.; Walley, S.M. Damage to Glass Surfaces by the Impact of Small Glass and Steel Spheres. *Philos. Mag. A* **1978**, *37*, 153–165. [CrossRef]
25. Maeda, H.; Egami, N.; Kagaya, C.; Inoue, N.; Takesita, H.; Ito, K. Analysis of Particle Velocity and Temperature Distribution of Struck Surface in Fine Particle Peening. *Trans. Jpn. Soc. Mech. Eng.* **2001**, *67*, 2700–2706. [CrossRef]
26. Ciszak, C.; Popa, I.; Monceau, D.; Chevalier, S. High Temperature Behaviour of Ti Alloys in Moist Air. *Ann. Chim. Sci. Mater.* **2015**, *39*, 149–157. [CrossRef]
27. Melentiev, R.; Fang, F. Investigation of Erosion Temperature in Micro-Blasting. *Wear* **2019**, *420–421*, 123–132. [CrossRef]
28. Zahouani, H.; Vargiolu, R.; Loubet, J.-L. Fractal Models of Surface Topography and Contact Mechanics. *Math. Comput. Model.* **1998**, *28*, 517–534. [CrossRef]
29. Oshida, Y.; Munoz, C.A.; Winkler, M.M.; Hashem, A.; Itoh, M. Fractal Dimension Analysis of Aluminum Oxide Particle for Sandblasting Dental Use. *Bio Med. Mater. Eng.* **1993**, *3*, 117–126. [CrossRef]

30. Perrotti, V.; Aprile, G.; Degidi, M.; Piattelli, A.; Iezzi, G. Fractal Analysis: A Novel Method to Assess Roughness Organization of Implant Surface Topography. *Int. J. Periodontics Restor. Dent.* **2011**, *31*, 632.
31. Berkmans, F.; Lemesle, J.; Guibert, R.; Wieczorowski, M.; Brown, C.; Bigerelle, M. Two 3D Fractal-Based Approaches for Topographical Characterization: Richardson Patchwork versus Sdr. *Materials* **2024**, *17*, 2386. [CrossRef]
32. Kelechava, B. ASME B46.1-2019: Surface Texture (Roughness, Waviness, Lay). *The ANSI Blog*, 7 August 2020.
33. Krystek, M. A Fast Gauss Filtering Algorithm for Roughness Measurements. *Precis. Eng.* **1996**, *19*, 198–200. [CrossRef]
34. Yuan, Y.-B.; Qiang, X.-F.; Song, J.-F.; Vorburger, T.V. A Fast Algorithm for Determining the Gaussian Filtered Mean Line in Surface Metrology☆. *Precis. Eng.* **2000**, *24*, 62–69. [CrossRef]
35. Hara, S.; Tsukada, T.; Sasajima, K. An In-Line Digital Filtering Algorithm for Surface Roughness Profiles. *Precis. Eng.* **1998**, *22*, 190–195. [CrossRef]
36. Blunt, L.; Jiang, X. *Advanced Techniques for Assessment Surface Topography: Development of a Basis for 3D Surface Texture Standards "Surfstand"*; Elsevier: Amsterdam, The Netherlands, 2003.
37. Brinkmann, S. Development of a Robust Gaussian Regression Filter for Three-Dimensional Surface Analysis. In Proceedings of the 10th International Colloquium on Surface, Chemnitz, Germany, 31 January–2 February 2000.
38. *ISO 16610-21:2011*; Geometrical Product Specifications (GPS)—Filtration: Part 21: Linear Profiling Filters—Moving Average Filters. International Organization for Standardization: Geneva, Switzerland, 2011. Available online: https://www.iso.org/fr/standard/50176.html (accessed on 18 December 2024).
39. Raja, J.; Muralikrishnan, B.; Fu, S. Recent Advances in Separation of Roughness, Waviness and Form. *Precis. Eng.* **2002**, *26*, 222–235. [CrossRef]
40. Sahoo, P.; Barman, T.; Davim, J.P. Fractal Analysis in EDM. In *Fractal Analysis in Machining*; SpringerBriefs in Applied Sciences and Technology; Springer: Berlin/Heidelberg, Germany, 2011; Volume 3, pp. 69–81. ISBN 978-3-642-17921-1.
41. Chen, H.; Zhou, Y. Fractal Characteristics of 3D Surface Topography in Laser Machining. *IOP Conf. Ser. Mater. Sci. Eng.* **2018**, *382*, 042045. [CrossRef]
42. Brown, C.A.; Charles, P.D.; Johnsen, W.A.; Chesters, S. Fractal Analysis of Topographic Data by the Patchwork Method. *Wear* **1993**, *161*, 61–67. [CrossRef]
43. Mandelbrot, B. How Long Is the Coast of Britain? Statistical Self-Similarity and Fractional Dimension. *Science* **1967**, *156*, 636–638. [CrossRef]
44. Brown, C.A.; Hansen, H.N.; Jiang, X.J.; Blateyron, F.; Berglund, J.; Senin, N.; Bartkowiak, T.; Dixon, B.; Le Goïc, G.; Quinsat, Y.; et al. Multiscale Analyses and Characterizations of Surface Topographies. *CIRP Ann.* **2018**, *67*, 839–862. [CrossRef]
45. Efron, B.; Tibshirani, R. Bootstrap Methods for Standard Errors, Confidence Intervals, and Other Measures of Statistical Accuracy. *Stat. Sci.* **1986**, *1*, 54–75. [CrossRef]
46. Lieblich, M.; Barriuso, S.; Ibáñez, J.; Ruiz-de-Lara, L.; Díaz, M.; Ocaña, J.L.; Alberdi, A.; González-Carrasco, J.L. On the Fatigue Behavior of Medical Ti6Al4V Roughened by Grit Blasting and Abrasiveless Waterjet Peening. *J. Mech. Behav. Biomed. Mater.* **2016**, *63*, 390–398. [CrossRef]
47. Yang, J.; Song, Y.; Dong, K.; Han, E.-H. Research Progress on the Corrosion Behavior of Titanium Alloys. *Corros. Rev.* **2023**, *41*, 5–20. [CrossRef]
48. Yang, C.-K.; Cheng, C.-P.; Mai, C.-C.; Cheng Wang, A.; Hung, J.-C.; Yan, B.-H. Effect of Surface Roughness of Tool Electrode Materials in ECDM Performance. *Int. J. Mach. Tools Manuf.* **2010**, *50*, 1088–1096. [CrossRef]
49. Bok, W.-M.; Kim, S.-Y.; Lee, S.-J.; Shin, G.-S.; Park, J.-M.; Lee, M.-H. Surface Characteristics and Bioactivation of Sandblasted and Acid-Etched (SLA) Ti-10Nb-10Ta Alloy for Dental Implant. *Int. J. Precis. Eng. Manuf.* **2015**, *16*, 2185–2192. [CrossRef]
50. Bigerelle, M.; Giljean, S.; Anselme, K. Existence of a Typical Threshold in the Response of Human Mesenchymal Stem Cells to a Peak and Valley Topography. *Acta Biomater.* **2011**, *7*, 3302–3311. [CrossRef]

4.5 Conclusion of the chapter

By integrating the Gaussian-filtered, multi-scale Sdr descriptor with the Bootstrap-based uncertainty model, this chapter has completed the “quantitative-evaluation” tier of the Surface-Information Acquisition Spectrum (SIAS) on firmly industrial ground. Turned steels, grit-blasted alloys and benchmark roughness artefacts have shown that Sdr not only outperforms patchwork-style fractal estimators but also delivers process-relevant insights once its confidence bands are properly mapped. In other words, the SIAS has now proven its ability to translate a visual-syntax concept into a metrologically robust tool that withstands production-line variability.

With that industrial validation secured, the thesis is ready to cross the SIAS boundary back toward perception-driven surfaces. Chapter 5 will test the very same Sdr + Gaussian filter protocol on artistic substrates, Van Gogh’s impastos and painted surfaces probing whether the metric that decoded machining signatures can equally reveal an artist’s surface “morphological signature.” The journey thus moves from factory floor to gallery wall, completing the SIAS arc from language to syntax, to measurement, and now back to the realm where surface complexity meets human interpretation.

Chapter 5

Van Gogh and Fractal

A New Perspective for Surface Topography in Art

Prolegomena of the chapter 5

Located at the junction between perceptual insight and calibrated measurement within the Surface-Information Acquisition Spectrum (SIAS), Chapter 5 delivers the thesis's first full-scale application to heritage artefacts: Vincent van Gogh's impasto-rich paintings. Having secured a robust fractal metric in Chapter 4, coupling the ISO-25178 Sdr parameter with a multi-scale Gaussian filter, we now test whether that metric can capture the swirling energy that viewers intuitively associate with Van Gogh's brushwork. High-resolution images converted into surface topography of selected paint ridges is fed through the Sdr + Gaussian filter pipeline, while multispectral imaging supplies chromatic context; the resulting scale-resolved spectra are then correlated with art-historical descriptors such as "turbulence" and "vibration." This chapter therefore constitutes the SIAS's first passage from the laboratory to the gallery, showing how a quantitative tool forged in engineering metrology can illuminate aesthetic perception and, conversely, how artistic phenomena challenge and enrich surface science.

5.1 Introduction of the chapter

The study of an artist's style has long been a central focus in art history, with scholars analysing elements such as colour choices, composition, and iconographic themes to understand the unique signature of a painter. However, the advent of fractal geometry offers a novel and quantitative approach to this analysis, particularly in the context of surface topography and the material traces left by the artist. This chapter explores the application of fractal dimensions to study the distinctive style of Vincent Van Gogh, a painter renowned for his expressive and textured brushwork. By examining the fractal properties of his paintings, we aim to uncover patterns and characteristics that define his artistic identity. Fractal geometry, with its ability to describe complex, self-similar patterns, provides a powerful tool for analysing the intricate textures and layers of paint that Van Gogh applied to his canvases. The fractal dimension of a surface can reveal the complexity and roughness of the paint layer, offering insights into the artist's gestural signature. This approach goes beyond traditional visual analysis, allowing for a more objective and quantifiable assessment of style. In this study, we focus on Van Gogh's use of impasto and his distinctive style and brushstroke, which create a rich, multiscale surface topography. By calculating the fractal dimensions of these surfaces, we can quantify the complexity of his painting technique and compare it across different works. This method not only enhances our understanding of Van Gogh's style but also demonstrates the potential of fractal analysis as a tool for art historical research.

While this chapter centres on Van Gogh, the principles and methods discussed here can be applied to a broader range of artists and artistic movements. The use of fractal geometry in art analysis opens new avenues for exploring the materiality of artworks and the creative processes behind them. By bridging the gap between science and art, this interdisciplinary approach enriches our appreciation of artistic styles and their evolution over time.

5.1.1 About painting

When observing a painting, regardless of the era, artistic period, or artist, it is possible to begin with a simple observation of the work to appreciate its aesthetic qualities and consider whether it warrants a deeper analysis. However, if one wishes to uncover the essence, the richness of the work, one can delve into the choices of colours, composition, iconographic themes, and anecdotal details, as presented by Daniel Arasse [134]. Although the artist's technique is important in defining their style, the study of the paint layer and its relief created by the artist is generally analysed for the overall visual effect of the artwork. For example, pointillism or impasto is typically studied for its general visual rendering rather than as a 3D topographic system of paint layers with levels of detail at different scales which may carry, at the scale of the brushstroke decontextualized from the other elements of response regarding the painter's style. Focusing on the painter's trace on the material as a mark of their style, or at least a part of it, quickly shifts the art historian's analysis towards stylometry [135] or the potential quantification of certain traceable and measurable factors (e.g., chemical components). There are, however, traces of the question of roughness and style regarding the surface of the artwork influencing style in the analyses of art historians starting from the 19th century. On one hand, the notion of surface in our study concerns the geometry of the pictorial layer, the imprint of the painter's gesture. This is not the only mathematical approach corresponding to the definition of surface in art; in *De Pictura* by Alberti [136], one finds a notion closely tied to the Latin root of the word "surface." In Alberti, the surface is defined as the outermost part of a body, identifiable only by its length and width, without depth. However, in this study, we question the roughness of the surface, the roughness embedded in the material as a trace of the painter. From Rembrandt to Van Gogh, both of whom inspired painters like Eugène Leroy [137], artists have a relationship with their work in which the trace of the creative process is an integral part of the artwork. The pictorial surface thus becomes a multiscale surface: the lowest frequencies correspond to the slope of the canvas and variations in tension on the stretcher, the layering of paint represents the undulation of mid-range frequencies, while the imprint of the brush, knife, or finger corresponds to the highest frequencies. In this study, we present a reflection and a statistical method to link the artist's style to surface roughness and the microgeometry of the pictorial layer.

5.1.2 Style and roughness

Style in painting is a broad subject, which can be viewed as encompassing an era, a group of artists, or the unique touch of a single artist. Richard Wollheim [138] discusses in his article the distinction between the concept of an international style and individual style, which allows us, for instance, to recognize the prominence of Baroque or Impressionist styles through their distinctive characteristics, as well as to differentiate between a painting from Velázquez and a painting from Rembrandt. Thus, individual style emerges even when an artist works within a movement or under dominant stylistic conventions. Heinrich Wölfflin begins the introduction of his seminal work, *Principles of Art History* [139], with a short story about the painter Ludwig Richter. This painter and three of his friends set themselves the task of painting the same landscape outdoors. Although all three artists executed their works in a shared style reminiscent of the Pre-Raphaelites, the paintings differed in their representation of the same landscape. Several elements can constitute a painter's style: the themes explored through iconography, which may be more prominent in certain periods than others, and the composition, or the arrangement of elements within the pictorial space. Federico Zuccari, in his treatise *L'Idea de' pittori, scultori ed architetti* [140], embodies the Neoplatonic thought of the Renaissance concerning artistic practice. He defines *disegno interno* as the idea or mental conception of the artist. *Disegno esterno*, on the other hand, is the material expression of this idea, the drawing or physical artwork that results from it. The thematic and symbolic choices of the artist, connected to iconography, fall under the realm of mental conception. The work takes shape internally before its realization. Similarly, composition how pictorial space is structured (the guiding lines, relationships between forms) is also a preliminary stage before the execution of the artwork. *Disegno esterno* can be linked to the material representation of the artwork but it can be related to the execution of this artwork, such as the way the artist applies paint (e.g., brushstrokes, texture, fluidity). These elements relate to the technical and material aspects, reflecting the relationship between the artist and the medium. Another comment from Wölfflin says that by using relatively few elements, a wide diversity of distinct individual expressions has emerged. Countless artists have depicted the Virgin seated, with drapery gathered between her knees, and each time, a form has been discovered that reflects the entirety of a person. This psychological resonance of drapery is not limited to the grand tradition of Italian Renaissance art but extends even to the painterly style of 17th century Dutch genre painters. It is this concept of the *disegno esterno* that we need to focus on if we wish to study in more detail the notions of gesture and texture that constitute the painter's gestural signature (i.e., his style from a technical point of view). However, it is necessary to distinguish between pictorial techniques that better capture the idea of movement and the painter's gesture than others. For instance, the technique of *a fresco* painting, which involves applying pigments onto one or more layers of fresh plaster, can convey the artist's gesture through the lines, curves, modelling of flesh, and drapery of fabrics. However, the issue lies in that the surface relief and texture do not express a dynamic notion that could be referred to as the painter's morphological signature.

Similarly, certain types of painting techniques, as also distinguished by Wölfflin, transition over time from a linear style to a painterly or *Malerisch*. This word has, in German, two distinct meanings, one objective, a quality residing in the object, and the other subjective, a mode of apprehension and creation. To avoid confusion, they have been distinguished in English as “picturesque” and “painterly” respectively. The painterly style in Wölfflin implies seeing in patches of paint less than in lines. The distinction between the linear or "draughtsmanly" aspect of painting more present in the 16th century. The transition to the painterly style has set aside the reproduction of tangible objects through boundaries, surfaces, and contours (cf. Alberti). The texturing of the pictorial layer produces a visual sensation for the eye, offering different levels of realism. To quote the author: "*A very close view is senseless. Modelling by gradation has yielded to modelling in patches. The rough, furrowed surfaces have lost any possibility of comparison with life. They appeal only to the eye and are not meant to appeal to the senses as tangible surfaces*" [139] to confirm the rough and textured aspect of the surface observable in the painterly style. However, the painterly style can also apply to drawing, which completely negates the notion of texture in the sense of surface roughness. Nevertheless, this observation does not contradict the fact that, for the painter, the concept of gesture is more prominent in the painterly style.

Ancient philosophy, especially Pythagorean and Platonic thought, structured the world through a series of binary oppositions, light/darkness, form/matter, good/evil, that medieval Christian thinkers adopted and reinforced. These dualistic frameworks long shaped artistic and theoretical conceptions of creation, drawing a clear line between the artist's inner intention (preparatory drawing, idea) and its outward execution (material, technique). With Rembrandt, however, this conceptual architecture seems to dissolve. The pictorial gesture no longer seeks to translate a preconceived idea; it becomes a space where light, matter, and figuration merge. The boundary between inner design and outer execution blurs, opening a non-binary way of thinking about the artwork, in which the visible itself is a site of becoming. Painting is no longer the outcome of a plan but the locus of emergence. This surpassing of dualism situates Rembrandt not only in a stylistic break but also in a broader reconfiguration of how the image and its genesis are conceived [141].

5.1.3 The artist and roughness

Painting, as an artistic practice, is deeply rooted in the interaction between material, tools, and the artist's gesture. Jean Dubuffet emphasizes this synergy, arguing that art emerges from the dialogue between these elements, retaining the traces of the process itself. According to Dubuffet, "Art must be born from the material and the tool, and it must bear the traces of both the tool and its struggle with the material. The artist must speak, but so must the tool and the material" [142]. This perspective underlines the essential role of texture as the outcome of this creative struggle. Texture, in Dubuffet's view, is not merely an aesthetic quality but a testament to the material's responsiveness to the artist’s hand, where the gesture leaves its imprint, and the material asserts its presence. As he notes, “Each material has its language, being a language, which admits no other and serves none other” [142].

This idea is vividly demonstrated in the manipulation of pigments, binders, and supports, where the choice and combination of materials profoundly influence the outcome. For example, ultramarine powder, when mixed with different binders such as oil, egg, or gum, produces entirely distinct textures and effects depending on whether it is applied to plaster, wood, or canvas. These textures are not arbitrary; they are the result of an intimate dialogue between the artist’s gesture and the intrinsic properties of the materials. The textural variations underscore the material’s active role, transforming it from a passive medium into a co-creator of the artwork.

The notion of texture also defines the generative process of painting, which, unlike sculpture, operates predominantly through addition rather than subtraction. This layering principle is exemplified in the works of Eugène Leroy, where successive layers of paint obscure the original figure, transforming it into points of colour that emerge only faintly through the thick strata. In such works, texture transcends its visual dimension, becoming a metaphor for the “flesh of the world,” as evoked in the visceral materiality of Rembrandt’s *The Slaughtered Ox*. Here, texture functions as both a physical manifestation of the painter’s gestures and a means of anchoring the artwork in the sensory, tangible world.

Through the works of Dubuffet and Leroy we see that texture is not simply a surface quality but a central element in the artistic process. It reveals the material's voice, the painter's gesture, and their interaction, producing a visual and tactile language that resonates with both the physical and the intangible.

5.1.4 The Impasto

The technique that best represents the material expression, the artist's trace in the painting, is the impasto technique, which consists of adding thick layers of paint to the canvas. There are testimonies about Rembrandt's painting techniques [143]. This technique is more closely linked to spontaneity in the artist's expression. While the draughtsmanly style requires prior preparation, with sketches and preliminary drawings, the painterly style with impasto is a constant iteration. The impulsiveness of impasto has led to numerous pentimenti in painting, indicating that the artist's final vision of the artwork changed during its creation. Rembrandt could, for example, add layers of paint until reaching a thickness of about half a finger [144]. Vincent Van Gogh used two types of white paints, sometimes on a single painting to create his impasto, zinc white [145] and lead white [146,147]. These two types of paints are the most used by Van Gogh, although these paintings are very colourful. The elements found in Van Gogh's letters [148] provide valuable indicators for understanding the relationship between the materials used and Van Gogh's typical impasto technique. Lead white, used until the 19th century, is toxic but has excellent covering power and dries faster than zinc white, which has better mixing properties with other pigments. By varying the two, Van Gogh could create a wide variety of textures ranging from smooth to rough, which is characteristic of his style.

5.2 Analysis of Surface Topography in Art

In the field of painting, the application of surface topography analysis is relatively recent, allowing for the examination of the intricate details of a pictorial surface. This microgeometry encapsulates information that can be interpreted as the morphological signature of an artist. Key elements such as the artist’s handedness, the type of brush employed, and the nature of the paint contribute to revealing the artist’s techniques and stylistic choices through surface characterization, integrating both biomechanical and mechanical factors.

Despite its potential, the study of surface topography in fine art remains underexplored. A review by Elkhuizen et al. [149] identified only 13 significant publications on three metrological methods: laser triangulation, structured light projection, and focus variation microscopy. Their comparative study of these techniques on Johannes Vermeer’s *Girl with a Pearl Earring* (c. 1665) demonstrated that multi-scale optical coherence tomography and 3D digital microscopy (via focus variation) provided the highest precision and accuracy. Further investigations by Bigerelle et al. categorized surface phenomena into three distinct scale ranges: 3-70 μm for brushstroke details, 70-700 μm for canvas texture, and above 700 μm for broader canvas undulations [150,151].

5.3 Research Objective and Selected Corpus

This chapter aims to compare fractal dimension calculations across ten surface topographies derived from paintings. Among these, eight are undisputed Van Gogh artworks, recognized by institutions. The remaining two include *Sunset at Montmajour*, recently authenticated by experts [152], and *The Plowmen*, a piece that sparked controversy in the French press during the early 2000s and was finally consider as a forgery.

Authentic works:

Dutch Period (1881-1886) :

- *Wheatfield with Partridge* (1887) – Oil on canvas, 53.7 cm × 65.2 cm, Van Gogh Museum, Amsterdam.
- *Two Women in the Moor* (1883) – Oil on canvas, 27.8 cm × 36.5 cm, Van Gogh Museum, Amsterdam.

French Period (1886-1890) :

- *Wheatfield with Crows* (1890) – Oil on canvas, 50.2 cm × 103 cm, Van Gogh Museum, Amsterdam.
- *Reaper* (1889) – Oil on canvas, 73.2 cm × 92.7 cm, Van Gogh Museum, Amsterdam.
- *The Bridge at Langlois* (1888) – Oil on canvas, 59.6 cm × 73.6 cm, Van Gogh Museum, Amsterdam.
- *The Starry Night* (1889) – Oil on canvas, 73.7 cm × 92.1 cm, Museum of Modern Art, New York.
- *Farmhouse in the Wheatfield* (1888) – Oil on canvas, 45.3 cm × 50.9 cm, Van Gogh Museum, Amsterdam.
- *Marguerite Gachet in the Garden* (1890) – Oil on canvas, 46 cm x 55 cm, Musée d'Orsay, France

Although *Wheatfield with Partridge* (1887) was painted during Van Gogh's early years in France, it is categorized within the Dutch period due to its stylistic resemblance to his earlier works. Van Gogh's transition to France in 1886 complicates strict period classifications [153].

To evaluate whether fractal dimension serves as a reliable parameter of Van Gogh's morphological signature, this chapter incorporates two additional paintings:

1. *Sunset at Montmajour* (1888) – An oil painting depicting a landscape near Arles, France. Initially forgotten in an attic, it was authenticated based on stylistic features and a letter from July 4, 1888, in which Van Gogh described the piece. The work measures 73.3 cm × 93.3 cm, but its current location remains undisclosed [152,154].
2. *The Plowmen* – A small oil painting (30.5 cm × 45.8 cm) on wood panel, discovered in Paris in the 1990s. Bearing the signature "Vincent," its authenticity was disputed by the Van Gogh Museum. Despite private evaluations suggesting a possible attribution, the painting's sale was suspended due to unresolved questions regarding its provenance [155–157] .

Through this comparative analysis, the chapter seeks to determine whether fractal complexity can serve as a reliable metric for artistic attribution and authentication.

5.4 Material and methods

Fractal surface analysis would typically require direct access to the artworks for digitization using optical measurement systems or other topographic measurement systems. While technically feasible, this study does not rely on direct topographic measurements of Van Gogh's works. Instead, it employs a conversion process that transforms very high-resolution images into topographic data.

This conversion is performed using an algorithm embedded in the surface analysis software MountainsMap® (Digital SurfTM, Besançon, France). The process involves several steps: first, the color image is converted into grayscale. Each pixel is then represented by a single value corresponding to its light intensity or brightness, which depends on the material properties of the object and the sensitivity of the camera sensor. Mathematically, a grayscale image can be described by a function $f(x, y)$, where each point (x, y) is assigned an intensity value $z = f(x, y)$. In the conversion to topography, these intensity values are interpreted as height data. However, these heights do not hold a strict metrological value; rather, they reflect variations in grayscale intensity rather than actual physical height measurements [158,159].

Two types of topographies were generated: one representing the entire artwork and another focusing on a specific detail (Appendix A). This distinction allows for an assessment of the overall fractal dimension of the painting, in other words, its general visual complexity. However, from a statistical perspective, large-scale analysis may be less meaningful. Van Gogh's expressive style is characterized by distinctive brushstrokes that often appear in specific areas of his paintings. Once the 3D topography is generated, it becomes possible to calculate the fractal dimension of the image (Figure 5.1).

(a) (b)

Figure 5.1 *Conversion of the painting image into 3D topography, (a) image of a painting of Van Gogh in high resolution (b) conversion into topography viewed from above using grayscale (GL)*

For the calculation of the fractal dimension, a new method was employed, derived from surface analysis research [132,133]. This method involves using a roughness parameter called Sdr with a series of low-pass Gaussian filters. The Sdr parameter, as defined in ISO 25178-2 [1], is classified as a hybrid parameter. While height parameters evaluate roughness, symmetry, and the distribution of surface heights including maximum height spatial parameters analyze the texture's directionality, isotropy, and autocorrelation decay rate. Hybrid parameters, in contrast, integrate both height and spatial characteristics, combining these aspects into a single measure [160]. The values of hybrid parameters depend on both the observation scale and the resolution of the measurement system [19,161].

Sdr quantifies surface complexity by computing the ratio between the developed surface area and the sampled surface area, as illustrated in Figure . This metric is highly sensitive to scale and data resolution, making it particularly relevant for applications such as wettability, coatings [162,163], and conductivity analysis [164]. It is also useful for monitoring surface modifications during processing, especially in adhesion-related studies. However, Sdr assumes that surfaces are differentiable at all points a condition that may not hold for fractal surfaces, which often contain singularities and abrupt variations.

Sdr is a robust parameter for characterizing measurement variability due to its sensitivity to fine-scale surface features. While this responsiveness enables the detection of subtle topographic variations, it also makes Sdr susceptible to high-frequency noise [23]. Additionally, as a global parameter, it accounts for all surface points. Research by Pawlus et al. highlights that Sdr is particularly sensitive to peak spikes and stitching artifacts, tends to yield higher values in optical measurements compared to tactile methods, and is influenced by factors such as sampling intervals and filtering techniques [165].

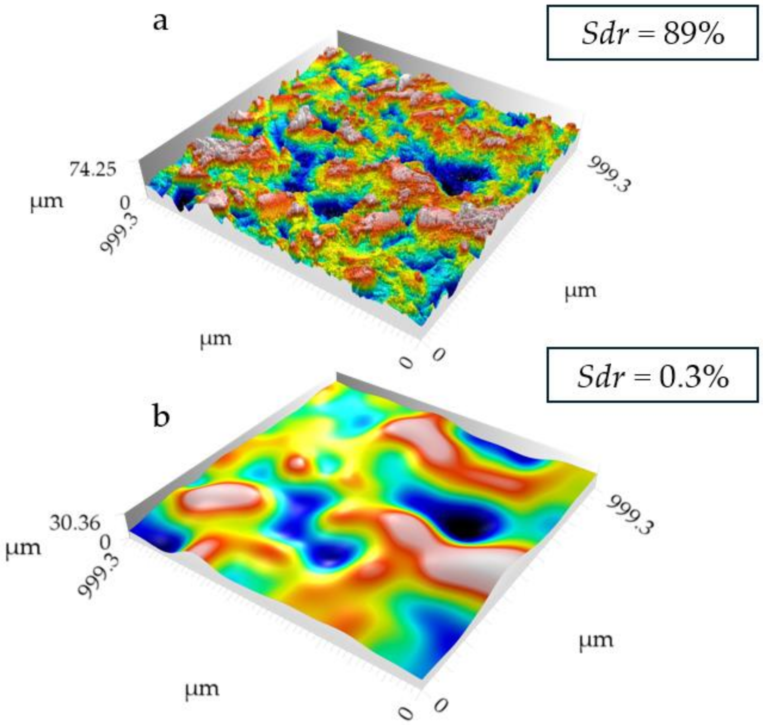

Figure 5.2 *Same surface before (a) and after (b) being filtered by low pass Gaussian filter with a cut off 250µm. It is possible to observe that the valleys remain the same, but the details have completely disappeared making the geometry far less complex and, therefore, an Sdr value of 0.3% compared to the full surface of 89% of ratio*

These equations describe the relationship between surface roughness and fractal complexity as a function of the observation scale. The equation 2, indicates that the developed surface area A follows a power law in relation to the scale ε, where $\varDelta$ is a parameter related to the fractal dimension of the surface. This relationship reflects the fact that surfaces with fractal complexity exhibit an apparent increase in surface area as they are observed at finer scales. Equation 3 defines the Sdr which measures the ratio between the developed area and the projected area $A0$, expressed as a percentage. This parameter is crucial for characterizing surface roughness, particularly in tribology and coating analysis.

$$A = a_0 \varepsilon^{2-\Delta} \tag{2}$$

$$Sdr = 100 \frac{A - A_0}{A_0} \tag{3}$$

The model presented in Equation 4 and used in this study introduce a double logarithmic transformation of the relationship between the Sdr parameter and the observation scale ε, expressed as $\mathrm{loglog}(\mathrm{Sdr}/100 + 1)$. This transformation aims to further linearize the relationship and mitigate the influence of extreme variations in Sdr, which may result from measurement noise or singularities in the surface. Compared to the previous model, where Sdr was expressed as a function of the fractal dimension Δ, this new formulation introduces a parameter Δ' that adjusts the dependency of Sdr on scale, while slightly modifying the interpretation of surface complexity. The coefficient $(1 - \Delta')$ replaces the previous $(2 - \Delta)$ term, suggesting an alternative approach to characterize the evolution of roughness across scales. This log-log transformation is particularly useful for surfaces exhibiting high variability at small scales, as it reduces the impact of extreme values and allows for a more robust estimation of fractal complexity over a broad range of scales. In the linear model $\mathrm{y} = \mathrm{a} + \mathrm{bx}$, y denotes the log-log values of Sdr; a is the intercept, b the slope, and x is the filter cut-off value in μm—i.e., ε on a log scale in the model. From this model, the fractal dimension is obtained as $(1-\Delta)$.

$$loglog\left(\frac{Sdr}{100}+1\right)=a+(1-\Delta)\log(\varepsilon) \qquad (4)$$

5.5 Results

In this section, the author aims to perform a discriminant analysis on Van Gogh's paintings by demonstrating that analysing style through fractal dimension can identify paintings that are indeed by the artist, distinguishing them from those that are not authenticated as such. To represent the relationship between the values of the Sdr parameter and the scales, linear regressions were calculated for the different paintings. These regressions reveal discriminating results concerning the forgery painting *The Plowmen*, as shown in Figure 5.3. Indeed, the distribution of values associated with this painting (in red) does not follow the same slope tendency as the other paintings (including *Sunset at Montmajour*).

From the slope of the linear regression, a fractal dimension value can be obtained. This fractal dimension calculation method is akin to the Patchwork, and box-counting methods ($1-\Delta'$). The values of this fractal dimension are presented in Figure 5.4 . It can be observed that the nine authentic paintings follow an approximately Gaussian distribution, while the painting *The Plowmen* is not included in this distribution. The authentic paintings exhibit a distribution centered around 2.85, while *Sunset at Montmajour* shows a slightly lower fractal dimension, though still within the range of authenticated works. In contrast, *The Plowmen* stands out with a significantly lower value (around 2.3), suggesting a marked stylistic difference. However, the limited number of values does not allow us to draw robust conclusions. This is why we applied a Bootstrap protocol to our data to analyse the distribution of values as if we had a large number of observations available. From these initial regressions on a log(log(Sdr)) and a log(ε), we were able to obtain the initial fractal dimensions.

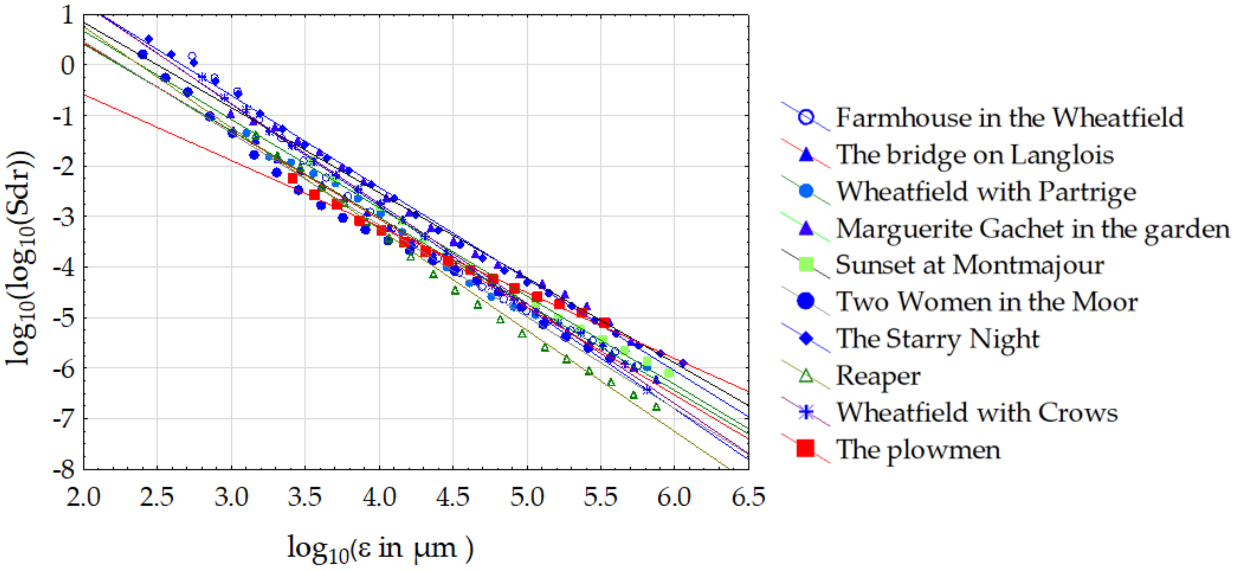

Figure 5.3 *Slope of the distribution of Sdr value on every scale. The rejected painting (The Plowmen is here depicted in red)*

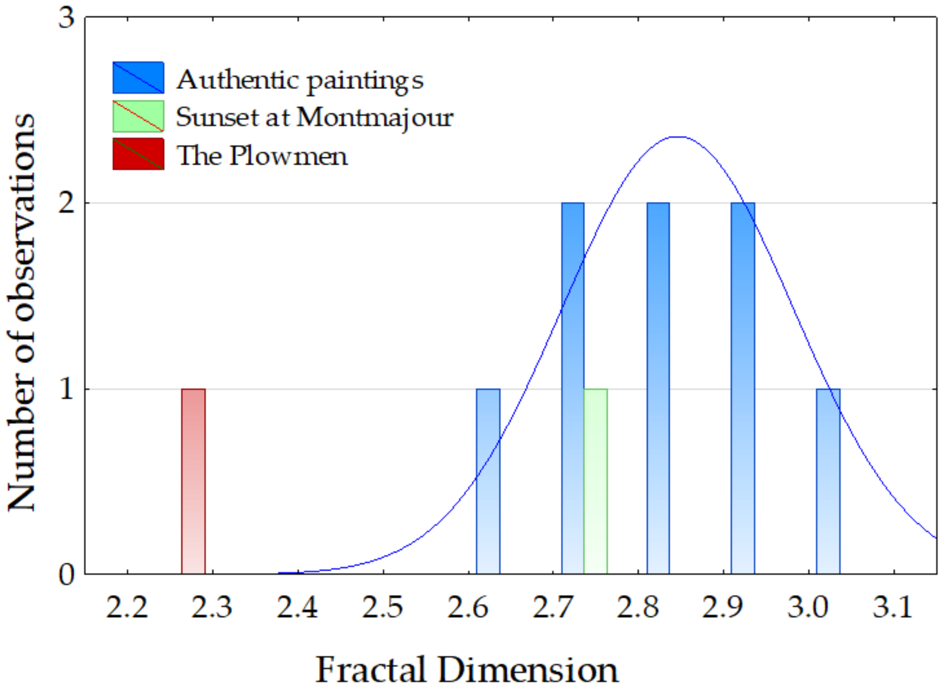

Figure 5.4 *Distribution of fractal dimensions values*

To account for variability in our model while preserving the structure of the initial regression, a two-step Bootstrap procedure was applied. First, the residuals from the initial regression were resampled with replacement, allowing us to simulate different realizations of the model's errors while maintaining their original distribution. In parallel, the predicted values from the regression were also resampled to capture variations in the estimated trend. These two resampled components were then combined by summing the Bootstrapped residuals and Bootstrapped predicted values, generating new simulated Sdr values. This approach ensures that the stochastic nature of the data is accurately reflected while maintaining the underlying relationship between Sdr and ε ,rather than directly resampling raw Sdr values, which could distort the model's structure. This process can be summarized in the following steps:

1. Initial Regression: A linear regression was performed on log(Sdr) as a function of log(epsilon) for each dataset (i.e., each painting).
2. Calculation of Residuals and Predictions: The residuals (differences between observed and predicted values) and the predicted values from the regression were computed.
    a. Bootstrap Resampling (100,000 replications):
    b. The residuals were resampled with replacement to preserve their statistical distribution.
3. The predicted values were also resampled with replacement to incorporate variability in the regression trend.
4. Generation of Simulated Sdr Values: Each new simulated Sdr value was obtained by summing a resampled prediction with a resampled residual, effectively creating a Bootstrapped realization of the data.
5. Repeated for Each Painting: This procedure was applied independently to each dataset, ensuring that the structure of each painting's regression was maintained.
6. Estimation of Fractal Dimension: New regression models were fitted to the Boostrapped dataset, providing a distribution of estimated slopes.
7. Analysis of the Bootstrap Results: The distribution of the fractal dimension estimates was analysed to assess its variability and to compare different paintings.

These steps allow us to generate Figures 5.5, in which the Bootstrapped distributions suggest that the painting *The Plowmen* is a forgery despite the large number of simulated data points generated through the Bootstrap process. Three modes can be observed; however, the rightmost mode corresponds to three paintings created by Van Gogh during his French period, accounting for three out of six paintings in this study. The painting *The Plowmen* remains in a separate mode from the others.

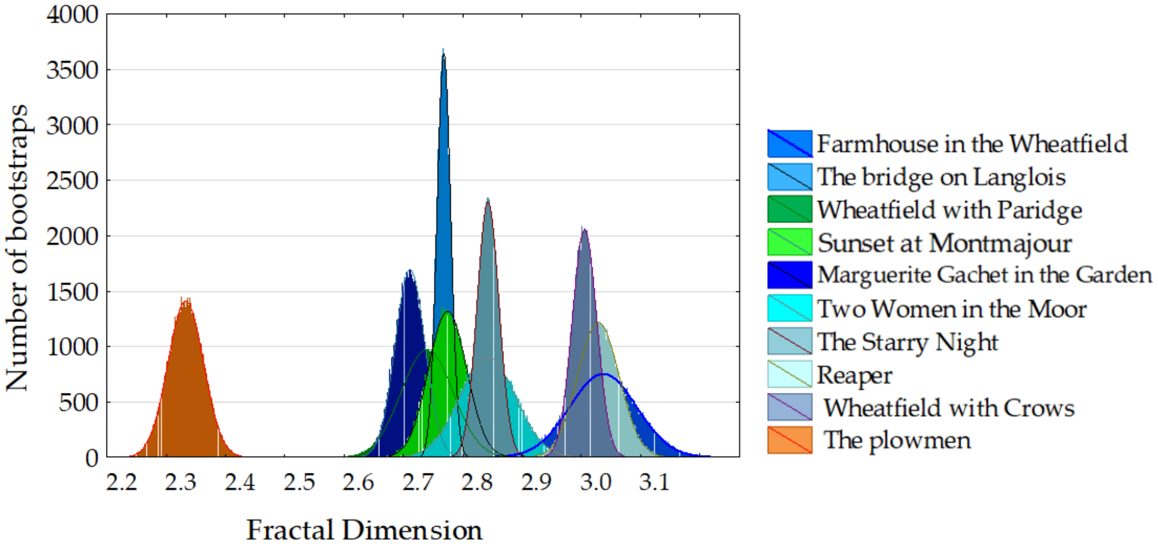

Figure 5.5 *Modes of distribution for the Bootstrapped values for fractal dimensions of the paintings*

To validate our hypothesis, that fractal dimension can be used to discriminate non-authentic Van Gogh works, we must compare these results with another widely used method in fractal surface analysis, namely the box-counting method.

5.6 Using the box counting method for topographical and fractal insight in authentication of Van Gogh's painting (currently in the process of peer review in Surface Topography: Metrology and Properties submitted in April 2025)

IOP Publishing Journal Title
Journal **XX** (XXXX) XXXXXX https://doi.org/XXXX/XXXX

Preserving Van Gogh's Painterly Heritage: Topographical and Fractal Insights in Authentication

Received xxxxxx
Accepted for publication xxxxxx
Published xxxxxx

Abstract

The studies determining methods for authenticating forgeries in artworks are of crucial importance. Some works, which can reach considerable market value, compel institutions or owners to be certain of the object's authorship. Furthermore, the diversity of methods is crucial as it allows for varied perspectives by considering different factors (e.g., chemical analysis, connoisseurship, carbon-14 dating). In this study, we propose an innovative method for authenticating artworks using the fractal dimension of the surface topography. The fractal calculation method used is the Box Counting method, also known as the Minkowski-Bouligand dimension calculation method. By utilizing 9 paintings from the corpus of Vincent Van Gogh and one false known as "The Ploughmen", we compare the results of fractal dimension calculations of the surface topography. High-resolution images were converted into 3D topographies, from which fractal dimensions were extracted. Our analysis rejects "The Ploughmen" (Z-value = -2.336) and validates a recently discovered work "Sunset at Montmajour" (Z-value = 1.64) as authentic. This innovative approach demonstrates that the fractal dimension of the paint layer can serve as a distinguishing parameter of the painter's morphological signature. The findings suggest that fractal analysis could complement traditional art authentication methods, providing a quantitative tool that can enhance the accuracy and reliability of authenticity assessments.

Keywords: Surface topography, fractal dimension, Van Gogh, art painting

Introduction

The painter we address in this study is none other than Vincent Van Gogh (1853-1890), a Dutch painter and draftsman whose style varies depending on the period, ranging from pointillism to expressionism [1]. His highly influential body of work ranks him as one of the most important artists in art history as a precursor of modern painting. Detailed analyses of his life and work, as well as monographs, number in the hundreds, and the primary aim of this study is not to provide an overview of art history research on Van Gogh. However, we can mention the significant biography of Naifeh and Smith [2] and the work of J-B Faille [3–5]. The works of a painter of such renown have acquired considerable value over time [6], which introduces a crucial question regarding the authentication of works discovered late as Sunset at Montmajour (Private collection, 1888. In the realm of contemporary art authentication, the pursuit of detecting forgeries has evolved, primarily leveraging three distinct methodologies: connoisseurship, which draws upon expert judgment and historical context; physico-chemical analyses, involving scientific examination of materials and pigments; and digital image processing involving the manipulation and analysis of digital images using computer algorithms. Through this study, a new method for detecting forgeries based on Van Gogh's work will be introduced. Indeed, the field of surface metrology has scarcely addressed the study of pictorial surfaces, let alone in the context of forgery detection. Therefore, following this introduction, the field of surface metrology will be presented.

1.1 Connoisseurs

Firstly, the case of connoisseurship in the work of Van Gogh possesses several renowned instances. This issue is at the heart of the Wacker affair, in which about thirty works attributed to Van Gogh were added to the artist's standard catalogue in the 1930s. Some of these works were forgeries, initially recognized as such, then rehabilitated before being definitively determined as fakes. Feilchenfeld [7] summarizes the affair in his study by specifying that there are three types of forgeries in Van Gogh's work :

- Forgeries: Works intentionally manufactured to deceive.
- Misattributed works: Works wrongly attributed to Van Gogh simply because they were among his brother Theo's estate.
- Mixed cases: Works incorrectly ascribed to van Gogh, signed "Vincent" with the intent to deceive, often involving forged documents.

Artwork authentication is a major step when orphan works need to be attributed to one artist or another before they enter auction networks, curation processes, museum and or private collections. The intervention of experts is regularly sought so that artworks wishing to enter the art market are recognized as having been indeed executed by a painter to whom the work is attributed. One can note that the experts, initially scholars in the painting of the great masters, are gradually complementing their analysis, which is both iconographic and stylistic, with a forensic analysis. The Research Laboratory of French Museums (LRMF) typically distinguishes between two primary categories of working methods: The first, Examination, primarily involves photographic and imaging techniques. The second, Analysis, is a structural study aimed at identifying the constituent materials of a work of art and understanding how they were used. It should be noted that in the methodology for detecting forgeries, Le Chanu positions the connoisseur or art historian as the first participant, leading the way with the examination phase preceding the analysis phase [8]. All analysis techniques ranging from X-ray fluorescence scanning [9] to computer vision [10], including Raman spectroscopy [11] are summarized in details in the book by Ragai [12].

1.2 Physico-chemical aspect

The physico-chemical studies in the authentication of Van Gogh's works also feature some intriguing cases. It is possible that other works have undergone analysis, but these cases have remained within the realm of private domain. The first study concerns a work by Van Gogh (Patch of Grass, Paris, Apr-June 1887) in which the artist covered a previous composition with a second one. Using synchrotron radiation-based X-ray fluorescence mapping, researchers revealed a hidden woman's head beneath his "Patch of Grass" painting. By visualizing specific elements in the paint layers, they reconstructed flesh tones, allowing comparison with Van Gogh's known works. This breakthrough offers unprecedented insight into hidden layers, opening new possibilities for non-destructive study in Van Gogh's oeuvre [13]. Underdrawings in paintings, previously obscured, were revealed with exceptional clarity through synchrotron X-ray techniques in another study. One such case study involves a floral still life initially doubted as a van Gogh due to its unconventional characteristics. Despite challenges in interpretation using conventional methods, synchrotron XRF imaging in 2012 unveiled a distinct under drawing of two wrestlers, confirming the painting's authenticity. This breakthrough underscores the transformative impact of synchrotron-based art analysis, enabling precise authentication and enriching our understanding of artistic processes[12]. Finally, Sunset at Montmajour, initially doubted as a forgery, was authenticated as an original Van Gogh by the Van Gogh Museum in 2013. Purchased in 1908, it faced scepticism after being stored in an attic upon suspicions of forgery. In 2011, its new owner presented it to the museum, prompting revaluation. Van Gogh's correspondence and matching catalogue numbers supported its authenticity. Stylistic analysis and pigment examination further affirmed its genuineness, with SEM-EDX analysis confirming the canvas weave. Technical research confirmed the pigments' alignment with van Gogh's Arles palette, solidifying its status as an authentic piece in the museum's collection[14,15].

1.3 Digital Image Processing and Stylometry

The technologies associated with painting authentication offer various possibilities to support expert opinions. Hence, scientists are exploring indicators of different natures, as illustrated by the literature review in this introduction. However, the processes require considerable technological resources, often involving the need to physically move the artwork or directly intervene in the institution where it is stored. That is why art historians, working in collaboration with researchers in technical sciences, often use stylometric analyses based on images from paintings. In painting, stylometry is a method used to study an artist's style through their works. This can involve analysing various visual characteristics, such as colour choice, composition, brushstroke type, or the depiction of recurring motifs. Stylometry can be used to identify an artist's works, analyse the evolution of their style over time, or distinguish authentic works from imitations or forgeries. A literature review for stylometric studies on paintings is summarized in the introduction of Liu et al.[16] and Hugues [17]. For insurance and security reasons, analyses based on high-quality images of the artworks represent a viable strategy. Images stored in databases have the advantage of being accessible to art historians, interoperable across institutions, and providing material for computer-aided image processing studies [18]. To stay at the cutting edge of studies focused on the analyses of Van Gogh's works, it is necessary to mention the Digital Painting Analysis (DPA) initiative. This initiative was supported by the Van Gogh Museum and the Kröller Müller Museum, which provided high-resolution digital images of paintings, mostly by van Gogh. The art historians presented challenges to the research teams, including authentication, dating, identifying distinguishing features, image enhancement, and inpainting. This initiative organised two workshops. (IP4AI or *Image Processing for Artist Identification*) and a symposium (celebrating the inauguration of TiCC, *Tilburg centre for Creative Computing*) [19,20]. Unfortunately, those images are not available nowadays. Since 2008, in the study by Johnson et al., [18] Van Gogh's works have been studied using image processing. The techniques used for image analysis to authenticate the author of a work are based on the principles of wavelets and Gabor wavelets. The principle of using wavelets for image processing, particularly in the fields of image recognition, feature detection, and texture classification (i.e., domains that can be used to authenticate a painting from an image) are addressed in Walker's [21] book and Choi & Baraniuk' study [22]. Wavelets also allow for a multifractal analysis of Van Gogh's paintings [23]. Methods using wavelets include Hidden Markov Models (HMMs), Support Vector Machines (SVMs), and Multidimensional Scaling (MDS).

Contrary to most image processing studies using wavelets, the study from Liu et al., proposes an analysis of brushstrokes using a geometric tight frame. Tight-frame transforms are redundant bases that can provide overcomplete but stable coding of directional variations. The geometric tight frame used in this study consists of 18 filters that capture the first- and second-order differences in the horizontal, vertical, and diagonal directions in small areas, allowing it to capture subtle oriented variations in the texture of the paintings.

Algorithms for edge detection are another method of studying pictorial style. These algorithms trace the contours of Van Gogh's brushstrokes and allow the painter's gestures to be isolated to quantify repetitive and patterned impressions. The study from Li et al., confirms that the combined brushwork features identified as unique to Van Gogh are consistently present throughout his French periods of production (1886-1890)[24]. This is relevant to attribution studies as there are paintings by other artists, including those in his inner circle, which were not created as deliberate copies or forgeries, but have been mistakenly attributed to Van Gogh for various reasons (i.e., the style of painting). A significant number of the paintings assessed by experts that are brought to the Van Gogh Museum fall into this category. Other algorithms used include Canny edge detection and Ant Colony Optimization methods [25].

This literature review indicates that the detection of forgeries in Van Gogh's work, and generally in painting, focuses on three approaches: one based on connoisseurship, another on physico-chemical analyses, and the last one on digital image processing. These methods are interconnected in the sense that connoisseurship relies on forensic study results (i.e., physicochemical analysis) to ensure the authenticity of a work, in addition to the connoisseur's expertise on the artist in question. Studies in image processing also assist the connoisseur in decision-making, offering the advantage of employing non-invasive analysis methods and enabling the analysis of a dispersed corpus of works. In this context, only images provided by institutions are necessary and can be digitally shared. In this study we aim to present a non-invasive method based on surface topography analysis. This approach would have the advantage to have been closer to the physical aspect of the surface in opposition to image analysis and can give indicators to help connoisseurs in their authentication process.

1.4 Surface topography and art

Surface metrology of topography is a method providing analysis over the geometric characteristics of the surface [26]. This method is usually studied in the industrial field to assess both the process of manufacturing and the optimisation of functionality on surface state [27]. Surface topography analysis in painting is a relatively new approach that studies the fine geometry of the pictorial surface. This microgeometry contains information related to what can be called the painter's morphological signature. Factors such as the handedness [28] , the type of brush used, and the type of the paint are indicators that connect the work to the painter through surface topography (i.e., biomechanical and mechanical factors related to artists choice). The study of surface topography in fine art paintings is not yet widespread. A 2019 review by Elkhuizen et al. [29] found only 13 comprehensive publications on three metrological techniques: laser triangulation, structured light projection, and focus variation microscopy. They compared three 3D scanning techniques on Johannes Vermeer's "Girl with a Pearl Earring" (c. 1665), concluding that 3D digital microscopy (using focus variation) and multi-scale optical coherence tomography offer the highest accuracy and precision. Further research by Bigerelle et al. [30,31] identified three distinct scale ranges for surface phenomena: 3-70 µm for brushstroke details, 70-700 µm for canvas fabric topography, and scales larger than 700 µm for canvas undulations.

1.4.1 Fractal methods

Among the methods of analysis in surface metrology, the incorporation of fractal aspects in the study or art tends to be a promising and innovative approach [32] . Characterization of surfaces involves the examination of the spatial configuration of details, brushstrokes, and patterns present in a painting, by scrutinizing these features at small scales, distinctive signatures specific to each artist can be discerned. However, to delve beyond the visual aspect, the integration of fractal aspects adds a mathematical dimension to this analysis. Fractal aspects, particularly measured through methods such as the box counting method [33,34], allow for the quantification of complexity and self-affinity within the topography of an artwork. This could be a valuable resource for establishing distinctive patterns and recurrent structures characteristic of a specific painter. In the context of artistic authentication, this approach provides an objective and quantifiable means of assessing the stylistic consistency of an artist over time. The hypothesis is that the pictorial surface has a geometric complexity unique to the artist, which can be calculated using fractal dimension. This complexity can be associated with a particular artist, allowing us to determine if a work does not belong to the artist's corpus because the geometric structural complexity would differ.

Studies on the fractal dimension of artworks are not numerous, two examples can be cited: The first concerns the paintings of Jackson Pollock, which highlight an analysis of the pattern associated with dripping (i.e the way Jackson Pollock was creating artwork). This study shows the complexity of the pattern created during the creative process rather than an analysis of the pictorial layer itself [35]. The second study explores the wavelet leader based multifractal formalism to characterize paintings, analysing digitized paintings for forgery detection and differences among Van Gogh's works and those of his contemporaries [23].

1.5 Objective and corpus

This study compares the fractal dimension calculations of 10 surface topography from paintings. Among these 10 works, 8 have been authenticated as Van Gogh paintings and are undisputed by institutions. Of the remaining two, one has been recently authenticated, which is "Sunset at Montmajour," and the other was subject to controversy called “The Ploughmen” that caused brief doubt in the French press in the 2000s. The list of authenticated works classified in the Dutch and French periods:

Dutch Period (1881-1886)

- Vincent Van Gogh, *Wheatfield with Paridge,* 1887, oil on canvas, 53.7 cm x 65.2 cm, Van Gogh Museum, Amsterdam, Netherlands.
- Vincent Van Gogh, *Two Women in the Moor,* 1883, oil on canvas, 27.8 cm x 36.5 cm, Van Gogh Museum, Amsterdam, Netherlands.

French Period (1886-1890)

- Vincent Van Gogh, *Wheatfield with Crows,* 1890, oil on canvas, 50.2 cm × 103 cm, Van Gogh Museum, Amsterdam, Netherlands.
- Vincent Van Gogh, *Reaper,* 1889, oil on canvas, 73.2 cm x 92.7 cm, Van Gogh Museum, Amsterdam, Netherlands.
- Vincent Van Gogh, *The bridge on Langlois,* 1888, oil on canvas, 59.6 cm x 73.6 cm, Van Gogh Museum, Amsterdam, Netherlands.
- Vincent Van Gogh, *The Starry Night,* 1889, oil on canvas, 73.7 cm × 92.1 cm, Museum of Modern Art, New York, United States
- Vincent Van Gogh, *Farmhouse in the Wheatfield,* 1888, oil on canvas, 45.3 cm x 50.9 cm, Van Gogh Museum, Amsterdam, Netherlands.

It should be noted that "Wheatfield with Partridge" (1887) is placed in the Dutch period for simplicity, even though 1887 is during his early time in France, as it reflects the style influenced by his Dutch years. The classification can be nuanced, as Van Gogh moved to France in 1886 [2].To address whether fractal dimension is indeed a significant parameter of the painter's morphological signature, we introduce two works into the study that can provide insights into our hypothesis. "Sunset at Montmajour," an oil painting from 1888, was revealed to the public by Van Gogh Museum director Axel Rueger, depicting a landscape of oaks near Arles, France. Purchased by a private collector in 1908 and forgotten in an attic, the painting was authenticated by scientists and Van Gogh experts using his typical techniques and a letter from July 4, 1888, in which he described the painting [14,15]. The painting dimension are 73,3 × 93,3 cm, the location is currently unknown, and the owner is private. The second painting is an oil on wood panel of small size 30,5 cm × 45,8 cm, discovered in Paris in the 1990s, nicknamed "The Ploughmen". The painting bore the signature "Vincent," characteristic of the artist's works. The authenticity of the canvas was refuted by the Van Gogh Museum authority, but the buyer conducted private expert evaluations, which provided elements without significant guarantees. The work attempted to be sold, but the auctions were cancelled due to the uncertain nature of its attribution to Van Gogh [36–38].

Materials and methods

2.1 Conversion from pictures to topographies

The use of surface topographies in fractal analysis would require access to the artworks and digitizing them using optical profilometers or other topography measurement systems. While this is technically possible, this study does not use topographical measurements of Van Gogh's works but rather a conversion of very high-resolution images into topographies. To achieve this, there is an algorithm for converting images into surface topographies in the surface analysis software MountainsMap® (Digital SurfTM, Besançon, France). The principle of this conversion involves several steps. The color image is converted to grayscale. Gray level images represent each pixel with a single value known as intensity or brightness. This intensity reflects the amount of light an object emits or reflects, influenced by the material properties of the object and the sensitivity of the camera sensors. A grey level image can be represented by a function of two variables, f(x, y), which gives a number z = f(x, y) corresponding to a grey level at a point (x, y). The intensity values of the grayscale represent the height values for the conversion to topography. The heights do not have metrological value in the sense that they do not represent actual height values but represent the gradients of the grayscale intensity [39,40]. Two types of topographies were generated: the first consisting of the topography of the entire artwork, and the second by extracting a detail of the artwork (Appendix A). This allows an overview of the overall fractal dimension of the artwork, or in other words, the general complexity of the painting. However, from a statistical standpoint, this calculation over a large area is less significant. Van Gogh's expressive style with specific brushstrokes often appears in certain areas of the artwork. For example, in 'Wheatfield with Crows,' the extracted area is in the wheat (Figure A.1.a), which shows a pattern where individual brushstrokes are distinguishable. Once the 3D topography is generated, it is possible to calculate the fractal dimension (Figure 1).

2.2 Fractal method of analysis

Each method for calculating fractal dimension has its advantages and limitations, and the choice of method often depends on the specific nature of the object under study and the questions being addressed [32,41–43]. The use of the box-counting method, also known as the Minkowski-Bouligand dimension, to analyze the topography of an artistic painting is justified by its ability to quantify fractal complexity and self-affinity within the structure of the artwork. This approach provides a mathematical perspective for exploring the patterns and details that contribute to the visual richness of a painting. The box-counting method involves subdividing the topography into boxes of increasing sizes *s* and then measuring the number of boxes *N(s)* needed to cover the object at each scale. Using this mathematical method the box-counting method brings an element of objectivity to the analysis of artistic topography. The calculation of the fractal dimension *D* is also referred as Sfd parameter in ISO 25 178-2 [44].

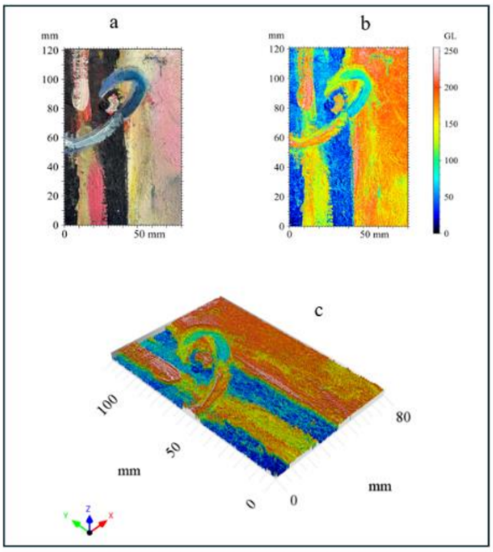

Figure 1. Conversion of the painting image into 3D topography, (a) image from a detail of a painting photograph, (b) conversion into topography viewed from above using the grayscale (GL) scale, (c) 3D view of the surface topography.

The Minkowski-Bouligand dimension, employed in the box-counting method, is based on such a formulation. This dimension quantifies the complexity of a surface by describing how the number of covering elements scales with their size. For 3D surfaces, it is expressed mathematically as:

$$D = -\lim_{s \to 0} \left[\frac{\log N(s)}{\log(s)} \right] \qquad [1]$$

where:

- *N(s)* is the number of cubic boxes of size s required to cover the measured surface.
- *s* is the box size.

Formally, if *N(s)* is analytically known, *D* can be calculated directly using Eq.1 However, in the context of experimental data or when *N(s)* is a discretized function; we obtain only a finite set of discrete points rather than a continuous function. As such, it is no longer possible to calculate *D* analytically since the limit *s*→0 cannot be practically achieved. Instead, numerical evaluations of *D* rely on certain assumptions. To numerically estimate D on this set, a critical assumption often made is that $N(s) \propto s^{-D}$, which implies a power-law relationship between $N(s)$ and s. This hypothesis is essential because it indicates that the relationship holds over a finite range of scales, not merely asymptotically. If this scaling law is valid, the fractal dimension D can be determined by examining the linearity of the relationship between $\log(N(s))$ and $\log(s)$ over this range.

However, it is important to recognize two assumptions Scaling Range assumption: The observed linearity in logarithmic coordinates over a finite range is a necessary but not sufficient condition for D to be the true Minkowski-Bouligand fractal dimension. If the power-law behavior is verified, D derived from the slope of the log-log graph is a reliable approximation of the true fractal dimension. Otherwise, D may only represent an effective or apparent fractal dimension, specific to the analyzed scale range.

The Practical Implications for Painting Topographies show that for applying this method to topographic measurements of paintings, the three following considerations are critical: The topographic surface is represented by a finite grid of measured points (x,y,z). This discretization introduces limitations in both the smallest s (resolution) and the largest s (surface dimensions). The linearity of log(N(s)) vs. log(s) over a finite range must be carefully analyzed to ensure the validity of the scaling law. Deviations from linearity suggest that the power-law assumption may not hold, limiting the reliability of the fractal dimension estimate. The validity of the fractal dimension D depends on the existence of a finite range of scales over which the power-law relationship applies. This range should ideally be broad enough to capture both small-scale details and larger structural patterns.

In the context of analyzing the surface of a painting, we propose a two-scale approach to calculating the fractal dimension using the box-counting method. This method will be applied at two distinct scale levels: a micro-scale to analyze homogeneous areas of the surface (representing the characteristics of the artist's brushstroke) and a macro-scale covering the entire painting, aimed at identifying fractal trends over heterogeneous entities that represent the artwork.

2.2.1 Micro-Scale: Characterizing the Artist’s Brushstroke. At the micro-scale, we focus on specific excerpts of the surface that are considered homogeneous. These areas are interpreted as characteristic of the artist's brushstroke, allowing us to understand their biomechanical movement and the uniqueness of their touch. This analysis helps quantify technical aspects such as the pressure applied, the direction of the brush, and the fluidity of the strokes. By calculating the fractal dimension at this scale, we aim to capture the fine and repetitive structure of the paint application, which can be seen as a personal and unique aspect of the artist’s technique.

2.2.2 Macro-Scale: Analyzing Artwork as a Whole. At the macro-scale, the analysis extends to the entire surface of the painting, with the goal of studying the fractal relationship in the broader context of the work. This analysis helps identify global trends in the surface of the painting, revealing interactions between individual brushstrokes and the larger, more complex structures formed by the entire artwork. At this scale, the fractal analysis allows us to describe the relationships between different heterogeneous entities that compose the painting, thereby integrating all visual aspects of the work.

The goal of this two-scale approach is to understand the continuity between the technical and sensory aspects of the artwork. By comparing the results of fractal analysis at both the micro and macro scales, we seek to assess how well the fractal dimension captures the smooth transition between the technical details of the brushstroke and the overall artistic expression of the painting. If the results from the micro and macro analyses are consistent, this suggests that the fractal analysis captures the continuum of the artist’s interpretation, where each technical gesture contributes to a broader artistic meaning, forming a coherent interpretation of the painting's technique and art.

Applying both analyses is essential for understanding the artwork in its entirety, enabling a deeper exploration of the interaction between the technical aspects (such as brushstroke technique) and the artistic aspects (sensory and visual effects of the artwork). To aid in illustrating the box-counting method, a simplified 2D version of the 3D approach used to calculate the fractal dimension is presented in Figure 2. This representation considers a 2D profile, with the boxes also being in 2D.

Calculating the fractal dimension *D* using the box counting method involves several steps. Mapping the image to intensity to topographical Map we Begin by discretizing the topographical map of the painting into boxes of increasing sizes. This can be done by subdividing this one into progressively smaller squares:

- Counting Boxes: For each box size, one counts the number of boxes required to cover the object in the topographical Map.

- Construct a log-log graph where the x-axis represents the box size (logarithmic scale), and the y-axis represents the corresponding number of boxes (logarithmic scale). Each point on the graph corresponds to the size of a box and the number of boxes needed to cover the object (Figure 3).

- Linear Regression: Ideally, the relationship between box size and the number of boxes follows a power law on the log-log graph. One Applies linear regression to fit a line to these points. The slope of this line is often referred to as the Minkowski-Bouligand dimension or the fractal dimension. Fractal Dimension Calculation is obtained by taking the negative of the slope of the linear regression line.

However, calculating the fractal dimension over the entire surface can present difficulties in interpreting the results. This is why we compare the fractal dimension results obtained on the entire surface as well as on a single isolated brushstroke. Indeed, a single brushstroke allows capturing the fractal dimension associated with a singular gesture of the painter. This is why, for each painting, a brushstroke was isolated to calculate its fractal dimension.

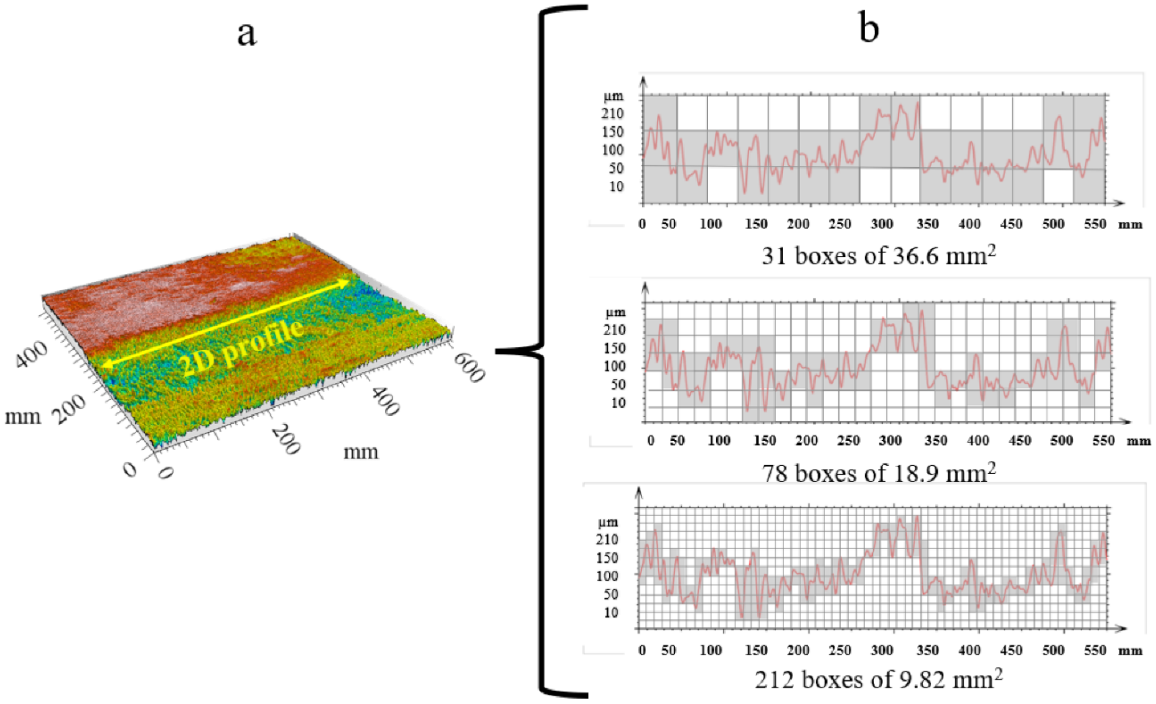

31 boxes of 36.6 mm^2

78 boxes of 18.9 mm^2

212 boxes of 9.82 mm^2

Figure 2. 2D representation of the Box Counting method, (a) the picture of the painting Marguerite Gachet in the garden is converted into height points using grey scale, a 3D topography representation of the painting is generated (b) the Box Counting method is here represented applied on a 2D profile extracted from the 3D topography indicated by the horizontal line. Three different scales of squares are applied: 36.6mm^2 squares need 31 boxes to enclose the profile, 78 squares with a size of 18.9mm^2 and 212 boxes with a size of 9.82mm^2. Those references are applied in a log log plot to compute the fractal dimension like in Figure 3

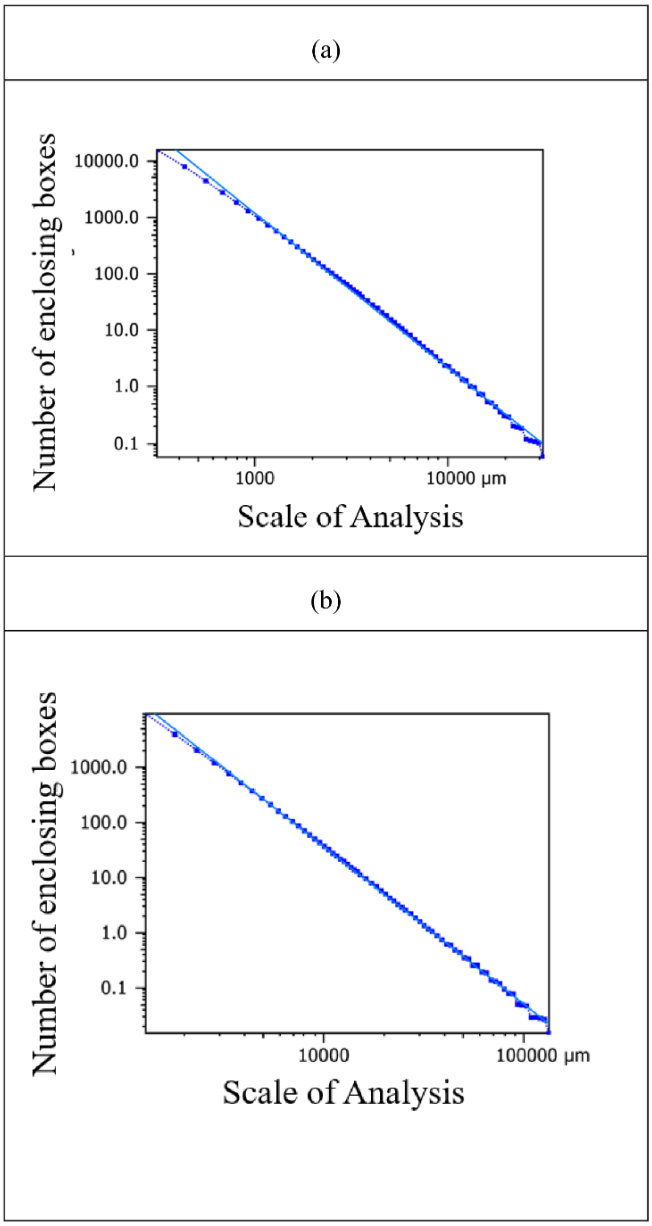

Figure 3. Log-log graph of the scale of analysis on the number of enclosing boxes, graph for the fractal dimension of "Wheatfield with Partridge" (a) on full scale with a fractal dimension of 2.75 (b) on brushstroke scale with a fractal dimension of 2.76

Results

The results of the fractal dimension calculations are presented in Table 1. Initially, these results pertain to works that have already been authenticated to create a statistical model and compare it with the data from the other two works, the recently authenticated one and the forgery. After calculating the fractal dimensions of the topographies derived from the paintings; it is now possible to create a statistical model to verify if a work different from those created by Van Gogh would not match the model. The qualitative descriptions of the surfaces presented in Table 1 mostly depict a complex surface. The surfaces presented in Appendix A indeed show high fractal dimensions for all the authenticated Van Gogh works. Although these surfaces are ultimately different from a qualitative point of view, they are still close in terms of their fractal dimension values except for "Marguerite Gachet in the Garden". One remark should be made about the painting 'Starry Night' as it has the highest fractal dimension. The iconic painting 'Starry Night' possesses a rich surface texture that visually represents the culmination of Van Gogh's research work. It can be imagined that this visual complexity, which stands out from his other works, is also reflected in the complexity of the texture, hence the fractal dimension value of 2.84. This analytical section presents the results of the statistical tests conducted with the two datasets. Initially, it focuses on the extracted areas, followed by the data on the complete paintings.

We conducted a normality test on the fractal dimension data of the study, excluding "Sunset at Montmajour", using the Shapiro-Wilk test. This test assesses whether the data follow a normal distribution. The mean of the fractal dimensions of the artworks, without "Sunset at Montmajour", is 2.76 with a standard deviation of 0.049. The test statistic W obtained is approximately 0.99, with an associated p-value of approximately 0.997. The chosen significance level is 0.05. The principle of the Shapiro-Wilk test is to compare the distribution of the data to a normal distribution. In this analysis, the p-value (0.997) is greater than 0.05, indicating that we do not reject the null hypothesis. Therefore, the data of fractal dimensions of the artworks, excluding "Sunset at Montmajour", appear to be approximately normally distributed. The fact that the fractal dimension data of Van Gogh's artworks follow a Gaussian distribution suggests that Van Gogh had a well-defined and consistent artistic style.

3.2.1 Analysis of fractal dimension at the scale of extracted areas After comparing the fractal value of "Sunset at Montmajour" to those of other Van Gogh's paintings, a test is conducted to evaluate whether the fractal dimension of "Sunset at Montmajour" is like the other mentioned Van Gogh artworks. By using the Z-score test, we compare the value of "Sunset at Montmajour" with the mean and standard deviation of the other artworks to determine if it falls within the same range of values. For a Z-score of 1.6, the corresponding probability in a bilateral normal distribution can be calculated using a Z-table or a statistical calculator. Consulting a Z-table, the probability associated with a Z-score of 1.6 is approximately 0.9452 for one tail of the distribution, meaning there is about a 94.52% chance of obtaining a fractal dimension value equal to or lower than 2.84 in a normal distribution. This suggests that the fractal dimension value of "Sunset at Montmajour" is relatively close to the average of the other paintings, indicating that it shares similar characteristics with them in terms of fractal dimension. Thus, from a statistical perspective, the fractal dimension of "Sunset at Montmajour" does not appear to be significantly different from that of other Van Gogh's paintings (Figure 5). These findings reinforce the authenticity and consistency of the artwork within the context of the artist's body of work. However, it is important to note that this analysis is based on statistical criteria and does not consider other aesthetic or historical aspects that may influence the interpretation of the artwork. We will then calculate the probability of finding a fractal dimension value equal to 2.54 or lower, if the other 8 follow a Gaussian distribution. We find that the probability of obtaining a fractal dimension value equal to 2.54 or lower, assuming a normal distribution for the other 8 paintings, is extremely low. This probability is almost zero. The very low probability indicates that the fractal dimension value of “The Ploughmen” (2.54) is statistically significantly different from the other paintings. This suggests that “The Ploughmen” may have been executed in a different style from that of Van Gogh or that other factors may be at play.

(a)	(b)
Wheatfields with Crows	Reaper
Fractal dimension of the painting = 2.76	Fractal dimension of the painting = 2.77
Fractal dimension of the extracted area = 2.80	Fractal dimension of the extracted area = 2.79
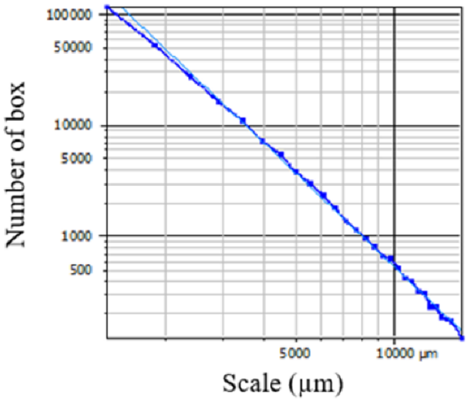	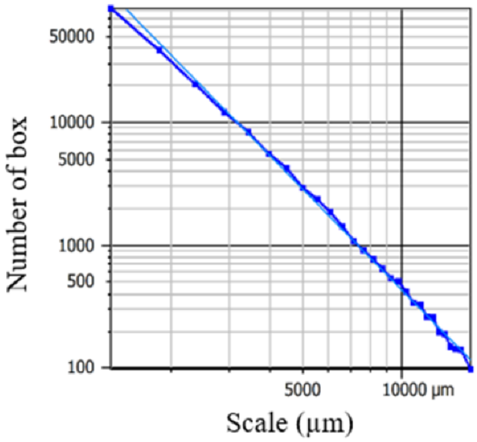

(c)	(d)
The bridge on Langlois	Two Women in the Moor
Fractal dimension of the painting = 2.66	Fractal dimension of the painting = 2.70
Fractal dimension of extracted area = 2.74	Fractal dimension of the extracted area = 2.73
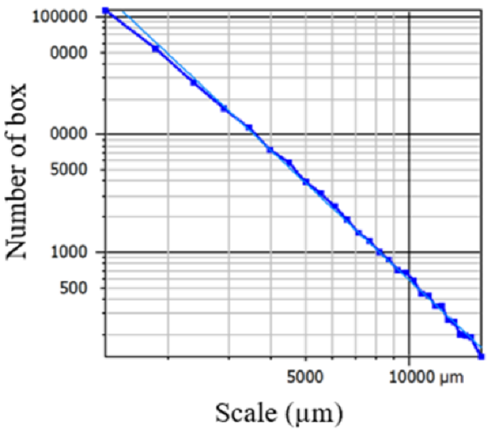	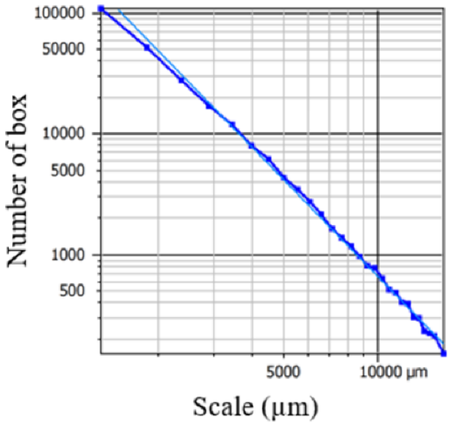
(e)	(f)
Wheatfield with Partridge	Farmhouse in a wheat field
Fractal dimension of the painting = 2.75	Fractal dimension of the painting = 2.82
Fractal dimension of extracted area = 2.76	Fractal dimension of extracted area = 2.77
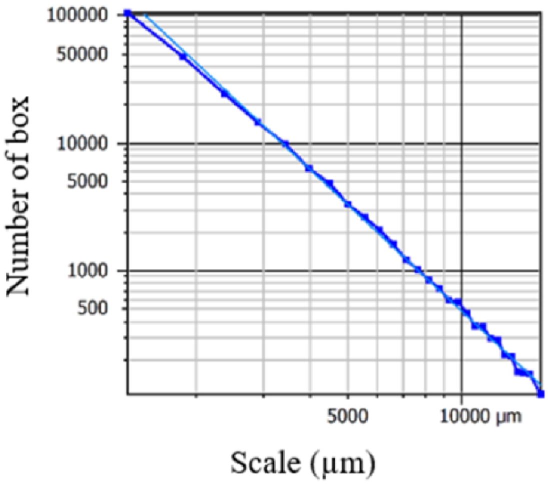	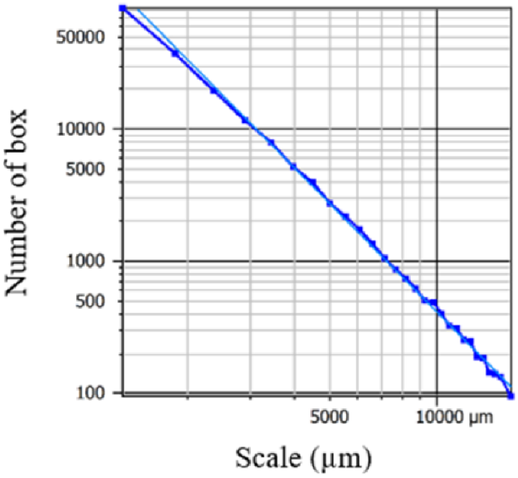

(g)	(h)
Marguerite Gachet in the Garden	The Starry Night
Fractal dimension of the painting = 2.68	Fractal dimension of the painting = 2.85
Fractal dimension of extracted area = 2.67	Fractal dimension of extracted area = 2.84
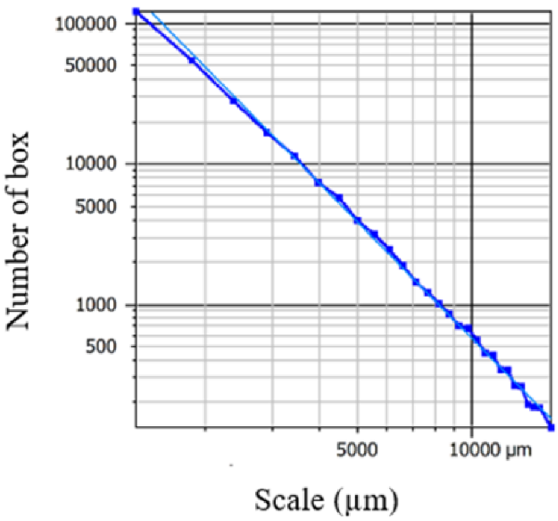	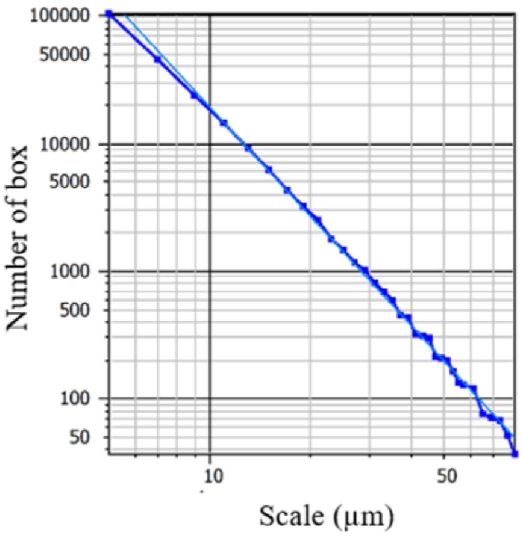

Figure 4. Graph of the fractal dimension calculations for authentic paintings. The log-log graphs represent the number of boxes in relation to the scale. For every painting the values of fractal dimension for the extracted area and the whole painting are given.

Sunset at Montmajour

Fractal dimension of the painting = 2.83

Fractal dimension of the extracted area = 2.84

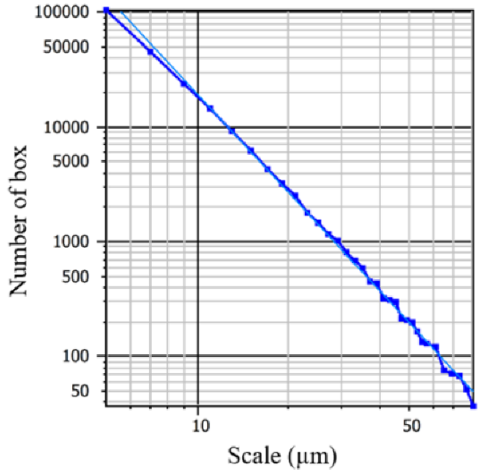

Figure 5. Graph of the fractal dimension calculation for the painting “The Ploughmen”. The values for fractal dimension of the whole painting and the extracted area are given.

The Ploughmen

Fractal dimension of the painting = 2.57

Fractal dimension of the extracted area = 2.54

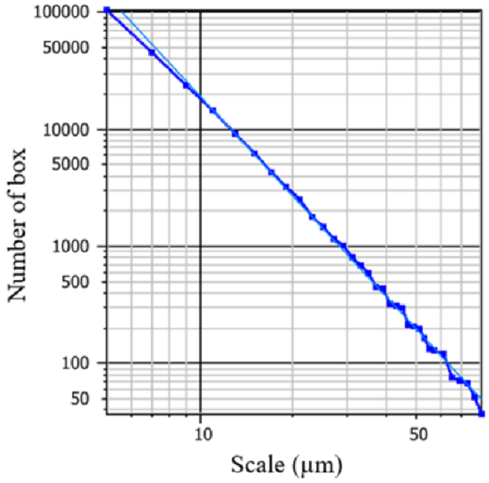

Figure 6. Graph of the fractal dimension calculation for the painting “The Ploughmen”. The values for fractal dimension of the whole painting and the extracted area are given.

Painting	Fractal Dimension of the painting	Fractal Dimension of extracted areas	Description
The Starry Night	2.85	2.84	Complex, Harmonious
Wheatfields with Crows	2.76	2.80	Complex, Irregular
Reaper	2.77	2.79	Dynamic, Complex
The Bridge on Langlois	2.66	2.74	Complex, Orderly
Two Women in the Moor	2.70	2.73	Complex, Harmonious
Wheatfield with Partridge	2.75	2.76	Complex, Balanced
Farmhouse in a Wheat Field	2.82	2.77	Complex, Balanced
Marguerite Gachet in the Garden	2.68	2.67	Simple, Orderly

Table 1. Summary of fractal dimension values for every surface from extracted areas and qualitative description of the aspect of the texture.

3.2.2 Computation of fractal dimension at the Whole Scale. This section conducts a normality test on the fractal dimension data of the artworks, excluding "Sunset at Montmajour," using the Shapiro-Wilk test. The mean fractal dimension of the artworks, without "Sunset at Montmajour," is approximately 2.73 with a standard deviation of about 0.07. The test statistic W obtained is around 0.99, with an associated p-value of approximately 0.94. The chosen significance level is 0.05. In this case, the p-value (0.94) is greater than 0.05, indicating that the normal hypothesis is not rejected. Therefore, it is concluded that the fractal dimension data of the artworks, excluding "Sunset at Montmajour," appear to be normally distributed. For "The Ploughmen," the probability corresponding to a Z-value of -2.336 is extremely low, indicating that the fractal dimension of "The Ploughmen" is significantly different from the average of the other paintings. For "Sunset at Montmajour," the probability corresponding to a Z-value of 1.64 is relatively high, indicating that the fractal dimension of "Sunset at Montmajour" is closer to the average of the other paintings. These results suggest that "The Ploughmen" exhibits distinct characteristics compared to the other Van Gogh works, while "Sunset at Montmajour" appears to be more consistent with the rest of the collection.

Discussion

The results of analyses indicate the possibility of performing stylometric analyses using the calculation of fractal dimension as a determining variable. However, it is necessary to determine the limitations of our method, which in some cases may not be significant. The disadvantages can be divided into three categories: firstly, the creative aspect and the relationship between the artist and the surface topography; secondly, the material aspect concerning the pictorial surface itself; and finally, the computational aspect with uncertainties induced by digital transformations that can influence the calculations.

Van Gogh's painting technique is an important element to consider. The painter was in constant aesthetic exploration, as mentioned in bibliographical works. This iteration on his technique naturally led to changes in terms of gestures and types of execution in the creative process. Oscillating between Post-Impressionism and Symbolism, Van Gogh's work had a considerable influence on Expressionism. One can consider that, in terms of calculating fractal dimension, a more exhaustive study would show a significant difference between the Dutch period (1880-1886) and the French period (1886-1890), culminating in his iconic style as seen in “The Starry Night”. It can be considered that this application of material, creating the texture of the work, is essential for conducting a relevant topographic study. Therefore, Van Gogh is well-suited for this type of study on the topographic signature of the painter. However, one of the limitations concerning materiality arises with other techniques, such as the glazing typical of the Renaissance. Glazing involves a very thin, smooth, and transparent layer applied over an already dry layer of oil paint. The inherent lack of texture in this technique only affects the colours and light absorption, not the materiality of the paint layer. It is easy to imagine that a study of surface topographies would be difficult in such cases. In addition to the painting technique, which can be described as impasto, the materials used are also a key factor in surface analysis. Berkmans et al. [28] present results from studies conducted with different types of brushes, round and flat, indicating an impact of the materials on surface morphology. Van Gogh primarily used flat and filbert brushes. It is evident that varying the types of materials used will have an impact on surface morphology.

This last sentence indeed relates to the material aspect of painting. The painting object is a material that evolves over time, depending on various factors. The mechanical principles of paint evolution over time will create stresses that typically manifest visibly as cracks and sometimes as blisters [45,46]. These phenomena are not the result of the artist's work and can alter the surface topography. By adding reliefs that did not originally exist i.e., by modifying the morphology due to mechanical stresses, the evolution of the paint might not yield an authentic fractal dimension value.

Finally, within the limits of our study, we can discuss how image processing may influence the calculation of the fractal dimension. Indeed, the transformation into topography is based on the intensity of the grayscale levels to interpret height points. The conditions under which the photograph was taken can significantly affect this intensity, such as the type of lighting, white balance, and file encoding. For example, the type of lighting can influence the shadows, which may obscure some texture details and lower the intensity of the grayscale levels. Additionally and to quote the study of Abry et al. [23], multifractal analysis should not be indiscriminately applied to arbitrary sections of images or paintings, as these often comprise a mix of different textures and various objects or subjects. A meaningful analysis necessitates the careful selection of areas with homogeneous textures. Here, the expertise of art specialists becomes invaluable: they can identify specific areas of interest based on the techniques used, the condition of the colours, the uniqueness of a particular section of the painting, and other relevant factors. This is why a more in-depth study using actual surface topographies, rather than those generated from photographs, is an interesting future project. Surface topography has the potential to assist art experts in making identifications.

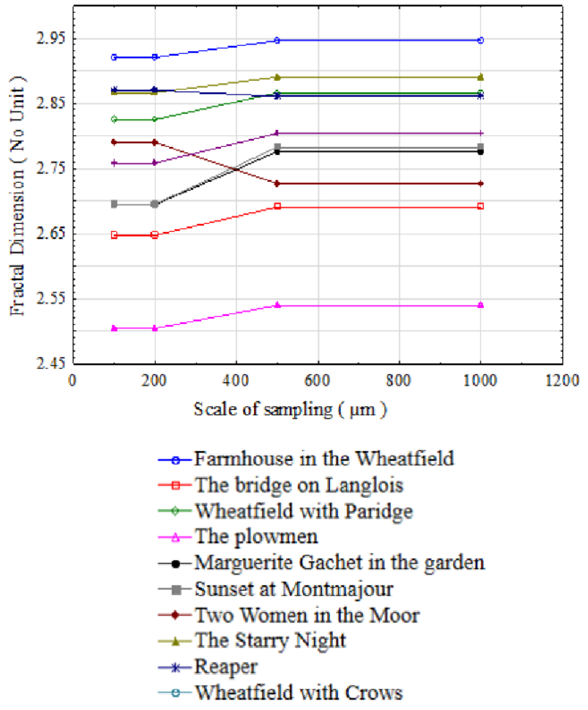

Figure 6. Variations of the fractal dimension depending on the sampling scale.

That said, it is also possible that the sampling rate influences the fractal dimension. To investigate this, we also computed the fractal dimension values using different sampling rates. The results presented in Figure 6 show that the initial hypothesis, that the fractal dimension of “The Plowmen” is significantly different from the fractal dimensions of the other works regardless of the sampling rate, holds true.

Regarding the details of the painting "The Ploughmen" topographic differences compared to other works could be observed in several aspects. For instance, the density of brushstrokes and the texture of the paint might be less complex, with less defined outlines and smoother transitions between different colour areas. Details of landscape elements such as trees, fields, or buildings could be less elaborate, with fewer variations in tonality and subtleties in textures. Additionally, the spatial composition of the painting, including the arrangement of main elements and perspective, could differ from other works, perhaps featuring a simplified organization or a focus on more elementary patterns. These differences in the painting's details could contribute to the perception of a distinct aesthetic and the recognition of "The Ploughmen" as a potentially unique piece within van Gogh's artistic corpus. This is just an additional element of authentication compared to the methods traditionally employed. While the fractal dimension provides valuable insight into the structural complexity of the painting, it's essential to recognize that authentication in the art world is a multifaceted process. Alongside technical analyses like fractal dimension measurement, authentication typically involves in-depth examinations of provenance, historical records, stylistic characteristics, and expert opinions. Each piece of evidence contributes to a more comprehensive understanding of the artwork's origins and attribution.

Conclusion

In our analysis, we examined the fractal dimensions of several Van Gogh artworks, including "Sunset at Montmajour" and "The Ploughmen." The paintings of Van Gogh, known for their expressive and tumultuous nature, exhibit a relatively high fractal dimension of the topography, typically ranging between 2.7 and 2.8 (following a Gaussian curve. These statistical analyses provided insights into the authenticity and stylistic consistency of the Van Gogh paintings, suggesting potential differences in artistic approach. The analysis rejects "The Ploughmen" as a Van Gogh, but not "Sunset at Montmajour." The results support the analyses of the Van Gogh Museum in Amsterdam. These statistical analyses provided insights into the authenticity and stylistic consistency of the Van Gogh paintings, suggesting potential differences in artistic approach. It's essential to note that fractal dimension analysis is just one complementary method among existing techniques for artwork authentication and stylistic assessment.

In perspectives, the multifractal analysis serves as an expansion of the box-counting method, a widely utilized technique for assessing the complexity and structure of fractal objects. Imagine fractal artwork as a landscape filled with intricate patterns and shapes, each exhibiting varying levels of complexity across different spatial scales. By applying advanced mathematical concepts like Hölder spectra, this approach delves into the local variations of fractal dimension at different spatial scales, akin to zooming in and out on a digital image to explore its finer details. Consider a painting by Vincent van Gogh: within the strokes of his brush lies a rich tapestry of textures and forms, each contributing to the overall composition. With multifractal analysis, experts can dissect these nuances, uncovering subtle variations in fractal dimensions that may signal unique characteristics of the artwork.

Acknowledgement

The images from this publication are all licensed under Wikipedia Creative Commons.

References

[1] Hulsker J and Gogh V van 1996 The New Complete Van Gogh: Paintings, Drawings, Sketches: Revised and enlarged edition of the catalogue raisonné of the works of Vincent van Gogh *(No Title)*

[2] Naifeh S W and Smith G W 2011 *Van Gogh: The Life* (Random House Incorporated)

[3] De La Faille J B 1930 *Les Faux Van Gogh. Avec 176 reproductions* (Impr. Arrault et Cie)

[4] de La Faille J B, van Gogh V and Hammacher A M 1970 *L'oeuvre de Vincent van Gogh. Catalogue raisonné. The works of Vincent van Gogh. His paintings and drawings.(Editorial board for the revised, augmented and annotated edition... Abraham M. Hammacher, President and others.).* (Meulenhoff international)

[5] de La Faille J-B, van Gogh V, de LaFaille J-B, de La Faille J B and Terrasse C 1939 *Vincent van Gogh* (Hypérion)

[6] Spaenjers C, Goetzmann W N and Mamonova E 2015 The economics of aesthetics and record prices for art since 1701 *Explorations in Economic History* **57** 79–94

[7] Feilchenfeldt W 1989 Van Gogh fakes: the Wacker affair, with an illustrated catalogue of the forgeries *Simiolus: Netherlands Quarterly for the History of Art* **19** 289–316

[8] Le Chanu P 1998 Contributions and limitations of scientific examination and analysis in the detection of forgeries of old masters' paintings *Scientific Detection of Fakery in Art* vol 3315 (SPIE) pp 62–73

[9] Saverwyns S, Currie C and Lamas-Delgado E 2018 Macro X-ray fluorescence scanning (MA-XRF) as tool in the authentication of paintings *Microchemical Journal* **137** 139–47

[10] Elgammal A, Kang Y and Den Leeuw M 2018 Picasso, matisse, or a fake? Automated analysis of drawings at the stroke level for attribution and authentication *Proceedings of the AAAI Conference on Artificial Intelligence* vol 32

[11] Fikiet M A, Khandasammy S R, Mistek E, Ahmed Y, Halámková L, Bueno J and Lednev I K 2018 Forensics: evidence examination via Raman spectroscopy *Physical Sciences Reviews* **4** 20170049

[12] Ragai J 2015 *Scientist and the forger, the: insights into the scientific detection of forgery in paintings* (World Scientific)

[13] Dik J, Janssens K, Van Der Snickt G, van der Loeff L, Rickers K and Cotte M 2008 Visualization of a Lost Painting by Vincent van Gogh Using Synchrotron Radiation Based X-ray Fluorescence Elemental Mapping *Anal. Chem.* **80** 6436–42

[14] van Tilborgh L, Meedendorp T and van Maanen O 2013 " Sunset at Montmajour": a newly discovered painting by Vincent van Gogh *Burlington magazine* **155** 696–705

[15] Anon 2013 Vincent Van Gogh painting Sunset at Montmajour discovered in attic unveiled in Amsterdam *The Telegraph*

[16] Liu H, Chan R H and Yao Y 2016 Geometric tight frame based stylometry for art authentication of van Gogh paintings *Applied And Computational Harmonic Analysis* **41** 590–602

[17] Hughes J M, Mao D, Rockmore D N, Wang Y and Wu Q 2012 Empirical mode decomposition analysis for

visual stylometry *IEEE Transactions on pattern analysis and machine intelligence* **34** 2147–57

[18] Johnson C R, Hendriks E, Berezhnoy I J, Brevdo E, Hughes S M, Daubechies I, Li J, Postma E and Wang J Z 2008 Image processing for artist identification *IEEE Signal Processing Magazine* **25** 37–48

[19] Cornelis B, Dooms A, Cornelis J, Leen F and Schelkens P 2011 Digital painting analysis, at the cross section of engineering, mathematics and culture *2011 19th European Signal Processing Conference* (IEEE) pp 1254–8

[20] Cornelis B, Dooms A, Daubechies I and Schelkens P 2009 Report on Digital Image Processing for Art Historians *SAMPTA'09* ed L Fesquet and B Torrésani (Marseille, France) p Special session on sampling and (in)painting

[21] Walker J S 2008 *A Primer on Wavelets and Their Scientific Applications* (CRC Press)

[22] Choi H and Baraniuk R G 1999 Image segmentation using wavelet-domain classification *Mathematical Modeling, Bayesian Estimation, and Inverse Problems* Mathematical Modeling, Bayesian Estimation, and Inverse Problems vol 3816 (SPIE) pp 306–20

[23] Abry P, Wendt H and Jaffard S 2013 When Van Gogh meets Mandelbrot: Multifractal classification of painting's texture *Signal Processing* **93** 554–72

[24] Li J, Yao L, Hendriks E and Wang J Z 2011 Rhythmic brushstrokes distinguish van Gogh from his contemporaries: findings via automated brushstroke extraction *IEEE transactions on pattern analysis and machine intelligence* **34** 1159–76

[25] Ibrahim L M 2018 Design and implementation of an automated system for analyzing brushstrokes to distinguish between Van Gogh and his contemporaries by using swarm intelligent method *Int. J. Comput. Appl* **179**

[26] Whitehouse D J 2010 *Handbook of Surface and Nanometrology* (Boca Raton: CRC Press)

[27] Brown C A, Hansen H N, Jiang X J, Blateyron F, Berglund J, Senin N, Bartkowiak T, Dixon B, Le Goïc G, Quinsat Y, Stemp W J, Thompson M K, Ungar P S and Zahouani E H 2018 Multiscale analyses and characterizations of surface topographies *CIRP Annals* **67** 839–62

[28] Berkmans F, Robache F, Mironova A, Nys L, Wieczorowski M and Bigerelle M 2024 Brushes and brains: Does handedness influence surface topography of art painting? *Measurement* **230** 114521

[29] Elkhuizen W S, Callewaert T W, Leonhardt E, Vandivere A, Song Y, Pont S C, Geraedts J M and Dik J 2019 Comparison of three 3D scanning techniques for paintings, as applied to Vermeer's 'Girl with a Pearl Earring' *Heritage Science* **7** 1–22

[30] Bigerelle M, Guibert R, Mironova A, Robache F, Deltombe R, Nys L and Brown C A 2023 Fractal and statistical characterization of brushstroke on paintings *Surf. Topogr.: Metrol. Prop.* **11** 015019

[31] Mironova A, Robache F, Deltombe R, Guibert R, Nys L and Bigerelle M 2020 Digital Cultural Heritage Preservation in Art Painting: A Surface Roughness Approach to the Brush Strokes *Sensors* **20** 6269

[32] Brown C A 2013 Areal Fractal Methods *Characterisation of Areal Surface Texture* ed R Leach (Berlin, Heidelberg: Springer) pp 129–53

[33] Liebovitch L S and Toth T 1989 A fast algorithm to determine fractal dimensions by box counting *physics Letters A* **141** 386–90

[34] Panigrahy C, Seal A, Mahato N K and Bhattacharjee D 2019 Differential box counting methods for estimating fractal dimension of gray-scale images: A survey *Chaos, Solitons & Fractals* **126** 178–202

[35] Taylor R P, Guzman R, Martin T P, Hall G D R, Micolich A P, Jonas D, Scannell B C, Fairbanks M S and Marlow C A 2007 Authenticating Pollock paintings using fractal geometry *Pattern Recognition Letters* **28** 695–702

[36] Noce V Les errances d'un vrai-faux Van Gogh *Libération*

[37] Anon 2003 France - Un tableau attribué à Van Gogh est retiré de la vente *Le Devoir*

[38] Anon 2003 Querelles d'experts autour d'un Van Gogh vendu aux enchères en Gironde *Le Monde.fr*

[39] Nixon M S and Aguado A S 2012 Chapter 13 - Appendix 4: Color images *Feature Extraction & Image Processing for Computer Vision (Third Edition)* ed M S Nixon and A S Aguado (Oxford: Academic Press) pp 541–600

[40] Blackledge J M 2005 Introduction *Digital Image Processing* Woodhead Publishing Series in Electronic and Optical Materials ed J M Blackledge (Woodhead Publishing) pp 1–21

[41] Dubuc B, Zucker S W, Tricot C, Quiniou J F, Wehbi D and Berry M V 1997 Evaluating the fractal dimension of surfaces *Proceedings of the Royal Society of London. A. Mathematical and Physical Sciences* **425** 113–27

[42] Dubuc B, Quiniou J F, Roques-Carmes C, Tricot C and Zucker S W 1989 Evaluating the fractal dimension of profiles *Phys. Rev. A* **39** 1500–12

[43] Blunt L and Jiang X 2003 *Advanced techniques for assessment surface topography: development of a basis for 3D surface texture standards" surfstand"* (Elsevier)

[44] 25178-2:2021 *ISO*

[45] Keck S 1969 MECHANICAL ALTERATION OF THE PAINT FILM *Studies in Conservation* **14** 9–30

[46] Pauchard L and Giorgiutti-Dauphiné F 2020 Craquelures and pictorial matter *Journal of Cultural Heritage* **46** 361–73

Appendix A

This appendix provides an overview of the selected areas extracted from the paintings for the calculation of fractal dimension. Each painting was converted into a surface topography using the grayscale levels of the images. Each area was extracted using the Mountain map software.

(a)
Wheatfield with Crows
(i)


<table>
<tr><td>(ii)</td><td>(iii)</td></tr>
<tr><td>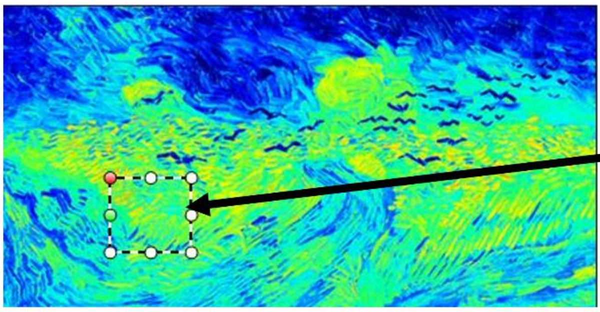</td><td>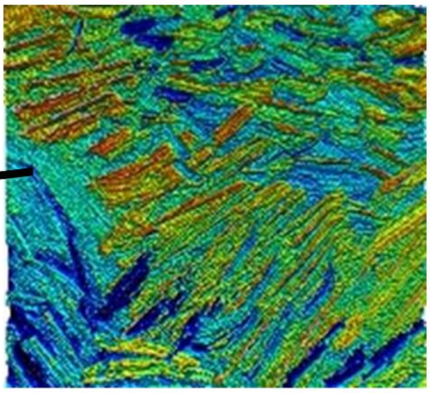</td></tr>
<tr><td colspan="2">(b)</td></tr>
<tr><td colspan="2">Reaper</td></tr>
<tr><td colspan="2">(i)</td></tr>
<tr><td colspan="2">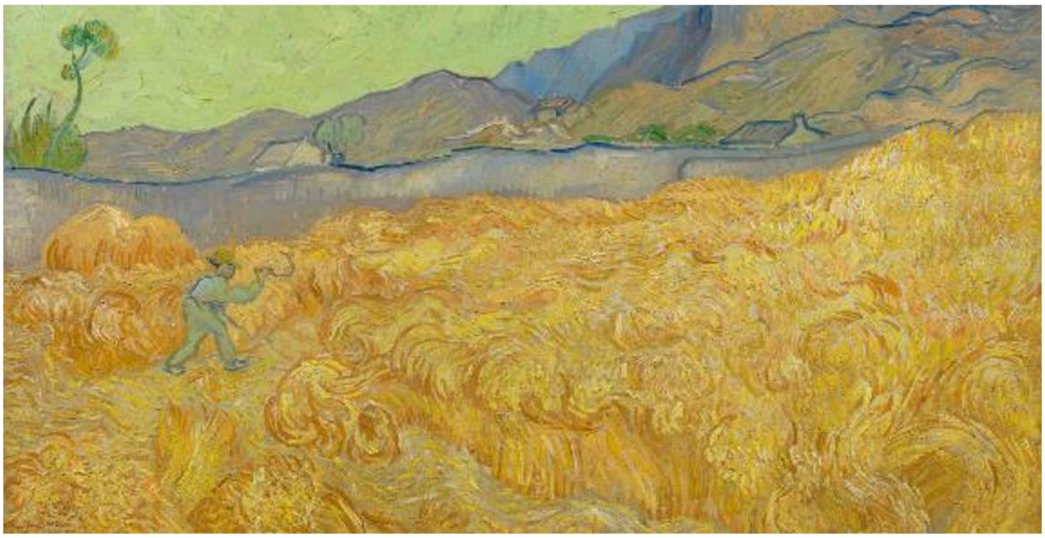</td></tr>
</table>

<table>
<tr><td>(ii)</td><td>(iii)</td></tr>
<tr><td>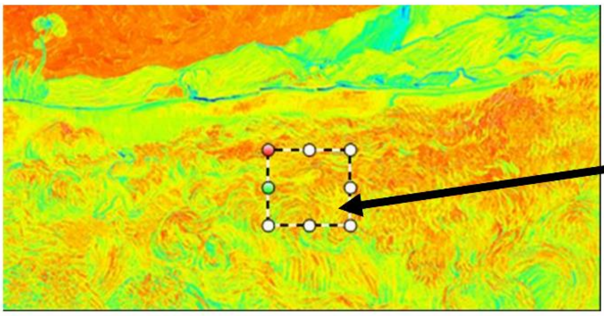</td><td>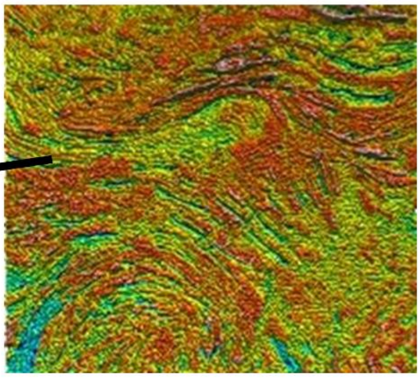</td></tr>
<tr><td colspan="2">(c)</td></tr>
<tr><td colspan="2">The bridge on Langlois</td></tr>
<tr><td colspan="2">(i)</td></tr>
<tr><td colspan="2">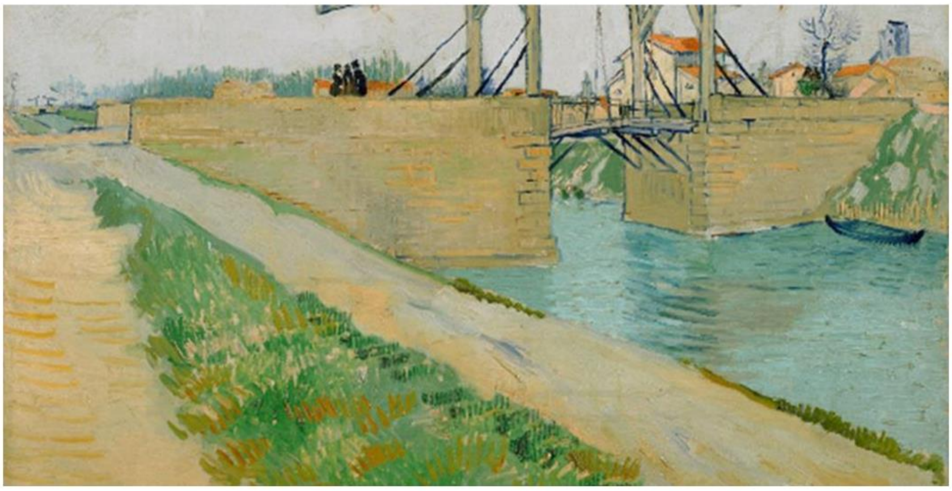</td></tr>
<tr><td>(ii)</td><td>(iii)</td></tr>
<tr><td>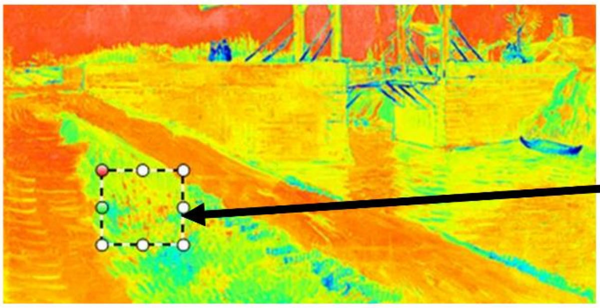</td><td>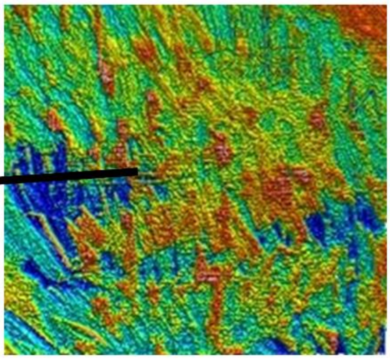</td></tr>
</table>

<table>
<tr><td colspan="2">(d)</td></tr>
<tr><td colspan="2">Two Women in the Moor</td></tr>
<tr><td colspan="2">(i)</td></tr>
<tr><td colspan="2"></td></tr>
<tr><td>(ii)</td><td>(iii)</td></tr>
<tr><td>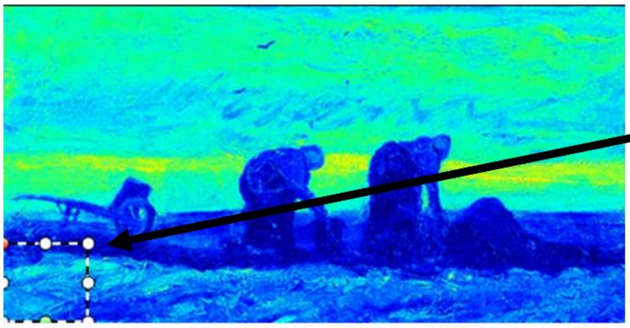</td><td>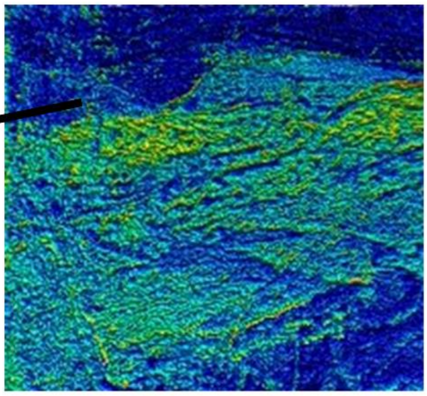</td></tr>
</table>

(e)
Wheatfield with Partridge
(i)
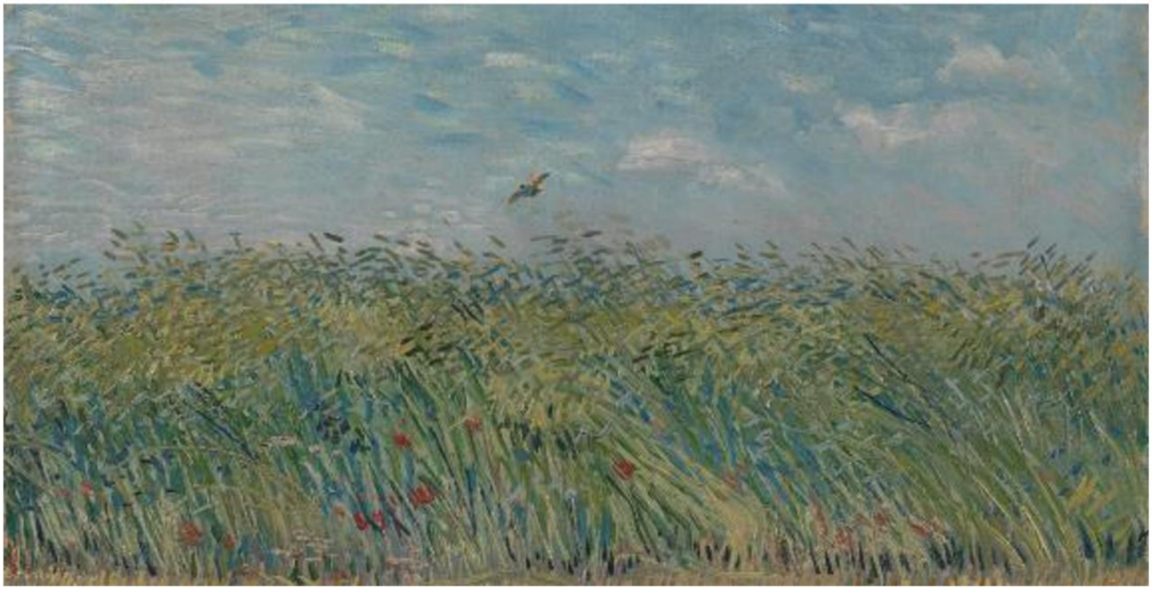

(ii)	(iii)
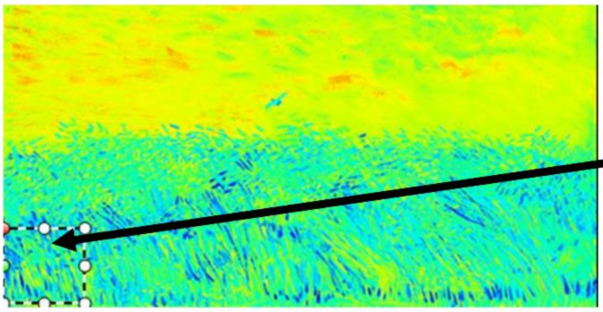	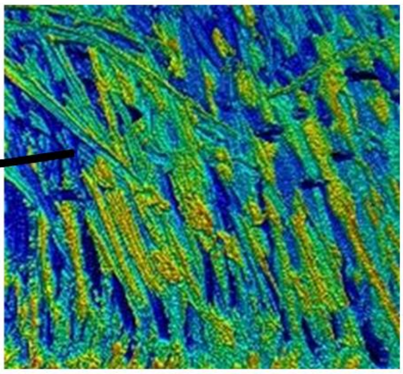

(f)

Farmhouse in a wheat field

(i)

(ii)

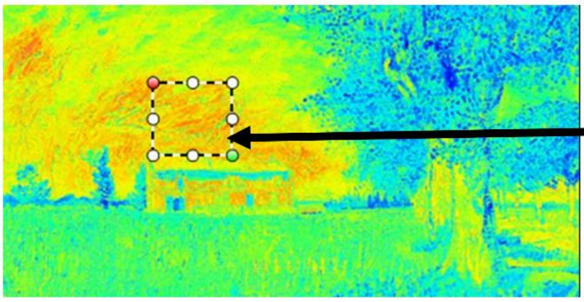

(iii)

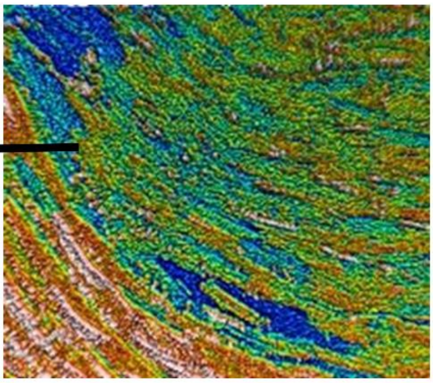

(g)

Marguerite Gachet in the Garden

(i)

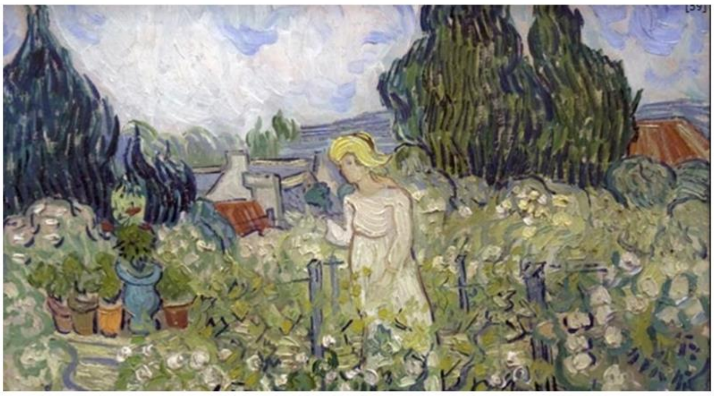

<table>
<tr><td>(ii)</td><td>(iii)</td></tr>
<tr><td>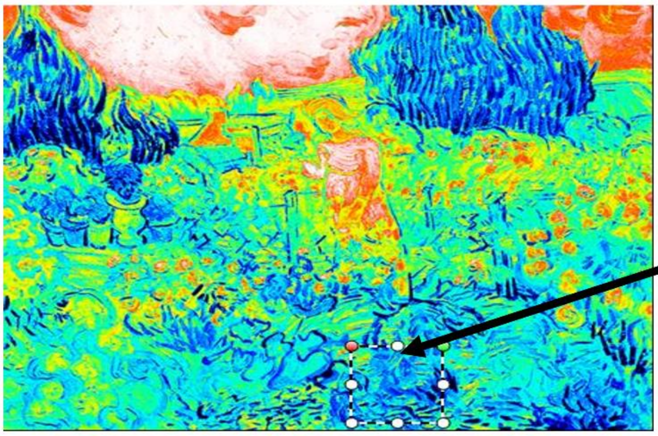</td><td>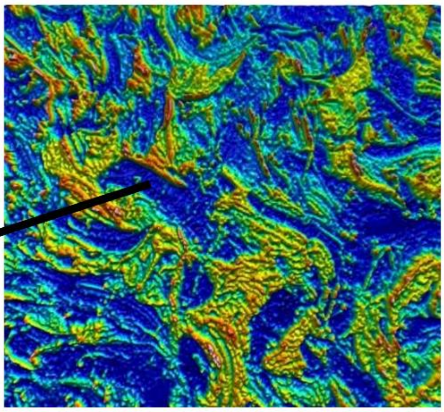</td></tr>
<tr><td colspan="2">(h)</td></tr>
<tr><td colspan="2">The Sarry Night</td></tr>
<tr><td colspan="2">(i)</td></tr>
<tr><td colspan="2"></td></tr>
</table>

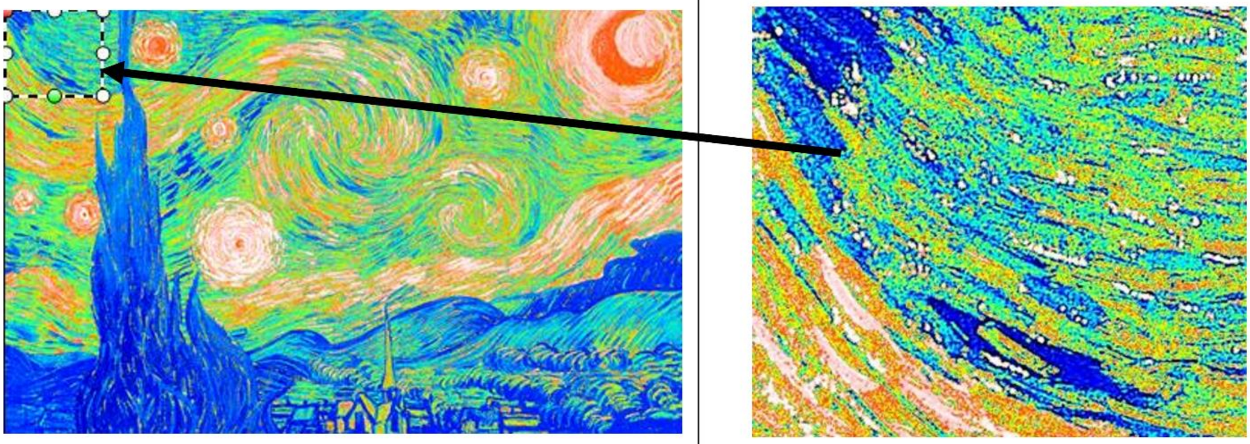

(ii)

(iii)

Figure A.1. Pictures of the painting from the authentic paintings catalogue from Van Gogh in (i) are the picture of the artworks (ii) the conversion of the painting into surface topography and (iii) the details of the extracted areas.

Sunset at Montmajour

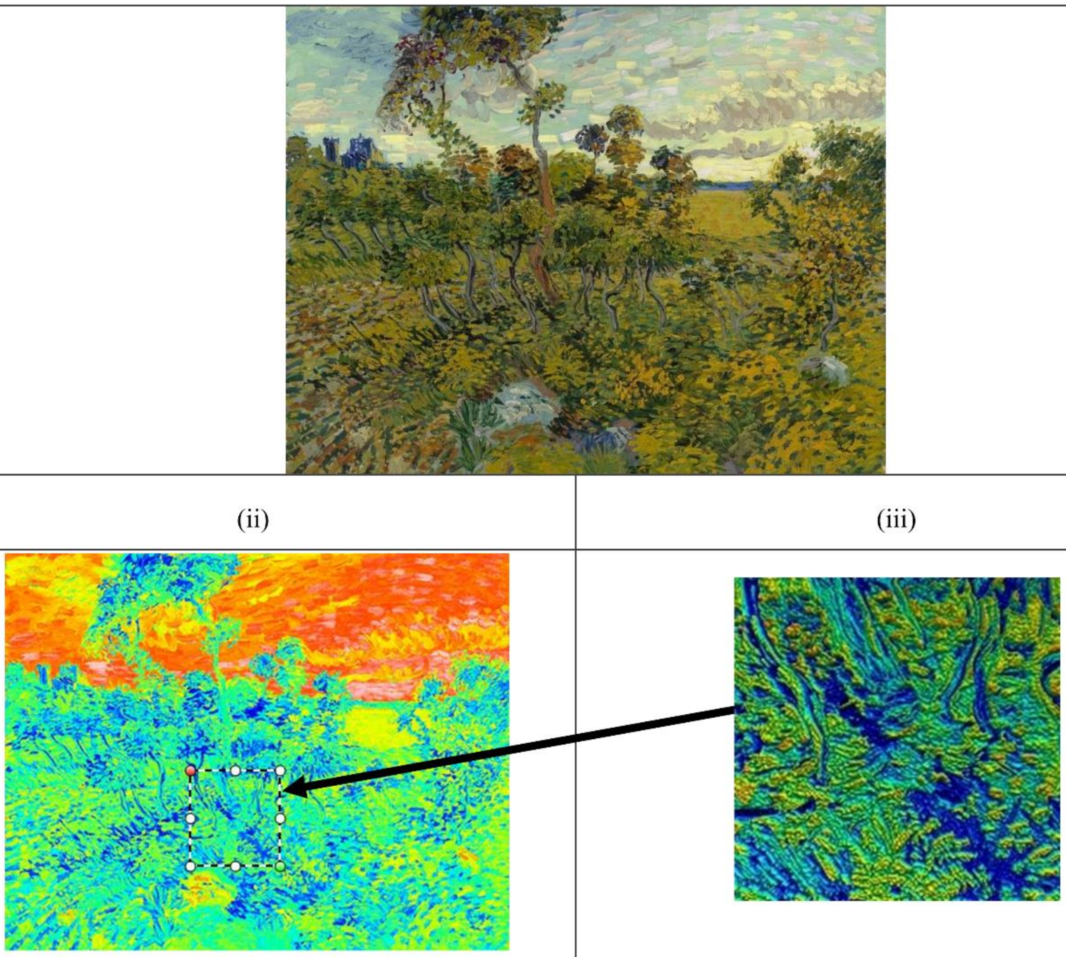

(i)

(ii)

(iii)

Figure A.2. Pictures of the painting “Sunset at Montmajour” in (i) are the picture of the artwork (ii) the conversion of the painting into surface topography and (iii) the details of the extracted area.

<table>
<tr><td colspan="2">The Ploughmen</td></tr>
<tr><td colspan="2">(i)</td></tr>
<tr><td colspan="2"></td></tr>
<tr><td>(ii)</td><td>(iii)</td></tr>
<tr><td>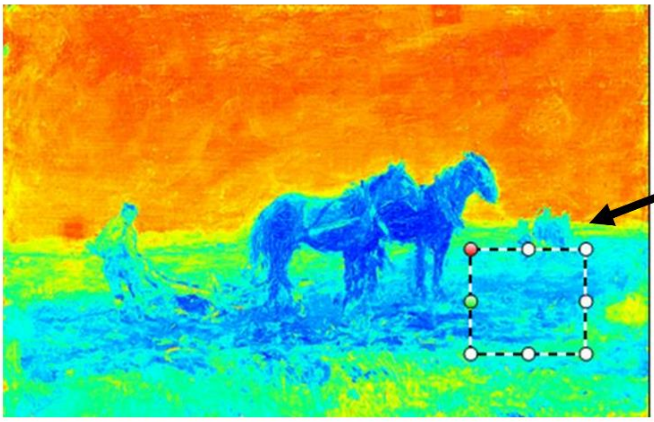</td><td>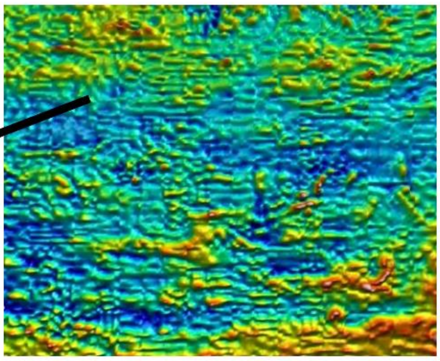</td></tr>
<tr><td colspan="2">Figure A.3. Pictures of the painting of “the Ploughmen” in (i) are the picture of the artwork (ii) the conversion of the painting into surface topography and (iii) the details of the extracted area.</td></tr>
</table>

5.7 Conclusion of the Chapter

This chapter has shown that the Sdr–Gaussian protocol calibrated in Chapter 4 can be transferred, without changing the tooling, to pictorial surfaces: the selected impastos exhibit scale-consistent topographic signatures, and Bootstrap confidence bands help separate instrumental variability from what belongs to gesture and material. Correlated with simple indicators (the multi-scale distribution of Sdr, local slopes, and, as a complement, a box-counting window), the analysis brings out differences in structural complexity that resonate with stylistic descriptors (turbulence, vibration, ridge continuity). In other words, the SAIS here completes its arc “from words to measurement and back to meaning”: the precise terminology (Chap. 1) and visual syntax (Chap. 2) find their quantitative fulfilment (Chaps. 3–4) in an interpretable reading of art surfaces. This approach nevertheless depends on the quality of image-to-topography conversion, on the heterogeneity of supports and media, and on corpus size. With these guardrails in place, the chapter establishes the feasibility of a prudent multi-scale diagnosis, neither purely stylistic nor purely metrological, paving the way for Chapter 6 (or the General Conclusion), where we discuss generalisation to other artists/materials, integration into annotation databases, and standardisation avenues (multi-scale reporting and uncertainty).

General Conclusion

This dissertation has demonstrated that the Surface-Information Acquisition Spectrum (SIAS) can carry surface knowledge from language to visual syntax, through visualisation/discretisation, into quantitative evaluation, and back to interpretation across industrial and artistic contexts. The chapters collectively show that once the tiers of the SIAS are made explicit, and each tier is given its own methods and quality controls, surfaces become commensurable: we can name what we see, state how parts combine, control how images become data, and report what the numbers mean with uncertainty before we act or interpret. Rather than simply recapitulating results, this conclusion sets a path for consolidating the work into an operational pipeline.

Chapter 1 (Language tier) established a phenomenon-centred OWL ontology that reconciles scattered vocabularies and enables humans and machines to refer to the same objects of discourse. The next step is to harden this layer for reuse: align classes and relations systematically with ISO 25178-2 and ASME B46.1 through explicit SKOS mappings; provide "competency questions" and a SPARQL cookbook so that queries become reproducible acts rather than ad-hoc scripts; extend labels and definitions across languages and domains, particularly toward heritage vocabularies where terms like *toolmark* or *impasto ridge* must be anchored without ambiguity; and release citable versions with semantic versioning and DOIs. A small web-based annotator that writes valid OWL individuals and enforces domain/range constraints would make the ontology practical beyond this manuscript.

Chapter 2 (Visual-syntax tier) treated heraldry as a 2.5-D information surface governed by a grammar whose complexity can be quantified. The immediate prospect is to generalise beyond the present corpus by testing other traditions and periods so that any "complexity window" observed is not a parochial artefact. This can be strengthened by linking text and image through a rules-first blazon parser that outputs a canonical, machine-readable assembly of each coat; complexity can then be measured directly from structure rather than from pictures alone. A basic psychophysical programme, recognition accuracy as a function of viewing distance for coats stratified by complexity, would test whether the distributional fits identified here predict legibility in practice. Finally, a grammar-constrained generator for heraldic designs would let us run controlled experiments and power analyses, turning qualitative claims into testable models.

Chapter 3 (Visualisation/Discretisation tier) used the Koch snowflake to expose how sampling density, indentation geometry and mesh choices bias fractal estimates and to justify Gaussian low-pass filtering within a documented safe-resolution envelope. The prospect here is twofold: move from curves to surfaces and from idealised to instrument-realistic simulations. Synthetic 3-D fractal surfaces and engineered textures can extend the rules-of-thumb to areal data, while injecting point-spread functions and realistic noise will bring simulations closer to interferometry and focus-variation reality. A systematic comparison of filter families—Gaussian, robust Gaussian, morphological, should clarify when robustness trumps optimality in the presence of outliers. Publishing closed-form guidance (or tables) relating curvature, node density and target error would convert this chapter's insights into quick reference for practitioners.

Chapter 4 (Quantitative-evaluation tier) fused the previous insights into a multi-scale Sdr descriptor with Gaussian prefiltering and residual-bootstrap uncertainty, validated against alternative estimators and applied to grit-blasted and turned metals. To make this portable, the method should be wrapped as an operational SOP: acquisition settings, filtering, multi-scale Sdr computation, bootstrap configuration, and a standard reporting template with cut-offs and confidence ribbons. Coupling the output to simple process-control dashboards and change-point detection would carry the approach from analysis into decision-making on production lines. A multi-lab round-robin with shared artefacts can then test inter-instrument reproducibility, paving the way for a pre-standardisation note on multi-scale reporting with uncertainty. Hybrid descriptors that combine Sdr with slope and feature counts could improve sensitivity to specific process signatures, provided the accompanying uncertainty remains first-class output rather than an appendix.

Chapter 5 (Artistic transfer) applied the same Sdr Gaussian Bootstrap pipeline to impasto-rich paintings, revealing scale-consistent topographic signatures and cautious correspondences with stylistic descriptors. The methodological priority now is to stabilise the acquisition chain for artworks: non-invasive protocols for illumination, safety and registration; mock-up canvases with known textures to calibrate the full image-to-topography conversion; and expansion of the corpus beyond a single artist to include contemporaries, studio works, copies and restorations, paired with material dossiers that control for binders and fillers. On the interpretive side, Bayesian models that incorporate art-historical priors alongside topographic evidence can separate questions of provenance from questions of style or process, keeping in view that uncertainty is part of the result. FAIR data releases, with locational and acquisition metadata, would enable curators and conservators to reanalyse and cross-compare beyond this thesis.

Taken together, these prospects outline a realistic trajectory for the next three years: a first year focused on ontology hardening and public releases of analysis code; a second year dedicated to round-robins, new heraldic corpora and 3-D discretisation studies; and a third year in which at least one industrial line and one museum partner run the full SIAS pipeline on their own data. If carried out, this will shift the contribution from a proof-of-concept across domains to a shared practice: the same conceptual tiers, the same documented filters, the same uncertainty conventions, serving both the factory floor and the gallery wall. In that sense, the SIAS is not merely a map of ideas; it is a concrete path that others can walk, confident that language, structure, sampling and measurement have been bound together in a way that makes surfaces intelligible, comparable and meaningful.

Appendix A

Corpus of Scientific Articles with Extracted Vocabulary for Surface Description

In this appendix, the author presents the scientific articles used for the corpus analysis in Chapter 1. These articles were analysed manually due to the lack of terminological data on the textual description of surfaces.

N°	Title of the article	DOI	Terms present in the article
1	Comparison of three multiscale methods for topographic analyses	10.1088/2051-672X/ab8348	NA
2	A multiscale topographical analysis based on morphological information: The HEVC Multiscale decomposition	https://doi.org/10.3390/ma13235582	NA
3	Ion excitation and etching effects on top-surface properties of sp2 T nanocrystallited carbon films	https://doi.org/10.1016/j.apsusc.2018.08.148	NA
4	High-Performance Inverted Perovskite Solar Cells with Mesoporous NiOx Hole Transport Layer by Electrochemical Deposition	https://doi.org/10.1021/acsomega.8b02612	NA
5	Effect of surface modifications of additively manufactured Ti-6Al-4V alloys on apatite formation ability for biomedical applications	https://doi.org/10.1016/j.jallcom.2021.161445	NA
6	Determination of an Objective Criterion for the Assessment of the Feasibility of an Instrumented Indentation Test on Rough Surfaces	https://doi.org/10.3390/ma13071589	NA
7	How to Select 2D and 3D Roughness Parameters at Their Relevant Scales by the Analysis of Covariance	https://doi.org/10.3390/ma13071526	NA
8	Mechanical Integrity of 3D Rough Surfaces during Contact	https://doi.org/10.3390/coatings10010015	NA
9	Analyses of tribological properties of castor oil with various carbonaceous micro- and nano- friction modifiers	https://doi.org/10.1115/1.4036379	NA
10	Development and characterization of glycerol coating on the PAN/PVDF composite membranes	10.1088/1757-899X/458/1/012006	NA
11	Texturation de surface par LASER femtoseconde en régime ElastoHydro-Dynamique et limite : application au contact Segment/Piston/Chemise d’un moteur thermique à combustion	HAL index : tel-00688051	NA
12	Analyse et optimisation des surfaces des chemises de moteurs thermiques	https://pastel.archives-ouvertes.fr/pastel-00002512	platea+O13:O87ux lisses et réguliers, stries de lubrification
13	Contacts ElastoHydroDynamiques micro-texturés	HAL Id: hal-03391280	cavités
14	Fretting fatigue and fretting wear	https://doi.org/10.1016/0301-679X(89)90081-9	cracked surface
15	The effect of surface regular microtopography on fretting fatigue life	https://doi.org/10.1016/S0043-1648(02)00148-5	NA
16	Surface texturing for adaptive surface solid lubrication	https://doi.org/10.1016/j.surfcoat.2008.07.033	grids, pores, dimples
17	Mechanisms of self-lubrication in patterned TiN coatings containing solid lubricant microreservoirs	https://doi.org/10.1016/j.surfcoat.2010.01.012	pattern, wafer, scratches, holes, reservoirs, islands,
18	Fabrication and tribological properties of composite coatings produced by lithographic and microbeading methods	https://doi.org/10.1016/j.surfcoat.2009.05.031	NA
19	Laser surface texturing for adaptive solid lubrication	https://doi.org/10.1016/j.wear.2006.03.013	dimple
20	Review of engineered tribological interfaces for improved boundary lubtication	https://doi.org/10.1016/j.triboint.2004.08.008	dimple
21	Additional Tribological Effect of Laser Surface Texturing and Diamond-Like Carbon Coating for medium carbon steel at near room temperature	https://doi.org/10.3390/coatings10100929	smooth, textured; coated, worn
22	Laser microstructuring of steel surfaces for tribological applications	https://doi.org/10.1007/s003390051073	micro-hole, 2D array, hole, sharp-edged craters
23	The effect of laser surface texturing on transitions in lubrication regimes during unidirectional sliding contact	https://doi.org/10.1016/j.triboint.2004.08.004	polished, ground, standard LST, higher dimple density, standard unlapped, lower dimple density; dimples
24	Friction and Wear Propierties of Micro Textured DLC Coated Surfaces in Boundary Lubricated Sliding	https://doi.org/10.1023/B:TRIL.0000044504.76164.4e	grooved oriented perpendicular to the sliding direction, squared texture, grooved oriented surface along the direction of sliding, un textured surface, grooved surface turned 45° from the sliding direction
25	Tribological characterization of different geometries generated with laser surface texturing for tooling applications	https://doi.org/10.1016/j.wear.2021.203856	micro cavities, microgrooves, lines, crosshatch, dimple, triangle, circle, "S" groove, square, cross lines
26	The influence of the tool surface texture on friction and the surface layers properties of formed component	DOI: 10.12913/22998624/85704	dimple-like depression, ellipsoid, circular groove, "S" groove , radial, tetragonal, hexagonal
27	Precise fabrication of microtextured stainless steel surfaces using metal injection moulding	https://doi.org/10.1016/j.precisioneng.2019.11.012	round shaped micropillars, round shaped micropits, square shaped micropillars with protective pillars, hexagonal arrangements
28	Mechanical micro-texturing and charactirization on Ti6Al4V for the improvement of surface properties	https://doi.org/10.1016/j.surfcoat.2019.125087	Micro dimple textured surfaces, micro dimples with extruded center
29	Assessment of Super-Hydrophobic Textured Coatings on AA6082 Aluminium Alloy / Appendix 1	https://doi.org/10.3390/coatings9060352	Low surface energy, hierarchical rough surface, homogeneous structure, flower-like structure, flakes clusters, petal like flakes, bimodal structure, coral network structure, pixel like structure
30	Precise control of surface texture on carbon film by ion etching through filter : Optimization of texture size for improving tribological behavior	https://doi.org/10.1016/j.surfcoat.2019.01.095	holes ,pit-type array
31	Production and Tribolofical Characterization of Tailored Laser-Induced Surface 3D Microtextures	doi:10.3390/lubricants7080067	Laser-induced periodic surface structures (LIPSS), pinhole, inhomogeneities, plateau
32	Surface texture Manufacturing techniques and tribological effect of surface texturing on cutting tool performance : A review	https://doi.org/10.1080/10408436.2016.1186597	sine wave texture , banded nano/micro textured ,cross patterned , sine wave shaped , linear grooves , pit shaped , dot shaped, banded grooves , pyramid shaped grooved
33	Effect of surface texturing on friction reduction between ceramic and steel materials under lubricated sliding contact	https://doi.org/10.1016/S0043-1648(03)00004-8	spherical morphology, angular dimples, micro dimples.
34	The lubrication effect of micro-pits on Parallel sliding faces of SiC in Water	https://doi.org/10.1080/10402000208982552	pits, micro pits , cavitation, square array
35	The effect of laser texturing of SiC surface on the critical load for the transition of water lubrication mode from hydrodynamic to mixed	https://doi.org/10.1016/S0301-679X(01)00063-9	pores
36	Dimples shape and distribution effect on characteristics of Stribeck curve	https://doi.org/10.1016/j.triboint.2009.06.001	oil pocket, holes, dimples, pits, spherical holes, drop shape long and short
37	The effet of surface texturing on seizure resistence of a steel-bronze assembly	https://doi.org/10.1016/j.triboint.2010.04.016	pockets, oil pockets, dimple, pit, micropits
38	Micro-Textures in Concentrated Conformal-Contact Lubrication: Effects Of Texture Bottom Shape and Surface Relative Motion	https://doi.org/10.1007/s11249-008-9302-9	texture bottom shape, dimple, flat and arc bottom; the arrow indicates the motion direction of textured surfaces , equilateral triangle matrix, hollow cylinder,
39	Experimental study of the effect of microtexturing on oil lubricated ceramic / steel friction pairs	https://doi.org/10.1016/j.wear.2008.12.108	NA
40	Friction-Reducing Surface-Texturing in Reciprocating Automotive Components	https://doi.org/10.1080/10402000108982468	longitudinal pores column, pores distribution, micro-pores
41	Performance Improvement of Graphene/Silicon Solar Cells via Inverted Pyramid Texturation Array	https://doi.org/10.1007/s12633-022-01725-4	inverted pyamid arrays,
42	Enhanced efficiency of graphene-silicon schottky junction solar cell through pyramid arrays texturation	10.1007/s12633-021-01579-2	pyramid,
43	Study of femtosecond laser multi-scale textured steel surfaces on the wettability in relation to aging	https://doi.org/10.1007/s10853-021-06574-x	ridges, trenches, protrusions, double scale hierarchical structures, lotus leaves morphology, trenches, grid,
44	A correlation between tribological behaviour and crystal structure of cobalt-based hardfacings	https://doi.org/10.1016/j.wear.2019.01.091	columnar grains with dendritic microstructures, dendritic matrix, interdendritic carbids
45	Texturation and superhydrophobicity of polyethylene terephtalate thanks to plasma technology	http://dx.doi.org/10.1016/j.apsusc.2013.12.051	textured, hemispheres

46	Identification of local lubrication regimes on textured surfaces by 3D roughness curvature radius	10.4028/www.scientific.net/AMR.966-967.120	cavities, plateau, flat surfaces, peaks, anisotropy
47	Durability of an As2S3 chalcogenide glass : Optical properties and dissolution kinetics	10.1016/j.jnoncrysol.2010.09.020	surface flaws (micro scaled cracks), cup-like shapes,
48	Interface roughness effect on friction map under fretting contact conditions	10.1016/j.triboint.2010.02.010	highly anisotropic textures, orthogonally oriented by the sliding direction,
49	Processing and characterization of GaAs surface-barrier heterostructures with texturized interface	10.1109/ASDAM.1998.730169	dendrite, quasigrating type,
50	Plasma modification and synthesis of membrane materials—a mechanistic review	10.3390/membranes8030056	pores
51	Enhanced thermoelectric properties of highly textured Bi20-xSe1+x with liquid-phase mechanical exfoliation	https://doi.org/10.1016/j.scriptamat.2019.12.003	NA
52	Study of the electro-responsiveness and surface texturing of pedot : PSS for smart mems interface applications	10.1109/TRANSDUCERS.2017.7994317	NA
53	Plasma induced physicochemical effects on a poly(amide) thin-film composite membrane	https://doi.org/10.1016/j.desal.2016.06.009	smoothed, roughening, smoothed morphology, pore diameters
54	Double texturations for light trapping in Thin Film Crystalline Silicon Solar Cells	10.1109/PVSC.2014.6924999	2D DGs, with random texturation, patterned, nano holes, vertical sidewalls
55	Influence of Laser Bean Polarization on Laser Micro-Machining of Molybdenum	DOI: 10.2961/jlmn.2013.03.0001	parallel lines, grave and conicity of groove, triangular shape, nanostructures, ripples, lines,
56	Effect of surface texturing on rolling contact fatigue within mixed lubricated non-conformal rolling/sliding contacts	https://doi.org/10.1016/j.triboint.2010.02.002	micro-dents; triangular arrangements; square arrangements; shallow dents
57	Effect of laser surface texturing (LST) on tribological behavior of double glow plasma surface zirconizing coating on Ti6Al4V allow	https://doi.org/10.1016/j.surfcoat.2019.04.038	dimple patterns,
58	Effect of Shape, density, and an Array of Dimples on the friction and wear performance of laser textured bearing steel under dry sliding	https://doi.org/10.1007/s11665-020-04816-8	dimples, dimples density, bi-triangular, circular dimples, micro-pores
59	Surface texturing using pulsed air arc treatment	https://doi.org/10.1016/j.wear.2006.11.043	micro-reservoirs, micro-traps, hollow hemisphere,
60	Surface texturing techniques to enhance tribological performance : A review	https://doi.org/10.1016/j.surfin.2021.101463	pas de mots c'est un review
61	Design and development of surface texture for tribological application	doi:10.4028/www.scientific.net/KEM.803.55	square, circular, triangular texture shapes, dimples
62	Effect of Low Depth Surface Texturing on Friction Reduction in Lubricated Sliding Contact	https://doi.org/10.3390/lubricants6030062	grid-like pattern, dimples, line like
63	Tribological effects of laser surface texturing and residual stress	https://doi.org/10.1108/ILT-11-2016-0282	No texture , circular dimple, elliptical dimple, groove
64	The effect of laser surface texturing on the tribological performance of different Sialon ceramic phases	http://dx.doi.org/10.1016/j.pnsc.2016.08.003	dimple, dimple pitch
65	Dry sliding wear behavior of TC11 alloy at 500°C : Influence of laser surface texturing	http://dx.doi.org/10.1016/j.triboint.2015.06.003	dimples,
66	Enhancement of substrate-coating adherence of boron-doped diamond electrodes by nanosecond laser surface texturing pretreatment	https://doi.org/10.1016/j.surfcoat.2018.12.098	valley shape, cluster structure, concave structure, cracks, irregular edge morphology, spherical particles, speroidization effect, spherical spatter and cracks
67	Study and analysis the Cu nanoparticle assested texturisation forming low reflective silicon surface for solar cell application	https://doi.org/10.1063/1.5109003	inverted shape almost similar to inverted pyramids or porous surface, irregular surface, grooved surface, pyramidal and semi pyramidal porous surface,
68	Novel laser textured surface designs for improved zirconia implants performance	https://doi.org/10.1016/j.msec.2019.110390	micro scale grooves, cavities, pillars
69	Design of "double layer" texture to obtain superhydrophobic and high wear-resistant PTFE coatings on the surface of AL203/Ni layered ceramics	https://doi.org/10.1016/j.triboint.2019.04.004	micro-dimples, micro-grooves, and micro-meshes, micro-squares,
70	Short and Long-Term Wettability Evolution and Corossion Resistence of uncoated and Polymer-Coated Laser-Textured Steel surface	http://dx.doi.org/10.3390/coatings9090592	0°/90° scanning strategy, x, y μchannel pattern, line separations, consequence overlap channel
71	High friction and low wear propoerties of laser-textured ceramic surface under dry friction	http://dx.doi.org/10.1016/j.optlastec.2017.01.032	linear grooves, wavy grooves, wavy pattern
72	Comparison of the effect of typical patterns on friction and wear properties of chromium alloy prepared by laser surface texturing	https://doi.org/10.1016/j.optlastec.2018.04.020	micro dimples; micro-grooves; micro-grids
73	A critical assessment of surface texturing for friction and wear improvement	http://dx.doi.org/10.1016/j.wear.2016.11.020	Penrose-like textures, Laser interference of polymide sheets, pyramidal texturing, honeycomb-like patterns, micro coining of 100Cr6 steel, regular arrays of V -shaped
74	Friction control by surface engineering of ceramic sliding pairs in water	doi:10.1016/j.wear.2006.11.024	polished, parallel oriented, elongated dimples, crossed microchannels
75	Effects of laser texturing on the wear and failure mechanism of grey cast iron reciprocating against steel under starved lubrication conditions	http://dx.doi.org/10.1016/j.wear.2017.05.015	none
76	Moving textures : Simulation of a ring sliding on a textured liner.	https://doi.org/10.1016/j.triboint.2013.12.013	close packed arrays of circular pockets; pocketed surface, ellipsoidal-bottomed dimple, square array of pockets,
77	Minimize friction of lubricated laser-microtextured-surfaces by tuning microholes depth	https://doi.org/10.1016/j.triboint.2014.03.014	micro-holes, oil pocket,
78	The surface texture and its influence on the tribological characteristics of a friction pair : metal-polymer	https://doi.org/10.1016/j.acme.2016.10.011	irregularities, i.e. valleys, holes, hills, their number and size, scratched, dents, cracks, small cavities, horizontal trace
79	The effect of attributes of micro-shapes of laser surface texture on the wettability of WC-CrCo metal ceramic coatings	https://doi.org/10.1016/j.surfcoat.2017.12.001	grooves, dimples, grids,
80	Friction and wear on laser textured Ti6Al4V surface subjected to laser shock peening with contacting foil	https://doi.org/10.1016/j.optlastec.2017.12.044	micro-dimples, micro cracks;
81	Impact of Plateaued surfaces on tribological performance	https://doi.org/10.1080/10402009608983538	plateaued surface, non plateaued surface, plateau-honed surface
82	Laser texturing for low-flying-height media	http://dx.doi.org/10.1063/1.347908	crater shaped dimples
83	New methodology to evaluate the rolling contact fatigue performance of bearing stells with surface dents : application to 32CrMov13 (Nitrided) and M50 steels	https://doi.org/10.1115/1.1924462	NA
84	Effect of building directions on the surface roughness, microstructure, and tribological properties of selective laser melted Inconel 625	https://doi.org/10.1016/j.jmatprotec.2020.116878	stair steps, stair stepping effect, balling phenomenon
85	Surface design and texturing of strip steel using nanosecond pulsed lasers for simulated roughness transfer and paint appearance	https://doi.org/10.1016/j.jmatprotec.2019.116365	silngle crater morphology, micro-dimples, rectangular and offset, crater overlapping,
86	Influence of Surface Morphology on Absoptivity of Light-Absorbing Materials	https://doi.org/10.1155/2019/1476217	V-type groove structure, Sinusoidal structure, random structure
87	Surface roughness evaluation in thin EN AW-6086-T6 Allow Plates after face milling process with different strategies	https://doi.org/10.3390/ma14113036	texture grooves,
88	Effect of shot peening on the surface integrity and fatigue proerty of gear steel 16Cr3NiWMoVNbE at room temperature	https://doi.org/10.1016/j.ijfatigue.2023.107668	parallel grinding tool marks with sharp bottoms
89	Changes in surface integrity of cemented tungsten carbide with shot peening treatment.	https://doi.org/10.1016/j.surfcoat.2021.127710	none
90	Research status of the influence of machining processes and surfaces modification technology on the surface integrity of bearing steel materials	https://doi.org/10.1007/s00170-023-10960-x	NA
91	Residual oxygen content and powder recycling :Effects on surface roughness and porosity of additively manufactured Ta-6Al-4V	https://doi.org/10.1016/j.addma.2021.102093	uniform topography, a texture in dependence on the scan direction,
92	Roughness-dependant wetting and surface tension of molten lead on alumina	https://doi.org/10.1016/S1003-6326(21)65671-6	" the more concentrated the colors are, the rougher the surface should be", rather smooth surface
93	Thermal-cycling, simulated brushing, and beverages induced color changes and roughness of CAD / CAM poly (methyl methcrylate) denture resins	https://doi.org/10.1088/2053-1591/ac406e	uniform surface, striations or groves following surface, uneven coating of dislodged tea layer, deeper grooves

94	The effect of coffee and whitening systems on surface roughness and gloss of CAD/CAM lithium disilicate glass ceramics	https://doi.org/10.1177/22808000211058866	brushing strikes, pitted surfaces, less deep and shallower indentation and appeared to have a smoother surface
95	Influence of Semi-Random and Regular Shot Peening on Selected Surface Layer Properties of Aluminium Alloy	https://doi.org/10.3390/ma14247620	dimples, orderly sequence, " there is no "contact" between the dimples", the dimples uniformly cover the machined surface, greater uniformity
96	Analysis of Surface Properties of Nickel Alloy Elements Exposed to impulse shot peening with the use of Positron Annihilation	https://doi.org/10.3390/ma14237328	even distribution of micro-roughness with clearly visible elevations and depressions resulting from the geometric-kinematic mapping of the tool in the workpiece. The elevation and depressions represent similar proportions in the total surface profile. The surface topography should be classified as a directed structure.
97	Surface texturing of fan-blade body by random-orbital polishing with in-line aqueous mist	https://doi.org/10.1007/s00170-021-07877-8	circumferential pattern, matte with anisotropic finish, shiny with fine scratch marks in cross-hatched circular pattern, satin with isotropic non-directional finish and homogeneous, sharp-peaked scallop height features, surface valleys, uniform, shallow furrows, sparse areas, deep furrows, localized areas, furrows, distributed areas
98	Roughness influence on the optical properties and scratch behavior of acrylic coating deposited on sandblasted glass	https://doi.org/10.1016/j.porgcoat.2016.09.014	cracks, asperities, radial cracks
99	A numerical and experimental investigation on the evolution of three-dimensional surface topography of 12Cr2Ni4A steel in shot peening	https://doi.org/10.1016/j.jmapro.2021.08.032	dimples
100	Effect of ultrasonic shot peening on surface integrity and fatigue performance of single-crystal superallow	https://doi.org/10.1016/j.jmatprotec.2021.117209	NA
101	Surface texture metrology for metal additive manufacturing: a review	https://doi.org/10.1016/j.precisioneng.2016.06.001	hatching lines, sharp protrusion, open pores, closed pores

Table A.1 *Corpus of the scientific with DOI and extracted terms*

(NA = no terms founded to describe surface)

Appendix B

Description of Heraldic vocabulary from Chapter 2

B.1 Tinctures (metals, colours, furs)

- argent: the metal silver; shown as white.
- or / gold: the metal gold; shown as yellow.
- silver: synonym of argent.
- gules: red.
- azure: blue.
- sable: black.
- vert / sinople: green (modern French sinople = vert).
- purpure: purple/violet.
- tenné / tenne: tawny; orange-brown “stain” colour.
- sanguine: blood-red/brownish red “stain.”
- murrey: mulberry; dark reddish-purple “stain.”
- cendree: ash-grey (rare).
- ermine: white fur powdered with black ermine spots.
- counter-ermine: white field with white ermine spots outlined black (or full inversion by tradition).
- vair: fur of alternating bell-shaped blue and white pieces.
- counter-vair: vair with columns reversed head-to-tail.
- potent: fur of T-shaped “potents” alternating in two tinctures.
- counter-potent: potent with columns reversed head-to-tail.
- pean: black field powdered with gold ermine spots.
- proper / au naturel: the charge in its natural (non-heraldic) colours.

B.2 Partitions (divisions of the field)

- per pale: divided vertically.
- per fess: divided horizontally.
- per bend: divided diagonally from dexter chief to sinister base.
- per bend sinister: diagonal the other way.
- per chevron: divided in an inverted V.
- per saltire: divided in an X.
- per pile: divided by a wedge/triangle pointing to base.
- per pall: divided in a Y (three parts meeting).
- quarterly: divided into four quarters.
- tierced: divided into three equal parts (direction must be stated).
- gyronny: field of triangular gyrons radiating from centre (e.g., of 8).
- bendy: field of parallel diagonal bands (multiple bends).
- paly: field of multiple pales (vertical stripes).
- barry: multiple horizontal bars/fesses of equal width.
- chevronny: repeated chevrons across the field.
- lozengy: field of alternating lozenges (diamonds).
- fusilly: field of elongated lozenges (fusils).
- compony / compony: a row of small rectangles (componés).
- countercompony: two rows of alternated rectangles forming a chequer.
- écartelé: French for quarterly.
- parti: French for per pale.
- coupé: French for per fess.
- tranché: French for per bend.

- taillé: French for per bend sinister.
- gironné: French for gyronny.
- burelé: many narrow bars.
- fascé: French for barry/fessy (stacked fesses).
- palé: French for paly.
- losangé: French for lozengy.
- chaussé: wedges from the flanks meeting at base, leaving a triangular field at chief.
- barry wavy: horizontal wavy bars alternating tinctures.
- tierced in pairle: three parts arranged in a Y (syn. per pall).

B.3 Figures (charges)

B.3.1 Ordinaries (honourable charges)

- chief: broad horizontal band at the top.
- pale: broad vertical band down the centre.
- bend: broad diagonal band (dexter chief to sinister base).
- bend sinister: diagonal the other way.
- fess: broad horizontal band across the middle.
- bar: a narrower horizontal band (often in multiples).
- chevron: inverted V-shape.
- cross: a cross throughout unless limited.
- saltire: X-shaped cross.
- pile: triangle issuing from chief toward base.
- pall: Y-shaped ordinary (pairle).
- orle: inner border following the shield’s outline.
- bordure: border around the edge.
- escutcheon: a small shield placed on the field.
- canton: small square, usually in dexter chief.
- inescutcheon: an escutcheon used as an overall charge (often “overall” or “in surtout”).

B.3.2 Roundels

- roundel: a plain disc (colour unspecified).
- bezant: gold roundel.
- plate: silver/white roundel.
- torteau: red roundel.
- hurt: blue roundel.
- pellet: black roundel.

B.3.3 Animals & creatures

- lion: heraldic lion (various attitudes).
- leopard: (heraldry) lion passant guardant; in modern English also the spotted cat—context rules.
- eagle: often displayed (wings spread, affronty).
- falcon / hawk: birds of prey (falcon/goshawk).
- dove: dove.
- raven: raven.
- martlet / merlette: footless stylised bird.
- griffin: lion’s body, eagle’s head and wings.
- wyvern: two-legged dragon.
- dragon: four-legged dragon.
- unicorn: unicorn.
- horse: horse.
- ox / bull / cow: ox / bull / cow.
- boar: wild boar.
- bear: bear.
- stag / hart: stag (male deer).
- goat / ram / sheep: goat / ram / sheep.
- cat / dog / wolf / fox: as named.
- tiger / panther: tiger / (in heraldry, panther may be spotted/flaming).
- serpent / snake: snake (often nowed = knotted).

B.4 Variants & Qualifiers

B.4.1 Animal postures (attitudes)

- rampant: reared up on one hind leg (lions).
- passant: walking, head in profile.
- passant guardant: walking, head facing the viewer.
- statant / statant guardant: standing still / facing viewer.
- couchant: lying down, head raised.
- courant: running.
- salient: springing; forelegs raised together.
- sejant / sejant erect: seated / seated upright.
- displayed: (birds) wings and legs spread, affronty (classic eagle).
- rising / volant: (birds) about to fly / in flight.
- naiant / hauriant: (fish) swimming horizontally / upright.
- addorsed: two charges back-to-back.
- respectant: two charges face-to-face.
- affronté / affronté(e): facing the viewer.
- contourné / contourné(e): turned to sinister.
- regardant: looking back over the shoulder.
- dormant: sleeping.

B.4.2 Qualifiers

- guardant: head facing the viewer (on a profile beast).
- armed: claws, beak, horns, etc., of a different tincture.
- langued: tongue of a different tincture.
- crowned / collared / gorged: wearing a crown / a collar / a collar (often of a coronet).
- winged: winged.
- queue fourchée: forked tail.
- couped: cut off cleanly (e.g., a head couped).
- caboshed: head affronty, no neck (stags, bulls, etc.).
- noduled: knotted/with nodes (cf. nowed for snakes).
- enfiled: threaded/pierced through by another charge (e.g., a crown enfiled by a sword).
- pierced: with a hole through it.
- charged: bearing a smaller charge on it.
- holding / supporting / seized: grasping / supporting / seizing an object.
-

B.4.3 Line shapes (edge treatments)

- engrailed / invected: scallops with points outward / inward.
- indented / dancetty: small serrations / deep zigzags.
- embattled: battlemented like a wall.
- raguly: rough, like lopped branches.
- dovetailed: interlocking dovetails.
- wavy: undulating.
- nebuly: cloud-like bulges.
- flory (fleury): edged with fleurs-de-lys.
- potenty: edged with T-shaped potents.
- masoned: with visible masonry joints.

References

1. ISO 25178-2:2021 Available online: https://www.iso.org/fr/standard/74591.html (accessed on 16 April 2023).
2. Lowe, J.M. Sensations et perceptions visuelles et tactiles de matériaux texturés., Université de Lyon, 2017.
3. Saussure, F. de *Cours de linguistique générale*; Otto Harrassowitz Verlag, 1989; ISBN 978-3-447-00798-6.
4. Charles, O.; Ivor, R. The Meaning of Meaning. A Study of the Influence of Language upon Thought and of the Science of Symbolism. **1923**.
5. ISO 704:2022 Available online: https://www.iso.org/fr/standard/79077.html (accessed on 25 August 2023).
6. Castellví, M.T.C. *Terminology: Theory, Methods and Applications*; John Benjamins Publishing, 1999; ISBN 978-90-272-9865-2.
7. Lerat, P. Approches linguistiques des langues spécialisées. *ASp. la revue du GERAS* **1997**, 1–10, doi:10.4000/asp.2926.
8. Desmet, I. Caractéristiques Morphologiques, Sémantiques, Syntaxiques et Discursives Des Vocabulaires Spécialisés. In Proceedings of the COFDELA Actes du 2 e colloque de Linguistique Appliquée; 1998; pp. 292–305.
9. Humbley, J. Is Terminology Specialized Lexicography? The Experience of French-Speaking Countries. *HERMES-Journal of Language and Communication in Business* **1997**, 13–31.
10. Mortureux, M.-F. Les Vocabulaires Scientifiques et Techniques. *Les Carnets du Cediscor. Publication du Centre de recherches sur la didacticité des discours ordinaires* **1995**, 13–25.
11. Leach, R. *Optical Measurement of Surface Topography*; Springer, 2011; Vol. 8;.
12. Surface Roughness Analysis and Measurement Techniques. In *Modern Tribology Handbook, Two Volume Set*; CRC Press, 2000 ISBN 978-0-429-12672-7.
13. Leach, R. *Characterisation of Areal Surface Texture*; Springer, 2013; ISBN 3-642-36458-6.
14. Whitehouse, D.J. *Handbook of Surface Metrology*; Routledge: New York, 2023; ISBN 978-0-203-75260-9.
15. Jiang, X.; Scott, P. j; Whitehouse, D. j; Blunt, L. Paradigm Shifts in Surface Metrology. Part I. Historical Philosophy. *Proceedings of the Royal Society A: Mathematical, Physical and Engineering Sciences* **2007**, *463*, 2049–2070, doi:10.1098/rspa.2007.1874.
16. Jiang, X.; Scott, P. j; Whitehouse, D. j; Blunt, L. Paradigm Shifts in Surface Metrology. Part II. The Current Shift. *Proceedings of the Royal Society A: Mathematical, Physical and Engineering Sciences* **2007**, *463*, 2071–2099, doi:10.1098/rspa.2007.1873.
17. Zanini, F.; Pagani, L.; Scott, P.J.; Savio, E.; Carmignato, S. Measurement of Additively Manufactured Surfaces with Re-Entrant Features by x-Ray Computed Tomography. In; American Society for Precision Engineering, ASPE, 2018 ISBN 978-1-887706-76-6.
18. Stout, K.J. The Development of Methods for the Characterisation of Roughness in Three Dimensions. *EUR 15178 EN of Commission of the European Communities* **1994**, *358*.
19. Blunt, L.; Jiang, X. *Advanced Techniques for Assessment Surface Topography: Development of a Basis for 3D Surface Texture Standards" Surfstand*"; Elsevier, 2003;
20. Kelechava, B. ASME B46.1-2019: Surface Texture (Roughness, Waviness, Lay). *The ANSI Blog* 2020.
21. Scheffer, B *Etat de Surface: Comparaison Des Différentes Normes Nationales. Rapport de La Régie Nationale Des Usines Renault et de La Direction Générale de La Recherche Scientifique et Technique*; Régie nationale des usines renault.; 1969;

22. Crameri, F.; Shephard, G.E.; Heron, P.J. The Misuse of Colour in Science Communication. *Nat Commun* **2020**, *11*, 5444, doi:10.1038/s41467-020-19160-7.
23. Whitehouse, D.J. *Handbook of Surface and Nanometrology*; 2nd ed.; CRC Press: Boca Raton, 2010; ISBN 978-0-429-14069-3.
24. Taniguchi, N. Current Status in, and Future Trends of, Ultraprecision Machining and Ultrafine Materials Processing. *CIRP Annals* **1983**, *32*, 573–582, doi:10.1016/S0007-8506(07)60185-1.
25. De Chiffre, L.; Lonardo, P.; Trumpold, H.; Lucca, D.A.; Goch, G.; Brown, C.A.; Raja, J.; Hansen, H.N. Quantitative Characterisation of Surface Texture. *CIRP Annals* **2000**, *49*, 635–652.
26. Forbes, A.B. Least-Squares Best-Fit Geometric Elements. Available online: https://eprintspublications.npl.co.uk/5050/ (accessed on 6 May 2025).
27. Brinkmann, S.; Bodschwinna, H.; Lemke, H.-W. Accessing Roughness in Three-Dimensions Using Gaussian Regression Filtering. *International Journal of Machine Tools and Manufacture* **2001**, *41*, 2153–2161, doi:10.1016/S0890-6955(01)00082-7.
28. Lou, S.; Jiang, X.; Scott, P.J. Application of the Morphological Alpha Shape Method to the Extraction of Topographical Features from Engineering Surfaces. *Measurement* **2013**, *46*, 1002–1008, doi:10.1016/j.measurement.2012.09.015.
29. KC, A. Introduction to Surface Roughness Measurement 2012.
30. Blateyron, F. The Areal Field Parameters. In *Characterisation of Areal Surface Texture*; Leach, R., Ed.; Springer: Berlin, Heidelberg, 2013; pp. 15–43 ISBN 978-3-642-36458-7.
31. Anselme, K.; Ponche, A.; Bigerelle, M. Relative Influence of Surface Topography and Surface Chemistry on Cell Response to Bone Implant Materials. Part 2: Biological Aspects. *Proc Inst Mech Eng H* **2010**, *224*, 1487–1507, doi:10.1243/09544119JEIM901.
32. Lemesle, J.; Moreau, C.; Deltombe, R.; Martin, J.; Blateyron, F.; Bigerelle, M.; Brown, C.A. Height Fluctuations and Surface Gradients in Topographic Measurements. *Materials* **2023**, *16*, 5408, doi:10.3390/ma16155408.
33. Lemesle, J.; Moreau, C.; Deltombe, R.; Blateyron, F.; Martin, J.; Bigerelle, M.; Brown, C.A. Top-down Determination of Fluctuations in Topographic Measurements. *Materials* **2023**, *16*, 473, doi:10.3390/ma16020473.
34. Lemesle, J.; Guibert, R.; Bigerelle, M. A Novel 3D Topography Stitching Algorithm Based on Reflectance and Multimap. *Applied Sciences* **2023**, *13*, 857, doi:10.3390/app13020857.
35. Berkmans, F.; Robache, F.; Mironova, A.; Nys, L.; Wieczorowski, M.; Bigerelle, M. Brushes and Brains: Does Handedness Influence Surface Topography of Art Painting? *Measurement* **2024**, *230*, 114521, doi:10.1016/j.measurement.2024.114521.
36. Bataille, C.; Luc, E.; Bigerelle, M.; Deltombe, R.; Dubar, M. Rolls Wear Characterization in Hot Rolling Process. *Tribology International* **2016**, *100*, 328–337, doi:10.1016/j.triboint.2016.03.012.
37. Bobrovskij, I.N. How to Select the Most Relevant Roughness Parameters of a Surface: Methodology Research Strategy. *IOP Conf. Ser.: Mater. Sci. Eng.* **2018**, *302*, 012066, doi:10.1088/1757-899X/302/1/012066.
38. 14:00-17:00 ISO 21920-3:2021 Available online: https://www.iso.org/standard/72228.html (accessed on 10 May 2023).
39. 14:00-17:00 ISO 25178-6:2010 Available online: https://www.iso.org/fr/standard/42896.html (accessed on 19 April 2023).
40. Helmholtz, H. von Helmholtz's Treatise on Physiological Optics, Vol 1 (Trans. from the 3rd German Ed.). **1924**, doi:10.1037/13536-000.
41. Helmli, F. Focus Variation Instruments. In *Optical measurement of surface topography*; Springer, 2011; pp. 131–166.
42. Danzl, R.; Helmli, F.; Scherer, S. Focus Variation -- a Robust Technology for High Resolution Optical 3D Surface Metrology. | EBSCOhost Available online:

https://openurl.ebsco.com/contentitem/doi:10.5545%2Fsv-jme.2010.175?sid=ebsco:plink:crawler&id=ebsco:doi:10.5545%2Fsv-jme.2010.175 (accessed on 4 February 2025).

43. Helmli, F.; Danzl, R.; Prantl, M.; Grabner, M. Ultra High Speed 3D Measurement with the Focus Variation Method. In Proceedings of the Fringe 2013; Osten, W., Ed.; Springer: Berlin, Heidelberg, 2014; pp. 617–622.
44. ISO 25178-606:2015 Available online: https://www.iso.org/fr/standard/59716.html (accessed on 4 February 2025).
45. Groot, P. de; Lega, X.C. de; Su, R.; Leach, R. Does Interferometry Work? A Critical Look at the Foundations of Interferometric Surface Topography Measurement. In Proceedings of the Applied Optical Metrology III; SPIE, September 3 2019; Vol. 11102, pp. 121–131.
46. DIN 4761 - 1978-12 - DIN Media Available online: https://www.dinmedia.de/en/standard/din-4761/725613 (accessed on 29 April 2025).
47. VSM-58070, Oberflächentypologie. Eingetragene Norm Der Scweizerischen Norm-Vereinigung. 1976.
48. ISO 1302:2002 Available online: https://www.iso.org/fr/standard/28089.html (accessed on 7 May 2025).
49. ISO 21920-1:2021 Available online: https://www.iso.org/fr/standard/72196.html (accessed on 7 May 2025).
50. ISO 8785:1998(Fr), Spécification Géométrique Des Produits — Imperfections de Surface — Termes, Définitions et Paramètres Available online: https://www.iso.org/obp/ui/#iso:std:iso:8785:ed-1:v1:fr (accessed on 10 May 2023).
51. Scott, P.J. Foundations of Topological Characterization of Surface Texture. *International Journal of Machine Tools and Manufacture* **1998**, *38*, 559–566, doi:10.1016/S0890-6955(97)00102-8.
52. Scott, P.J. Pattern Analysis and Metrology: The Extraction of Stable Features from Observable Measurements. *Proceedings of the Royal Society of London. Series A: Mathematical, Physical and Engineering Sciences* **2004**, *460*, 2845–2864, doi:10.1098/rspa.2004.1291.
53. Thomas, T.R. *Rough Surfaces, 2nd Edition*; World Scientific, 1998; ISBN 978-1-78326-236-6.
54. Evans, C.J.; Bryan, J.B. “Structured”, “Textured” or “Engineered” Surfaces. *CIRP Annals* **1999**, *48*, 541–556, doi:10.1016/S0007-8506(07)63233-8.
55. Lefèvre, M. Terminologie et Discours" Empratique". *Cahiers du CIEL* **2004**, *2004,* 53–70.
56. Bühler, K. *Sprachtheorie*; Jena Fischer, 1934; Vol. 2;.
57. Suh, N.P.; Saka, N. Surface Engineering. *CIRP Annals* **1987**, *36*, 403–408, doi:10.1016/S0007-8506(07)62632-8.
58. Stout, K.J. Engineering Surfaces—a Philosophy of Manufacture (a Proposal for Good Manufacturing Practice). *Proceedings of the Institution of Mechanical Engineers, Part B: Journal of Engineering Manufacture* **1998**, *212*, 169–174.
59. Stout, K.J.; Blunt, L. A Contribution to the Debate on Surface Classifications—Random, Systematic, Unstructured, Structured and Engineered. *International Journal of Machine Tools and Manufacture* **2001**, *41*, 2039–2044, doi:10.1016/S0890-6955(01)00069-4.
60. Torres, R.; Kaempfe, T.; Delaigue, M.; Parriaux, O.; Hoenninger, C.; Lopez, J.; Kling, R.; Mottay, E. Influence of Laser Beam Polarization on Laser Micro-Machining of Molybdenum. *Journal of Laser Micro Nanoengineering* **2013**, *8,* 188.
61. Basnyat, P.; Luster, B.; Muratore, C.; Voevodin, A.A.; Haasch, R.; Zakeri, R.; Kohli, P.; Aouadi, S.M. Surface Texturing for Adaptive Solid Lubrication. *Surface and Coatings Technology* **2008**, *203,* 73–79, doi:10.1016/j.surfcoat.2008.07.033.
62. Voevodin, A.A.; Zabinski, J.S. Laser Surface Texturing for Adaptive Solid Lubrication. *Wear* **2006**, *261*, 1285–1292, doi:10.1016/j.wear.2006.03.013.

63. Erdemir, A. Review of Engineered Tribological Interfaces for Improved Boundary Lubrication. *Tribology International* **2005**, *38*, 249–256, doi:10.1016/j.triboint.2004.08.008.
64. Kovalchenko, A.; Ajayi, O.; Erdemir, A.; Fenske, G.; Etsion, I. The Effect of Laser Surface Texturing on Transitions in Lubrication Regimes during Unidirectional Sliding Contact. *Tribology International* **2005**, *38*, 219–225, doi:10.1016/j.triboint.2004.08.004.
65. Maldonado-Cortés, D.; Peña-Parás, L.; Martínez, N.R.; Leal, M.P.; Quintanilla Correa, D.I. Tribological Characterization of Different Geometries Generated with Laser Surface Texturing for Tooling Applications. *Wear* **2021**, *477*, 203856, doi:10.1016/j.wear.2021.203856.
66. Šugárová, J.; Šugár, P.; Frnčík, M.; Necpal, M.; Moravčíková, J.; Kusý, M. The Influence of the Tool Surface Texture on Friction and the Surface Layers Properties of Formed Component. *Adv. Sci. Technol. Res. J.* **2018**, *12*, 181–193, doi:10.12913/22998624/85704.
67. Jain, A.; Bajpai, V. Mechanical Micro-Texturing and Characterization on Ti6Al4V for the Improvement of Surface Properties. *Surface and Coatings Technology* **2019**, *380*, 125087, doi:10.1016/j.surfcoat.2019.125087.
68. Wakuda, M.; Yamauchi, Y.; Kanzaki, S.; Yasuda, Y. Effect of Surface Texturing on Friction Reduction between Ceramic and Steel Materials under Lubricated Sliding Contact. *Wear* **2003**, *254*, 356–363, doi:10.1016/S0043-1648(03)00004-8.
69. Xu, C.; Xu, F.; Shi, L.; Gao, J.; Tu, L.; Zuo, D. Enhancement of Substrate-Coating Adherence of Boron-Doped Diamond Electrodes by Nanosecond Laser Surface Texturing Pretreatment. *Surface and Coatings Technology* **2019**, *360*, 196–204, doi:10.1016/j.surfcoat.2018.12.098.
70. Elleb, R.; Engel, T.; Antoni, F.; Fontaine, J.; Mermet, F.; Poncin-Epaillard, F. Study of Femtosecond Laser Multi-Scale Textured Steel Surfaces on the Wettability in Relation to Aging. *J Mater Sci* **2021**, *56*, 20169–20180, doi:10.1007/s10853-021-06574-x.
71. Laouamri, H.; Giljean, S.; Arnold, G.; Kolli, M.; Bouaouadja, N.; Tuilier, M.-H. Roughness Influence on the Optical Properties and Scratch Behavior of Acrylic Coating Deposited on Sandblasted Glass. *Progress in Organic Coatings* **2016**, *101*, 400–406, doi:10.1016/j.porgcoat.2016.09.014.
72. Danaraj, E.J.; Yeo, S.H. Surface Texturing of Fan-Blade Body by Random-Orbital Polishing with in-Line Aqueous Mist. *Int J Adv Manuf Technol* **2021**, *117*, 3011–3027, doi:10.1007/s00170-021-07877-8.
73. Sager, J.C. *Practical Course in Terminology Processing*; John Benjamins Publishing, 1990; ISBN 978-90-272-2076-9.
74. Santos, C.A. Terminological Contributions in Ontology Building: The Informal Specification Stage. *TOTh 2011 Proceedings-Terminology & Ontology: Theories and applications* 185.
75. Marsh, E.E.; Domas White, M. A Taxonomy of Relationships between Images and Text. *Journal of Documentation* **2003**, *59*, 647–672, doi:10.1108/00220410310506303.
76. Blunt, L.; Jiang, X.; Scott, P.J. Future Developments in Surface Metrology. In *Advanced Techniques for Assessment Surface Topography*; Elsevier, 2003; pp. 339–347 ISBN 978-1-903996-11-9.
77. Godly, T. Terminological Principles and Methods in the Subject Field of Chemistry. *Terminology: Applications in interdisciplinary communication. Amsterdam/Philadelphie: John Benjamins* **1993**, 141–164.
78. Antoniou, G.; Harmelen, F. van Web Ontology Language: OWL. In *Handbook on Ontologies*; Staab, S., Studer, R., Eds.; Springer: Berlin, Heidelberg, 2009; pp. 91–110 ISBN 978-3-540-92673-3.
79. Pérez, J.; Arenas, M.; Gutierrez, C. Semantics and Complexity of SPARQL. *ACM Trans. Database Syst.* **2009**, *34*, 16:1-16:45, doi:10.1145/1567274.1567278.

80. Senin, N.; Leach, R. Information-Rich Surface Metrology. *Procedia CIRP* **2018**, *75*, 19–26, doi:10.1016/j.procir.2018.05.003.
81. Senin, N.; Blunt, L. Characterisation of Individual Areal Features. In *Characterisation of Areal Surface Texture*; Leach, R., Ed.; Springer: Berlin, Heidelberg, 2013; pp. 179–216 ISBN 978-3-642-36458-7.
82. Hiltmann, T.; Riechert, T. Digital Heraldry. *The State of the*.
83. Schneider, P. Heraldry as a Historical Source to Conceptualize Medieval Spaces and Agents. *Data for History* **2021**.
84. Kim, S.-J.; Kim, T.-H.; Kong, J.-H.; Kim, Y.; Cho, C.-R.; Kim, S.-H.; Lee, D.-W.; Park, J.-K.; Lee, D.; Kim, J.-M. Dual-Scale Artificial Lotus Leaf Fabricated by Fully Nonlithographic Simple Approach Based on Sandblasting and Anodic Aluminum Oxidation Techniques. *Applied surface science* **2012**, *263*, 648–654.
85. Bhushan, B. Bioinspired Structured Surfaces. *Langmuir* **2012**, *28*, 1698–1714, doi:10.1021/la2043729.
86. Mazuel, L.; Sabouret, N. Semantic Relatedness Measure Using Object Properties in an Ontology. In Proceedings of the The Semantic Web - ISWC 2008; Sheth, A., Staab, S., Dean, M., Paolucci, M., Maynard, D., Finin, T., Thirunarayan, K., Eds.; Springer: Berlin, Heidelberg, 2008; pp. 681–694.
87. Matuszak, J.; Zaleski, K.; Skoczylas, A.; Ciecieląg, K.; Kęcik, K. Influence of Semi-Random and Regular Shot Peening on Selected Surface Layer Properties of Aluminum Alloy. *Materials* **2021**, *14*, 7620, doi:10.3390/ma14247620.
88. Hartig, O.; Bizer, C.; Freytag, J.-C. Executing SPARQL Queries over the Web of Linked Data. In Proceedings of the The Semantic Web - ISWC 2009; Bernstein, A., Karger, D.R., Heath, T., Feigenbaum, L., Maynard, D., Motta, E., Thirunarayan, K., Eds.; Springer: Berlin, Heidelberg, 2009; pp. 293–309.
89. Pastoureau, M. Figures de l'héraldique. *(No Title)* **1996**.
90. Menestrier, C.-F. *Le Veritable Art Du Blason Et L'Origine Des Armoiries*; Amaulry, 1675;
91. Pastoureau, M. *Traité d'héraldique*; Picard, 1993;
92. Galbreath, D.L.; Jéquier, L.; La Force, A. de C. *Manuel Du Blason*; Spes, 1977;
93. d'Haucourt, G.; Durivault, G. *Le Blason*; FeniXX, 1956;
94. Gide, A. *Journals: 1889-1913*; University of Illinois Press, 2000; ISBN 978-0-252-06929-1.
95. Edgar, G.A. *Classics on Fractals*; CRC Press, 2019; ISBN 0-429-71123-9.
96. Miton, H.; Morin, O. When Iconicity Stands in the Way of Abbreviation: No Zipfian Effect for Figurative Signals. *PLOS ONE* **2019**, *14*, e0220793, doi:10.1371/journal.pone.0220793.
97. Zipf, G.K. *Human Behavior and the Principle of Least Effort*; Human behavior and the principle of least effort; Addison-Wesley Press: Oxford, England, 1949; pp. xi, 573;.
98. Ferrer-i-Cancho, R.; Lusseau, D. Efficient Coding in Dolphin Surface Behavioral Patterns. *Complexity* **2009**, *14*, 23–25, doi:10.1002/cplx.20266.
99. Semple, S.; Hsu, M.J.; Agoramoorthy, G. Efficiency of Coding in Macaque Vocal Communication. *Biology Letters* **2010**, *6*, 469–471, doi:10.1098/rsbl.2009.1062.
100. Piantadosi, S.T.; Tily, H.; Gibson, E. Word Lengths Are Optimized for Efficient Communication. *Proceedings of the National Academy of Sciences* **2011**, *108*, 3526–3529.
101. Sigurd, B.; Eeg-Olofsson, M.; Van Weijer, J. Word Length, Sentence Length and Frequency – Zipf Revisited. *Studia Linguistica* **2004**, *58*, 37–52, doi:10.1111/j.0039-3193.2004.00109.x.
102. Zipf, G.K. *The Psycho-Biology of Language: An Introduction to Dynamic Philology*; Routledge, 2013; ISBN 1-315-00942-0.
103. Parker, J. A Glossary of Terms Used in Heraldry. *(No Title)*.
104. Burke, J.; Burke, B. *A General Armory of England, Scotland, and Ireland*; Edward Churton, 1842;

105. Tsizhmovska, N.L.; Martyushev, L.M. Word Length in Political Public Speaking: Distribution and Time Evolution. *Entropy* **2024**, *26*, 180, doi:10.3390/e26030180.
106. Mandelbrot, B.B.; Mandelbrot, B.B. *The Fractal Geometry of Nature*; WH freeman New York, 1982; Vol. 1;.
107. Steinhaus, H. Length, Shape and Area. In Proceedings of the Colloquium mathematicum; Polska Akademia Nauk. Instytut Matematyczny PAN, 1954; Vol. 3, pp. 1–13.
108. Richardson, L.F. The Problem of Contiguity: An Appendix to Statistics of Deadly Quarrels. *General systems yearbook* **1961**, *6*, 139–187.
109. Mandelbrot, B. How Long Is the Coast of Britain? Statistical Self-Similarity and Fractional Dimension. *science* **1967**, *156*, 636–638.
110. Mating, D.H. How Long Is a Piece of String? *The Cartographic Journal* **1968**, doi:10.1179/caj.1968.5.2.147.
111. Håkanson, L. The Length of Closed Geomorphic Lines. *Mathematical Geology* **1978**, *10*, 141–167, doi:10.1007/BF01032862.
112. Cross, S.S. The Application of Fractal Geometric Analysis to Microscopic Images. *Micron* **1994**, *25*, 101–113, doi:10.1016/0968-4328(94)90057-4.
113. Pippa, N.; Dokoumetzidis, A.; Demetzos, C.; Macheras, P. On the Ubiquitous Presence of Fractals and Fractal Concepts in Pharmaceutical Sciences: A Review. *International journal of pharmaceutics* **2013**, *456*, 340–352.
114. Tian, F.; Jiang, A.; Yang, T.; Qian, J.; Liu, R.; Jiang, M. Application of Fractal Geometry in Gas Sensor: A Review. *IEEE Sensors Journal* **2021**, *21*, 14587–14600, doi:10.1109/JSEN.2021.3072621.
115. Sánchez, I.; Uzcátegui, G. Fractals in Dentistry. *Journal of Dentistry* **2011**, *39*, 273–292, doi:10.1016/j.jdent.2011.01.010.
116. Stachowiak, G.W. Numerical Characterization of Wear Particles Morphology and Angularity of Particles and Surfaces. *Tribology International* **1998**, *31*, 139–157.
117. Chamorro-Posada, P. A Simple Method for Estimating the Fractal Dimension from Digital Images: The Compression Dimension. *Chaos, Solitons & Fractals* **2016**, *91*, 562–572, doi:10.1016/j.chaos.2016.08.002.
118. Reiss, M.A.; Sabathiel, N.; Ahammer, H. Noise Dependency of Algorithms for Calculating Fractal Dimensions in Digital Images. *Chaos, Solitons & Fractals* **2015**, *78*, 39–46, doi:10.1016/j.chaos.2015.07.004.
119. Koch, H.V. Sur Une Courbe Continue sans Tangente, Obtenue Par Une Construction Géométrique Élémentaire. *Arkiv for Matematik, Astronomi och Fysik* **1904**, *1*, 681–704.
120. Weierstrass, K. *Mathematische Werke*; G. Olms, 1902; Vol. 4;.
121. Gardner, M. Mathematical Games–in Which “Monster” Curves Force Redefinition of the Word “Curve.” *Scientific American* **1976**, *235*, 124–133.
122. Tricot, C. *Courbes et Dimension Fractale*; Springer Science & Business Media, 1999;
123. Peitgen, H.-O.; Jürgens, H.; Saupe, D. *Chaos and Fractals*; Springer New York: New York, NY, 2004; ISBN 978-1-4684-9396-2.
124. Eglash, R. *African Fractals: Modern Computing and Indigenous Design*; Rutgers University Press, 1999;
125. Vinoy, K.J.; Abraham, J.K.; Varadan, V.K. IMPACT OF FRACTAL DIMENSION IN THE DESIGN OF MULTI-RESONANT FRACTAL ANTENNAS. *Fractals* **2004**, *12*, 55–66, doi:10.1142/S0218348X04002288.
126. Rani, M.; Haq, R.U.; Verma, D.K. Variants of Koch Curve: A Review. *Int. J. Comput. Appl* **2012**, *2*, 20–24.
127. Barcellos, A. The Fractal Geometry of Mandelbrot. *The Two-Year College Mathematics Journal* **1984**, *15*, 98–114.
128. Vinoy, K.J.; Jose, K.A.; Varadan, V.K. Multi-Band Characteristics and Fractal Dimension of Dipole Antennas with Koch Curve Geometry. In Proceedings of the IEEE Antennas and

Propagation Society International Symposium (IEEE Cat. No. 02CH37313); IEEE, 2002; Vol. 4, pp. 106–109.

129. Efron, B. Bootstrap Methods: Another Look at the Jackknife. In *Breakthroughs in Statistics: Methodology and Distribution*; Kotz, S., Johnson, N.L., Eds.; Springer: New York, NY, 1992; pp. 569–593 ISBN 978-1-4612-4380-9.
130. Efron, B.; Tibshirani, R.J. *An Introduction to the Bootstrap*; Chapman and Hall/CRC: New York, 1994; ISBN 978-0-429-24659-3.
131. Whitehouse, D.J. The Parameter Rash — Is There a Cure? *Wear* **1982**, *83*, 75–78, doi:10.1016/0043-1648(82)90341-6.
132. Berkmans, F.; Lemesle, J.; Guibert, R.; Wieczorowski, M.; Brown, C.; Bigerelle, M. Two 3D Fractal-Based Approaches for Topographical Characterization: Richardson Patchwork versus Sdr. *Materials* **2024**, *17*, 2386, doi:10.3390/ma17102386.
133. Berkmans, F.; Lemesle, J.; Guibert, R.; Wieczorowski, M.; Brown, C.; Bigerelle, M. Uncertainty-Based Scale Identification and Process–Topography Interaction Analysis via Bootstrap: Application to Grit Blasting. *Fractal and Fractional* **2025**, *9*, 48, doi:10.3390/fractalfract9010048.
134. Arasse, D. *Le Détail : Pour Une Histoire Rapprochée de La Peinture*; Flammarion, 2021;
135. Qi, H.; Hughes, S. A New Method for Visual Stylometry on Impressionist Paintings. In Proceedings of the 2011 IEEE International Conference on Acoustics, Speech and Signal Processing (ICASSP); May 2011; pp. 2036–2039.
136. Alberti, L.B.; Bertolini, L. De Pictura : Redazione Volgare. **2011**, 1–471.
137. Beyaert, A. Plasticité et signification : le cas d'Eugène Leroy. *pr* **1999**, *27*, 125–131, doi:10.7202/030565ar.
138. Wollheim, R. Pictorial Style: Two Views. In *The Concept of style*; Lang, B., Ed.; Cornell University Press, 1987; pp. 183–202.
139. Wölfflin, H. *Principles of Art History*; Göteborgs universitet, 2009;
140. Zuccari, F. L'Idea de'Pittori, Scultori Ed Architetti, Turin 1607. *NAMEN-UND SACHVERZEICHNIS* **1961**.
141. Alpers, S. *Rembrandt's Enterprise: The Studio and the Market*; University of Chicago Press, 1990; ISBN 978-0-226-01518-7.
142. Dubuffet, J. *L'homme Du Commun à l'ouvrage*; Collection Folio/esSIAS; Gallimard, 1973;
143. White, R.; Kirby, J. Rembrandt and His Circle: Seventeenth-Century Dutch Paint Media Re-Examined'. *National Gallery technical bulletin* **1994**, *15*, 64–78.
144. Cominciamento, e Progresso Dell'arte Dell'intagliare in Rame : Colle Vite Di Molti de'più Eccellenti Maestri Della Stessa Professione | CiNii Research Available online: https://cir.nii.ac.jp/crid/1130282270547121536 (accessed on 3 February 2025).
145. Kühn, H. Zinc White. In *Artists' pigments; A handbook of their history and characteristics*; 1986; Vol. 1, pp. 169–186.
146. Salvant Plisson, J.; de Viguerie, L.; Tahroucht, L.; Menu, M.; Ducouret, G. Rheology of White Paints: How Van Gogh Achieved His Famous Impasto. *Colloids and Surfaces A: Physicochemical and Engineering Aspects* **2014**, *458*, 134–141, doi:10.1016/j.colsurfa.2014.02.055.
147. Gettens, R.J.; Kühn, H.; Chase, W.T. Lead White. In *Artists' pigments: a handbook of their history and characteristics. Volume 2*; 1993; pp. 67–81.
148. Gogh, V. van; Jansen, L.; Bakker, N.; Luijten, H. *Vincent Van Gogh : Les Lettres : Édition Critique Complète Illustrée*; Actes sud and Van Gogh museum and Huygens institute, 2009;
149. Elkhuizen, W.S.; Callewaert, T.W.; Leonhardt, E.; Vandivere, A.; Song, Y.; Pont, S.C.; Geraedts, J.M.; Dik, J. Comparison of Three 3D Scanning Techniques for Paintings, as Applied to Vermeer's 'Girl with a Pearl Earring.' *Heritage Science* **2019**, *7*, 1–22.

150. Mironova, A.; Robache, F.; Deltombe, R.; Guibert, R.; Nys, L.; Bigerelle, M. Digital Cultural Heritage Preservation in Art Painting: A Surface Roughness Approach to the Brush Strokes. *Sensors* **2020**, *20*, 6269, doi:10.3390/s20216269.
151. Bigerelle, M.; Guibert, R.; Mironova, A.; Robache, F.; Deltombe, R.; Nys, L.; Brown, C.A. Fractal and Statistical Characterization of Brushstroke on Paintings. *Surf. Topogr.: Metrol. Prop.* **2023**, *11*, 015019, doi:10.1088/2051-672X/acbe53.
152. Vincent Van Gogh Painting Sunset at Montmajour Discovered in Attic Unveiled in Amsterdam Available online: https://www.telegraph.co.uk/culture/art/art-news/10295733/Vincent-Van-Gogh-painting-Sunset-at-Montmajour-discovered-in-attic-unveiled-in-Amsterdam.html (accessed on 15 February 2024).
153. Naifeh, S.W.; Smith, G.W. *Van Gogh: The Life*; Random House Incorporated, 2011; ISBN 0-375-50748-5.
154. van Tilborgh, L.; Meedendorp, T.; van Maanen, O. “ Sunset at Montmajour”: A Newly Discovered Painting by Vincent van Gogh. *Burlington magazine* **2013**, *155*, 696–705.
155. Noce, V. Les errances d’un vrai-faux Van Gogh Available online: https://www.liberation.fr/culture/2003/12/13/les-errances-d-un-vrai-faux-van-gogh_455199/ (accessed on 4 March 2024).
156. France - Un tableau attribué à Van Gogh est retiré de la vente Available online: https://www.ledevoir.com/culture/arts-visuels/42836/france-un-tableau-attribue-a-van-gogh-est-retire-de-la-vente (accessed on 10 June 2024).
157. Querelles d’experts autour d’un Van Gogh vendu aux enchères en Gironde. *Le Monde.fr* 2003.
158. Nixon, M.S.; Aguado, A.S. Chapter 13 - Appendix 4: Color Images. In *Feature Extraction & Image Processing for Computer Vision (Third Edition)*; Nixon, M.S., Aguado, A.S., Eds.; Academic Press: Oxford, 2012; pp. 541–600 ISBN 978-0-12-396549-3.
159. Blackledge, J.M. Introduction. In *Digital Image Processing*; Blackledge, J.M., Ed.; Woodhead Publishing Series in Electronic and Optical Materials; Woodhead Publishing, 2005; pp. 1–21 ISBN 978-1-898563-49-5.
160. Lu, W.; Zhang, G.; Liu, X.; Zhou, L.; Chen, L.; Jiang, X. Prediction of Surface Topography at the End of Sliding Running-In Wear Based on Areal Surface Parameters. *Tribology Transactions* **2014**, *57*, 553–560, doi:10.1080/10402004.2014.887165.
161. Lonardo, P.M.; Trumpold, H.; De Chiffre, L. Progress in 3D Surface Microtopography Characterization. *CIRP Annals* **1996**, *45*, 589–598, doi:10.1016/S0007-8506(07)60513-7.
162. Zhang, Y.; Fu, T.; Zhu, J.; Zhang, X. Microstructure Evolution, Growth Kinetics and Formation Mechanisms of Silicon-Rich NbSi2 Coatings on Nb Substrate. *Journal of Materials Research and Technology* **2023**, *24*, 6076–6087, doi:10.1016/j.jmrt.2023.04.222.
163. Winkeljann, B.; Leipold, P.-M.A.; Lieleg, O. Macromolecular Coatings Enhance the Tribological Performance of Polymer-Based Lubricants. *Advanced Materials Interfaces* **2019**, *6*, 1900366, doi:10.1002/admi.201900366.
164. Patois, T.; Lakard, B.; Monney, S.; Roizard, X.; Fievet, P. Characterization of the Surface Properties of Polypyrrole Films: Influence of Electrodeposition Parameters. *Synthetic Metals* **2011**, *161*, 2498–2505, doi:10.1016/j.synthmet.2011.10.003.
165. Pawlus, P.; Reizer, R.; Wieczorowski, M.; Krolczyk, G.M. Study of Surface Texture Measurement Errors. *Measurement* **2023**, *210*, 112568, doi:10.1016/j.measurement.2023.112568.

Résumé

Cette thèse de doctorat propose un changement de paradigme méthodologique dans le domaine de la métrologie des surfaces, en remettant en question le cadre binaire dominant qui se concentre principalement sur l'influence des procédés de modification des surfaces ou sur l'optimisation de certaines fonctionnalités de surface. Le cadre proposé, conceptualisé sous la forme d'un *Spectre d'Acquisition de l'Information de Surface*, repositionne l'analyse des surfaces dans une perspective épistémologique et interdisciplinaire plus large, dépassant le strict cadre des applications industrielles. Chaque chapitre contribue à l'élaboration de ce cadre inédit : le chapitre 1 établit un système terminologique standardisé pour la description des surfaces, inspiré des conventions héraldiques ; le chapitre 2 quantifie la complexité graphique et textuelle multi-échelle des systèmes héraldiques à travers des modèles mathématiques ad hoc ; le chapitre 3 aborde les artefacts de discrétisation numérique dans les géométries fractales en prenant pour cas d'étude le flocon de Von Koch ; le chapitre 4 introduit une nouvelle méthode de caractérisation fractale des surfaces sablées à l'aide du paramètre de rugosité Sdr et d'un filtre gaussien ; enfin, le chapitres 5 prolongent cette méthodologie à l'analyse topographique d'objets d'art. En intégrant des champs conceptuels tels que la théorie du langage, la syntaxe de l'image, la complexité fractale et l'évaluation des surfaces, cette recherche établit les fondements d'une reconfiguration transdisciplinaire de la métrologie des surfaces et ouvre la voie à l'émergence de nouveaux sous-domaines dans cette discipline.

Mots clés : *Topographie de surface, rugosité, terminologie, ontologie, analyse multiéchelle, patrimoine, héraldique, fractals, complexité, art, peinture*

Streszczenie

Niniejsza rozprawa doktorska wprowadza alternatywny paradygmat metodologiczny w obszarze metrologii powierzchni, podważając dominującą, dwutorową ramę analityczną, koncentrującą się głównie albo na wpływie procesów modyfikacji powierzchni, albo na optymalizacji określonych funkcjonalności powierzchni. Proponowane ujęcie, konceptualizowane jako Spektrum Pozyskiwania Informacji o Powierzchni, na nowo sytuuje analizę powierzchni w szerszym kontekście epistemologicznym i interdyscyplinarnym, wykraczając poza ramy zastosowań przemysłowych. Każdy rozdział tej pracy współtworzy owo nowe ujęcie: Rozdział 1 formułuje zestandaryzowany system terminologiczny opisu powierzchni inspirowany konwencjami heraldycznymi; Rozdział 2 ilościowo określa wieloskalową złożoność graficzną i tekstową systemów heraldycznych za pomocą dedykowanych modeli matematycznych; Rozdział 3 analizuje artefakty dyskretyzacji cyfrowej w geometriach fraktalnych, wykorzystując płatek śniegu von Kocha jako punkt odniesienia; Rozdział 4 wprowadza nową metodę charakteryzacji fraktalnej powierzchni piaskowanych z użyciem parametru chropowatości Sdr oraz filtrowania Gaussa; a Rozdział 5 rozszerza tę metodykę na topograficzną analizę obiektów sztuki. Integrując domeny pojęciowe, takie jak teoria języka, składnia obrazu, złożoność fraktalna i ocena powierzchni, niniejsze badania ustanawiają podstawy transdyscyplinarnej rekonfiguracji metrologii powierzchni i wskazują ścieżki powstawania nowych subdyscyplin w jej obrębie.

Słowa kluczowe : *Topografia powierzchni, chropowatość, terminologia, ontologia, analiza wieloskalowa, dziedzictwo kulturowe, heraldyka, fraktale, złożoność, sztuka, malarstwo*

Abstract

This doctoral dissertation introduces an alternative methodological paradigm within the domain of surface metrology, challenging the dominant dual-axis framework which primarily focuses on either the impact of surface modification processes or the optimization of specific surface functionalities. The proposed framework, conceptualized as the *Surface Information Acquisition Spectrum*, repositions surface analysis within a broader epistemological and interdisciplinary context, extending beyond the confines of industrial applications. Each chapter of this work contributes to the articulation of this new framework: Chapter 1 formulates a standardized terminological system for surface description inspired by heraldic conventions; Chapter 2 quantifies the multi-scale graphical and textual complexity of heraldic systems through bespoke mathematical models; Chapter 3 addresses digital discretization artifacts in fractal geometries, using the Von Koch snowflake as a benchmark; Chapter 4 introduces a novel method for fractal characterization of sandblasted surfaces via the Sdr roughness parameter and Gaussian filtering; and Chapter 5 extend this methodology to the topographic analysis of art objects. By integrating conceptual domains such as language theory, image syntax, fractal complexity, and surface evaluation, this research establishes the foundations for a transdisciplinary reconfiguration of surface metrology and suggests pathways for the emergence of new subfields within the discipline.

Key words: *Surface topography, roughness, terminology, ontology, multiscale analysis, cultural heritage, heraldry, fractals, complexity, art, painting*